Resonant Inelastic X-ray Scattering Studies of Elementary Excitations

Luuk Ament

Resonant Inelastic X-ray Scattering Studies of Elementary Excitations

PROEFSCHRIFT

ter verkrijging van
de graad van Doctor aan de Universiteit Leiden,
op gezag van Rector Magnificus prof. mr. P. F. van der Heijden,
volgens besluit van het College voor Promoties
te verdedigen op donderdag 11 november 2010
klokke 13.45 uur

door

Lucas Johannes Peter Ament

geboren te Winterswijk in 1982

Promotiecommissie:

Promotor: prof. dr. J. van den Brink
Overige leden: prof. dr. J. P. Hill (Brookhaven National Laboratory)
prof. dr. J. M. van Ruitenbeek (Universiteit Leiden)
prof. dr. C. W. J. Beenakker (Universiteit Leiden)
prof. dr. M. A. van Veenendaal (Argonne Nat. Lab. & Northern Illinois University)
prof. dr. G. Ghiringhelli (Politecnico di Milano)

ISBN 978-90-8593-087-7
Casimir PhD Series, Delft-Leiden 2010-25
The research presented in this thesis was supported by FOM.

Contents

1 **Introduction** **1**
- 1.1 Resonant Inelastic X-ray Scattering (RIXS) 1
- 1.2 Excitations of strongly correlated systems 9
- 1.3 This thesis 11

2 **Theory of Resonant Inelastic X-ray Scattering** **13**
- 2.1 Introduction 13
- 2.2 Electron-photon coupling 14
- 2.3 Kramers-Heisenberg equation 20
- 2.4 Direct and Indirect RIXS 26
- 2.5 Ultra-short core hole lifetime expansion 28

3 **Charge excitations** **31**
- 3.1 Introduction 31
- 3.2 UCL approach to charge scattering 32
- 3.3 Corrections to the cross section for strong core hole potentials . . . 48
- 3.4 Polarization dependence of transition metal K edge RIXS 50
- 3.5 Comparison to experiments 52

4 **Magnetic RIXS on 2D cuprates** **53**
- 4.1 Introduction 53
- 4.2 Theory of magnetic excitations 55
- 4.3 Magnetic RIXS scattering amplitude 60
- 4.4 Copper K edge 64
- 4.5 Copper L edge 80
- 4.6 Copper L edge of doped cuprates 93
- 4.7 Oxygen K edge 98
- 4.8 Two-magnon screening of holes in the t-J model probed by angle-resolved photoemission 106

5 Orbital RIXS 115
5.1 Introduction 115
5.2 Theory 116
5.3 RIXS spectra of 2D e_g systems 119
5.4 RIXS spectra of $YTiO_3$ 126

6 RIXS in systems with strong spin-orbit coupling 151
6.1 Introduction 151
6.2 Theory of Sr_2IrO_4 153
6.3 Iridium L edge cross section 156

7 Phonon RIXS 171
7.1 Introduction 171
7.2 Electron-phonon coupling 173
7.3 RIXS cross section for phonons 175
7.4 dd excitations dressed by phonons 181
7.5 Conclusions 183

8 Outlook – X-ray Free Electron Lasers 185
8.1 Bosonic enhancement in an XFEL 186
8.2 X-ray scattering with an XFEL 186

Appendices 191

A QED 191
A.1 H_Ψ to second order 191
A.2 H_Ψ to third order 192

B $YTiO_3$ 197
B.1 RIXS – Single site processes 197
B.2 Multiplet factors 198
B.3 The operators $\hat{\Gamma}$ in terms of orbitons 199
B.4 RIXS – two-site processes with superexchange model 201

C Phonon RIXS 203

D Magnetic spectral weight at the Γ point in 2D cuprates 205
D.1 $\bar{H}^{(4)}_{\text{eff}}$ to fourth order in t/U 205
D.2 Scattering amplitude to fourth order in t/U 210

Bibliography 213

Samenvatting 227

Publications 231

Curriculum vitae **233**

Chapter 1

Introduction

The subject of this thesis is Resonant Inelastic X-ray Scattering (RIXS), which is a technique to study, amongst others, the properties of materials. This is done by making a sort of X-ray photo (called a spectrum) in a synchrotron – a huge, circular particle accelerator (with a circumference of a few hundred meters) that produces very high intensity X-rays. These X-ray spectra are compared to calculations based on various models of the material under study. This way, it is possible to falsify the models.

An improtant category of materials that are often investigated with RIXS are the stongly correlated electron materials. To this class belong, for instance, the high critical temperature superconductors that can conduct an eletrical current without resistance when they are cooled below the so-called critical temperature. In this thesis, we calculate and discuss the RIXS spectra for various models of a range of strongly correlated electron materials, each with its own special properties.

1.1 Resonant Inelastic X-ray Scattering (RIXS)

1.1.1 What is RIXS?

RIXS is an X-ray ‘photon in – photon out’ technique, meaning that one irradiates a sample with X-rays, and observes the scattered X-ray photons. In RIXS, one is only interested in processes in which the photons lose energy (and momentum) to the sample, leaving it in an excited state. Hence the ‘inelastic’. RIXS is a resonant technique, meaning that the energy of the incident photons corresponds to a certain resonance in the system: an electron from a deep-lying atomic core state is promoted to an empty state around the Fermi level. An example is the atomic 1s → 4p transition in Cu^{2+} ions. After a very short time, the hole in the core levels (the so-called core hole) is filled by the same or another electron, producing the outgoing X-ray photon.

The quantities one measures in RIXS are the momentum and energy of the outgoing photons. Because the energy and momentum of the incident photons can be chosen by the experimentalist, one can deduce what energy and momentum were left behind in the sample, using conservation laws. Thus RIXS enables one to measure the dispersion of excitations. In principle, it is also possible to measure the outgoing photon's polarization, although this has rarely been done in practice yet [1]. It would provide additional information on the type of excitations that are created in the RIXS process. Basically all excitations of solids can be probed by RIXS, ranging from charge, spin, orbital and lattice excitations to exotic mixed spin-orbital ones. In principle, the only constraint is that the excitations should be overall charge-neutral, as no electrons are added to or removed from the system.

One might wonder what the advantage is of tuning to a resonance, because the theoretical treatment of resonant scattering processes is much more complicated than non-resonant ones. A big advantage is that at resonance, the cross section is enhanced by many orders of magnitude. Choosing a resonance also gives control over where in the unit cell excitations are made. Further, the more complicated scattering process enables one to probe more types of excitations, like magnetic ones.

Comprehensive overviews of RIXS can be found in Refs. [2] and [3]. Much of this chapter is published in the latter work.

1.1.2 Direct and indirect RIXS

Excitations can be made in two distinct ways, which are called *direct* RIXS and *indirect* RIXS. Direct RIXS is the simplest of the two: a core electron is excited into the valence band, and then an electron from another valence state fills the core hole, emitting an outgoing X-ray photon. The process is illustrated in Fig. 1.1. The RIXS process creates a valence excitation with momentum $\hbar\mathbf{k} - \hbar\mathbf{k}'$ and energy $\hbar\omega_{\mathbf{k}} - \hbar\omega_{\mathbf{k}'}$, where the primed quantities refer to the outgoing photon and the unprimed ones to the incoming photon.

Indirect RIXS has one extra step compared to direct RIXS: in the intermediate state, the valence electrons scatter off the core hole. This leads to excitations of the valence electrons. When the core hole decays, the system is left in an excited state. This process is shown in Fig. 1.2. The interaction is mediated either by the Coulomb force of (mainly) the localized core hole, or by the Pauli exclusion principle. The latter interaction occurs when the photo-excited electron blocks the movements of the valence electrons. Typically, the photo-excited electron ends up far above the Fermi level and acts as a spectator, *i.e.*, it does not interact

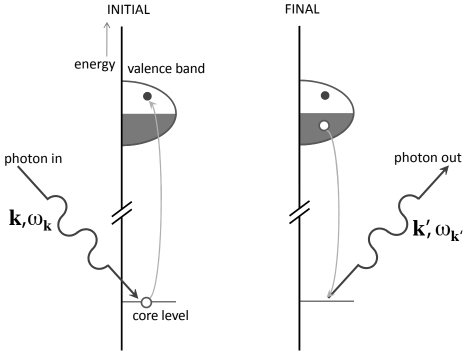
INITIAL
FINAL
energy
valence band
photon in
$\mathbf{k},\omega_{\mathbf{k}}$
core level
photon out
$\mathbf{k}',\omega_{\mathbf{k}'}$

Figure 1.1: In the direct RIXS process the incoming X-ray photon excites an electron from a deep-lying core level into an empty valence level. The empty core state is then filled by an electron from the occupied valence states under the emission of an X-ray. Figure reproduced with permission from Ref. [3].

strongly with the valence electrons [4, 5].

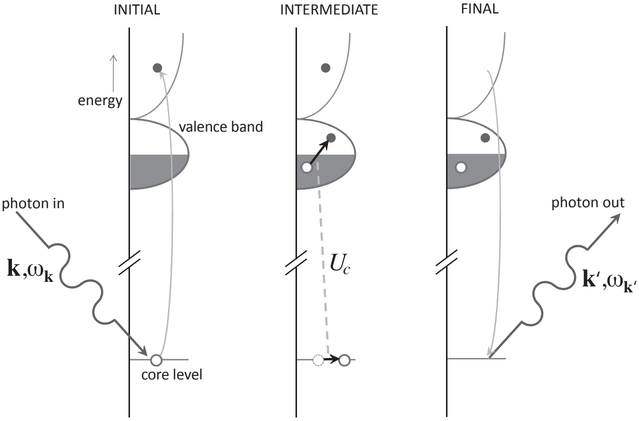
INITIAL
INTERMEDIATE
FINAL
energy
valence band
photon in
$\mathbf{k},\omega_{\mathbf{k}}$
U_c
core level
photon out
$\mathbf{k}',\omega_{\mathbf{k}'}$

Figure 1.2: In an indirect RIXS process, an electron is excited from a deep-lying core level into the conductance band. Excitations are created through the Coulomb interaction U_c between the core hole (and in some cases the photo-excited electron) and the valence electrons. In chapter 4, we show that the interaction can also be the consequence of the Pauli exclusion principle. Finally, the core hole is filled by the photo-excited electron. Figure reproduced with permission from Ref. [3].

1.1.3 Features and limitations of RIXS

RIXS has a number of features that set it apart from other spectroscopic techniques like Angle-Resolved Photo-Emission Spectroscopy (ARPES) and inelastic neutron scattering:

1. RIXS measures the *energy and momentum dependence* of excitations in a

large part, or even all, of the Brillouin zone. This comes about because X-ray photons have a very high energy and momentum, in contrast to optical photons (see Sec. 1.1.4). Therefore, the available phase space for RIXS experiments is huge compared to many other probes.

2. *Polarization sensitivity.* In principle, it is possible to measure the outgoing photon's polarization. This has rarely been done in practice yet [1], though the incident photon's polarization is frequently varied. One can make use of various polarization-related selection rules to characterize the symmetry and nature of the excitations. It is important to note that a polarization change of the photon is related to an angular momentum change. Conservation of angular momentum ensures that any angular momentum lost by the scattered photons has been transferred to the excitations in the solid.

3. *Chemical specificity.* Varying the energy of the incident photons, it can be tuned to different resonances, and one can choose which core electron to excite to which valence orbital. The different resonances are called 'edges'[1]. This makes RIXS not only element-specfic, but also orbital-specific. Further, it is possible to tune the incident photons to chemically inequivalent ions, like in $\mathrm{La}_{2-x}\mathrm{Sr}_x\mathrm{CuO}_4$, where one can probe either occupied or unoccupied copper ions, see Sec. 4.6. This is possible only if the two chemically inequivalent sites are resolvable in the X-ray absorption spectrum.

4. *Bulk sensitivity.* The penetration depth of X-rays depends strongly on their energy. This depth can be of the order of a few μm in the hard x-ray regime (*i.e.*, around 10 keV) and of the order of 0.1 μm in the soft x-ray regime (around 1 keV). This makes RIXS bulk-sensitive: in general, the scattering takes place far away from the surface of the sample.

5. *Small sample volume.* Compared to neutron scattering, X-ray scattering experiments need only very tiny samples. This is because neutron sources produce much less particles per second per m^2 than X-ray synchrotrons. Further, the interaction of neutrons with the sample is much weaker than that of X-rays. That RIXS needs only very small samples enables one to study nano objects or materials that can only be grown in thin films.

There are also a number of limitations to RIXS:

1. The experiments require *many incident photons* to collect enough scattered photons in a reasonable time. Higher energy and momentum resolutions require more time.

---

[1] The edges are labelled according to the core electron that is excited: promoting an electron with principal quantum number $n = 1$ is called the K edge, $n = 2$ is called the L edge, $n = 3$ M edge, etc. [6]

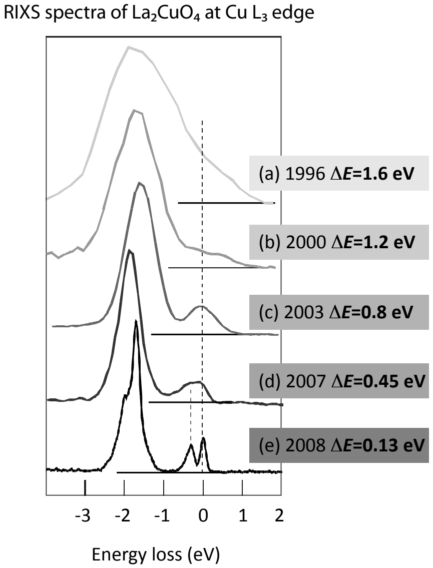

Figure 1.3: Progress in RIXS resolution at the Cu L edge (931 eV). (a) Ichikawa *et al.* [7], BLBB @ Photon Factory (b) Duda *et al.* [8], I511-3 @ MAX II, (c) Ghiringhelli *et al.* [9], AXES @ ID08, ESRF (d) Braicovich *et al.* [10], AXES @ ID08, ESRF (e) Braicovich *et al.* [11], SAXES @ SLS. Figure by G. Ghiringhelli and L. Braicovich, reproduced with permission.

2. *Energy resolution.* Because there is a huge difference between the energy scale of the X-ray photons and the energy scale of the elementary excitations we are interested in, a tremendous resolving power is needed for RIXS experiments. For example, at the Cu^{2+} 1s → 4p transition (corresponding to roughly 9 keV) the resolving power needs to be 10^5 in order to get an energy resolution of 90 meV. For a long time, RIXS has been limited to energy resolutions of the order of 1 eV. However, recent progress in RIXS instrumentation has been dramatic and this situation is now changing, see Fig. 1.3.

Note that these two limitations are not independent of each other: a low photon flux can be one of the factors that limit the energy resolution. (Other factors that play a role are, *e.g.*, the instrument's spectrometer or the distribution of the energy of the incident photons.)

1.1.4 Comparison to other spectroscopies

When one wants to probe the properties of solid state systems, there are many spectroscopies available, each with its own advantages and disadvantages. In this section we briefly outline the contrasts of RIXS with some of the more established experimental techniques of condensed matter physics. We restrict ourselves to spectrosopies that do not change the total charge of the system.

- IXS. The term inelastic X-ray scattering (IXS) is reserved for non-resonant processes where the photon scatters inelastically by interacting with the charge density of the system. IXS does not involve core holes to excite the system. It measures the dynamics charge structure factor $S(\mathbf{q},\omega)$.

- XAS. X-ray absorption spectroscopy (XAS) is the first step of the RIXS process: an electron is excited from a core orbital to an empty state, above the Fermi level. A common way to measure X-ray absorption is to study the decay products of the core hole that the absorbed X-ray has created, either by measuring the electron yield from a variety of Auger and higher-order processes (known as electron yield) or by measuring the radiative decay (fluorescence yield). The total fluorescence yield corresponds approximately to the integration of all possible RIXS processes.

- Raman scattering. Raman scattering with optical or UV photons is confined to zero momentum transfer because of the low energy of these photons[2]. It is still possible to probe elementary excitations with non-zero momentum $\hbar\mathbf{k}$ in an indirect way by exciting two of them: one with momentum $+\hbar\mathbf{k}$ and one with $-\hbar\mathbf{k}$. This is done in, for instance, bimagnon Raman scattering in the high-T_c cuprates. An advantage of Raman scattering over RIXS is its energy resolution, which not only makes it possible to probe excitations at very low energies, but also resolve their line shapes. Optical Raman scattering can be employed at resonance as well, although it is restricted to resonances up to a few eV due to the low energy of the optical photons.

- Inelastic neutron scattering. The dispersion of neutrons in free space is $E = (\hbar\mathbf{k})^2/2m$ where $m = 1.67 \cdot 10^{-27}$ kg. To reach the Brillouin zone boundary at momentum $\hbar k \approx 1\ \hbar\text{Å}^{-1}$, the neutrons need to have an energy of at least $E \approx 2.1$ meV. This is a problem for probing excitations at the energy scale of 1 eV, some two orders of magnitude larger than the energy carried by neutrons with momenta corresponding to the inverse lattice parameter. High energy neutrons pass through the crystal very fast, reducing the already small neutron cross section. Further, spin-1/2 neutrons can transfer 0 or 1 unit of angular momentum to the system, while spin-1 photons can also probe $\Delta J_z = 2$ final states.

- EELS. The Electron energy loss spectroscopy (EELS) cross section is determined by the charge structure factor $S(\mathbf{q},\omega)$ of the system under study [12, 13] and is, therefore, closely related to IXS and RIXS (see chapter 3). It is an electron-in electron-out process. The EELS intensity is limited due to space charge effects in the beam. It has the advantage that it is very sensitive for low momentum transfers, but its intensity rapidly decreases for large momentum transfers. Further, at large momentum transfer, multiple scattering effects become increasingly important, making it hard to interpret the spectra above $\sim 0.5 - 1.0$ Å^{-1}. Since momentum resolved EELS is measured in transmission, it requires thin samples. Measurements in the presence of electromagnetic fields are not possible due to their detrimental effect on the electron beam. There are no such restrictions for X-ray scattering.

---

[2] Visible light has a wave length of $\lambda \approx 500$ nm, and therefore carries momentum $\hbar k = 2\pi\hbar/\lambda \approx 1.3 \cdot 10^{-3}\ \hbar\text{Å}^{-1}$. At the edge of the Brillouin zone, the momentum is typically $\pi\hbar/a \sim 10^{10}\ \hbar\text{m}^{-1} \approx 1\ \hbar\text{Å}^{-1}$ (assuming a lattice constant $a \approx 3$ Å). Therefore, Raman scattering experiments can only probe the center of the Brillouin zone. For comparison, the photon energy necessary to probe this Brillouin zone boundary is approximately $\hbar ck \approx 2.0$ keV.

1.1.5 General features of RIXS spectra

Most RIXS spectra have a number of features in common: almost all have an elastic peak, *i.e.*, scattered photons with zero energy loss. Next to the elastic peak, there is the inelastic spectral weight, in which one is ultimately interested because it gives information about the energy and momentum of the excitations of the material. Then, there is the question of normalization of the data, which comes up in every RIXS study. In the next chapters of this thesis, the inelastic features are extensively discussed. Here, we will briefly touch upon the elastic line and the normalization.

Elastic line. Elastic scattering obscures the low energy excitations in many RIXS experiments. For instance, at the transition metal K and M edge, the elastic line is huge compared to the low energy inelastic features [14, 15].

The amplitude for elastically scattering a photon from wave vector $\mathbf{k}$ to $\mathbf{k}'$, starting from a source at position $\mathbf{r}_a$ and scattering from an ion at position $\mathbf{r}$ to the detector at position $\mathbf{r}_b$, is composed of three parts. First, the amplitude to go from the source to the scattering ion is[3] $e^{i\mathbf{k}\cdot(\mathbf{r}-\mathbf{r}_a)}$. Second, the amplitude of the scattering event itself, including both resonant and non-resonant scattering, is denoted by the complex number ζ. Third, the amplitude to go from the ion to the detector is $e^{i\mathbf{k}'\cdot(\mathbf{r}_b-\mathbf{r})}$. Multiplying all amplitudes, we get a total scattering amplitude of $\zeta e^{i(\mathbf{k}-\mathbf{k}')\cdot\mathbf{r}} e^{-i\mathbf{k}\cdot\mathbf{r}_a+i\mathbf{k}'\cdot\mathbf{r}_b}$. The second exponential does not depend on the position of the scattering ion, and it may be absorbed in ζ.

RIXS is a coherent process, which means that an incident photon can be absorbed at any of the N equivalent sites i of the solid, and all these processes interfere. The total elastic scattering amplitude is therefore

$$\mathcal{F}_{\text{el}} = \frac{1}{N} \sum_i \zeta_i e^{i(\mathbf{k}-\mathbf{k}')\cdot\mathbf{r}_i}. \tag{1.1}$$

In the case of a perfect crystal, all ζ_i are equal, resulting in Bragg peaks: $\mathcal{F}_{\text{el}} = \zeta \sum_{\mathbf{G}} \delta_{\mathbf{q},\mathbf{G}}$ where $\mathbf{q} = \mathbf{k} - \mathbf{k}'$ and $\mathbf{G}$ is a reciprocal lattice vector. For transferred momenta away from Bragg conditions, there is no elastic line. Note that this is a general statement, independent of the details of the scattering process. The question therefore is not why transition metal L edges have a small elastic line, but why it is big at the K and M edges (see, *e.g.*, Refs. [11, 14, 15]).

---

[3] We discard the modulus of this amplitude because it is irrelevant to the calculation.

One reason could be that the huge observed elastic peaks are not truely elastic peaks, but rather consist of low energy excitations, like phonons, that cannot be resolved from the true elastic signal [3]. There is evidence for this from high resolution measurements at the Cu K edge of CuO_2 by Yavaş *et al.* [16].

Elastic scattering can also be seen away from Bragg conditions for crystals with imperfections. There are many ways for crystals to be imperfect:

- N does not go to infinity, for example, because the X-ray beam illuminates only a finite volume, or some ions are missing. When the sample is a very smooth slab of finite thickness (say n ions), crystal truncation rods appear: the Bragg peaks broaden in the direction perpendicular to the slab as $2/nq_\perp^2$ where n is the thickness (in number of layers) and $q_\perp$ is the transferred momentum perpendicular to the surface, measured from the Bragg peak [17]. Taking into account the penetration depth gives a similar effect.

- Thermal motion, defects or inhomogeneities, strain, etc. cause the ions to go out of their equilibrium position: $\mathbf{r}_i = \mathbf{R}_i + \mathbf{u}_i$, where $\mathbf{u}_i$ is the displacement from the equilibrium position $\mathbf{R}_i$. For small, uncorrelated displacements in an otherwise perfect crystal, one finds to order $\mathcal{O}(\langle \mathbf{u}^2 \rangle)$:

$$\langle I_{\mathrm{el}}(\mathbf{q}) \rangle = \sum_{\mathbf{G}} \delta_{\mathbf{q},\mathbf{G}} \left(1 - \frac{1}{3} \langle \mathbf{u}^2 \rangle \mathbf{G}^2 \right) + \frac{1}{3N} \langle \mathbf{u}^2 \rangle \mathbf{q}^2 \tag{1.2}$$

  where $\langle \dots \rangle$ denotes an average over many experiments, assuming that the lattice moves a lot over the course of the experiment. Spectral weight is transferred from the Bragg peaks to other parts of the Brillouin zone. The elastic scattering away from Bragg conditions increases with $\mathbf{q}^2$, and is therefore expected to be strongest at the high energy edges [18].

- $\zeta_i \neq \zeta_j$. When one ion's electronic structure is different, the amplitude for scattering a photon changes. When the change is periodic, as in typical resonant (elastic) X-ray scattering experiments, this generates additional elastic peaks away from the Bragg peaks.

Normalization. The theoretical calculations of RIXS cross sections presented in this thesis are often given in arbitrary units. For current experiments, this suffices because one cannot measure the cross section on an absolute scale. Even comparing spectra at different transferred momenta is difficult because the scale might not be the same. There are two main factors that set the intensity scale in experiments:

- Self-absorption. A scattered photon might be absorbed a second time by the sample. Since the vast majority of core hole decay processes are through

Auger or fluorescence channels, self-absorption attenuates the RIXS intensity. The longer the path of the scattered photons through the sample is, the stronger is the attenuation. Self-absorption is $\mathbf{q}$ dependent because different $\mathbf{q}$ generally have different scattering geometries, meaning exit paths of different lengths. Self-absorption can be corrected for, see for example Ref. [4].

- Irradiated volume. The cross section scales with the irradiated part of the sample volume: if a photon meets more ions, that increases the probability of scattering. The irradiated volume is not easily determined because of the penetration depth (which depends on, amongst others, polarization), beam profile, surface effects, etc. In practice, correcting for the effects that determine the irradiated volume is very difficult.

Further, variations in the beam's intensity can also play a role. Obtaining experimental RIXS spectra on an absolute intensity scale is thus near-impossible, making comparison of spectra at different $\mathbf{q}$ a complicated affair. If one wants to compare the intensities at different $\mathbf{q}$, one has to normalize the data in one way or another. There are several options:

- Normalization to acquisition time. This is the simplest approach, which basically ignores the normalization problems. In experiments on thin films, however, this might be a viable approach since the penetration depth and beam size can be larger than the sample, reducing the uncertainty in the irradiated volume. Note that self-absorption and variations in the beam intensity should be corrected for in this approach.

- Normalization to well-known features. If one of the features in the experimental RIXS spectra is very well understood, it can be used as a reference for normalization. In experiments at the Cu L edge of cuprates, for example, the line shapes of the dd excitations are reproduced very well by theory [19, 20], and one can normalize the data to the spectral weight of the dd excitations [21].

1.2 Excitations of strongly correlated systems

In this thesis, we investigate how numerous types of excitations show up in RIXS spectra. The types of excitations that one encounters in this thesis are briefly reviewed here. The focus is on strongly correlated systems. Fig. 1.4 schematically indicates the energy scales of the excitations.

Charge transfer excitations. In a Mott insulator, the electrons are distributed over the ions of the material in such a way to minimize Coulomb repulsion between them. The electrons are very much localized: because of their

Figure 1.4: Approximate energy scales of different excitations in condensed matter systems. Reproduced with permission from Ref. [3].

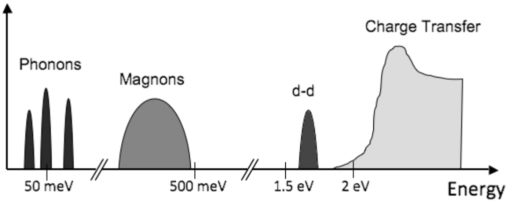

large Coulomb repulsion, they block each other's way. On top of this ordering, one can create charge transfer excitations: an electron is transferred from one type of ion to another. The energy scale of such an excitation is set by the intra-ionic Coulomb repulsion, which can be several eV in typical Mott insulators, and the on-site energies of the different ions [22]. Charge excitations across the Mott gap between ions of the same type are very similar; only the energy scale is different. In chapter 3, we study the RIXS spectra of, amongst others, a single-band Hubbard model, and find that the cross section is proportional to the dynamical charge response function $S(\mathbf{q}, \omega)$ for spinless fermions, a model applicable to many doped cuprates. Charge transfer excitations are interesting by themselves, and in addition they can provide us with the parameters of the high energy theories of solids (*e.g.*, the Hubbard model's t and U), who in turn determine the parameters of the effective low energy theories.

Orbital excitations. Many strongly correlated systems exhibit an orbital degree of freedom, that is, the valence electrons can occupy different sets of orbitals. Orbitally active ions are also magnetic: they have a partially filled outer shell. The orbital degree of freedom determines many physical properties of the solid, both directly, and because the orbitals couple to other degrees of freedom. For instance, the orbital's charge distribution couples to the lattice, and according to the Goodenough-Kanamori rules for superexchange the orbital order also determines the spin-spin interactions. The orbitally active ions can couple to each other via the lattica or via superexchange interactions. Both can drive the system into an orbitally ordered state.

Orbital excitations appear in many different forms. They all have in common that they involve a transition of an electron from one orbital to another, on the same ion. In some materials, the crystal field is very large, and the orbitals are split by ~ 1 eV. The transitions between the crystal field levels are called dd excitations (in transition metal compounds, the 3d levels are the orbitally active levels, hence the name). In highly symmetric materials, the crystal field splitting is small and the orbital dynamics are dominated by superexchange interactions between neighboring ions. In this case, collective orbital excitations arise. These excitations, called orbitons, are the main subject of chapter 5. The energy scale of orbitons is thus set by superexchange interactions, which can be as large as 250 meV.

Magnetic excitations. Many transition metal compounds contain magnetic ions, whose outer shell is only partly filled. The magnetic moments of these ions often interact with each other, and this can result in magnetic order: the global spin rotation symmetry in the material is broken. As a result, characteristic collective magnetic excitations emerge. These quasiparticles (*e.g.*, magnons and spinons), and the interactions between them determine all low temperature magnetic properties. Magnon energies can extend up to ~ 0.4 eV (*e.g.*, in cuprates) and their momenta up to $\sim 1\ \hbar\ \text{Å}^{-1}$, covering the entire Brillouin zone. Melting of the long-range ordering, for instance through the introduction of mobile charge carriers in a localized spin system or by the frustration of magnetic interactions between the spins, can result in the formation of spin-liquid groundstates. Spin liquids potentially have elusive properties such as high-temperature superconductivity or topological ordering.

In most transition metal compounds, the magnetic interaction is governed by superexchange, which yields an isotropic, Heisenberg form of the interaction between neighboring spins. Alternatively, spin ice compounds [23] with their huge magnetic moments also have magnetic dipole-dipole interactions, leading to an Ising interaction. Often, the strength of a magnetic bond is determined by the involved orbitals, as described above.

Combined spin-orbital excitations. When the crystal field forces the orbitals to order, the magnetic degrees of freedom are usually still active: the magnetic and orbital degrees of freedom are separated. Alternatively, when the crystal field is weak, the spin and orbital degrees of freedom can become intertwined. This can happen, for example, via Kugel-Khomskii superexchange interactions [24] or via intra-ionic, relativistic spin-orbit coupling [25]. The energy scale of the excitations of these models is set, respectively, by the superexchange interaction ($\sim 50 - 500$ meV) and by the relativistic spin-orbit coupling (~ 400 meV in the late transition metals).

Phonons. Excitations of the lattice are found at low energies ($10 - 100$ meV), comparable to the present state-of-the-art energy resolution of RIXS experiments. The spatial arrangment of the lattice is adapted to minimize the total Coulomb energy of the system. Lattice displacements can be induced by changes in the distribution of the electrons of the solid, as the ions are charged as well. The quanta of lattice displacement modes are called phonons. Phonons are crucial for many properties of condensed matter, ranging from sound propagation to superconductivity.

1.3 This thesis

Now that we have given a general introduction to RIXS, how it works, and what it can measure, we will proceed with the theory of RIXS in chapter 2. The basic formula for the RIXS cross section (the Kramers-Heisenberg formula) is (re-)derived and discuss in detail the approximation scheme used often in this thesis: the Ultra-short Core hole Lifetime (UCL) expansion. In the following chapters, we set out to investigate how RIXS probes the various excitations discussed above. Chapters 3, 4, 5, 6, and 7 deal with charge, magnetic, orbital, combined spin-orbital and lattice response, respectively. Finally, we conclude this work with an outlook in chapter 8.

CHAPTER 2

THEORY OF RESONANT INELASTIC X-RAY SCATTERING

2.1 Introduction

Before embarking on the calculation of RIXS cross sections, we consider the basic theory in this chapter. Starting at a very basic level, we first review how the X-ray photons interact with matter. The relativistic theory of quantum electrodynamics (QED) gives a general desciption of this interaction, but it deals with positrons which are obviously not needed to describe RIXS experiments on condensed matter systems. Therefore, we start this chapter with an approximation scheme to QED at low energies. This low energy expansion yields a Hamiltonian, which has only two components (electrons with spin up and down) instead of the four degrees of freedom of QED which also include positrons.

The low energy limit of QED requires small electromagnetic fields, and therefore interactions between photons and electrons are weak: the interaction strength is controlled by the dimensionless fine structure constant $\alpha = e^2/4\pi\epsilon_0\hbar c \approx 1/137$. We treat interactions with X-ray photons as a perturbation to the quantum system under study. Resonant X-ray scattering processes can be described by the Fermi Golden Rule to second order. The result is the Kramers-Heisenberg equation, which describes the resonant cross section.

The Kramers-Heisenberg cross section contains many quantities, some pertaining to the material, and some to the experimental setup. It is possible to disentangle them, although this is beyond the scope of this thesis [3, 26]. We consider only dipole transitions, and isolate the polarization dependence from the collective response of the system.

In Sec. 2.4, we distinguish two RIXS processes: direct and indirect RIXS. Direct RIXS corresponds to two consecutive dipole transitions, with no scattering from the core hole in the intermediate state. Because the RIXS process is a very fast one, this is often a good way of thinking about RIXS: the core hole has decayed before it can scatter an electron. However, some transitions, like the 1s → 4p edge, cannot produce any excitation unless the core hole and the valence electrons scatter off each other. This process, where the core hole has an impact on the valence electrons in between the two dipole transitions, is called indirect RIXS.

The Kramers-Heisenberg equation is difficult to solve exactly, and we are able to come up with an exact solution only in the case of localized excitations. In Sec. 2.5, we develop an approximation to the Kramers-Heisenberg equation: the Ultra-short Core hole Lifetime (UCL) expansion. It makes use of the fact that RIXS processes are usually very fast, leaving little time for the valence electrons to react to the core hole. The UCL series expansion trades the sum over intermediate states (which is hard to compute) for an expansion in the lifetime of the core hole.

This chapter is organized as follows: we start out with the basic electron-photon coupling theory in Sec. 2.2. Then, we use it to obtain the Kramers-Heisenberg equation in Sec. 2.3. The distinction between direct and indirect RIXS is illustrated in Sec. 2.4. The chapter will be conculded by the introduction of the UCL expansion in Sec. 2.5.

2.2 Electron-photon coupling

To develop the theory of RIXS, one needs to consider the interaction of the X-ray photons with the electrons in the sample under study. This interaction is described by the theory of quantum electrodynamics (QED). A treatment of the RIXS cross section in terms of QED would be very complicated, and one would prefer to use an effective low-energy approximation to QED where the positron degrees of freedom are integrated out. In this section, such a low-energy expansion of QED is developed, which produces a Hamiltonian that describes the interaction of photons with electrons. The expansion applies to cases where the electrons are non-relativistic and the electromagnetic fields are small compared to the electron mass. It is equivalent to the approach of Foldy and Wouthuysen [27].

2.2.1 Low energy expansion of QED

The electromagnetic field, including the incident X-rays, are described by an electric potential $\phi(\mathbf{r})$ and a vector potential $\mathbf{A}(\mathbf{r})$, which are combined in the four-vector $A^\mu = (\phi/c, \mathbf{A})$. The coupling between such a field and electrons is given by the theory of QED, see Peskin and Schroeder [28] for details. In SI units, the QED action is

$$S_{\text{QED}} = \int d^4x \; \bar{\psi} \left(i\hbar \not{D} - mc \right) \psi + S_{\text{EM}} \tag{2.1}$$

with m the mass of the electron, and where S_{EM} is the action for the electromagnetic field, which contains Maxwell's equations. ψ is a four-component vector describing the fermion field (whose excitation quanta are electrons and positrons), and $\bar{\psi} = \psi^\dagger \gamma^0$. Further, $\not{D} = \gamma^\mu D_\mu = \gamma^\mu (\partial_\mu - ieA_\mu/\hbar)$ with the elementary charge $e \approx +1.6 \cdot 10^{-19}$ C, and γ^μ are the gamma matrices. From this action, one obtains the Euler-Lagrange equation for $\bar{\psi}$:

$$\left(i\hbar \not{D} - mc \right) \psi = 0. \tag{2.2}$$

This is the Dirac equation in the presence of an electromagnetic field. The theory has a conserved current $j^\mu = \bar{\psi}\gamma^\mu\psi$, *i.e.*, $\partial_\mu j^\mu = 0$ if ψ obeys the Dirac equation (including A^μ). The formula for the associated conserved charge, $Q = \int d^3x \; j^0 =$ const., is a normalization condition, which can be set to 1 by rescaling ψ:

$$\int d^3x \; \psi^\dagger \psi = 1. \tag{2.3}$$

Eq. (2.2) contains both electrons and positrons, but at the low energy scales of condensed matter physics, the latter are irrelevant. They can be integrated out by taking two limits, and the result will be the Schrödinger equation for electrons in an electromagnetic field. First, we consider the case of the fermions having low speeds v compared to the speed of light, as is typical for condensed matter systems without very heavy nuclei. Second, the electromagnetic field strength is low compared to twice the mass of the electron: $eA^\mu/c \ll 2m$.

In the limiting case $A^\mu = 0$, the solutions to the Dirac equation are plane waves. In the Dirac basis, the fermion field is

$$\psi(x) = e^{-ip\cdot x/\hbar} \begin{pmatrix} \alpha(p) \\ -\frac{\sigma^i p_i}{p_0 + mc} \alpha(p) \end{pmatrix}. \tag{2.4}$$

where the four-vector $p^\mu = (E/c, \mathbf{p})$ must satisfy Einstein's energy-momentum relation $E^2 = (mc^2)^2 + (\mathbf{p}c)^2$. $\alpha(p)$ can be any two-component spinor. The solution for $\mathbf{p} = 0$ in zero field is $\psi(x) = e^{-ip_0 x^0/\hbar} \begin{pmatrix} \alpha \\ 0 \end{pmatrix}$ with $p_0 = mc$ and $x^0 = ct$. For small momenta, the lower spinor is of order $\mathcal{O}(p^i/mc) \sim \mathcal{O}(v/c)$. The plane wave solutions have two degrees of freedom in $\alpha(p)$, corresponding to an electron with spin up and down. In other words, $\psi(x)$ is the mode whose excitation quanta are electrons with momentum $\mathbf{p}$.

Another solution can be obtained by taking $\psi(x) = e^{ip\cdot x} v(p)$, which again has two degrees of freedom. These are the positron modes, which will not be considered here.

In order to derive the effective low energy electron-photon coupling Hamiltonian from Eq. (2.2), we introduce a small electromagnetic field $eA^\mu/c \ll m$ and allow the electron to have a finite (but small) speed $v \ll c$. In this regime, the equation of motion for the electron is the Schrödinger equation with electron-photon coupling. Departing as said from the extreme limit, the Ansatz $\psi = e^{-imc^2t/\hbar}\begin{pmatrix} \alpha(x) \\ \beta(x) \end{pmatrix}$ is introduced in Eq. (2.2). The idea behind this Ansatz is that for small electromagnetic fields and slow electrons $\alpha(x)$ and $\beta(x)$ will start to oscillate, but at a frequency much lower than $mc^2/\hbar$. One finds

$$i\hbar D_0\alpha(x) + i\hbar\sigma^i D_i\beta(x) = 0 \tag{2.5}$$

$$\left(2mc + i\hbar D_0\right)\beta(x) + i\hbar\sigma^i D_i\alpha(x) = 0 \tag{2.6}$$

where σ^i are the Pauli spin matrices. Eq. (2.6) can be rewritten as

$$\beta(x) = \tilde{D}\alpha(x) + \tilde{D}_0\beta(x) = \sum_{n=0}^{\infty} \tilde{D}_0^n\tilde{D}\alpha(x). \tag{2.7}$$

where $\tilde{D} = \frac{-i\hbar}{2mc}\sigma^i D_i$ and $\tilde{D}_0 = \frac{-i\hbar}{2mc}D_0$. (One can think of these quantities as part of the four-vector product $-i\hbar\sigma^\mu D_\mu/2mc$, with σ^0 the 2×2 unit matrix.) These results are still exact. By substituting Eq. (2.7) in Eq. (2.5), a Schrödinger equation for $\alpha(x)$ can be obtained.

The high-n terms in Eq. (2.7) will be small in the limit of interest: the total wave function has an oscillation frequency set by the energy of the electron, and since the rest energy was explicitly isolated in the Ansatz, the oscillation frequency of $\alpha(x)$ is $(E - mc^2)/\hbar$. For a slow electron in a small elecromagnetic field, this is much smaller than $2mc^2/\hbar$. Therefore Eq. (2.7) enables one to expand the Dirac equation in a controlled way, and obtain the Schrödinger equation to any order of precision. A convenient way to keep track of the orders in the expansion is the mass: order n gives a contribution to the Hamiltonian that is proportional to $1/m^{n+1}$.

The expansion is controlled as long as one satisfies the two limits. The first of these was that the electrons should be non-relativistic, i.e., they that travel at speeds small compared to the speed of light. This is a good approximation, even for, for instance, graphene where the Fermi velocity $v_F \approx c/300$, or for copper 1s core electrons, where we estimate $v \sim \hbar Z/ma_0 \approx 0.21c$ with Z the atomic number for copper and a_0 the Bohr radius. At first glance, v/c might appear not small here, but $\gamma = 1/\sqrt{1 - v^2/c^2} \approx 1.02$ and relativistic effects are still small. The second limit was that the potentials related to both the electrons and photons are small compared to twice the mass of the electron: $e\phi/2mc^2$, $e\left|\mathbf{A}\right|/2mc \ll 1$ (m is the electron mass). Because the potentials can be gauged, this means that the expansion breaks down if there is a potential *difference* in the problem enough to have an electron gain $2mc^2$ in energy, enough to produce electron-positron pairs. The intrinsic potentials of materials do not strictly satisfy this condition close to the nuclei. However, the expansion can be consistently applied to cases where the average of the potentials over a region of the size of the reduced Compton wave length satisfies this limit [29]. A crude estimate indicates that the expansion may be applied to all known elements: up to $Z \sim 2 \cdot 10^2$, see also Ref. [30]. However, in future very strongly focussed X-ray Free Electron Lasers, the electric field of the photons is projected to exceed 10^{16} V/m [31], which gives $e\,|\mathbf{A}| \sim 2mc$ at a photon energy of ~ 8 keV, so the low energy expansion of QED breaks down.

2.2.2 Evaluation of the expansion to third order

First order. The first order of the expansion is obtained by approximating $\beta(x)$ to order $n = 0$. Substitution of $\beta(x)$ in Eq. (2.5) gives the equation of motion for $\alpha(x)$. Using

$$(2mc\tilde{D})^2 = (-i\hbar)^2 \left(\delta^{ij} + i\epsilon^{ijk}\sigma^k\right) D_i D_j = (\mathbf{p} + e\mathbf{A})^2 + e\hbar\boldsymbol{\sigma} \cdot \mathbf{B}, \tag{2.8}$$

one obtains the Schrödinger equation

$$i\hbar\partial_t\alpha(x) = \left[\frac{1}{2m}(\mathbf{p} + e\mathbf{A})^2 + \frac{e\hbar}{2m}\boldsymbol{\sigma} \cdot \mathbf{B} - e\phi\right] \alpha(x). \tag{2.9}$$

The expression in straight brackets is the electron-photon coupling Hamiltonian to order $n = 0$ (order $1/m$). The first term contains the kinetic energy of the electron $\mathbf{p}^2/2m$, and two different electron-photon coupling terms: $e\mathbf{p} \cdot \mathbf{A}/m$ and $e^2\mathbf{A}^2/2m$. The other terms are the Zeeman and Coulomb energies, respectively.

Second order. Going to second order ($n = 1$) in Eq. (2.7) yields the equation of motion

$$i\hbar D_0\alpha(x) + i\hbar\sigma^i D_i \left(\tilde{D} + \tilde{D}_0\tilde{D}\right) \alpha(x) = 0. \tag{2.10}$$

Using

$$i\hbar\,[D_0, D_i] = i\,[\partial_0, -ieA_i] + i\,[-ieA_0, \partial_i] = e\,[(\partial_0 A_i) - (\partial_i A_0)] = \frac{e}{c}E^i \tag{2.11}$$

with E^i the electric field components, the $n = 1$ equation of motion is simplified to

$$\begin{aligned} i\hbar\partial_t\alpha(x) = &\left[\frac{(\mathbf{p} + e\mathbf{A})^2}{2m} + \frac{e\hbar}{2m}\boldsymbol{\sigma} \cdot \mathbf{B} - e\phi\right] \alpha(x) \\ &- \left(\frac{-i\hbar}{2mc}\right)^2 \sigma^i\sigma^j \left(i\hbar c D_i D_j D_0 + eD_i E^j\right) \alpha(x) = \Big[\dots\Big]\alpha(x) \\ &- \left(\frac{-i\hbar}{2mc}\right)^2 \sigma^i\sigma^j \left(D_i D_j i\hbar c D_0 + e(\partial_i E^j) + eE^j D_i\right) \alpha(x) \end{aligned} \tag{2.12}$$

To obtain a Schrödinger equation from this equation, *i.e.*, an equation linear in ∂_t, one substitutes D_0 on the right hand side by the $n=0$ Schrödinger equation. The result of this substitution is of higher order than $\mathcal{O}(m^{-2})$, and will be dropped here. The other correction terms become

$$\begin{aligned}\sigma^i\sigma^j e\left((\partial_i E^j) + E^j D_i\right)\alpha(x) &= e\left(\delta^{ij} + i\epsilon^{ijk}\sigma^k\right)\left((\partial_i E^j) + E^j D_i\right)\alpha(x)\\ = e\left(\frac{\rho}{\epsilon_0} + \frac{i}{\hbar}\mathbf{E}\cdot(\mathbf{p}+e\mathbf{A}) + \boldsymbol{\sigma}\cdot\left[\frac{1}{\hbar}\mathbf{E}\times(\mathbf{p}+e\mathbf{A}) - i\partial_t\mathbf{B}\right]\right)\alpha(x) \qquad (2.13)\end{aligned}$$

where Maxwell's equations $\nabla\cdot\mathbf{E} = \rho/\epsilon_0$ and $\nabla\times\mathbf{E} = -\partial_t\mathbf{B}$ are used. The equation of motion for $\alpha(x)$ becomes

$$\begin{aligned} i\hbar\partial_t\alpha(x) = &\left[\frac{(\mathbf{p}+e\mathbf{A})^2}{2m} + \frac{e\hbar}{2m}\boldsymbol{\sigma}\cdot\mathbf{B} - e\phi + \frac{e\hbar}{(2mc)^2}\boldsymbol{\sigma}\cdot\mathbf{E}\times(\mathbf{p}+e\mathbf{A})\right.\\ &\left.+\frac{e\hbar^2\rho}{(2mc)^2\epsilon_0}\right]\alpha(x) + \frac{ie\hbar}{(2mc)^2}\left[\mathbf{E}\cdot(\mathbf{p}+e\mathbf{A}) - \boldsymbol{\sigma}\cdot(\hbar\partial_t\mathbf{B})\right]\alpha(x). \qquad (2.14)\end{aligned}$$

The appearance of imaginary terms is natural: from the normalization condition Eq. (2.3), one finds

$$\int d^3x\ \left[\alpha(x)^\dagger\alpha(x) + \beta(x)^\dagger\beta(x)\right] = 1 \qquad (2.15)$$

and it is clear that when β acquires a finite value, α cannot constitute the normalized wave function anymore. If one tries to obtain an equation of the form $i\hbar\partial_t\alpha = H_\alpha\alpha$, H_α is expected to have non-Hermitian terms as soon as β acquires a non-zero value. These terms vanish when α is normalized at this stage [32]. We define $\Psi(x) = \Omega\alpha(x)$, and require that Ψ is normalized to 1. Up to order $\mathcal{O}(m^{-2})$, the normalization condition is

$$\int d^3x\ \left(\alpha(x)^\dagger\alpha(x) + \left(\tilde{D}\alpha(x)\right)^\dagger\tilde{D}\alpha(x)\right) = 1. \qquad (2.16)$$

Integrating by parts (assuming that the boundary term vanishes), one obtains

$$\int d^3x\ \alpha(x)^\dagger\left(1+\tilde{D}^2\right)\alpha(x) = 1. \qquad (2.17)$$

This gives, to order $\mathcal{O}(m^{-2})$,

$$\Omega = 1 + \frac{1}{2}\tilde{D}^2 = \Omega^\dagger. \qquad (2.18)$$

Ψ then obeys the equation

$$i\hbar\partial_t\Psi(x) = \left[\Omega H_\alpha\Omega^{-1} + i\hbar(\partial_t\Omega)\Omega^{-1}\right]\Psi(x) \qquad (2.19)$$

with $\Omega^{-1} = 1 - \frac{1}{2}\tilde{D}^2$. The Hamiltonian for Ψ is therefore $H_\Psi = \Omega H_\alpha \Omega^{-1} + i\hbar(\partial_t \Omega)\Omega^{-1}$. The normalization procedure can also be applied at an earlier stage, before expanding the Dirac equation [27]. In that case, it is just a transformation to a different representation of the Dirac theory.

The normalization is non-local and introduces coarse-graining on the scale of the Compton wave length [27,29]. This can be seen by writing the wave functions in the position representation:

$$\langle \mathbf{x} | \alpha \rangle = \langle \mathbf{x} | \, e^{-\tilde{D}^2/2} \, | \Psi \rangle \tag{2.20}$$

In the absence of electromagnetic fields, this becomes

$$\begin{aligned} \langle \mathbf{x} | \alpha \rangle &= \frac{1}{(2\pi\hbar)^3} \iint d\mathbf{p} \; d\mathbf{x}' \; e^{i\mathbf{p}\cdot(\mathbf{x}-\mathbf{x}')/\hbar} e^{-\mathbf{p}^2/8(mc)^2} \, \langle \mathbf{x}' | \, \Psi \rangle \\ &= \lambda_C^{-3} \sqrt{(2/\pi)^3} \int d\mathbf{x}' \; e^{-2(\mathbf{x}-\mathbf{x}')^2/\lambda_C^2} \, \langle \mathbf{x}' | \, \Psi \rangle \end{aligned} \tag{2.21}$$

where the reduced Compton wave length $\lambda_C = \hbar/mc$. For a specific solution $\Psi(\mathbf{x})$, one obtains $\alpha(\mathbf{x})$ by averaging Ψ over a region around $\mathbf{x}$ of the size of the Compton wave length.

The detailed calculation of H_Ψ is given in Appendix A. The result is

$$\begin{aligned} H_\Psi^{(2)} = &\frac{(\mathbf{p} + e\mathbf{A})^2}{2m} + \frac{e\hbar}{2m}\boldsymbol{\sigma}\cdot\mathbf{B} - e\phi + \frac{e^2\hbar}{(2mc)^2}\boldsymbol{\sigma}\cdot\mathbf{E}\times\mathbf{A} + \frac{1}{2}\frac{e\hbar^2\rho}{(2mc)^2\epsilon_0} \\ &+ \frac{e\hbar}{2(2mc)^2}\boldsymbol{\sigma}\cdot(\mathbf{E}\times\mathbf{p} - \mathbf{p}\times\mathbf{E}). \end{aligned} \tag{2.22}$$

This result slightly differs from those of Blume [33] and in the book of Schülke [34]. In the case of electrostatics, it coincides with previous work [32, 35].

The term proportional to ρ is called the Darwin term. In the hydrogen atom, this term shifts the energy of the s orbitals, because they are the only ones to overlap with the charge density of the nucleus. The last term of Eq. (2.22) contains relativistic spin-orbit coupling. This can be seen by inserting the electric field of a nucleus with charge Ze: ignoring commutation relations, one gets $\frac{e^2 Z\hbar}{(2mc)^2 r^3}\boldsymbol{\sigma}\cdot\mathbf{r}\times\mathbf{p} = \frac{e^2 Z}{2(mc)^2 r^3}\mathbf{S}\cdot\mathbf{L}$ [32]. In the absence of electron-electron interactions, the expectation value of $1/r$ is proportional to the charge of the nucleus Ze. The relativistic spin-orbit coupling is then proportional to Z^4, meaning it is strong in the heavy elements like iridium, the object of study in chapter 6. Further, it can be seen that for fixed Z, the core orbitals with their small $\langle r \rangle$ have a much larger spin-orbit coupling than the valence orbitals, which is important, *e.g.*, for probing the magnon dispersion in cuprates (see chapter 4).

Third order. The derivation of the third order H_Ψ ($n = 2$ or m^{-3}) is given in appendix A. The procedure is analogous to the second order calculation above.

The result is

$$H_{\Psi}^{(3)} = \cdots + \frac{1}{(2mc)^3}\Big[-c\left\{(\mathbf{p}+e\mathbf{A})^2 + e\hbar\boldsymbol{\sigma}\cdot\mathbf{B}\right\}^2 + \frac{e\hbar^2}{2c}\left\{(\partial_t\mathbf{E})\cdot(\mathbf{p}+e\mathbf{A}) + (\mathbf{p}+e\mathbf{A})\cdot(\partial_t\mathbf{E}) + \hbar\boldsymbol{\sigma}\cdot(\partial_t^2\mathbf{B})\right\}\Big]. \tag{2.23}$$

We interpret the different correction terms. In the absence of electromagnetic fields, only the term proportional to $\mathbf{p}^4$ is left. It gives a relativistic correction to the classical kinetic energy of the electron. The terms involving time derivatives disappear for static fields, but when one considers plane wave radiation of angular frequency ω, they renormalize lower order terms: $\partial_t\mathbf{E} \to \omega^2\mathbf{A}$ and $\partial_t^2\mathbf{B} \to -\omega^2\mathbf{B}$, renormalizing the first order Hamiltonian. The renormalization is of order $(\hbar\omega/mc^2)^2$. In these simple cases of static fields or radiation fields, only the term without time derivatives yields new electron-photon interaction processes, involving three and four photons. Another interesting case is when no electrons are present. Of the three- and four-photon terms, only the $\mathbf{A}^4$ term remains and gives photon-photon scattering and conversion of three low energy photons to one high energy photon (or vice versa), and is relevant in, for instance, Free Electron Lasers [36].

To conclude this section, we consider the limit of high fields in an X-ray Free Electron Laser (XFEL). The electric field for the LCLS XFEL beam is designed to reach $2.5 \cdot 10^{10}$ V/m for an unfocussed beam at a wave length of $\lambda = 1.5$ Å (corresponding to a photon energy $\hbar\omega = 8.3$ keV) [31]. The electric field strength is related to the vector potential by $|\mathbf{A}| = |\mathbf{E}|/\omega$, where we assumed that the beam is a plane wave in free space. We see that the low field limit is satisfied by the unfocussed beam: $e|\mathbf{A}|/2mc = 5.8 \cdot 10^{-7}$. The electric field can be increased to $\sim 10^{14}$ V/m by focusing the beam to a 100 nm spot, and with future technology, this can perhaps be increased to fields as strong as $\sim 10^{18}$ V/m for a 1 nm spot [37] . At field strengths beyond $|\mathbf{E}| = 4 \cdot 10^{16}$ V/m, $e|\mathbf{A}|/2mc$ is larger than unity and the low energy expansion of QED breaks down.

2.3 Kramers-Heisenberg equation

Now that the Hamiltonian describing the interaction of the X-ray photons with the electrons in the material under study is derived, we proceed to analyze X-ray scattering processes. This section is largely along the lines of Ref. [3].

The initial state of the scattering process is $|\mathtt{g}\rangle = |g; \mathbf{k}\boldsymbol{\epsilon}\rangle$, which describes the state g of the material under study, and a photon with wave vector $\mathbf{k}$, angular frequency $\omega_{\mathbf{k}} = c|\mathbf{k}|$, and polarization $\boldsymbol{\epsilon}$. After the scattering process is completed, the material is left in the state f and the photon is scattered to $\mathbf{k}', \omega_{\mathbf{k}'}, \boldsymbol{\epsilon}'$. The total final state is denoted as $|\mathtt{f}\rangle = |f; \mathbf{k}'\boldsymbol{\epsilon}'\rangle$.

We separate the Hamiltonian (2.22) into $H_0 + H'$ where H_0 affects only the electrons or only the photons, while the perturbation H' contains electron-photon interaction terms. H_0 contains the electron's kinetic and potential energy, the Darwin term, and relativistic spin-orbit coupling. The free photon's energy was omitted after Eq. (2.1), but is also included in H_0. The states $|\mathtt{g}\rangle$ and $|\mathtt{f}\rangle$ are eigenstates of H_0 with energies $E_{\mathtt{g}} = E_g + \hbar\omega_{\mathbf{k}}$ and $E_{\mathtt{f}} = E_f + \hbar\omega_{\mathbf{k}'}$, respectively, where E_g and E_f are the initial and final state energy of the material. Photon scattering can induce a transition in the material from the intial state $|g\rangle$ to final state $|f\rangle$, but total energy and momentum are conserved in the scattering process. The photons appear in the electron-photon Hamiltonian through $\mathbf{A}$, which can be expanded in plane waves as

$$\mathbf{A}(\mathbf{r}) = \sum_{\boldsymbol{\kappa},\boldsymbol{\varepsilon}} \sqrt{\frac{\hbar}{2\mathcal{V}\epsilon_0\omega_{\boldsymbol{\kappa}}}} \left(\boldsymbol{\varepsilon}\; a_{\boldsymbol{\kappa}\boldsymbol{\varepsilon}} e^{i\boldsymbol{\kappa}\cdot\mathbf{r}} + \boldsymbol{\varepsilon}^* a^\dagger_{\boldsymbol{\kappa}\boldsymbol{\varepsilon}} e^{-i\boldsymbol{\kappa}\cdot\mathbf{r}}\right), \qquad (2.24)$$

where $\mathcal{V}$ is the volume of the system. When the electromagnetic field is quantized, $a^{(\dagger)}_{\boldsymbol{\kappa}\boldsymbol{\epsilon}}$ annihilates (creates) a photon in the mode with wave vector $\boldsymbol{\kappa}$ and polarization vector $\boldsymbol{\varepsilon}$. The electric and magnetic fields in the electron-photon coupling Hamiltonian can be expressed in the potentials ϕ and $\mathbf{A}$.

H' can be treated as a perturbation to H_0 because electon-photon interactions are controlled by the small fine structure constant. We now calculate the X-ray scattering amplitude in this perturbation scheme. Fermi's Golden Rule to second order gives the transition rate w for scattering processes in which the photon loses momentum $\hbar\mathbf{q} = \hbar\mathbf{k} - \hbar\mathbf{k}'$ and energy $\hbar\omega = \hbar\omega_{\mathbf{k}} - \hbar\omega_{\mathbf{k}'}$ to the sample:

$$w = \frac{2\pi}{\hbar} \sum_{\mathtt{f}} \left| \langle \mathtt{f}| H' |\mathtt{g}\rangle + \sum_n \frac{\langle \mathtt{f}| H' |n\rangle \langle n| H' |\mathtt{g}\rangle}{E_{\mathtt{g}} - E_n} \right|^2 \delta(E_{\mathtt{f}} - E_{\mathtt{g}}) \qquad (2.25)$$

where the $|n\rangle$ are intermediate states, which are eigenstates of H_0 with energy E_n. The first order amplitude in general dominates the second order, but when the incoming X-rays are in resonance with a specific transition in the material ($E_{\mathtt{g}} \approx E_n$), then the second order amplitude becomes large. The second order amplitude contains resonant scattering, while the first order yields non-resonant scattering only. Third order contributions to w are neglected because they are at least of order $\alpha^{3/2}$.

It is useful to classify the electron-photon coupling terms by powers of $\mathbf{A}$. Terms of H that are quadratic in $\mathbf{A}$ are the only ones to contribute to the first order scattering amplitude, because they contain terms proportional to $a^\dagger_{\mathbf{k}'\boldsymbol{\epsilon}'} a_{\mathbf{k}\boldsymbol{\epsilon}}$ and $a_{\mathbf{k}\boldsymbol{\epsilon}} a^\dagger_{\mathbf{k}'\boldsymbol{\epsilon}'}$. To be specific, the quadratic terms of (2.22) give rise to non-resonant scattering [first term of (2.22)] and magnetic non-resonant scattering [fourth term of (2.22)]. Although both appear in the first order scattering amplitude, they in principle also contribute to the second order, but we neglect these processes because they are of order $\alpha^{3/2}$.

The interaction terms of H that are linear in $\mathbf{A}$ do not contribute to the first order scattering amplitude, but do contribute to the second order. They thus may give rise to resonant processes. In the following, we neglect such contributions that come from the $\boldsymbol{\sigma} \cdot \boldsymbol{\nabla}\phi \times \mathbf{A}$ term and from the last term of (2.22), because they are of second order in two separate expansions [33]. First, these terms of H are of second order in the low energy expansion of QED, and second, they appear in the second order of the scattering amplitude.

The relevant remaining terms are

$$H' = \sum_{i=1}^{N} \left[\frac{e}{m}\mathbf{A}(\mathbf{r}_i) \cdot \mathbf{p}_i + \frac{e^2}{2m}\mathbf{A}^2(\mathbf{r}_i) + \frac{e\hbar}{2m}\boldsymbol{\sigma}_i \cdot \nabla \times \mathbf{A}(\mathbf{r}_i) \right. \\ \left. - \frac{e^2\hbar}{(2mc)^2}\boldsymbol{\sigma}_i \cdot \frac{\partial \mathbf{A}(\mathbf{r}_i)}{\partial t} \times \mathbf{A}(\mathbf{r}_i) \right], \tag{2.26}$$

where the gauge was fixed by choosing $\nabla \cdot \mathbf{A}(\mathbf{r}) = 0$, and the sum is over all N electrons in the sample.

The two terms of H' that contribute to the first order amplitude are the one proportional to $\mathbf{A}^2$ and the $\boldsymbol{\sigma} \cdot (\partial \mathbf{A}/\partial t) \times \mathbf{A}$ term. The latter is smaller than the former by a factor $\hbar\omega_{\mathbf{k}(')}/mc^2 \ll 1$, and is therefore neglected [33]. The first order term in Eq. (2.25) then becomes

$$\frac{e^2}{2m} \langle \mathtt{f}| \sum_i \mathbf{A}^2(\mathbf{r}_i) |\mathtt{g}\rangle = \frac{\hbar e^2}{2m\mathcal{V}\epsilon_0} \frac{\boldsymbol{\epsilon}'^* \cdot \boldsymbol{\epsilon}}{\sqrt{\omega_{\mathbf{k}}\omega_{\mathbf{k}'}}} \langle f| \sum_i e^{i\mathbf{q}\cdot\mathbf{r}_i} |g\rangle \tag{2.27}$$

with $\mathbf{q} = \mathbf{k} - \mathbf{k}'$. When the incident energy $\hbar\omega_{\mathbf{k}}$ is much larger than any resonance of the material, the scattering amplitude is dominated by this channel, which is called Thompson scattering (see, for instance, page 51 of Ref. [32]). In scattering from a crystal at zero energy transfer, this term contributes amongst others to the Bragg peaks. It also gives rise to non-resonant inelastic scattering. In practice, RIXS spectra show a strong resonance behavior, demonstrating that, for RIXS, it is the second order scattering amplitude that dominates the first order. Also single atom LDA calculations show that the resonant cross section is larger than the non-resonant cross section by two orders of magnitude [38]. We therefore omit the $\mathbf{A}^2$ contribution in the following. More details on non-resonant inelastic X-ray scattering can be found in, for instance, Refs. [34, 39].

The second order scattering amplitude in Eq. (2.25) becomes large when $\hbar\omega_{\mathbf{k}}$ matches a resonance energy of the system, and the incoming photon is absorbed first in the intermediate state, creating a core hole. The denominator $E_g + \hbar\omega_{\mathbf{k}} - E_n$ is then small, greatly enhancing the second order scattering amplitude. We neglect the other, off-resonant processes here, though they do give an important contribution to non-resonant scattering, as in the case of Rayleigh scattering [32, 33]. The resonant part of the second order amplitude is

$$\frac{e^2\hbar}{2m^2\mathcal{V}\epsilon_0\sqrt{\omega_{\mathbf{k}}\omega_{\mathbf{k}'}}} \sum_n \sum_{i,j=1}^{N} \frac{\langle f| e^{-i\mathbf{k}'\cdot\mathbf{r}_i} \left(\boldsymbol{\epsilon}'^* \cdot \mathbf{p}_i - \frac{i\hbar}{2}\boldsymbol{\sigma}_i \cdot \mathbf{k}' \times \boldsymbol{\epsilon}'^*\right) |n\rangle}{E_g + \hbar\omega_{\mathbf{k}} - E_n + i\Gamma_n} \\ \times \langle n| e^{i\mathbf{k}\cdot\mathbf{r}_j} \left(\boldsymbol{\epsilon} \cdot \mathbf{p}_j + \frac{i\hbar}{2}\boldsymbol{\sigma}_j \cdot \mathbf{k} \times \boldsymbol{\epsilon}\right) |g\rangle, \tag{2.28}$$

where a lifetime broadening Γ_n is introduced for the intermediate states to accounts for the usually short lifetime of the core hole (see, for instance, page 341 of Ref. [40]). The decay is dominated by channels other than RIXS, such as Auger decay and fluorescent decay, see page 13 in Ref. [6]. Usually, these processes only involve the core levels, and all Γ_n at a certain edge can then be assumed equal. In the rest of this thesis, we take $\Gamma_n = \Gamma$.

Resonant scattering can thus occur via a non-magnetic and magnetic term. An estimate shows that the former dominates. The size of localized 1s copper core orbitals is roughly $a_0/Z \approx 0.018$ Å so that for 10 keV photons the exponential $e^{i\mathbf{k}\cdot\mathbf{r}}$ is close to unity and can be expanded. In a typical RIXS experiment, the X-ray energy is tuned to a dipole transition. The magnetic terms can then be neglected because they generate only very small dipole transitions. The non-magnetic term can induce a dipole transition of order $|\mathbf{p}| \sim \hbar Z/a_0 \sim 5.9{\cdot}10^{-23}$ kg m/s, whereas the magnetic term gives a dipole transition of order $(\mathbf{k}\cdot\mathbf{r})\hbar\,|\mathbf{k}|\,/2 \sim 2.5\cdot 10^{-25}$ kg m/s. We therefore ignore the magnetic term here, and the relevant transition operator for the RIXS cross section is

$$\boxed{\mathcal{D} = \frac{1}{im\omega_{\mathbf{k}}}\sum_{i=1}^{N} e^{i\mathbf{k}\cdot\mathbf{r}_i}\boldsymbol{\epsilon}\cdot\mathbf{p}_i,} \tag{2.29}$$

where a prefactor has been introduced for convenience in the following expressions.

The double-differential cross section is obtained by multiplying w by the density of photon states in the solid angle $d\Omega$ $(= \mathcal{V}\mathbf{k}'^2 d|\mathbf{k}'|d\Omega/(2\pi)^3)$, and dividing by the incident photon flux $c/\mathcal{V}$ [32–34, 41, 42]:

$$\boxed{\frac{d^2\sigma}{d\hbar\omega d\Omega} = r_e^2 m^2 \omega_{\mathbf{k}'}^3 \omega_{\mathbf{k}} \sum_f \left|\mathcal{F}_{fg}\right|^2 \delta(E_g - E_f + \hbar\omega),} \tag{2.30}$$

where the classical electron radius $r_e = \frac{1}{4\pi\epsilon_0}\frac{e^2}{mc^2}$. The scattering amplitude $\mathcal{F}_{fg}$ at zero temperature is given by

$$\boxed{\mathcal{F}_{fg}(\mathbf{k},\mathbf{k}',\boldsymbol{\epsilon},\boldsymbol{\epsilon}',\omega_{\mathbf{k}},\omega_{\mathbf{k}'}) = \sum_n \frac{\langle f|\,\mathcal{D}'^{\dagger}\,|n\rangle\,\langle n|\,\mathcal{D}\,|g\rangle}{E_g + \hbar\omega_{\mathbf{k}} - E_n + i\Gamma},} \tag{2.31}$$

where the prime in $\mathcal{D}'$ indicates it refers to transitions related to the outgoing X-rays. Eqs. (2.30) and (2.31) are referred to as the Kramers-Heisenberg equation, which is generally used to calculate the RIXS cross section.

At finite temperature T, this generalizes to

$$\frac{d^2\sigma}{d\hbar\omega d\Omega} = r_e^2 m^2 \omega_{\mathbf{k}'}^3 \omega_{\mathbf{k}} \sum_{i,f} \frac{1}{Z} e^{-E_i/k_B T} \left|\mathcal{F}_{fi}\right|^2 \delta(E_i - E_f + \hbar\omega), \tag{2.32}$$

where k_B is Boltzmann's constant and Z is the partition function.

Alternatively, we can rewrite the denominator for the intermediate states in terms of a Green's function, which is also referred to as the core hole propagator:

$$G(z_{\mathbf{k}}) = \frac{1}{z_{\mathbf{k}} - H_0} = \sum_n \frac{|n\rangle \langle n|}{z_{\mathbf{k}} - E_n}, \tag{2.33}$$

where $\{|n\rangle\}$ forms a complete basis set and

$$z_{\mathbf{k}} = E_g + \hbar\omega_{\mathbf{k}} + i\Gamma. \tag{2.34}$$

In the following we will often suppress the explicit label $\mathbf{k}$ of $z_{\mathbf{k}}$ and denote it simply by z, with an implicit incident energy dependence. With the core hole propagator G and transition operators $\mathcal{D}$ in place, the RIXS scattering amplitude $\mathcal{F}_{fg}$ finally reduces to the elegant expression

$$\mathcal{F}_{fg} = \langle f| \mathcal{D}'^{\dagger} G(z_{\mathbf{k}}) \mathcal{D} |g\rangle . \tag{2.35}$$

2.3.1 Dipole approximation and separation of polarization dependence

Eqs. (2.30) and (2.31) give the Kramers-Heisenberg expression for RIXS. One typically wants to separate the part pertaining to the geometry of the experiment from the fundamental scattering amplitudes that relate to the physical properties of the system. We restrict ourselves here to dipole transitions. Higher multipoles of the transition operator $\mathcal{D}$ can be found in, for instance, Ref. [3].

In the dipole limit, one asumes that $e^{i\mathbf{k}\cdot\mathbf{r}_i}$ is approximately constant at the length scale of the atomic wave functions: $e^{i\mathbf{k}\cdot\mathbf{r}_i} \approx e^{i\mathbf{k}\cdot\mathbf{R}_i}$ where $\mathbf{R}_i$ points to the nucleus of the atom to which the electron i is bound. $\mathbf{R}_i$ is not an operator. This has as a result that the electronic transitions are due to the momentum operator $\mathbf{p}$ and Eq. (2.29) becomes

$$\mathcal{D} = \boldsymbol{\epsilon} \cdot \mathbf{D} \quad \text{with} \quad \mathbf{D} = \frac{1}{im\omega_{\mathbf{k}}} \sum_{i=1}^{N} e^{i\mathbf{k}\cdot\mathbf{R}_i} \mathbf{p}_i, \tag{2.36}$$

Generally, the matrix elements are expressed in terms of the position operator $\mathbf{r}$. For example, in the absorption step, one can write

$$\begin{aligned} \langle n| \mathbf{D} |g\rangle &= \sum_{i=1}^{N} \frac{1}{im\omega_{\mathbf{k}}} e^{i\mathbf{k}\cdot\mathbf{R}_i} \langle n| \mathbf{p}_i |g\rangle = \sum_{i=1}^{N} \frac{1}{\hbar\omega_{\mathbf{k}}} e^{i\mathbf{k}\cdot\mathbf{R}_i} \langle n| [\frac{\mathbf{p}_i^2}{2m}, \mathbf{r}_i] |g\rangle \\ &\approx \sum_{i=1}^{N} \frac{1}{\hbar\omega_{\mathbf{k}}} e^{i\mathbf{k}\cdot\mathbf{R}_i} (E_n - E_g) \langle n| \mathbf{r}_i |g\rangle \approx \sum_{i=1}^{N} e^{i\mathbf{k}\cdot\mathbf{R}_i} \langle n| \mathbf{r}_i |g\rangle \end{aligned} \tag{2.37}$$

where $\hbar\omega_{\mathbf{k}} \approx E_n - E_g$. The operator thus reduces to the well-known dipole operator $\mathbf{D} = \sum_{i=1}^{N} e^{i\mathbf{k}\cdot\mathbf{R}_i}\mathbf{r}_i$ that causes electronic transitions.

After making the dipole approximation, the next step is to separate the part that pertains to the geometry of the experiment (the polarization vectors $\boldsymbol{\epsilon}'$ and $\boldsymbol{\epsilon}$) from the physical properties of the system. Ultimately, our interest lies in the spectral functions of a material. The experimental geometry is chosen in an optimal way to measure them.

In second quantization, the dipole operator reads

$$\mathbf{D} = \sum_{i=1}^{N} e^{i\mathbf{k}\cdot\mathbf{R}_i} \sum_{n,\nu,m,\mu} c^{\dagger}_{n\nu} \langle \phi_{n\nu} | \, \mathbf{r}_i \, | \phi_{m\mu} \rangle \, c_{m\mu} \tag{2.38}$$

where $\phi_{n\nu}$ is the ν^{th} Wannier wave function on site n, and $c_{n\nu}$ is the corresponding annihilation operator. For definiteness, one can use the transition metal K edge (1s → 4p) as an example. Then, $\phi_{m\mu}$ would be the transition metal 1s core states (μ indexes the 1s states with spin up and down) and $\phi_{n\nu}$ would be the transition metal 4p states (ν could index the orbitals $4\text{p}_{x,y,z}$ and spin up and down).

Because the core states are very much localized, only excited states on the same ion are reached[1]: $n = m$. The Wannier wave functions are the same at all lattice sites, so

$$\mathbf{D} \approx \sum_{\nu,\mu} \langle \phi_{\nu} | \, \mathbf{r} \, | \phi_{\mu} \rangle \sum_{i} e^{i\mathbf{k}\cdot\mathbf{R}_i} c^{\dagger}_{i\nu} c_{i\mu} \tag{2.39}$$

where the wave functions ϕ are centered at the origin. For our purposes, the sum over i can be restricted to electrons in the core states. For de-excitation,

$$\mathbf{D}'^{\dagger} \approx \sum_{\nu,\mu} \langle \phi_{\mu} | \, \mathbf{r} \, | \phi_{\nu} \rangle \sum_{i} e^{-i\mathbf{k}'\cdot\mathbf{R}_i} c^{\dagger}_{i\mu} c_{i\nu}. \tag{2.40}$$

Note that the spin is not changed in the radiative transitions, and ν and μ have the same spin.

Since the core orbitals are very small compared to the lattice parameters, it is often assumed that the core hole does not disperse during the RIXS process: it is created and annihilated at the same site. In this case, the scattering amplitude (2.31) is

$$\mathcal{F}_{fg} = \sum_{\mu',\nu',\nu,\mu} T_{\mu'\nu'\nu\mu}(\boldsymbol{\epsilon}', \boldsymbol{\epsilon}) \sum_{i} e^{i\mathbf{q}\cdot\mathbf{R}_i} \sum_{n} \frac{\langle f | \, c^{\dagger}_{i\mu'} c_{i\nu'} \, | n \rangle \langle n | \, c^{\dagger}_{i\nu} c_{i\mu} \, | g \rangle}{E_g + \hbar\omega_{\mathbf{k}} - E_n + i\Gamma}, \tag{2.41}$$

---

[1] Considering, for instance, the transition metal K edge, one could object that the 4p wave functions are quite large, and there is some overlap between the core states on one ion and the 4p wave functions of neighboring ions. However, dipole transitions are still very small since the 4p wave functions from the neighboring ions are approximately constant over the core state's volume.

where the polarization factor is

$$T_{\mu'\nu'\nu\mu}(\boldsymbol{\epsilon}', \boldsymbol{\epsilon}) = \langle \phi_{\mu'} | \, \boldsymbol{\epsilon}'^{*} \cdot \mathbf{r} \, | \phi_{\nu'} \rangle \, \langle \phi_{\nu} | \, \boldsymbol{\epsilon} \cdot \mathbf{r} \, | \phi_{\mu} \rangle \, . \tag{2.42}$$

μ', ν', ν and μ index the different scattering channels, which have different polarization dependencies $T_{\mu'\nu'\nu\mu}(\boldsymbol{\epsilon}', \boldsymbol{\epsilon})$. In practice, we replace the Wannier wave functions by the atomic wave functions to compute it. The radial parts of the dipole transition amplitudes in Eq. (2.42) are often irrelevant, as they only give an overall scaling factor to the RIXS spectra. In the absence of inter-ionic interactions, $T_{\mu'\nu'\nu\mu}(\boldsymbol{\epsilon}', \boldsymbol{\epsilon})$ gives the full RIXS scattering amplitude. We therefore name it the 'atomic scattering factor'. It does not carry any information on the material's correlation functions. The incident energy dependence is the only RIXS-specific part of the cross section that is not included in the atomic scattering factor.

In a typical RIXS experiment, the polarization of the incoming photon is linear. It is mostly chosen to be either parallel ($\boldsymbol{\epsilon}_{\pi}$) or perpendicular ($\boldsymbol{\epsilon}_{\sigma}$) to the scattering plane[2] (the plane spanned by $\mathbf{k}$ and $\mathbf{k}'$). The outgoing photon's polarization is not measured, and the cross section should therefore be summed over two orthogonal outgoing polarizations.

2.4 Direct and Indirect RIXS

In Sec. 2.3, the Kramers-Heisenberg expression for the RIXS scattering amplitude $\mathcal{F}_{fg}$, Eq. (2.31), was derived and re-expressed as a product of a photon absorption operator $\mathcal{D}$, the intermediate state propagator G and a photon emission operator $\mathcal{D}^{\dagger}$, sandwiched between the RIXS final state and ground state, yielding Eq. (2.35). The presence of the intermediate state propagator is what makes the theory of RIXS complicated – and interesting. The propagator G is defined in terms of the inverse of the total Hamiltonian H of the material, $G(z_{\mathbf{k}}) = (z_{\mathbf{k}} - H)^{-1}$, where the operator H naturally divides into the ground-state Hamiltonian H_0 (governing the quantum system without a core hole) and the core hole Hamiltonian H_C perturbing the system after photon absorption: $H = H_0 + H_C$. It should be noted that even if one commonly refers to H_C as the core hole Hamiltonian, it also includes the interaction between the electron excited into the conduction band and the rest of the material. As core hole and excited electron together form an exciton, their separate effects on the system cannot, in principle, be disentangled.

At this point it is useful to separate the full propagator G into an unperturbed one $G_0 = (z_{\mathbf{k}} - H_0)^{-1}$ and a term that contains the core hole Hamiltonian H_C, using the identity $G = G_0 + G_0 H_C G$. This also separates the RIXS amplitude into two parts, which define *direct* and *indirect* RIXS [3, 49]:

$$\mathcal{F}_{fg}^{direct} = \langle f | \, \mathcal{D}^{\dagger} G_0 \mathcal{D} \, | g \rangle \qquad \text{for direct RIXS} \tag{2.43}$$

---

[2] π and σ come from the German *parallel* and *senkrecht* – parallel and perpendicular.

Intermediate State Propagator			
Definition	RIXS amplitude $\mathcal{F}_{fg} = \langle f \vert\, \mathcal{D}^\dagger G \mathcal{D} \,\vert g \rangle$ Intermediate State Propagator $G(z_{\mathbf{k}}) = \frac{1}{z_{\mathbf{k}} - H}$; $H = H_0 + H_C$ H_0 ground state, H_C core hole Hamiltonian		
Exact G	$G = G_0 + G_0 H_C G$ $\swarrow \quad \searrow$		
	Direct RIXS $\mathcal{F}_{fg}^{direct} = \langle f \vert\, \mathcal{D}^\dagger G_0 \mathcal{D} \,\vert g \rangle$	*Indirect RIXS* $\mathcal{F}_{fg}^{indirect} = \langle f \vert\, \mathcal{D}^\dagger G_0 H_C G \mathcal{D} \,\vert g \rangle$	
	$\downarrow$	$\swarrow \quad \searrow$	
Approximate G	Fast Collision [26] $G(z_{\mathbf{k}}) \to 1/z_{\mathbf{k}}$	Perturbation Expansion [26, 38, 43–47] $G_0 H_C G \to G_0 H_C G_0$	UCL [48–50] $G_0 H_C G \to G_0 H_C G_C$
Valence excitation	caused by $\mathcal{D}$'s	caused by H_C	

Table 2.1: Theoretical approach to the intermediate state propagator, classifying direct and indirect RIXS processes and common approximations to the propagator. $G_C = (z - H_C)^{-1}$.

and

$$\mathcal{F}_{fg}^{indirect} = \langle f|\, \mathcal{D}^{\dagger} G_0 H_C G \mathcal{D}\, |g\rangle \qquad \text{for indirect RIXS.} \tag{2.44}$$

Note that this definition of direct and indirect RIXS, based on the Kramers-Heisenberg expression, is exact. Adding the two amplitudes, one retrieves the total scattering amplitude $\mathcal{F}_{fg}$. Table 2.1 summarizes the categorization of the scattering amplitude into direct and indirect RIXS, and also shows the subsequent approximations that are often used.

For the direct RIXS amplitude, the core hole does not play a role – the photon absorption and emission matrix elements determine which electronic transitions are allowed. The physical picture that arises for direct RIXS is that an incoming photon promotes a core electron to an empty valence states and subsequently an electron from a different state in the valence band decays, annihilating the core hole (see Fig. 1.1). Thus for direct RIXS to occur, both photoelectric transitions – the initial one from core to valence state and the succeeding one from valence state to fill the core hole – must be possible. These transitions can, for example, be an initial dipolar transition of 1s → 2p followed by the decay of another electron in the 2p band: 2p → 1s. This happens at the K edge of oxygen, carbon and silicon. At transition metal L edges, dipole transitions causing direct RIXS are possible via 2p → 3d and 3d → 2p dipolar transitions. In all these cases, RIXS probes the valence and conduction states directly.

For indirect RIXS, the scattering amplitude depends critically on the perturbing core hole Hamiltonian – without it the indirect scattering amplitude vanishes. In general, the scattering amplitude $\mathcal{F}_{fg}^{indirect}$ arises from the combined impact of H_C and the transition matrix elements $\mathcal{D}$. Most often, for indirect RIXS $\mathcal{D}/\mathcal{D}^{\dagger}$ create/annihilate an electron in the same state, far above the Fermi level. For instance at the transition metal K edge, the 1s ↔ 4p process creates/annihilates an electron in 4p states several electonvolts above the transition metal 3d valence shell. The delocalized 4p electron can then be approximated as being a *spectator* because (Coulomb) interactions involving the localized core hole are usually much stronger and dominate the scattering cross section.

It should be noted that if scattering is direct, as for instance at transition metal L edges, indirect processes can also contribute to the total scattering amplitude. However, as indirect scattering arises in this case as a higher order process, it is normally weaker than the leading order direct scattering amplitude. We speak of indirect RIXS when direct processes are absent.

2.5 Ultra-short core hole lifetime expansion

The potential that the core hole exerts on the valence electrons of transition metals is strong: the attraction between a 1s core hole and 3d electron is typically $\sim 6 - 8$ eV, which is of the same order as the 3d-3d intra-ionic Coulomb interaction. Treating such a strong interaction as a weak perturbation renders a perturbation expansion uncontrolled. To deal with the strong core hole interaction, the Ultrashort Core hole Lifetime (UCL) expansion was developed in Refs. [48–50], which treats the core hole potential as the dominating energy scale (see Table 2.1).

For most RIXS intermediate states, the core hole lifetime broadening is quite large: typically Γ is of the order of 1 eV. This yields a timescale $\tau = 1/2\Gamma = 4$ fs. Only during this ultrashort time, the system is perturbed by the core hole. Many elementary excitations have an intrinsic timescale that is much larger than 4 fs. For example, phonons have a typical energy scale up to 100 meV, and magnons up to 350 meV, thus corresponding to timescales almost an order of magnitude larger. Even low energy electronic valence band excitations can be within this range.

The resulting physical picture of a RIXS process involving low energy excitations is that the dynamics in the intermediate state are limited because of lack of time.

The calculation of the RIXS amplitude within the UCL expansion in Refs. [48–50] is based on a series expansion of the Kramers-Heisenberg equation, Eq. (2.31), which is elaborated on in chapter 3. Here we present an analogous derivation. We first introduce the identity

$$G(z) = \sum_n \frac{|n\rangle\langle n|}{z - E_n} = \frac{1}{i\hbar}\int_0^\infty dt\; e^{-i(H-z)t/\hbar}. \qquad (2.45)$$

The scattering amplitude then becomes

$$\mathcal{F}_{fg} = \frac{1}{i\hbar}\int_0^\infty dt\,\langle f|\,\mathcal{D}^\dagger e^{-i(H-z)t/\hbar}\mathcal{D}\,|g\rangle\,, \qquad (2.46)$$

which gives a natural picture of the RIXS process: it starts with excitation, then the intermediate state evolves over a time t, followed by radiative decay of the core hole. Since z has an imaginary part, RIXS processes with long intermediate state lifetimes are suppressed. Because the decay time t is not measured, all processes with different t's interfere, hence the integral.

Because Γ is assumed to be the largest energy scale in the problem, we factorize the exponential $e^{-i(H-z)t/\hbar} = e^{-i(H-\mathfrak{Re}\{z\})t/\hbar}e^{-\Gamma t/\hbar}$ in Eq. (2.46), and expand the exponential with the smallest exponent:

$$\mathcal{F}_{fg} = \frac{1}{i\hbar}\int_0^\infty dt\,\langle f|\,\mathcal{D}^\dagger \sum_{l=0}^{\infty}\frac{1}{l!}\left(\frac{-i\tilde{H}t}{\hbar}\right)^l e^{-\Gamma t/\hbar}\mathcal{D}\,|g\rangle\,, \qquad (2.47)$$

where $\tilde{H} = H - E_g - \hbar\omega_{\mathbf{k}}$. Integration over time gives

$$\mathcal{F}_{fg} = \frac{1}{i\hbar}\langle f|\,\mathcal{D}^\dagger \sum_{l=0}^{\infty}\left(\frac{-i\tilde{H}}{\hbar}\right)^l \frac{\hbar^{l+1}}{\Gamma^{l+1}}\mathcal{D}\,|g\rangle = \frac{1}{i\Gamma}\sum_{l=0}^{\infty}\langle f|\,\mathcal{D}^\dagger\left(\frac{\tilde{H}}{i\Gamma}\right)^l\mathcal{D}\,|g\rangle\,, \qquad (2.48)$$

The sum over intermediate states is traded for a series in $\tilde{H}/\Gamma$, which converges if the lifetime broadening is the largest energy scale in the problem: $\Gamma > |E_n - E_g - \hbar\omega_{\mathbf{k}}|$ for all n. The idea now is to approximate the series with the first few terms. One just has to calculate the matrix elements of (some power of) H to get the scattering amplitude.

The simplest approximation is to retain only $l = 0$. This is called the fast collision approximation (see table 2.1): the RIXS process is completely determined by the dipole transitions, without any dynamics in the intermediate state. For indirect RIXS, the cross section is therefore zero in this approximation. For direct RIXS however, the fast collision approximation yields a simple description of, *e.g.*, single magnon RIXS in the cuprates (chapter 4) and the L edge cross section of iridates (chapter 6). In certain cases, one can resum a series of terms with different l [48–50].

Convergence is not a priori guaranteed for the expansion: when the incoming photons are far off resonance, $|E_n - E_g - \hbar\omega_{\mathbf{k}}| > \Gamma$. This divergence can easily be removed by modifying the expansion. To better account for the effect of detuning from the resonant edge, we introduce the resonance energy $\hbar\omega_{\text{res}}$, which is chosen to be somewhere in the resonant absorption region (*e.g.*, the peak of the absorption spectrum). Writing $e^{-i(H-z)t/\hbar} = e^{-i(H-E_g-\hbar\omega_{\text{res}})t/\hbar} e^{i(\hbar[\omega_{\mathbf{k}}-\omega_{\text{res}}]+i\Gamma)t/\hbar}$, we find

$$\mathcal{F}_{fg} = \frac{1}{\Delta} \sum_{l=0}^{\infty} \langle f| \mathcal{D}^{\dagger} \left(\frac{H - E_g - \hbar\omega_{\text{res}}}{\Delta} \right)^{l} \mathcal{D} |g\rangle \,, \tag{2.49}$$

with $\Delta = \hbar(\omega_{\mathbf{k}} - \omega_{\text{res}}) + i\Gamma$. This is the UCL expansion. Now, the series converges if $(E_n - E_g - \hbar\omega_{\text{res}})^2 < (\hbar\omega_{\mathbf{k}} - \hbar\omega_{\text{res}})^2 + \Gamma^2$. Physically, this means that off-resonant scattering is an even faster process than resonant scattering. We conclude that far off resonance, the UCL expansion (2.49) form converges very rapidly.

The UCL series formally diverges in another way: there are always some intermediate states for which $|E_n - E_g - \hbar\omega_{\mathbf{k}}| > \Gamma$, for example, states from another edge. Only when such intermediate states give sufficiently small contributions to the scattering amplitude can one hope to obtain a sensible result from the UCL expansion. Usually, that is the case as these states are far off-resonance. The Hamiltonian can be replaced by an effective Hamiltonian where the far off-resonant states have been integrated out (see, for instance, the treatment of magnetic indirect RIXS in cuprates in chapter 4).

An alternative approach with Green's functions is equally viable [3]. Besides charge excitations [48–50], many other excitations that arise in indirect RIXS were studied with the UCL expansion. The single- and two-magnon response of antiferromagnetic La_2CuO_4 was calculated within the UCL expansion [19,51,52], agreeing nicely with experiments [11, 14, 53]. Collective orbital excitations were investigated theoretically for $LaMnO_3$ [54]. Indirect RIXS investigations within the UCL expansion on charge, magnetic, orbital and lattice excitations will be reviewed in chapters 3, 4, 5, and 7, respectively.

Chapter 3

Charge excitations

3.1 Introduction

Charge excitations occur at quite high energies (typically, the gap of Mott insulators is of the order of a few eV), which placed them within reach of RIXS experiments already in the early stages of the development of the technique. Charge excitations, both charge transfer excitations and exctitations across the Mott gap [22], are interesting by themselves, but also because the high energy theory that describes them contains the low energy physics as well. The latter are of interest when one studies the elementary magnetic and orbital excitations of the solid.

Other questions that can be addressed with RIXS relate to the nature of the charge excitations – whether or not they form bound exciton states, if these propagate coherently, etc. [3].

In this chapter, we study the indirect RIXS response of Hubbard models. The simplest case of a single band Hubbard model with spinless fermions yields a RIXS spectrum proportional to the dynamic charge correlation function $S(\mathbf{q},\omega)$. This model is of interest in, *e.g.*, doped cuprates, since the Coulomb repulsion is so large that doubly occupied sites only virtually form. The spin degree of freedom is, to first order, irrelevant for the charge excitations in these systems. Introducing spin or multiple bands complicates this picture somewhat, and yields less simple correlation functions. The work in Sec. 3.2 is published in Phys. Rev. B. We present some extensions of that work after fruitful discussions with Y.-J. Kim, describing in more detail the difference between the well and poorly screened intermediate states. The experimental results of Y.-J. Kim are reviewed at the end of this chapter. In Sec. 3.3, the first order corrections to the charge scattering cross section for strong core hole potentials are presented, which yield information about the hopping amplitudes. Sec. 3.4 contains an analysis of the polarization dependence of transition metal K edge RIXS.

3.2 UCL approach to charge scattering

Published as '*Ultrashort Lifetime Expansion for Indirect Resonant Inelastic X-ray Scattering*' in Phys. Rev. B **75**, 115118 (2007) with Fiona Forte and Jeroen van den Brink.

Abstract. *In indirect resonant inelastic X-ray scattering (RIXS) an intermediate state is created with a core hole that has an ultra-short lifetime. The core hole potential therefore acts as a femtosecond pulse on the valence electrons. We show that this fact can be exploited to integrate out the intermediate states from the expressions for the scattering cross section. By doing so we obtain an effective scattering cross section that only contains the initial and final scattering states. This effective cross section which turns out to be a resonant scattering factor times a linear combination of the charge response function* $S(\mathbf{q}, \omega)$ *and the dynamic longitudinal spin density correlation function, both with a resonant prefactor. This result is asymptotically exact for both strong and weak local core hole potentials and ultra-short lifetimes. The resonant scattering pre-factor is shown to be weakly temperature dependent. We also derive a sum rule for the total scattering intensity and generalize the results to multi-band systems. One of the remarkable outcomes is that one can change the relative charge and spin contribution to the inelastic spectral weight by varying the incident photon energy.*

3.2.1 Introduction

It is a well-known fact that the 1s core hole that is created in indirect RIXS has an ultra-short lifetime, of the order of femtoseconds. The reason is that the core hole has a very high energy and is prone to decay via all sorts of radiative and non-radiative processes, severely cutting down the efficiency of RIXS. In the canonical theoretical treatments of RIXS this lifetime effect is normally introduced as a core hole broadening and disregarded from that point on.

In a previous study [49], however, we have shown that from the theory perspective there is a great advantage to the extremely short lifetime of the core hole. The ultra-short lifetime implies that for the electrons in the solid –particularly for the slow ones that are close to the Fermi-energy– the core hole potential is almost an instantaneous delta-function in time. Although the core hole potential by itself can be large and therefore a strong perturbation to the electrons, the very short duration of this perturbing potential allows for a systematic expansion of the scattering cross section in terms of the core hole lifetime. Here we present a detailed derivation and various generalizations of this result. We shall see that the most important consequence of the ultra-short core hole lifetime is that for indirect RIXS the effective scattering cross section is proportional to the charge structurefactor $S(\mathbf{q},\omega)$ and the longitudinal spin structure factor that is associated with it.

The indirect RIXS process is shown schematically in Fig. 1.2. In transition metal systems the photo-electron is promoted from a 1s core orbital to empty 4p states that are far (10-20 eV) above the Fermi level. So the X-rays do not cause direct transitions of the 1s electron into the lowest 3d-like conduction bands of the system. Still RIXS is sensitive to excitations of electrons near the Fermi level. The Coulomb potential of 1s core hole causes, *e.g.*, very low energy electron-hole excitations in the conduction/valence band: the core hole potential is screened by the valence electrons. When the excited 4p electron recombines with the 1s core hole and the outgoing photon is emitted, the system can therefore be left behind in an excited final state. Since the excitations are caused by the core hole, we refer to this scattering mechanism as *indirect* RIXS.

In this chapter, we derive in detail the dynamical correlation function that is measured in indirect RIXS. We aim to give a full and self-contained derivation of the results that were presented earlier [49] and we elaborate on several generalizations. In particular we will show that for local core hole potentials and ultra-short lifetimes, the dynamical correlation function is a linear combination of the charge density and longitudinal spin density response function. For a single band system the actual linear combination that is measured depends on the energy of the incoming photons and we determine the precise energy dependence of its coefficients. A sum rule is derived and we generalize these results to the case of finite temperature and for multi-band systems.

3.2.2 Series expansion of the scattering cross section

The Kramers-Heisenberg formula [33,41,42,55] for the resonant X-ray scattering cross section at finite temperature is given by Eq. (2.32). In the following we will take the groundstate energy of our system as reference energy for the electronic system: $E_g \equiv 0$. We define the resonance energy $\hbar\omega_{\text{res}}$ to be somewhere in the middle of the resonant edge: it is just a number serving as a reference energy in the intermediate state. The energy of the incoming X-rays with respect to the resonance energy is $\hbar\omega_{\text{in}}$ (this energy can thus either be negative or positive: $\omega_{\text{in}} = \omega_{\mathbf{k}} - \omega_{\text{res}}$) and in the following, E_n is the energy of intermediate state $|n\rangle$ with respect to the resonance energy. In the intermediate state a core hole and a photo-excited electron are present. When we take the Coulomb interaction between the intermediate state core hole and the valence band electrons into account, we obtain a finite inelastic scattering amplitude. In that case there is a non-zero probability that an electron-hole excitation is present in the final state, see Fig. 1.2.

Crucial to our further considerations will be the fact that the intermediate state is not a steady state. The reason is that the highly energetic 1s core hole quickly decays, *e.g.*, via Auger processes, and the core hole lifetime is very short. The Heisenberg time-energy uncertainty relationship then implies that the core hole energy has an appreciable uncertainty. This uncertainty appears in the formalism above as the core hole energy broadening Γ which is proportional to the inverse core hole lifetime, which is of the order of electronvolts as the lifetime is ultra-short, of the order of femtoseconds. Note that the lifetime broadening only appears in the intermediate states and not in the final or initial states –these both have very long lifetimes. This implies that the core hole broadening does not present an intrinsic limit to the experimental resolution of RIXS: the loss energy ω is completely determined by kinematics.

When the incoming energy of the X-rays is equal to a resonant energy of the system $\hbar\omega_{\text{in}} - E_n = 0$ and we see from Eqs. (2.30) and (2.31) that the resonant enhancement of the X-ray scattering cross section is $(\hbar\omega_{\text{res}}/\Gamma)^2$, which is $\sim 10^6$ for a transition metal K edge [33].

In a resonant scattering process, the measured system is generally strongly perturbed. Formally this is clear from the Kramers-Heisenberg formula (2.31), in which both the energy and the wavefunction of the intermediate state –where a potentially strongly perturbing core hole is present– appear. This is in contrast with canonical optical/electron energy loss experiments, where the probing photon/electron presents a weak perturbation to the system that is to be measured.

To calculate RIXS amplitudes, one possibility is to numerically evaluate the Kramers-Heisenberg expression. To do so, all initial, intermediate and final state energies and wavefunctions need to be known exactly, so that in practice a direct evaluation is only possible for systems that, for example, consist of a small cluster of atoms [56,57]. In this chapter, however, we show that under the appropriate conditions we can integrate out the intermediate states from the Kramers-Heisenberg expression. After doing so, we can directly relate RIXS amplitudes to linear charge and spin response functions of the unperturbed system. For non-resonant scattering, one is familiar with the situation that the scattering intensity is proportional to a linear response function, but for a resonant scattering experiment this is a quite unexpected result.

Let us proceed by formally expanding the scattering amplitude in a power series, following Eq. (2.49):

$$\mathcal{F}_{fg} = \frac{1}{\hbar\omega_{\text{in}} + i\Gamma} \sum_{l=0}^{\infty} M_l, \tag{3.1}$$

where we introduced the matrix elements

$$M_l = \sum_n \left(\frac{E_n}{\hbar\omega_{\text{in}} + i\Gamma} \right)^l \langle f| \mathcal{D}^\dagger |n\rangle \langle n| \mathcal{D} |g\rangle \, . \tag{3.2}$$

The formal radius of convergence of this power series is given by $E_n^2/[(\hbar\omega_{\text{in}})^2 + \Gamma^2]$, so that the series is obviously convergent when the incoming X-ray energy is, *e.g.*, far enough below the resonance, *i.e.*, when $|\omega_{\text{in}}| \gg 0$. But also at resonance, when $\omega_{\text{in}} = 0$ the series is convergent for intermediate energies that are smaller than the core hole broadening Γ. Thus this expansion is controlled for ultra-short core hole lifetimes, which implies that Γ is large. In the following we will be performing resummations of this series.

We denote the denominator of the expansion parameter $\hbar\omega_{\text{in}} + i\Gamma$ by the complex number Δ, so that

$$M_l = \frac{1}{\Delta^l} \sum_n \langle f| \mathcal{D}^\dagger |n\rangle \left(E_n\right)^l \langle n| \mathcal{D} |i\rangle = \frac{1}{\Delta^l} \langle f| \mathcal{D}^\dagger (H_{\text{int}})^l \mathcal{D} |i\rangle , \tag{3.3}$$

where H_{int} is the Hamiltonian in the intermediate state. We thus obtain the following series expansion for the resonant cross section:

$$\left.\frac{d^2\sigma}{d\omega d\Omega}\right|_{res} \propto \left\langle \sum_f \left| \frac{1}{\Delta} \sum_{l=0}^{\infty} M_l \right|^2 \delta(\omega - \omega_{fi}) \right\rangle_{\text{T}} \tag{3.4}$$

where $\langle \ldots \rangle_T$ denotes a thermal average and $\hbar\omega_{fi}$ is the energy gained by the material.

3.2.3 Indirect RIXS for spinless fermions: $T = 0$

As in Ref. [49], we will first calculate the resonant X-ray cross section at zero temperature in the case where the valence and conduction electrons are effectively described by a single band of spinless fermions: spin and orbital degrees of freedom of the valence electron system are suppressed. Physically this situation can be realized in a fully saturated ferromagnet.

The final and initial states of the system are determined by a Hamiltonian H_0 that describes the electrons around the Fermi level. The generic form of the full many-body Hamiltonian is

$$H_0 = \sum_{i,j} t_{ij}(c_i^\dagger c_j + c_j^\dagger c_i) + c_i^\dagger c_i V_{ij} c_j^\dagger c_j, \tag{3.5}$$

where i and j denote lattice sites with lattice vectors $\mathbf{R}_i$ and $\mathbf{R}_j$. Note that the sum is over each pair i, j once, with i, j ranging from 1 to N, where N is the number of sites in the system. The hopping amplitudes of the valence electrons are denoted by t_{ij} and the $c/c^\dagger$-operators annihilate/create such electrons. The Coulomb interaction between valence electrons is $V_{ij} = V(|\mathbf{R}_i - \mathbf{R}_j|)$, as the Coulomb interaction only depends on the relative distance between two particles.

The intermediate states are eigenstates of the Hamiltonian $H_{\text{int}} = H_0 + H_c$, where H_c accounts for the Coulomb coupling between the intermediate state core hole and the valence electrons:

$$H_c = \sum_{i,j} s_i s_i^\dagger V_{ij}^c c_j c_j^\dagger, \tag{3.6}$$

where s_i creates a core hole on site i. The form of H_c has been chosen such that the well-screened intermediate state is at energy $\hbar\omega_{\text{res}}$, so the UCL expansion is around the well-screened part of the absorption edge. We assume that the core hole is fully localized and has no dispersion. We will see shortly that this leads to major simplifications in the theoretical treatment of indirect RIXS. The core hole-valence electron interaction is attractive: $V^c > 0$. An analysis of the polarization dependence is given in Sec. 3.4. For now, we simplify the dipole operators by taking

$$\mathcal{D} = \sum_i e^{-i\mathbf{k}\cdot\mathbf{R}_i} s_i p_i^\dagger + e^{i\mathbf{k}'\cdot\mathbf{R}_i} s_i^\dagger p_i + \text{h.c.}, \tag{3.7}$$

where $p^\dagger$ creates a photo-excited electron in a 4p state and h.c. denotes the hermitian conjugate of both terms.

Short Lifetime Approximation: Algebraic Form. In order to calculate the cross section, we need to evaluate the operator $(H_{\text{int}})^l = (H_0 + H_c)^l$ in equation (3.3). A direct evaluation of this operator is complicated by the fact that $[H_0, H_c] \neq 0$. We therefore proceed by approximating H_{int}^l with a series that contains the leading terms to the scattering cross section for both strong and weak core hole potentials – as long as the core hole lifetime is short. After that we will do a full resummation of that series. This approximation is central to the results in this chapter.

Expanding $(H_0 + H_c)^l$ gives a series with 2^l terms of the form

$$H_{\text{int}}^l = H_c^l + \sum_{n=0}^{l-1} H_c^n H_0\, H_c^{l-n-1} + \cdots + \sum_{n=0}^{l-1} H_0^n H_c\, H_0^{l-n-1} + H_0^l. \tag{3.8}$$

Using $H_0 \mathcal{D} |g\rangle = \mathcal{D} H_0 |g\rangle \equiv 0$, this series reduces to

$$H_{\text{int}}^l \mathcal{D} |g\rangle = \left(H_c^l + \sum_{n=0}^{l-2} H_c^n H_0\, H_c^{l-n-1} + \cdots + H_0^{l-1} H_c \right) \mathcal{D} |g\rangle . \tag{3.9}$$

Using in addition that $\langle f| \mathcal{D}^\dagger H_0 = \langle f| H_0 \mathcal{D}^\dagger = E_f \langle f| \mathcal{D}^\dagger$, we find

$$\begin{aligned} \langle f| \mathcal{D}^\dagger H_{\text{int}}^l \mathcal{D} |g\rangle = & \langle f| \mathcal{D}^\dagger \Big(H_c^l + E_f H_c^{l-1} + \sum_{n=1}^{l-2} H_c^n H_0\, H_c^{l-n-1} \\ & + \cdots + E_f^{l-1} H_c \Big) \mathcal{D} |g\rangle . \end{aligned} \tag{3.10}$$

For strong core hole potentials, the leading term of H_{int}^l is H_c^l. Corrections to this term contain at least one factor of H_0 and are therefore smaller by a factor of t/V^c. For weak core hole potentials, the leading order term, H_0^l, vanishes because $[H_0, \mathcal{D}] = 0$. In this limit, the leading term in the inelastic scattering amplitude is therefore $E_f^{l-1}H_c$. Correction terms contain at least two factors of H_c, which make them at least a factor of V^c/t smaller.

Let us now consider the approximate expression

$$H_{\text{int}}^l \mathcal{D}\left|g\right\rangle \approx \sum_{m=0}^{l} H_0^m H_c^{l-m} \mathcal{D}\left|g\right\rangle . \tag{3.11}$$

From the arguments above, it is easy to see that the leading order terms for both strong ($m = 0$) and weak ($m = l - 1$) core hole potentials are included in the sum; but a large series of other terms are included as well; they can be neglected in the case that we strictly consider either limit. Including them, however, means that we consider in addition a set of higher order scattering processes. A major advantage of including these is that the terms will give rise to a smooth interpolation between the two extreme limits. Note that the $m = l$ term in Eq. (3.11) is 0, so that it can be removed from the sum. After performing the same manipulations as above, we obtain

$$\begin{aligned}\left\langle f\right| \mathcal{D}^\dagger \sum_{m=0}^{l-1} H_0^m H_c^{l-m} \mathcal{D}\left|g\right\rangle &= \sum_{m=0}^{l-1} E_f^m \left\langle f\right| \mathcal{D}^\dagger H_c^{l-m} \mathcal{D}\left|g\right\rangle \\ &= \left\langle f\right| \mathcal{D}^\dagger \left(H_c^l + E_f H_c^{l-1} + \cdots + E_f^{l-1} H_c \right) \mathcal{D}\left|g\right\rangle . \end{aligned} \tag{3.12}$$

Comparing Eqs. (3.10) and (3.12), it can be seen that the approximation (3.11) is exact in the limit of both strong and weak core hole potentials.

Short Lifetime Approximation: Graphical Representation. We can also represent the series expansion and its approximation graphically (Fig. 3.1). When we expand $(A+B)^l$, where A and B are non-commuting operators, each term in the series corresponds to a graph on the grid of graph 1. Each graph occurs only once and can be constructed by starting at the lower left corner of the grid and moving either to the right, representing an A, or up, representing a B. At the next vertex a new move (right or up) is made. We perform this procedure l times and in this way we can obtain 2^l distinct graphs, each corresponding to a term in the expansion of $(A+B)^l$. For example moving l times to the right represents the term A^l and moving l times up corresponds to B^l, see graphs 2 and 3. All other terms in the series can be constructed by moving up and right a different number of times and in different order. As we consider a fixed value of l ($l = 8$ in Fig. 3.1), all graphs must end on the diagonal of the triangle that forms the grid. In the series for $(H_0+H_c)^l \mathcal{D}\left|g\right\rangle$ ($H_0 = A$ and $H_c = B$) we have the simplification that terms ending with H_0 acting on the groundstate give zero. These terms can thus be removed from the expansion. The graphs for this expansion now live on a reduced grid where the horizontal grid-lines at the diagonal of the triangle are absent, see graph 5: these represent all terms ending on A.

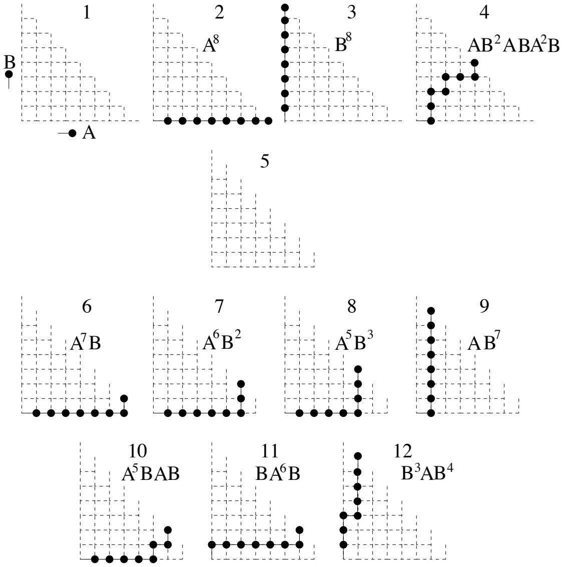

Figure 3.1: Graphical representation of the expansion of $(A + B)^l$, where $A = H_0$ and $B = H_c$ are two non-commuting operators. In this example $l = 8$.

In Fig. 3.1 we also represent the approximate series of the right-hand side of Eq. (3.11). Graphically this sum corresponds to the set of graphs on the reduced grid of graph 5, with either one kink (graphs 6-9) or without kinks (graphs 2 and 3). Thus, in our approximation in Eq. (3.11) of the exact series for $(H_0 + H_c)^l$ we neglect all graphs with two or more kinks (graphs 4, 10-12). In the limit of either very A or very large B, the graphs that we neglect correspond to sub-leading order corrections. When A is largest, the leading terms are, first, graph 2, which is however zero because it ends on A. The leading term is therefore of the order A^7 and shown in graph 6. Other higher order terms are shown in the graphs 7, 8, 10 and 11. The last two graphs are neglected in our approximate expansion. In case B is dominating, the leading term is B^8, graph 3, and next to leading is graph 9, with B^7. The highest order terms that are neglected in our approximate series are of the type shown in graph 12.

Resummation of Series for Scattering Cross Section. In order to obtain M_l and from there the scattering amplitude $\mathcal{F}_{fg}$ and finally the scattering cross section, in Eq.(3.12) we need to evaluate expressions of the kind

$$H_c^n \mathcal{D} \left| g \right\rangle = H_c^{n-1} \sum_{i,l,j} s_l s_l^\dagger V_{lj}^c c_j c_j^\dagger e^{-i\mathbf{k}\cdot\mathbf{R}_i} s_i p_i^\dagger \left| g \right\rangle . \tag{3.13}$$

In the initial state no core hole is present: just one core hole is created by the dipole operator. We therefore have that $s_l s_l^\dagger s_i \left| g \right\rangle = \delta_{l,i} s_i \left| g \right\rangle$. Inserting this in

Eq. (3.13), we obtain

$$H_c^n \mathcal{D} |g\rangle = H_c^{n-1} \sum_i e^{-i\mathbf{k}\cdot\mathbf{R}_i} s_i p_i^\dagger \sum_j V_{ij}^c c_j c_j^\dagger |g\rangle \tag{3.14}$$

and by recurrence

$$H_c^n \mathcal{D} |g\rangle = \sum_i e^{-i\mathbf{k}\cdot\mathbf{R}_i} s_i p_i^\dagger \left[\sum_j V_{ij}^c c_j c_j^\dagger \right]^n |g\rangle . \tag{3.15}$$

Let us for the moment consider the strong core hole potential limit and keep in the expansion Eq. (3.11) only the term $m = 0$. Inserting the results above in Eq. (3.3), we find that

$$M_l = \frac{1}{\Delta^l} \langle f| \sum_i e^{i\mathbf{q}\cdot\mathbf{R}_i} \left[\sum_j V_{ij}^c c_j c_j^\dagger \right]^l |g\rangle \quad \text{if} \quad V^c \gg t \tag{3.16}$$

where the transfered momentum $\hbar\mathbf{q} \equiv \hbar\mathbf{k}' - \hbar\mathbf{k}$.

The first important observation is that the term $l = 0$ does not contribute to the inelastic X-ray scattering intensity because $M_0 = \langle f| \sum_i e^{i\mathbf{q}\cdot\mathbf{R}_i} |g\rangle = N\delta_{\mathbf{q},\mathbf{0}}\delta_{f,g}$, which only contributes to the elastic scattering intensity at $\mathbf{q} = \mathbf{0}$ (and other multiples of the reciprocal lattice vectors). From inspection of equation (3.2) we see immediately that the $l = 0$ term actually vanishes irrespective of the strength of the core hole potential. This is of relevance when we consider the scattering cross section in the so-called ‘fast collision approximation’ [58]. This approximation corresponds to the limit where the core hole lifetime broadening is the largest energy scale in system ($\Gamma \rightarrow \infty$ or, equivalently, $\mathfrak{Im}\{\Delta\} \rightarrow \infty$). In this limit only the $l = 0$ term contributes to the indirect RIXS amplitude and the resonant inelastic signal vanishes. In any theoretical treatment of indirect resonant scattering one therefore needs to go beyond the fast-collision approximation.

This vanishing of spectral weight is ultimately due to an interference effect. If we study a process in which we start from the initial state and reach a certain final state, we need to consider all different possible paths for this excitation–de-excitation process. When the core hole broadening is very large we can reach the final state via any intermediate state and in order to obtain the scattering amplitude we thus add up coherently the contributions of all intermediate states. We then obtain $\mathcal{F} = \sum_n \langle f|n\rangle \langle n|g\rangle$. When the set of intermediate states that we sum over is complete (which by definition is the case when $\Gamma \rightarrow \infty$), this leaves us with $\mathcal{F} = \langle f|g\rangle$ which is, because of the orthogonality of eigenstates, only nonzero when the initial and final state are equal–hence only when the scattering is elastic. Alternatively, one could say that the scattering process happens so fast that the valence electrons do not have enough time to react: they remain in the ground state.

The second observation is that M_l is a 2^l-particle correlation function. If we measure far away from resonance, where $|\mathfrak{Re}\{\Delta\}| \gg 0$, the scattering cross section is dominated by the $l = 1$, two-particle, response function. When the incoming photon energy approaches the resonance, gradually the four, six, eight etc. particle response functions add more and more spectral weight to the inelastic scattering amplitude. Generally these multi-particle response functions interfere. We will show, however, that in the local core hole approximation the multi-particle correlation functions in expansion (3.11) collapse onto the dynamic two-particle (charge-charge) and four-particle (spin-spin) correlation function.

Local core hole potentials. In hard X-ray electron spectroscopies one often makes the approximation that the core hole potential is local. This corresponds to the widely used Anderson impurity approximation in the theoretical analysis of, *e.g.*, X-ray absorption and photo-emission, introduced in Refs. [59–61]. This approximation is reasonable as the Coulomb potential is certainly largest on the atom where the core hole is located.

In the present case, moreover, we can consider the potential generated by both the localized core hole and photo-excited electron at the same time. As this exciton is a neutral object, its monopole contribution to the potential vanishes for distances larger than the exciton radius. The multi-polar contributions that we are left with in this case are generally small and drop off quickly with distance.

We insert a local core hole potential $V^c_{ij} = U\delta_{ij}$ in our equations and aim to resum the approximate series expansion in Eq. (3.11) for arbitrary values of the local core hole potential. We find from Eq. (3.15) that

$$H_c^n \mathcal{D} |g\rangle = \sum_i e^{-i\mathbf{k}\cdot\mathbf{R}_i} s_i p_i^\dagger U^n [c_i c_i^\dagger]^n |g\rangle \tag{3.17}$$

Using that for fermions $[c_i c_i^\dagger]^n = c_i c_i^\dagger$, we obtain for our spinless fermions

$$M_l^{sf} = \frac{1}{\Delta^l} \langle f| \sum_i e^{i\mathbf{q}\cdot\mathbf{R}_i} c_i c_i^\dagger |g\rangle \sum_{m=0}^{l-1} E_f^m U^{l-m}. \tag{3.18}$$

The sum over m can easily be performed:

$$\sum_{m=0}^{l-1} E_f^m U^{l-m} = U^l \sum_{m=0}^{l-1} (E_f/U)^m = \frac{U^l - E_f^l}{1 - E_f/U} \tag{3.19}$$

and we obtain for the inelastic part

$$M_l^{sf} = -\frac{1}{\Delta^l} \frac{U^l - E_f^l}{1 - E_f/U} \langle f| \sum_i e^{i\mathbf{q}\cdot\mathbf{R}_i} c_i^\dagger c_i |i\rangle . \tag{3.20}$$

Note that $\sum_i e^{i\mathbf{q}\cdot\mathbf{R}_i} c_i^\dagger c_i = \sum_{\mathbf{k}} c^\dagger_{\mathbf{k}-\mathbf{q}} c_{\mathbf{k}} \equiv \rho_{\mathbf{q}}$ is the density operator.

We now have to perform the sum over l in equation (3.1). The $l = 0$ term is zero, as we discussed above, so that the scattering amplitude is

$$\mathcal{F}_{fg} = \frac{1}{\Delta} \sum_{l=1}^{\infty} M_l. \tag{3.21}$$

Using

$$\sum_{l=1}^{\infty} (U/\Delta)^l - (E_f/\Delta)^l = \Delta \frac{U - E_f}{(\Delta - U)(\Delta - E_f)} \tag{3.22}$$

we finally find that the indirect resonant inelastic scattering amplitude for spinless fermions is

$$\mathcal{F}_{fg}^{sf} = P_1(\omega, U) \langle f| \rho_{\mathbf{q}} |g\rangle , \tag{3.23}$$

where the resonant enhancement factor is $P_1(\omega, U) \equiv -U[(\Delta - U)(\Delta - \hbar\omega)]^{-1}$ and $\hbar\omega = E_f$. For spinless fermions with a local core hole potential the scattering cross section thus turns out to be the density response function –a two-particle correlation function– with a resonant prefactor $P_1(\omega)$ that depends on the loss energy $\hbar\omega$, the distance from resonance $\hbar\omega_{\text{in}}(= \mathfrak{Re}\{\Delta\})$, on the core hole potential U and on the core hole lifetime broadening $\Gamma(= -\mathfrak{Im}\{\Delta\})$. We see that the resonant enhancement is largest when the energy of the incoming photons is either equal to the core hole potential ($\hbar\omega_{\text{in}} = U \Rightarrow \hbar\omega_{\mathbf{k}} = \hbar\omega_{\text{res}} + U$) or to the loss energy, which one could refer to as a "final state resonance" ($\hbar\omega_{\text{in}} = \hbar\omega \Rightarrow \hbar\omega_{\mathbf{k}'} = \hbar\omega_{\text{res}}$).

Alternatively, one can perform the UCL expansion at a different intermediate state/$\hbar\omega_{\text{res}}$. Expanding around the poorly screened state by taking

$$H_c = U \sum_i s_i s_i^\dagger c_i^\dagger c_i \tag{3.24}$$

one gets

$$\mathcal{F}_{fg} = P_1(\omega, -U) \langle f| \rho_{\mathbf{q}} |g\rangle . \tag{3.25}$$

Now, $\hbar\omega_{\text{res}}$ refers to the poorly screened state, which is at an energy U above the well-screened state $\hbar\omega_{\text{res}}^{ws}$. Resonance is thus expected when $\hbar\omega_{\text{in}} = -U \Rightarrow \hbar\omega_{\mathbf{k}} = \hbar\omega_{\text{res}}^{ws}$ and $\hbar\omega_{\text{in}} = \hbar\omega \Rightarrow \hbar\omega_{\mathbf{k}'} = \hbar\omega_{\text{res}}^{ws} + U$. This corresponds to energy gain scattering, but that does not occur at low temperatures. Therefore, this resonant behavior cannot be seen in practice.

One then might wonder around which $\hbar\omega_{\text{res}}$ to expand, since the choice of $\hbar\omega_{\text{res}}$ determines the resonant behavior. One way to deal with this problem is simply to take an average of both expansion points. Both resonances are recovered, of which one (the energy-gain resonance) is experimentally inaccessible.

The density response function is related to the dielectric function $\epsilon(\mathbf{q}, \omega)$ and the dynamic structure factor $S(\mathbf{q}, \omega)$ (see, *e.g.*, Ref. [62], p. 322), so that we obtain for the resonant scattering cross section

$$\left.\frac{d^2\sigma}{d\Omega d\omega}\right|_{res}^{sf} \propto -\left|P_1(\omega)\right|^2 \mathfrak{Im}\left\{\frac{1}{V_{\mathbf{q}}\epsilon(\mathbf{q}, \omega)}\right\} \propto \left|P_1(\omega)\right|^2 S(\mathbf{q}, \omega), \tag{3.26}$$

for a fixed value of the core hole potential U. $V_{\mathbf{q}}$ is the Fourier transform of the Coulomb potential. For weak core hole potentials the total scattering intensity is proportional to U^2 and for strong core hole potentials, where $U \gg \Gamma$, the scattering intensity at resonance ($\omega_{\text{in}} = 0$) is to first order independent of the strength of the core hole potential. Far away from the edge, however, where $|\hbar\omega_{\text{in}}| \gg U$, the scattering intensity is again proportional to U^2, just as for weak core hole potentials. Integrating $|P_1(\omega)|^2$ over all incoming photon energies, we obtain the integrated inelastic intensity at fixed loss energy $\hbar\omega$ and momentum $\hbar\mathbf{q}$

$$\int_{-\infty}^{\infty} d(\hbar\omega_{\text{in}}) \frac{d^2\sigma}{d\Omega d\omega}\bigg|_{\text{res}}^{sf} = r_e^2 m^2 \omega_{\text{res}}^4 \frac{2\pi U^2}{\Gamma(4\Gamma^2 + (U - \hbar\omega)^2)} S(\mathbf{q}, \omega) \tag{3.27}$$

where we have taken $\omega_{\mathbf{k}(')}$ constant ($= \omega_{\text{res}}$) in the domain of integration: $(-\infty, +\infty)$ implies integration over the energy range described by our theory, *i.e.*, $\sim$ 10 eV around the edge. It seems that the resonant enhancement factor of the integrated intensity has a maximum when the loss energy is equal to the core hole potential. However, the core hole potential is attractive and therefore lower than zero, and the loss energy $\hbar\omega$ is by definition greater than zero. So the integrated intensity is maximal at energy loss $\hbar\omega = 0$.

3.2.4 Indirect RIXS for spinless fermions: finite T

In this section, we generalize the previous calculation to the case of finite temperature. The starting point is Eq. (2.32):

$$\frac{d^2\sigma}{d\Omega d\omega}\bigg|_{\text{res}} \propto \frac{1}{Z} \sum_{i,f} e^{-\beta E_i} \left|\mathcal{F}_{fi}\right|^2 \delta(\omega - \omega_{fi}), \tag{3.28}$$

where $Z = \sum_i e^{-\beta E_i}$ is the partition function and $\beta = 1/k_B T$. Eq. (3.28) represents the statistical average over all the initial states $|i\rangle$, where now the more general relation $H_0 |i\rangle = E_i |i\rangle$ holds.

We expand the scattering amplitude $\mathcal{F}_{fi}$, using again the ultra-short lifetime of the core hole as in Eq. (3.1). We are left with the evaluation of the operator $(H_{\text{int}})^l$. We proceed by expanding it in the following way:

$$\begin{aligned}(H_{\text{int}})^l \mathcal{D} |i\rangle &= (H_0 + H_c)^l \mathcal{D} |i\rangle \\ &\approx \sum_{n=0}^{l-1} \sum_{m=0}^{l-n-1} (H_0)^m (H_c)^{l-m-n} (H_0)^n \mathcal{D} |i\rangle, \end{aligned} \tag{3.29}$$

where we neglected the term H_0^l, as it will not contribute to the inelastic scattering cross section. This approximation reproduces the correct leading order terms, which represent the strong and weak coupling case, respectively. Moreover, it is a generalization of (3.11), that takes into account that the initial state is no longer the ground state so that $H_0 \left| i \right\rangle = E_i \left| i \right\rangle$. In our graphical representation, with respect to the $T = 0$ case, it corresponds to retain all the additional terms, having more than one kink, that start and finish with a horizontal step. In doing this, we are neglecting again the sub-leading order terms $H_c^{l-1-n} H_0 H_c^n$.

After inserting expansion (3.29) in the expression (3.3) for M_l, we finally have to evaluate

$$\left\langle f \right| \mathcal{D}^\dagger \sum_{n,m} (H_0)^m (H_c)^{l-m-n} (H_0)^n \mathcal{D} \left| i \right\rangle = \sum_{n,m} E_f^m E_i^n \left\langle f \right| \mathcal{D}^\dagger H_c^{l-m-n} \mathcal{D} \left| i \right\rangle . \quad (3.30)$$

In the local core hole approximation, we can resum this approximate series expansion. By using the results of Eqs. (3.17) and (3.18), we obtain for spinless fermions

$$M_l^{sf} = -\frac{1}{\Delta^l} \left\langle f \right| \rho_{\mathbf{q}} \left| i \right\rangle \sum_{n,m} E_f^m E_i^n U^{l-m-n}. \quad (3.31)$$

By performing the sums over n and m

$$\sum_{n,m} E_f^m E_i^n U^{l-m-n} = U^l \sum_{n=0}^{l-1} (E_i/U)^n \sum_{m=0}^{l-n-1} (E_f/U)^m, \quad (3.32)$$

and after summing over l, we finally obtain

$$\mathcal{F}_{fi}^{sf} = P_1(E_f, U) \frac{\Delta}{\Delta - E_i} \left\langle f \right| \rho_{\mathbf{q}} \left| i \right\rangle . \quad (3.33)$$

This equation clearly shows that one of the main effects of finite temperature is to modify the resonant enhancement factor, nevertheless preserving the same structure for the scattering amplitude.

At this point we observe that at resonance $|\Delta| = \Gamma$, which is of the order of electronvolts and thus several orders of magnitude larger than E_i, even at high temperature. This allows us to approximate the prefactor in Eq. (3.33) as

$$P_1(E_f, U) \frac{\Delta}{\Delta - E_i} \approx P_1(\omega, U) \left(1 + \frac{E_i}{\Delta - \hbar\omega} + \ldots \right) \left(1 + \frac{E_i}{\Delta} + \ldots \right) . \quad (3.34)$$

At the lowest order in E_i/Γ, the prefactor is not modified by T at all, hence we conclude that the major modifications to the cross section are induced by thermal averaging of the correlation function. After integrating over all the incoming photon energies, we get the following approximate expression for the thermal average of the inelastic intensity at loss energy $\hbar\omega$ and momentum $\hbar\mathbf{q}$:

$$\left. \frac{d^2\sigma}{d\Omega d\omega} \right|_{\mathrm{res,T}} \propto |P_1(\omega)|^2 \left\langle S(\mathbf{q}, \omega) \right\rangle_{\mathrm{T}} . \quad (3.35)$$

In this expression the temperature dependence is entirely due to the temperature dependence of $S(\mathbf{q},\omega)$. The prefactor is in leading order temperature independent. Note that at finite temperatures also energy gain scattering occurs: the photon can gain an energy of the order of k_BT from the system, which corresponds to a negative energy loss.

3.2.5 Fermions with spin

We generalize the calculation above to the situation where the electrons have an additional spin degree of freedom. In the Hamiltonians (3.5) and (3.6) we now include a spin index σ (with $\sigma =\uparrow$ or $\downarrow$) to the annihilation and creation operators: $c_i \to c_{i\sigma}$ and $c_j \to c_{j\sigma'}$ and sum over these indices, taking into account that the hopping part of the Hamiltonian is diagonal in the spin variables. In order to resum the series in Eq. (3.11) we now need to evaluate expansions of the kind $(n_\uparrow + n_\downarrow)^l$ when we expand around the unscreened part of the resonant edge. Using

$$(n_\uparrow + n_\downarrow)^l = n_\uparrow + n_\downarrow + (2^l - 2)n_\uparrow n_\downarrow, \tag{3.36}$$

for $l > 0$, we obtain for the inelastic part

$$\mathcal{F}_{fi} = \langle f|\left(P_1(\omega,-U)[\rho_\mathbf{q} - 2\rho_\mathbf{q}^{\uparrow\downarrow}] + 2P_2(\omega,-U)\rho_\mathbf{q}^{\uparrow\downarrow}\right)|i\rangle\,, \tag{3.37}$$

with $P_2(\omega,U) = P_1(\omega,2U)/2$ and $\rho_\mathbf{q}^{\uparrow\downarrow} \equiv \sum_i e^{i\mathbf{q}\cdot\mathbf{R}_i} n_{i\uparrow}n_{i\downarrow}$. We see that in the case that each site can only be occupied by at most one valence electron, this equation reduces to Eq. (3.23) with $\rho_\mathbf{q} = \rho_\mathbf{q}^\uparrow + \rho_\mathbf{q}^\downarrow$. The two terms in the scattering amplitude can also be written in terms of density and spin operators. Using $(n_{i\uparrow} - n_{i\downarrow})^2 = (2S_i^z)^2 = \frac{4}{3}\mathbf{S}_i^2$, we obtain $\rho_\mathbf{q} - 2\rho_\mathbf{q}^{\uparrow\downarrow} = \mathbf{S}_\mathbf{q}^2$, where we introduce the longitudinal spin density correlation function $\mathbf{S}_\mathbf{q}^2 \equiv \frac{1}{S(S+1)}\sum_\mathbf{k} \mathbf{S}_{\mathbf{k}+\mathbf{q}}\cdot\mathbf{S}_{-\mathbf{k}}$. In terms of these correlation functions the scattering amplitude for spinfull fermions is

$$\mathcal{F}_{fi} = [P_1(\omega,-U) - P_2(\omega,-U)]\,\langle f|\,\mathbf{S}_\mathbf{q}^2\,|i\rangle + P_2(\omega,-U)\,\langle f|\,\rho_\mathbf{q}\,|i\rangle\,, \tag{3.38}$$

Clearly the contributions to the scattering rate from the dynamic longitudinal spin correlation function and the density correlation function need to be treated on equal footing as they interfere. On a heuristic basis sometimes only the charge density response function is considered for the calculation of RIXS spectra, *e.g.*, [63–66]. Note that based on qualitative arguments, it was anticipated that the RIXS cross section should depend on a dynamic four-particle correlation function [38].

The spin and charge correlation functions have different resonant enhancements, see Fig. 3.2. For instance when $\mathfrak{Re}\{\Delta\} = -U$, the scattering amplitude is dominated by $P_1(\omega)$ and hence by the longitudinal spin response function. When the photons are tuned to the well-screened intermediate state on the other hand, *i.e.*, where $\mathfrak{Re}\{\Delta\} = -2U$, $P_2(\omega)$ is resonating so that the contributions to the inelastic scattering amplitude of charge and spin are approximately equal.

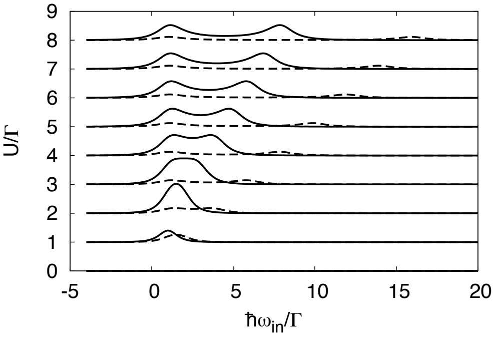

Figure 3.2: Prefactors to the scattering intensity at fixed loss energy ($\hbar\omega/\Gamma = 1$) as a function of incoming photon energy $\hbar\omega_{\mathrm{in}}/\Gamma$, for different values of the local core hole potential U/Γ. The solid line refers to $|P_1(\omega, U)|^2$ and the dashed line refers to $|P_2(\omega, U)|^2$.

Again, these resonances are at energy-gain scattering. Alternatively, we can expand around the well-screened intermediate states. We then use the core hole Hamiltonian

$$H_c = U \sum_i s_i s_i^\dagger (2 - n_{i\uparrow} - n_{i\downarrow}) = U \sum_i s_i s_i^\dagger (c_{i\uparrow} c_{i\uparrow}^\dagger + c_{i\downarrow} c_{i\downarrow}^\dagger) \tag{3.39}$$

and obtain by an analogous procedure

$$\mathcal{F}_{fi} = [P_2(\omega, U) - P_1(\omega, U)] \langle f | \mathbf{S}_{\mathbf{q}}^2 | i \rangle + [3P_2(\omega, U) - 2P_1(\omega, U)] \langle f | \rho_{\mathbf{q}} | i \rangle . \tag{3.40}$$

In the case of the cuprates, the spinless fermion scenario is appropriate when considering charge scattering: the intra-ionic Coulomb repulsion is so large that the fermions will virtually never occupy the same site ($n_\uparrow n_\downarrow = 0$), which makes the spin degree of freedom irrelevant. In this limit $\mathbf{S}_{\mathbf{q}}^2 = \rho_{\mathbf{q}}$, and the scattering amplitudes for the spinless and spinfull fermions, expanded around the unscreened intermediate states – Eqs. (3.25) and (3.38) respectively – are equal. The well-screened intermediate states do not have an analogue in the spinless case, as no two fermions can occupy the same site to screen the core hole.

3.2.6 Multi-band systems

Let us consider systems with more than one band and take as an explicit example a transition metal with a 3d and a 4s band. The Coulomb attraction between the 1s core hole and an electron in the 3d state (U_d) is much larger than the interaction with a 4s electron (U_s). Neglecting spin degrees of freedom we would naively expect that the indirect RIXS response in the two-band system is simply the sum of the responses of the two individual electronic systems, with possible interference between the two scattering channels: we expect the scattering amplitude to be equal to

$$\mathcal{F}_{fi}^{s+d} = P_1(\omega, U_d) \langle f | \rho_{\mathbf{q}}^d | i \rangle + P_1(\omega, U_s) \langle f | \rho_{\mathbf{q}}^s | i \rangle . \tag{3.41}$$

However, already from the calculation for the spinfull fermions we know that the situation should be more complicated, as in that case the full response function is not just the sum of the two response functions for spinless fermions. The point is that when both a 3d and 4s electron screen the core hole, the intermediate state is at a lower energy (at $\hbar\omega_{\text{in}} = U_d + U_s$) compared to the situation where only a single d or s electron screens the core hole (with a resonance at $\hbar\omega_{\text{in}} = U_d$ or U_s, respectively.) In the situation that both electrons screen the core hole, the resonance therefore appears at a different incoming photon energy.

According to Eq. (3.15), we now need to evaluate expressions of the sort $(U_d n^d + U_s n^s)^l$ for $l > 0$ when expanding around the unscreened intermediate states. After using the binomial theorem and summing the resulting series, we obtain

$$(U_d n^d + U_s n^s)^l = U_d^l n^d + U_s^l n^s + n^d n^s \left[(U_d + U_s)^l - U_d^l - U_s^l\right], \tag{3.42}$$

which leads to a scattering amplitude

$$\mathcal{F}_{fi}^{sd} = \mathcal{F}_{fi}^{s+d} + \left[P_1(\omega, -U_d - U_s) - P_1(\omega, -U_d) - P_1(\omega, -U_s)\right] \langle f|\, \rho_{\mathbf{q}}^{ds}\, |i\rangle\,, \tag{3.43}$$

where $\rho_{\mathbf{q}}^{ds} \equiv \sum_i e^{i\mathbf{q}\cdot\mathbf{R}_i} n_i^d n_i^s$. This is an interesting term, physically, as it directly measures the density correlations between the d and s electron density on a transition metal atom.

Alternatively, we again expand around the well-screened intermediate states where both the d and s orbitals are occupied:

$$H_c = \sum_i c_i c_i^\dagger (U_d d_i d_i^\dagger + U_s s_i s_i^\dagger) \tag{3.44}$$

where c_i, d_i and s_i represent the core, d and s electron annihilation operators respectively. The corresponding scattering amplitude is

$$\begin{aligned}\mathcal{F}_{fi}^{sd} =& \left[P_1(\omega, U_d + U_s) - P_1(\omega, U_s)\right] \langle f|\, \rho_{\mathbf{q}}^{d}\, |i\rangle \\ &+ \left[P_1(\omega, U_d + U_s) - P_1(\omega, U_d)\right] \langle f|\, \rho_{\mathbf{q}}^{s}\, |i\rangle \\ &+ \left[P_1(\omega, U_d) + P_1(\omega, U_s) - P_1(\omega, U_d + U_s)\right] \langle f|\, \rho_{\mathbf{q}}^{ds}\, |i\rangle\end{aligned} \tag{3.45}$$

where $\rho_{\mathbf{q}}^{d,s} \equiv \sum_i e^{i\mathbf{q}\cdot\mathbf{R}_i} n_i^{d,s}$. Note that $[P_1(\omega, U_d + U_s) - P_1(\omega, U_s)] = 0$ when $U_d = 0$.

3.2.7 Conclusions

On the basis of the ultra-short lifetime of the core hole in the intermediate state we presented a series expansion of the indirect resonant inelastic X-ray scattering amplitude, which is asymptotically exact for both small and large local core hole potentials. This algebraic series is also given in a graphical representation. By resumming the terms in the series, we find the dynamical charge and spin correlation functions that are measured in RIXS. The resonant prefactor is only weakly temperature dependent. We have also derived a sum rule for the total scattering intensity and considered RIXS in both single and multi-band systems. On the basis of our results, the charge and spin structure factor that is obtained from *ab initio* density functional calculations or from, *e.g.*, Hubbard-like model Hamiltonians can directly be compared to experimental RIXS spectra. Moreover, our results open up the possibility to compare the measurements of $S(\mathbf{q},\omega)$ by RIXS and, for instance, electron energy loss spectroscopy [67]. In this way one can actually determine experimentally the resonant scattering prefactors that we have calculated.

We should stress that four basic assumptions underly our results, which otherwise are general. First, the RIXS process that we consider is *indirect*, *i.e.*, in the scattering process electrons are *not* directly promoted into the conduction band of the solid. Rather the inelastic scattering that we consider is due to the potential of the core hole which is present in the intermediate state. This situation arises, for instance, at the K edge of transition metal atoms, but can also occur at the L edge of lanthanide ions. We assumed, furthermore, that the core hole is localized and that its lifetime is short – reasonable premises for the deep core holes that are involved. The final assumption is that scattering is dominated by the coupling between the core hole and electrons (of d character if we consider a transition metal K edge) *on the same atom*. This is a good approximation when the d electrons are localized and the on-site Coulomb interaction is much larger than the one between neighboring atoms. In that sense our ultra-short lifetime expansion is expected to work very well for 3d systems and possibly less so for the 4d or 5d transition metal ions.

Finally, we assumed that the charge and longitudinal spin responses of the system that we consider are not vanishing, *i.e.*, they are the leading order response function. In insulators at energies below the gap, however, these two response functions do vanish. This in principle opens a way to observe correlation functions beyond the ones that we have considered here, for instance, transversal spin (chapter 4) or orbital response functions (chapter 5) and thus to measure magnon dispersions or even orbiton properties with RIXS – a very exciting prospect indeed.

3.2.8 Acknowledgments

We thank Michel van Veenendaal and John P. Hill for stimulating our interest in the theory of indirect resonant inelastic X-ray scattering, for intense discussions, for critical reading of the manuscript and for their generous hospitality. We thank Stephane Grenier, Young-June Kim, Philip Platzman and George Sawatzky for fruitful discussions. We gratefully acknowledge support from the Argonne National Laboratory Theory Institute, Brookhaven National Laboratory (DE-AC02-98CH10996), and the Dutch Science Foundation FOM.

3.3 Corrections to the cross section for strong core hole potentials

In this section we consider the first order correction to the UCL results given in Sec. 3.2. We treat the cases of spinless fermions (Sec. 3.3.1) and fermions with spin (Sec. 3.3.2) in the limit of a strong core hole potential. The resulting correction terms to the RIXS scattering amplitude contain information on the hopping matrix elements.

3.3.1 Spinless fermions

In Sec. 3.2, H^l_{int} was approximated in the limit of a strong core hole potential as $(H_0+H_c)^l \approx H^l_c$. The first order correction to this approximation has one factor of H_0 and $l-1$ factors of H_c, and those terms are not properly included in the UCL expansion for $l \geq 2$. We therefore improve the approximation:

$$(H_0 + H_c)^l = H_c^l + \sum_{n=0}^{l-2} H_c^n H_0 H_c^{l-1-n} + \mathcal{O}(H_0^2) \tag{3.46}$$

for $l > 2$. The $l \leq 2$ terms were exact already in Sec. 3.2. The $n = 0$ term was also already included. The first order corrections to Eq. (3.2) for spinless fermions are therefore of the form

$$\langle f|\, \mathcal{D}^\dagger \sum_{n=1}^{l-2} H_c^n H_0 H_c^{l-1-n} \mathcal{D}\, |i\rangle = U^{l-1}(l-2) \,\langle f|\, \sum_i e^{i\mathbf{q}\cdot\mathbf{R}_i} c_i c_i^\dagger H_0 c_i c_i^\dagger \,|i\rangle \tag{3.47}$$

when expanding around the well-screened intermediate states.

Now we commute H_0 to the right:

$$\left[H_0, c_i c_i^\dagger\right] = \sum_j t_{ij} \left(c_i^\dagger c_j - c_j^\dagger c_i\right). \tag{3.48}$$

where we assumed t_{ij} and t_{ji} are equal and real numbers. The correction terms (3.47) then become

$$\langle f|\, \mathcal{D}^\dagger \sum_{n=1}^{l-2} H_c^n H_0 H_c^{l-1-n} \mathcal{D}\, |i\rangle = -U^{l-1}(l-2) \,\langle f|\, \sum_{i,j} e^{i\mathbf{q}\cdot\mathbf{R}_i} t_{ij} c_j^\dagger c_i \,|i\rangle\,. \tag{3.49}$$

Fourier transforming gives

$$\langle f|\, \mathcal{D}^\dagger \sum_{n=1}^{l-2} H_c^n H_0 H_c^{l-1-n} \mathcal{D}\, |i\rangle = -U^{l-1}(l-2) \,\langle f|\, \sum_{\mathbf{k}} t_{\mathbf{k}} c_{\mathbf{k}}^\dagger c_{\mathbf{k}-\mathbf{q}} \,|i\rangle\,, \tag{3.50}$$

where the $t_{\mathbf{k}} = \sum_i t_{i0} e^{-i\mathbf{k}\cdot\mathbf{R}_i}$ are the Fourier components of t_{ij}, assuming t_{ij} to be invariant under translations.

The inelastic scattering amplitude becomes

$$\mathcal{F}_{fi} = \frac{1}{\Delta} \sum_{l=1}^{\infty} \frac{1}{\Delta^l} \langle f| \mathcal{D}^\dagger (H_0 + H_c)^l \mathcal{D} |i\rangle \tag{3.51}$$

$$\approx P_1 \langle f| \rho_{\mathbf{q}} |i\rangle - \frac{U}{\Delta^3} \sum_{l=2}^{\infty} \left(\frac{U}{\Delta}\right)^{l-2} (l-2) \langle f| \sum_{\mathbf{k}} t_{\mathbf{k}} c^\dagger_{\mathbf{k}} c_{\mathbf{k}-\mathbf{q}} |i\rangle \tag{3.52}$$

$$= P_1 \langle f| \rho_{\mathbf{q}} |i\rangle + P_3 \langle f| \sum_{\mathbf{k}} t_{\mathbf{k}} c^\dagger_{\mathbf{k}} c_{\mathbf{k}-\mathbf{q}} |i\rangle \tag{3.53}$$

with $P_3 = -\frac{U^2}{\Delta^2(\Delta-U)^2}$. The correction terms carry information about the hopping matrix elements t_{ij}. They involve two-site correlation functions. Higher order correction terms can generate correlation functions with more and more sites. Especially for systems with only a single fermion, or at least very few fermions, that are at a fixed momentum, RIXS is able to directly probe the hopping matrix elements. It should be noted, however, that the P_1 and P_3 terms of the scattering amplitude interfere, and that this interference term is of order t_{ij}/Δ stronger than the $|P_3|^2$ term.

3.3.2 Fermions with spin 1/2

When the fermions have a spin index, we have to evaluate for $l > 2$:

$$\begin{aligned}
&\langle f| \mathcal{D}^\dagger \sum_{n=1}^{l-2} H_c^n H_0 H_c^{l-1-n} \mathcal{D} |i\rangle \\
&= U^{l-1} \sum_{n=1}^{l-2} \langle f| \sum_i e^{i\mathbf{q}\cdot\mathbf{R}_i} \left(\sum_\sigma c_{i\sigma} c^\dagger_{i\sigma}\right)^n H_0 \left(\sum_{\sigma'} c_{i\sigma'} c^\dagger_{i\sigma'}\right)^{l-1-n} |i\rangle \\
&= U^{l-1} \sum_{n=1}^{l-2} \langle f| \sum_i e^{i\mathbf{q}\cdot\mathbf{R}_i} \left(c_{i\uparrow} c^\dagger_{i\uparrow} + c_{i\downarrow} c^\dagger_{i\downarrow} + (2^n - 2) c_{i\uparrow} c^\dagger_{i\uparrow} c_{i\downarrow} c^\dagger_{i\downarrow}\right) \times \\
&\qquad H_0 \left(c_{i\uparrow} c^\dagger_{i\uparrow} + c_{i\downarrow} c^\dagger_{i\downarrow} + (2^{l-1-n} - 2) c_{i\uparrow} c^\dagger_{i\uparrow} c_{i\downarrow} c^\dagger_{i\downarrow}\right) |i\rangle \,.
\end{aligned} \tag{3.54}$$

H_0 is commuted to the right:

$$\begin{aligned}
&\left[H_0, \left(c_{i\uparrow} c^\dagger_{i\uparrow} + c_{i\downarrow} c^\dagger_{i\downarrow} + (2^{l-1-n} - 2) c_{i\uparrow} c^\dagger_{i\uparrow} c_{i\downarrow} c^\dagger_{i\downarrow}\right)\right] = \sum_{j,\sigma} t_{ij} \left(c^\dagger_{i\sigma} c_{j\sigma} - c^\dagger_{j\sigma} c_{i\sigma}\right) \\
&+ (2^{l-1-n} - 2) \left(\left[H_0, c_{i\uparrow} c^\dagger_{i\uparrow}\right] c_{i\downarrow} c^\dagger_{i\downarrow} + c_{i\uparrow} c^\dagger_{i\uparrow} \left[H_0, c_{i\downarrow} c^\dagger_{i\downarrow}\right]\right) \\
&= \sum_{j,\sigma} t_{ij} \left(c^\dagger_{i\sigma} c_{j\sigma} - c^\dagger_{j\sigma} c_{i\sigma}\right) \left(2^{l-1-n} - 1 + (2^{l-1-n} - 2) n_{i\bar{\sigma}}\right),
\end{aligned} \tag{3.55}$$

where $\bar{\sigma} = \uparrow$ if $\sigma = \downarrow$, and vice versa. We find after some algebra

$$\begin{aligned} &\langle f | \mathcal{D}^\dagger \sum_{n=1}^{l-2} H_c^n H_0 H_c^{l-1-n} \mathcal{D} | i \rangle \\ &\quad = U^{l-1} \sum_{i,j,\sigma} e^{i\mathbf{q}\cdot\mathbf{R}_i} t_{ij} \langle f | \Big[- (l-2)\, c^\dagger_{j\sigma} c_{i\sigma} - \big((l-3) 2^{l-1} + 4 - l \big)\, c_{i\bar{\sigma}} c^\dagger_{i\bar{\sigma}} c^\dagger_{j\sigma} c_{i\sigma} \\ &\qquad + \big(2^{l-1} - l \big)\, c_{i\bar{\sigma}} c^\dagger_{i\bar{\sigma}} c^\dagger_{i\sigma} c_{j\sigma} \Big] | i \rangle \,. \end{aligned} \tag{3.56}$$

The inelastic scattering amplitude $\mathcal{F}_{fi}$ is then

$$\mathcal{F}_{fi} = \frac{1}{\Delta} \sum_{l=1}^{\infty} \frac{1}{\Delta^l} \langle f | \mathcal{D}^\dagger (H_0 + H_c)^l \mathcal{D} | i \rangle \tag{3.57}$$

$$\begin{aligned} &\approx (\text{uncorrected terms}) + P_3 \sum_{i,j,\sigma} t_{ij} e^{i\mathbf{q}\cdot\mathbf{R}_i} \langle f | \Big[c^\dagger_{j\sigma} c_{i\sigma} \\ &\quad - \frac{\Delta}{\Delta - 2U} c_{i\bar{\sigma}} c^\dagger_{i\bar{\sigma}} c^\dagger_{i\sigma} c_{j\sigma} + \frac{\Delta^2 + 2U\Delta - 4U^2}{(\Delta - 2U)^2} c_{i\bar{\sigma}} c^\dagger_{i\bar{\sigma}} c^\dagger_{j\sigma} c_{i\sigma} \Big] | i \rangle \,, \end{aligned} \tag{3.58}$$

where "uncorrected terms" refers to Eq. (3.40).

For the special case of a half-filled system without doubly occupied sites in the initial state, the scattering amplitude is

$$\mathcal{F}_{fi} = (\text{uncorr.}) + P_3 \sum_{\mathbf{k},\sigma} \left[\frac{2\Delta(\Delta - U)}{(\Delta - 2U)^2} t_{\mathbf{k}+\mathbf{q}} - \frac{\Delta}{\Delta - 2U} t_{\mathbf{k}} \right] \langle f | c^\dagger_{\mathbf{k}+\mathbf{q},\sigma} c_{\mathbf{k}\sigma} | i \rangle \,. \tag{3.59}$$

3.4 Polarization dependence of transition metal K edge RIXS

In Sec. 3.2, the polarization details of the indirect RIXS scattering process at the transition metal K edge were neglected: all $T(\boldsymbol{\epsilon}', \boldsymbol{\epsilon})$ were set to 1. In this section, the polarization dependence of the two dipole transitions is investigated in more detail. The previous results is modified by a polarization-dependent prefactor $T(\boldsymbol{\epsilon}', \boldsymbol{\epsilon})$.

In the following, it is assumed that the 4p electron acts as a spectator, that is, different 4p states do not give rise to different scattering processes [4, 5]. These are determined by the 1s core hole alone.

In an octahedral crystal feld, the polarization dependence of indirect RIXS at the transition metal K edge might at first sight seem trivial: excitation of a 1s core electron into a 4p level and the consecutive de-excitation yields the polarization dependence (2.42)

$$T(\boldsymbol{\epsilon}',\boldsymbol{\epsilon}) = \sum_i \langle 1s|\, \boldsymbol{\epsilon}'^* \cdot \mathbf{r}\, |4p_i\rangle \langle 4p_i|\, \boldsymbol{\epsilon} \cdot \mathbf{r}\, |1s\rangle \propto \sum_{i,n,m} \iint d\mathbf{r}d\mathbf{r}'\ \epsilon'^*_n r'_n r'_i r_i \epsilon_m r_m$$
$$\propto \sum_{i,n,m} \epsilon'^*_n \delta_{n,i} \delta_{i,m} \epsilon_m = \boldsymbol{\epsilon}'^* \cdot \boldsymbol{\epsilon}. \qquad (3.60)$$

Deviations from octahedral symmetry induce an anisotropy. In La_2CuO_4, for instance, the $4p_z$ state is at a slightly different energy than the $4p_{x,y}$ because of the planar structure of the material. In the extreme case that the off-resonant $4p_z$ states do not contribute at all to the RIXS scattering amplitude, $T(\boldsymbol{\epsilon}',\boldsymbol{\epsilon}) = \epsilon'^*_x \epsilon_x + \epsilon'^*_y \epsilon_y$.

Apart from these local effects, however, there is another important anisotropic contribution to the polarization dependence. The 4p states form bands, and the $4p_x$ and $4p_y$ orbitals can mix. We now show the effect of this mixing in a minimal model for the 4p states. Nearest neighbor 4p orbitals only have non-zero hopping from $4p_x$ to $4p_x$ and from $4p_y$ to $4p_y$. Next-nearest neighbor hopping is substantial because of the extended nature of the 4p states. This can couple $4p_x$ and $4p_y$ orbitals, and we only include this part of the next-nearest neighbor hopping in the Hamiltonian:

$$H = -t \sum_{i,\delta} \left(p^\dagger_{x,i} p_{x,i+\delta} + p^\dagger_{y,i} p_{y,i+\delta} \right) - t' \sum_{i,\delta'} \left(p^\dagger_{y,i} p_{x,i+\delta'} + p^\dagger_{x,i} p_{y,i+\delta'} \right) \qquad (3.61)$$

where $p_{x,y}$ annihilates an electron in the $4p_{x,y}$ orbital. t is the nearest neighbor hopping amplitude, which is assumed to be equal in all directions for simplicity, and t' is the hopping amplitude for next-nearest neighbors. δ and δ' point to nearest and next-nearest neighbors, respectively. This Hamiltonian is easily diagonalized in $\mathbf{k}$ space:

$$H = \sum_{\mathbf{k}} \left[\left(-zt\gamma_{\mathbf{k}} + z't'\gamma'_{\mathbf{k}} \right) \alpha^\dagger_{\mathbf{k}} \alpha_{\mathbf{k}} + \left(-zt\gamma_{\mathbf{k}} - z't'\gamma'_{\mathbf{k}} \right) \beta^\dagger_{\mathbf{k}} \beta_{\mathbf{k}} \right] \qquad (3.62)$$

where $\gamma_{\mathbf{k}}(') = \sum_{\delta(')} e^{i\mathbf{k}\cdot\boldsymbol{\delta}(')}/z(')$ with z the number of nearest neighbors and z' the number of next-nearest neighbors. We introduced transformed fermion operators $\alpha_{\mathbf{k}}$ and $\beta_{\mathbf{k}}$:

$$\begin{pmatrix} p_{x,\mathbf{k}} \\ p_{y,\mathbf{k}} \end{pmatrix} = \frac{1}{\sqrt{2}} \begin{pmatrix} 1 & 1 \\ -1 & 1 \end{pmatrix} \begin{pmatrix} \alpha_{\mathbf{k}} \\ \beta_{\mathbf{k}} \end{pmatrix}. \qquad (3.63)$$

Within this model, the polarization factors (2.42) are

$$T_\alpha(\boldsymbol{\epsilon}',\boldsymbol{\epsilon}) = \langle 1s|\, \boldsymbol{\epsilon}'^* \cdot \mathbf{r}\, |\alpha_{\mathbf{k}}\rangle \langle \alpha_{\mathbf{k}}|\, \boldsymbol{\epsilon} \cdot \mathbf{r}\, |1s\rangle \propto \iint d\mathbf{r}d\mathbf{r}'\ \boldsymbol{\epsilon}'^* \cdot \mathbf{r}'(x'-y')(x-y)\boldsymbol{\epsilon} \cdot \mathbf{r}$$
$$\propto (\epsilon'^*_x - \epsilon'^*_y)(\epsilon_x - \epsilon_y), \qquad (3.64)$$

$$T_\beta(\boldsymbol{\epsilon}', \boldsymbol{\epsilon}) = \langle 1s| \boldsymbol{\epsilon}'^* \cdot \mathbf{r} \,|\beta_\mathbf{k}\rangle \,\langle \beta_\mathbf{k}| \,\boldsymbol{\epsilon} \cdot \mathbf{r} \,|1s\rangle \propto \iint d\mathbf{r} d\mathbf{r}' \;\boldsymbol{\epsilon}'^* \cdot \mathbf{r}'(x' + y')(x + y)\boldsymbol{\epsilon} \cdot \mathbf{r}$$
$$\propto (\epsilon_x'^* + \epsilon_y'^*)(\epsilon_x + \epsilon_y). \tag{3.65}$$

The 4p$_z$ states will contribute a term proportional to $\epsilon_z'^* \epsilon_z$. When $t' = 0$, $|\alpha_\mathbf{k}\rangle$ and $|\beta_\mathbf{k}\rangle$ are degenerate and we recover the result for atomic 4p states: $T_\alpha + T_\beta \propto \boldsymbol{\epsilon}'^* \cdot \boldsymbol{\epsilon}$. However, when next-nearest neighbor hopping is non-zero, the degeneracy of the 4p states is lifted. When this splitting becomes of the order of Γ, the energy denominator in Eq. (2.41) becomes appreciably different and the polarization dependences of T_α and T_β no longer add with equal weight.

In our simple model, the hopping t' introduces a mixing of 4p$_x$ and 4p$_y$ orbitals, which of course can also be introduced in other ways, like spin-orbit coupling, scattering off the valence electrons, etc. In general, all these effects, together with the deviations from the cubic crystal field mentioned above, will produce an anisotropic polarization dependence.

3.5 Comparison to experiments

The observation that within the UCL the RIXS cross section can be factored into a resonant prefactor and the dynamic structure factor $S(\mathbf{q}, \omega)$, was tested experimentally by Kim *et al.* [67]. They reported an empirical comparison of Cu K edge indirect RIXS spectra, taken at the Brillouin zone center, with optical dielectric loss functions measured in a number of copper oxides: Bi_2CuO_4, $CuGeO_3$, $Sr_2Cu_3O_4Cl_2$, La_2CuO_4, and $Sr_2CuO_2Cl_2$. Analyzing both incident and scattered photon resonances, they extracted a response function that is independent of the incident energy. The overall spectral features of the indirect RIXS spectral function were found to be in reasonable agreement with the optical dielectric loss function over a wide energy range. In the case of Bi_2CuO_4 and $CuGeO_3$, Ref. [67] observes that the incident energy-independent response function, $S(\mathbf{q} = \mathbf{0}, \omega)$, matches very well with the dielectric loss function, $-\mathfrak{Im}\{1/\epsilon(\omega)\}$ measured with spectroscopic ellipsometry, suggesting that the local core hole approximation treatment of the UCL works well in these more localized electron systems. Corner sharing two-dimensional copper oxides exhibit more complex excitation features than observed in the dielectric loss functions, likely related to non-local core hole screening effects.

CHAPTER 4

MAGNETIC RIXS ON 2D CUPRATES

4.1 Introduction

Over the past three years, RIXS has made tremendous progress in probing magnetic excitations. From the 3D material NiO via the 2D high-T_c superconductors to the 1D telephone number compounds, many materials have been studied with RIXS. What used to be the exlusive domain of neutron scattering, and to lesser degree Raman spectroscopy and optical conductivity measurements, now is being entered by RIXS.

Neutron scattering measures the dispersion, or, more generally, the dynamic spin susceptibility $\chi(\mathbf{q}, \omega)$ of magnetic compounds with a very high energy resolution (down to the μeV range [68]). Neutrons, however, have a number of intrinsic difficulties: they require large samples or very high flux, especially at high energy transfers. Some elements are intrinsically unsuitable for neutron scattering because they strongly absorb neutrons (*e.g.*, cadmium and gadolinium [68]).

RIXS does not suffer from these limitations. The energy resolution of RIXS experiments has improved dramatically over the last few years, allowing for the measurement of low energy magnetic excitations down to ~ 50 meV. This brings the high-T_c cuprates into the domain of magnetic RIXS, and this will be the main subject of this chapter.

Because of the very rapid developments in instrumentation, theory has trouble keeping up with experiments. Magnetic RIXS measurements on the 2D cuprates have been done at the Cu K edge [14, 53], L edge [10, 11, 21, 69], M edge [15] and O K edge [70, 71].

In the scattering process, angular momentum can be transferred to the solid. RIXS is not restricted to $\Delta S = 0, 1$ like neutrons, which carry spin 1/2, but can also transfer two units of angular momentum since photons have spin 1. Photons couple only very weakly to the spin angular momentum of the electron. Rather, the photon's angular momentum is transferred to the orbital angular momentum of the electron. This might seem a problem for creating magnetic excitations with X-rays, because in most solids the relativistic spin-orbit coupling is small.

However, for some core states involved in RIXS, the spin-orbit coupling is very large (of the order of 10 eV). Consequently, the spin and orbital degrees of freedom are coupled, so the photon's angular momentum can be transferred indirectly to the spins, creating a magnetic excitation with $\Delta S^z = \pm 1$ or ± 2. This channel is direct RIXS: the final state can be reached without any dynamics in the intermediate state.

1s core states have no orbital angular momentum, and therefore magnetic excitations with $\Delta S^z = \pm 1$ or ± 2 cannot be created at the K edges. However, it is possible to induce a $\Delta S^z = 0$ magnetic excitation, like in two-magnon Raman scattering in the cuprates. This process can arise because the RIXS process creates a magnetic impurity in the intermediate state, which is then screened by the surrounding valence electrons: the magnetic background is rearranged around the core hole site, and left behind in an excited final state. Note that indirect processes can also play a role at edges where there is strong core state spin-orbit coupling (and hence direct RIXS); the indirect RIXS spectral weight will be of sub-leading order, however.

Sec. 4.4 deals with indirect RIXS at the transition metal K edge, where the 1s core hole couples to the spin degree of freedom by locally modifying the superexchange interactions [14, 51–53]. In such a process, the total spin of the valence electrons is conserved, and only excitations where at least two spins are flipped (with total $\Delta S^z = 0$) are allowed. A similar indirect process can also occur at the oxygen K edge [70, 71], see Sec. 4.7.

The first theoretical work on magnetic excitations was done by De Groot *et al.* [72]. They studied Ni^{2+} and Cu^{2+} numerically, and showed that there are no pure spin flips present for a Cu^{2+} ion when the spin is aligned along the z axis and the hole occupies the $3\mathrm{d}_{x^2-y^2}$ orbital in a D_{4h} crystal field, see also Ref. [73]. Instead, they predict spin flips accompanying dd excitations. In Sec. 4.5 it will be shown that spin flips are possible when the spin is in the xy plane, and that the resulting RIXS spectrum follows the magnon dispersion [11, 19, 21, 69, 74]. For the cuprates, these results put L edge RIXS as a technique on equal footing with neutron scattering. The first observation of magnetic excitations with RIXS was done by Harada *et al.* [71], who claim to see two-magnon excitations at the oxygen K edge.

We distinguish between magnetic RIXS processes that locally change the size of the magnetic moment and those that do not. The final state contains respectively a longitudinal or a transversal magnetic excitation. Transitions with $\Delta S = 1$ and 2 are allowed for certain magnetic ions, for instance, a transition of

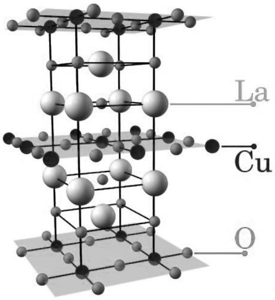

Figure 4.1: The crystal structure of La_2CuO_4. The CuO_2 layers are separated by electronically inactive LaO layers. Figure by M. Berciu.

high spin Ni^{2+} to its low spin state. The energy scale of excitations with $\Delta S \neq 0$ is set by Hund's rule coupling J_H, which is typically of the order of 1 eV. These excitations therefore have a much higher energy than the transversal ones, whose energy scale is usually set by the superexchange constant $J \sim 100$ meV. Magnetic excitations with $\Delta S \neq 0$ are described in chapter 3, and are beyond the scope of this chapter.

This chapter starts with a brief review of the theory for magnetic excitations in cuprates in Sec. 4.2. The following sections contain a general formulation of the magnetic RIXS cross section (Sec. 4.3), which is then applied in Sec. 4.4 to the copper K edge, in Sec. 4.5 to the copper L and M edges, and to the oxygen K edge in Sec. 4.7. Finally, the relevance of the screening of a magnetic impurity in the Heisenberg model for angle-resolved photo-emission spectroscopy will be discussed in Sec. 4.8.

4.2 Theory of magnetic excitations

4.2.1 Electronic structure of cuprates

All work in this chapter is focussed on cuprate supercondutors and their Mott insulating parent compounds. The cuprates investigated here have a perovskite structure, as shown in Fig. 4.1 for La_2CuO_4: layers of CuO_2 are stacked on top of each other, sometimes separated by a different layer (as in La_2CuO_4).

The copper ions are often situated at the center of octahedrons of oxygen ions. In the insulating state, the copper 3d subshell contains (approximately) 9 electrons, while the surrounding oxygen ions are in a $2p^6$ configuration, so they have a charge of $-2e$. This creates a crystal field that splits the Cu 3d states. If the oxygen ions form a perfectly cubic octahedron, the 5 Cu 3d levels are split in a t_{2g} triplet and an e_g doublet, see Fig. 4.2. The e_g orbitals point towards the negatively charged oxygen ions, and therefore have a higher Coulomb energy than the t_{2g} orbitals (which are directed away from the oxygen ions). Because of the stacking of the CuO_2 layers, the octahedra are usually elongated along the z axis (perpendicular to the CuO_2 planes), which splits the t_{2g} and e_g levels further, as shown in Fig. 4.2. In La_2CuO_4, for instance, the hole in the 3d subshell populates the $3d_{x^2-y^2}$ orbital in the ground state: the $3d_{3z^2-r^2}$ orbital is lowered in energy because its Coulomb interaction with the apical oxygen ions (*i.e.*, those along the z axis) is reduced. In other compounds, like Nd_2CuO_4 and $CaCuO_2$, the apical oxygens are absent, which could be regarded as if they are moved to infinity. Because the crystal field splitting is of the order of 2 eV in the insulating cuprates [70], the 3d orbital degree of freedom is frozen out already far above room temperature.

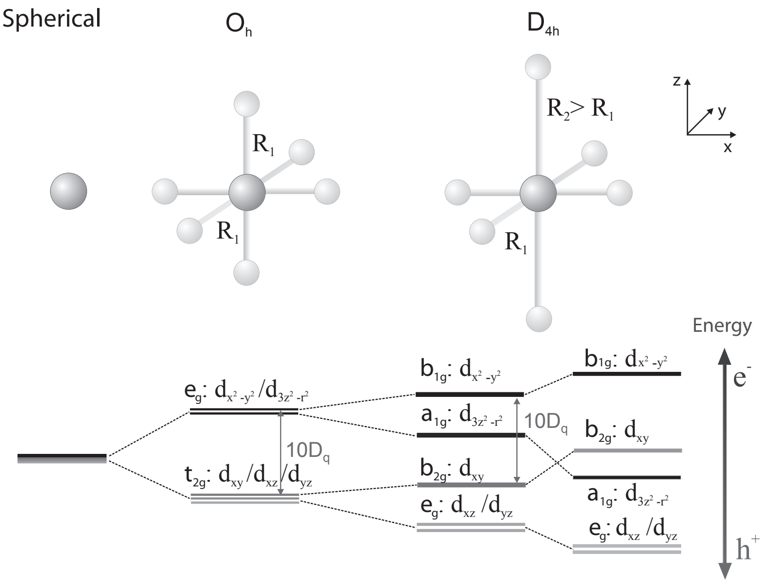

Figure 4.2: Crystal field splitting of the Cu 3d levels in an octahedral environment (O_h symmetry) and in an elongated octahedron (D_{4h} symmetry). Figure reproduced with permission from Ref. [70].

The electronic state of a $3d^9$ copper ion is still degenerate however, due to the spin degree of freedom. Superexchange interactions between neighboring Cu ions can split the spin states. In an antiferromagnetic superexchange process, a hole hops to a neighboring Cu ion that is populated by another hole of different spin. The latter hole moves in the opposite direction, and the two holes have effectively exchanged their spin [75]. Because of the Pauli exclusion principle, neighboring holes with the same spin cannot move to each other's site. This confinement increases their kinetic energy, and therefore the superexchange interaction is antiferromagnetic. In case the spins cannot reach each other's places as described above, as for instance when the Cu-O-Cu bonds make 90° angles, weakly ferromagnetic superexchange interactions can arise [76].

The undoped cuprates are well described at low temperature by the $S = 1/2$

Heisenberg model:

$$H_0 = J \sum_{\langle i,j \rangle} \mathbf{S}_i \cdot \mathbf{S}_j, \tag{4.1}$$

where the sum is over all pairs i, j of nearest neighbors.

The direction of the staggered magnetization is not yet fixed by the Heisenberg model; the isotropy is broken by perturbations. In the cuprates, the direction of the staggered magnetization is particularly important for single-magnon RIXS: alignment in the $\mathrm{CuO_2}$ planes gives the strongest signal. This alignment is favored by, for instance, the Dzyaloshinsky-Moriya interaction that arises when the $\mathrm{CuO_6}$ octahedra are rotated around the [110] direction [77, 78].

4.2.2 Boson mappings of the 2D Heisenberg model

No exact solution of the Heisenberg model in 2 dimensions is known. An approximate solution can be obtained by bosonizing the spins [79,80]. There are various boson formulations. We briefly review the Holstein-Primakoff and Dyson-Maleev approaches here.

Spin to boson mappings. In both boson mappings, the state of the spin is represented by a single boson mode. The state $|S, m\rangle$ with $m = +S$ is identified with the boson vacuum state. If the spin is lowered by n units, the state $m = S-n$ is represented by n bosons in the mode, etc. The angular momentum identities

$$\langle S, m| \, S^z \, |S, m\rangle = \hbar m \tag{4.2}$$

$$\langle S, m \pm 1| \, S^{\pm} \, |S, m\rangle = \hbar \sqrt{S(S+1) - m(m \pm 1)} \tag{4.3}$$

fix $S^z = \hbar(S - a^\dagger a)$, where $a^{(\dagger)}$ creates (annihilates) a boson. The bosons satisfy $[a, a^\dagger] = 1$. The form of the raising and lowering operators $S^{\pm}$ differs for the two mappings. In the Holstein-Primakoff mapping,

$$S^+ = \hbar\sqrt{2S}\sqrt{1 - \frac{a^\dagger a}{2S}}\; a \quad \text{and} \quad S^- = (S^+)^\dagger. \tag{4.4}$$

It can be easily verified that this mapping satisfies Eq. (4.3). The square-root of the boson operators is defined by the expansion $\sqrt{1-x} = 1 - x/2 - x^2/8 - \ldots$ This boson mapping satisfies the angular momentum commutation relations.

The expansion of the square-root introduces infinitely many multi-boson terms. This complicates the boson mapping as one has to decide where to cut off this expansion in practical calculations. The (conjugate) Dyson-Maleev mapping solves this problem by the alternative definition

$$S^+ = \hbar a, \tag{4.5}$$

$$S^- = \hbar\sqrt{2S} a^\dagger \left(1 - \frac{a^\dagger a}{2S}\right). \tag{4.6}$$

Note that with this mapping, $(S^+)^\dagger \neq S^-$. For convenience, we will set $\hbar = 1$ from hereon.

Both boson formulations suffer from the problem that the Hilbert spaces are not the same before and after the boson mapping: the boson mode can be populated by any number of bosons, which makes the Hilbert space infinite. On the other side, the spin can only be in $2S+1$ orthogonal states. Boson states with more than $2S$ bosons are therefore unphysical. Although $S^\pm$ do not take one out of the physical Hilbert space, they do if one approximates the square-root in the Holstein-Primakoff formulation. Therefore, all spin operators should be projected on the physical subspace after expansion of the square-root [81].

Holstein-Primakoff theory for the Heisenberg antiferromagnet. When boson theories are applied to the Heisenberg antiferromagnet, each spin in the system is represented by a boson mode. One takes the classical, antiferromagnetic Néel state as the reference state: it is identified with the boson vacuum. The boson vacuum should not be confused with the (approximate) ground state; it is just a zeroth order approximation to it, which will be refined within the boson formalism. When defining the Holstein-Primakoff bosons above, we assumed that the $m = S$ state was directed along the z direction. Therefore, we rotate the spin operators for every site to align them with the ordered moment. Then, we can still use the same boson definitions as above. Since the Heisenberg Hamiltonian is invariant under rotations, we might as well take spins of the spin-up sublattice to be aligned along the z axis, so that only the spins of the spin-down sublattice have to be rotated by 180° around the x axis: $S^\pm \mapsto S'^\mp$ and $S^z \mapsto -S'^z$. In these locally rotated coordinates, the antiferromagnetic Heisenberg model is

$$H_0 = J \sum_{i\in\uparrow,\delta} \left(-S_i'^z S_{i+\delta}'^z + \frac{1}{2}\left[S_i'^+ S_{i+\delta}'^+ + S_i'^- S_{i+\delta}'^- \right] \right) \tag{4.7}$$

where the sum over i is only over the spin-up sublattice, and δ points to the nearest neighbors. In terms of Holstein-Primakoff bosons, the Hamiltonian consists of two-boson terms and also many multi-boson interaction terms.

The Hamiltonian can be approximated by neglecting all interaction terms: all square roots are approximated with 1. This so-called linear spin wave theory becomes exact in the limit of large spin, but also turns out to work reasonably well for $S = 1/2$. One obtains

$$H_0 = -\frac{JzNS^2}{2} + JS \sum_{i\in\uparrow,\delta} \left(a_i^\dagger a_i + a_{i+\delta}^\dagger a_{i+\delta} + a_i a_{i+\delta} + a_i^\dagger a_{i+\delta}^\dagger \right), \tag{4.8}$$

where the constant represents the energy of the classical Néel state. A Fourier transform gives

$$H_0 = -\frac{JzNS^2}{2} + \frac{JzS}{2} \sum_{\mathbf{k}} \left(2a_{\mathbf{k}}^\dagger a_{\mathbf{k}} + \gamma_{\mathbf{k}} \left(a_{-\mathbf{k}} a_{\mathbf{k}} + a_{-\mathbf{k}}^\dagger a_{\mathbf{k}}^\dagger \right) \right), \tag{4.9}$$

where $\gamma_{\mathbf{k}} = \sum_\delta e^{i\mathbf{k}\cdot\boldsymbol{\delta}}/z$ with z the number of nearest neighbors. The result is Bogoliubov transformed as $a_{\mathbf{k}} = u_{\mathbf{k}}\alpha_{\mathbf{k}} - v_{\mathbf{k}}\alpha^\dagger_{-\mathbf{k}}$, where

$$u_{\mathbf{k}} = \sqrt{\frac{1}{2\sqrt{1-\gamma_{\mathbf{k}}^2}} + \frac{1}{2}} \quad \text{and} \quad v_{\mathbf{k}} = \mathrm{sign}(\gamma_{\mathbf{k}})\sqrt{\frac{1}{2\sqrt{1-\gamma_{\mathbf{k}}^2}} - \frac{1}{2}}. \tag{4.10}$$

Since the cuprates studied in this thesis are (approximately) invariant under inversion of space, $\gamma_{\mathbf{k}} = \gamma_{-\mathbf{k}}$, $u_{\mathbf{k}} = u_{-\mathbf{k}}$ and $v_{\mathbf{k}} = v_{-\mathbf{k}}$, and one obtains

$$H_0 = -\frac{JzNS^2}{2} + JzS\sum_{\mathbf{k}}\left(v_{\mathbf{k}}^2 - \gamma_{\mathbf{k}}u_{\mathbf{k}}v_{\mathbf{k}}\right) + \sum_{\mathbf{k}}\omega_{\mathbf{k}}\alpha^\dagger_{\mathbf{k}}\alpha_{\mathbf{k}}. \tag{4.11}$$

The Bogoliubov bosons are called magnons and are the quanta of the spin wave modes. Their dispersion is

$$\omega_{\mathbf{k}} = JzS\sqrt{1-\gamma_{\mathbf{k}}^2}. \tag{4.12}$$

The ground state (the magnon vacuum) has a reduced energy with respect to the Néel state because of quantum fluctuations. The magnon vacuum $|0\rangle$ is defined by $\alpha_{\mathbf{p}}|0\rangle = 0$, and is related to the Néel state $|\text{Néel}\rangle$ by

$$|0\rangle = e^{\sum_{\mathbf{k}}\theta_{\mathbf{k}}\left(a^\dagger_{\mathbf{k}}a^\dagger_{-\mathbf{k}} - a_{\mathbf{k}}a_{-\mathbf{k}}\right)}|\text{Néel}\rangle = e^{\sum_{i,j}\theta_{ij}\left(a^\dagger_i a^\dagger_j - a_j a_i\right)}|\text{Néel}\rangle \tag{4.13}$$

where $\tanh 2\theta_{\mathbf{k}} = -v_{\mathbf{k}}/u_{\mathbf{k}}$. In real space, $\theta_{ij} = \frac{1}{N}\sum_{\mathbf{k}} e^{i\mathbf{k}\cdot(\mathbf{R}_i - \mathbf{R}_j)}\theta_{\mathbf{k}}$. Note that $\theta_{\mathbf{k}}$ and θ_{ij} are real, so $\theta_{ij} = \theta_{ji}$. Further, $\theta_{\mathbf{k}+(\pi,\pi)} = -\theta_{\mathbf{k}}$, so $\theta_{ii} = 0$. Numerical evaluation shows that θ_{ij} is of the order of ± 0.02, which means that the magnon vacuum is quite close to the Néel state.

Because of the breaking of rotational invariance of the Heisenberg model by the antiferromagnetic ground state, a Goldstone boson is present. Indeed, the magnon dispersion goes to zero at the Γ point. Magnon-magnon interactions do not change the spectrum at the Γ point, and magnons around $\mathbf{k} = (0,0) \equiv \mathbf{0}$ are stable against decay into multiple bosons.

The Heisenberg model appears from the more general Hubbard model when correlations are very strong compared to the hopping. Starting from a single band Hubbard model, one can expand in the small parameter t/U and obtain, to lowest order, the Heisenberg model: the charge degree of freedom of the Hubbard model is frozen out, and only the spin degree of freedom remains. The next order contains further-neighbor exchange interactions, including ring exchange, which rearranges 4 neighboring spins on a square plaquette. The latter interaction is relatively strong because there are many hopping processes that lead to such interactions. The result of the expansion in t/U to fourth order is

$$\begin{aligned}H_0 = &\left(\frac{4t^2}{U} - \frac{24t^4}{U^3}\right) \sum_{\langle i,j\rangle_1} \mathbf{S}_i \cdot \mathbf{S}_j + \frac{4t^4}{U^3} \sum_{\langle i,j\rangle_2} \mathbf{S}_i \cdot \mathbf{S}_j + \frac{4t^4}{U^3} \sum_{\langle i,j\rangle_3} \mathbf{S}_i \cdot \mathbf{S}_j \\ &+ \frac{80t^4}{U^3} \sum_{\langle i,j,k,l\rangle} [(\mathbf{S}_i \cdot \mathbf{S}_j)(\mathbf{S}_k \cdot \mathbf{S}_l) + (\mathbf{S}_i \cdot \mathbf{S}_l)(\mathbf{S}_j \cdot \mathbf{S}_k) - (\mathbf{S}_i \cdot \mathbf{S}_k)(\mathbf{S}_j \cdot \mathbf{S}_l)]\end{aligned} \tag{4.14}$$

where $\langle i,j\rangle_n$ indicates all pairs of n^{th} neighbors [82]. $\langle i,jk,l\rangle$ indexes all square plaquettes, where i,j,k,l point to the spins on the corners of the squares in clock-wise order. When treated on a mean-field level, the ring exchange term renormalizes the first and second neighbor exchange interactions: $J \mapsto \frac{4t^2}{U} - \frac{64t^4}{U^3}$ and $J' \mapsto -\frac{16t^4}{U^3}$, respectively [83].

The linear spin wave solution of the nearest-neighbor Heisenberg model can be easily extended to interactions between more distant neighbors, as long as the ground state stays antiferromagnetic. The Hamiltonian can be written as

$$H_0 = \frac{1}{2} \sum_{i,j} J_{ij} \mathbf{S}_i \cdot \mathbf{S}_j, \tag{4.15}$$

where J_{ij} is the superexchange coupling between spins i and j. The sum is over all i,j, and the factor 1/2 prevents double counting of the bonds. The function J_{ij} is split in two: the first part contains coupling between different sublattices and the second part contains the intra-sublattice couplings. The Fourier transforms of these parts are $J_\mathbf{k}$ and $J'_\mathbf{k}$ respectively. Again, a Bogoliubov transform can be employed and one finds

$$H_0 = \text{const.} + \sum_\mathbf{k} \Omega_\mathbf{k} \alpha^\dagger_\mathbf{k} \alpha_\mathbf{k}, \tag{4.16}$$

where the magnon dispersion is

$$\Omega_\mathbf{k} = S\left[(J_\mathbf{0} - J'_\mathbf{0} + J'_\mathbf{k})(U^2_\mathbf{k} + V^2_\mathbf{k}) - 2J_\mathbf{k} U_\mathbf{k} V_\mathbf{k}\right], \tag{4.17}$$

and the new Bogoliubov coefficients are

$$U_\mathbf{k} = \sqrt{\frac{J_\mathbf{0} - J'_\mathbf{0} + J'_\mathbf{k}}{2\sqrt{(J_\mathbf{0} - J'_\mathbf{0} + J'_\mathbf{k})^2 - J^2_\mathbf{k}}} + \frac{1}{2}} \quad \text{and} \quad V_\mathbf{k} = \text{sign}(J_\mathbf{k})(U^2_\mathbf{k} - 1). \tag{4.18}$$

4.3 Magnetic RIXS scattering amplitude

As explained in Sec. 4.1, both direct and indirect RIXS can probe magnetic excitations, be it of different kind. For direct RIXS, single spin flip excitations can be made at the $2p, 3p \rightarrow 3d$ edges of transition metal ions because of the large spin-orbit coupling of the $2p$ core hole [19,72,73]. For copper, with its simple $3d^{10}$ intermediate state of the valence electrons, these edges split into intermediate states with total angular momentum in the core states of $J = 1/2$ (L_2, M_2 edges) and $J = 3/2$ (L_3, M_3 edges). The edges are well resolved in XAS spectra (particularly at the L edge [84]), and therefore in RIXS one selects either the intermediate states with $J = 1/2$ or $J = 3/2$. This allows neglecting contributions from one edge if the incoming X-ray photons are at resonance with the other, as can be seen explicitly from Eq. (2.41). This is the fast collision approximation. Because the p-like core states have a strong spin-orbit coupling, the spin and orbital angular momentum separately are no longer good quantum numbers in the separated $J = 1/2$ and $3/2$ intermediate states. Therefore orbital and spin orbital angular momentum can be exchanged and direct spin flip processes can in principle be allowed in RIXS, unlike in optical spectroscopy. Because of the superexchange interaction present in the cuprates, single spin flips will disperse: they are in essence a superposition of single magnon states. Direct RIXS is thus able to probe the single magnon dispersion [19, 74].

In addition to spin flip processes, RIXS can also reach final states with a different orbital occupation of the 3d levels via similar scattering channels. These excitations are called dd excitations, and can be accompanied by a spin flip. In Sec. 4.5.1, the cross sections for dd excitations and single spin flip excitations in the cuprates are calculated in a single ion model.

Indirect RIXS is always present, but in general becomes dominant only when direct RIXS is absent. This happens at the K edges of copper and oxygen, because there is no spin-orbit coupling in the 1s levels ($L = 0$). When indirect RIXS is not dominant, one can sometimes use the polarization dependence to resolve the indirect RIXS channel.

In the following, we discuss the polarization dependence (Sec. 4.3.1) of both direct and indirect magnetic RIXS. In Sec. 4.3.2 the mechanisms are discussed by which magnetic excitations are created.

4.3.1 Polarization dependence

Since all of the work in this chapter is focused on the cuprates, we analyze here the full RIXS scattering amplitude (2.41) for the Cu K edge and Cu L and M edges. The O K edge is a special case and will be treated separately in Sec. 4.7.

We classify the RIXS processes by the indices μ, ν, ν' and μ' as in Eq. (2.42), *i.e.*, by the dipole transitions. At the Cu K edge, one excites an electron with spin up or down from the 1s orbital into a 4p orbital: $\mu = 1\text{s}$, $\nu = 4\text{p}_{x,y,z}$. We assume that the 4p electron is a spectator, *i.e.*, it does not interact with the valence electrons [4, 5]. In that case, $\nu' = \nu$, and $\mu' = \mu$. Since the spin of the photo-excited electron is irrelevant if the 4p electron is only a spectator, we can integrate it out without effort. The only remaining index is ν $(= \nu') \in \{4\text{p}_{x,y,z}\}$. Next, one has to determine the energy of the 4p states. Since these are assumed to be decoupled from the valence electrons, this is a relatively simple task. As explained in Sec. 3.4, band effects play a role, as well as the crystal field. The simplest polarization dependence arises when we assume that all 4p states have an equal energy: the scattering amplitude at the Cu K edge then simplifies to

$$\mathcal{F}_{fg} = T_K(\boldsymbol{\epsilon}', \boldsymbol{\epsilon}) \sum_i e^{i\mathbf{q}\cdot\mathbf{R}_i} \sum_n \frac{\langle f| c^\dagger_{i,1s} |n\rangle \langle n| c_{i,1s} |g\rangle}{E_g + \hbar\omega_{\mathbf{k}} - E_n + i\Gamma}, \tag{4.19}$$

where the 4p states are integrated out, and

$$T_K(\boldsymbol{\epsilon}', \boldsymbol{\epsilon}) = \sum_i \langle 1s| \boldsymbol{\epsilon}'^* \cdot \mathbf{r} |4p_i\rangle \langle 4p_i| \boldsymbol{\epsilon} \cdot \mathbf{r} |1s\rangle \propto \boldsymbol{\epsilon}'^* \cdot \boldsymbol{\epsilon}. \tag{4.20}$$

At the Cu $L_{2,3}$ edges of the cuprates, the indices μ and μ' relate to the core orbitals. Since in the intermediate state a $3d^{10}$ configuration is created, the core orbitals do not interact with the on-site valence electrons. If one neglects longer range interactions, the core states decouple from the valence states, and they can be integrated out from the scattering amplitude. To do so, we first find the core hole's eigenstates, which are determined mainly by the core level spin-orbit coupling. They split in two sets ($J = 1/2$ and $J = 3/2$, corresponding to L_2 and L_3, respectively) which are well-separated in energy: ~ 20 eV [84]. Since the separation is an order of magnitude larger than Γ, we neglect any contribution from one edge (L_2 or L_3) if the X-ray photons are tuned to the other. At the L_2 edge, we therefore sum over the $J = 1/2$ core states $\mu = \mu'$ with $m_J = \pm 1/2$:

$$|m_J = +1/2\rangle = \sqrt{\tfrac{1}{3}} \left(|p_z \uparrow\rangle + |p_x \downarrow\rangle + i\, |p_y \downarrow\rangle \right), \tag{4.21}$$

$$|m_J = -1/2\rangle = \sqrt{\tfrac{1}{3}} \left(|p_z \downarrow\rangle - |p_x \uparrow\rangle + i\, |p_y \uparrow\rangle \right) \tag{4.22}$$

At the L_3 edge, we sum over all $J = 3/2$ core states

$$|m_J = +3/2\rangle = -\sqrt{\tfrac{1}{2}} \left(|p_x \uparrow\rangle + i\, |p_y \uparrow\rangle \right), \tag{4.23}$$

$$|m_J = +1/2\rangle = \sqrt{\tfrac{2}{3}}\, |p_z \downarrow\rangle + \sqrt{\tfrac{1}{6}} \left(|p_x \downarrow\rangle + i\, |p_y \downarrow\rangle \right), \tag{4.24}$$

$$|m_J = -1/2\rangle = \sqrt{\tfrac{2}{3}}\, |p_z \downarrow\rangle + \sqrt{\tfrac{1}{6}} \left(|p_x \uparrow\rangle - i\, |p_y \uparrow\rangle \right), \tag{4.25}$$

$$|m_J = -3/2\rangle = \sqrt{\tfrac{1}{2}} \left(|p_x \downarrow\rangle - i\, |p_y \downarrow\rangle \right). \tag{4.26}$$

When the core hole degree of freedom is integrated out from the scattering amplitude, we find for the $L_{2/3}$ edge:

$$\mathcal{F}_{fg} = \sum_{\nu'} T_{L_{2/3},\nu'}(\boldsymbol{\epsilon}', \boldsymbol{\epsilon}) \sum_i e^{i\mathbf{q}\cdot\mathbf{R}_i} \sum_n \frac{\langle f| c_{i,\nu'} |n\rangle \langle n| c^\dagger_{i,\nu} |g\rangle}{E_g + \hbar\omega_{\mathbf{k}} - E_n + i\Gamma}, \tag{4.27}$$

where the spin-orbital ν is fixed by the initial state: $c_\nu^\dagger$ fills the 3d hole of the initial state. ν' labels the different scattering channels. For example, $\nu' = \nu$ is the elastic scattering channel, and when ν' describes an electron in the same orbital as ν, but with opposite spin, we have spin flip scattering. Also, dd excitations can be described when ν' refers to other 3d orbitals than x^2-y^2.

Note that the Cu L and M edges are very similar: only the radial wave functions of the core states differ, giving different overal intensities; the angular parts are the same. The main difference between the edges is the maximum $\mathbf{q}$, which is larger at the L edge.

4.3.2 Direct & indirect magnetic RIXS – UCL expansion

After splitting off the polarization dependence from the scattering amplitude, the next step in obtaining the (approximate) cross sections of magnetic RIXS on the antiferromagnetic cuprates is to deal with the intermediate states. The UCL expansion (see Sec. 2.5) offers a convenient way to do that, as the energy scale of the magnetic excitations is usually much lower than Γ. To zeroth order, the Kramers-Heisenberg amplitude (2.41) is reduced to the operation of two dipole operators; there is not enough time available to allow for dynamics in the intermediate state. This is equivalent to the fast collision approximation [26], which is a good approximation to the direct RIXS scattering amplitude of 2D cuprates [11, 19, 21, 74].

At the Cu K edge, the direct scattering channel does not give inelastic intensity, but at the Cu $\mathrm{L}_{2,3}$ and $\mathrm{M}_{2,3}$ edges, spin flip processes can occur to zeroth order in the UCL expansion, as explained in Sec. 4.3.1. We get for the zeroth order

$$\mathcal{F}_{fg}^{(0)} = \frac{T_{\mathrm{sf}}(\boldsymbol{\epsilon}', \boldsymbol{\epsilon})}{i\Gamma} \langle f| \sum_i e^{i\mathbf{q}\cdot\mathbf{R}_i} c_{i\bar{\sigma}} c_{i\sigma}^\dagger |g\rangle , \tag{4.28}$$

where T_{sf} is the polarization factor for spin flip processes, and σ is the spin of the 3d hole (assuming it is fully polarized). $\bar{\sigma}$ is the opposite spin of σ. This amplitude will be discussed in more detail in Sec. 4.5.1.

To get the leading order scattering amplitude for the Cu K edge, we proceed to the next order of the UCL expansion, which introduces intermediate state dynamics:

$$\mathcal{F}_{fg}^{(1)} = \frac{T_K(\boldsymbol{\epsilon}', \boldsymbol{\epsilon})}{i\Gamma} \langle f| \sum_i e^{i\mathbf{q}\cdot\mathbf{R}_i} c_{i,1s}^\dagger \frac{\bar{H}}{i\Gamma} c_{i,1s} |g\rangle . \tag{4.29}$$

The 4p electrons have been integrated out since they are assumed to be spectators. The Hamiltonian describes the dynamics around the core hole site, where the superexchange bonds are frustrated. This creates two-magnon excitations, as will be discussed in Sec. 4.4. Higher orders of the UCL expansion will add excitations with even numbers of magnons. Odd numbers of magnons are not allowed because the Heisenberg form of the magnetic bonds conserves the total spin. A single magnon carries spin 1.

A simple example is given by the Heisenberg ferromagnet. At the Cu $L_{2,3}$ edges, the spin flip channel allows for single magnon scattering. The inelastic weight at the Cu K edge is zero because $\bar{H}$ rearranges the spins of a ferromagnet, which cannot create two-magnon excitations.

It might not be obvious from Eq. (4.28) that RIXS can measure the dispersion of magnons: the spin is flipped on site i, while the magnon is a highly delocalized magnetic excitation. One should keep in mind, however, that the incident photon can be scattered at any equivalent site, leading to a final state that is a superposition of spin flips at equivalent sites. Such a final state carries a non-local magnetic excitation with momentum $\hbar\mathbf{q}$. Just as in neutron scattering, the RIXS cross section therefore consists of a local structure factor (2.42) depending on the polarization and the excitation mechanism, multiplied by the appropriate spin susceptibility [19, 74]. For non-interacting spins, the susceptibility is uniform and featureless, but for systems with interatomic spin-spin interactions the susceptibility acquires a strong $\mathbf{q}$ dependence, which may be measured in momentum-resolved RIXS.

4.4 Copper K edge

Published as '*Magnetic Excitations in La_2CuO_4 probed by Indirect Resonant Inelastic X-ray Scattering*' in Phys. Rev. B **77**, 134428 (2008) with Fiona Forte and Jeroen van den Brink.

Abstract. Recent experiments on La_2CuO_4 suggest that indirect resonant inelastic X-ray scattering (RIXS) might provide a probe for transversal spin dynamics. We present in detail a systematic expansion of the relevant magnetic RIXS cross section by using the ultrashort core hole lifetime (UCL) approximation. We compute the scattering intensity and its momentum dependence in leading order of the UCL expansion. The scattering is due to two-magnon processes and is calculated within a linear spin wave expansion of the Heisenberg spin model for this compound, including longer range and cyclic spin interactions. We observe that the latter terms in the Hamiltonian enhance the first moment of the spectrum if they strengthen the antiferromagnetic ordering. The theoretical spectra agree very well with experimental data, including the observation that scattering intensity vanishes for the transferred momenta $\mathbf{q} = (0, 0)$ and $\mathbf{q} = (\pi, \pi)$. We show that at finite temperature there is an additional single-magnon contribution to the scattering with a spectral weight proportional to T^3. We also compute the leading corrections to the UCL approximation and find them to be small, putting the UCL results on a solid basis. All this univocally points to the conclusion that the observed low temperature RIXS intensity in La_2CuO_4 is due to two-magnon scattering.

Introduction. In indirect RIXS, the energy of the incoming photons is tuned to match a resonance that corresponds to exciting a core electron to an outer shell. The K edge of transition metal ions is particularly useful since it promotes a 1s core electron to an outer 4p shell, which is well above the Fermi level, so that the X-rays do not cause direct transitions of the 1s electron into the lowest 3d-like conduction bands [2, 44, 46, 57, 85–95].

Due to the large energy involved ($\sim 5-10$ keV), the core hole is ultrashortlived and it induces an almost delta function-like potential (in time) on the valence electrons [48–50]. Consequently, elementary excitations of the valence electrons will screen the local potential, but have little time to do so. When the core hole decays, the system can be left behind in an excited state. By observing the energy and momentum of the outgoing photon, one probes the elementary excitations of the valence electrons including, in particular, their momentum dependence.

Recently, RIXS measurements performed by J.P. Hill *et al.* on the high-T_c cuprate superconductor $La_{2-x}Sr_xCuO_4$ revealed that RIXS is potentially able to detect *transversal* spin excitations – magnons [14]. Later, Ellis *et al.* confirmed these measurements in a follow-up experiment [53]. The experiments show that the magnetic RIXS signal is strongest in the undoped cuprate La_2CuO_4. The magnetic loss features are at energies well below the charge gap of this magnetic insulator, at energies where the charge response function $S(\mathbf{q}, \omega)$ vanishes (see chapter 3), as well as the *longitudinal* spin one – which is in fact a higher order charge response function. The proposed scattering mechanism is a two-magnon scattering process in which two spin waves are created [14, 51].

In a previous theoretical analysis it was shown that the magnetic correlation function that is measured by indirect RIXS is a four-spin correlation one, probing two-magnon excitations [51]. This makes indirect RIXS a technique that is essentially complementary to magnetic neutron scattering, which probes single magnon properties and two-spin correlations. In this section, we present the theoretical framework of Ref. [51] in more detail and use it for an analysis of the experimental magnetic RIXS data on perovskite CuO_2 layers of La_2CuO_4.

We expand upon the previous considerations by providing a detailed comparison between the theory and experiment, including also longer range magnetic exchange interactions in the theory, with values known from neutron scattering data. We develop the theory to account also for the effects of finite temperature, which give rise to a non-trivial single-magnon contribution to the RIXS signal. We also compare with the results of Nagao and Igarashi [96], who computed the magnetic RIXS spectra based on the theoretical framework of Ref. [51], taking also some of the magnon-magnon interactions into account.

The theory is developed on basis of the UCL expansion. We compute leading order corrections to this expansion and show that they are small. This makes sure that the UCL approximation provides a reliable route to analyze the indirect RIXS spectra.

This section is organized as follows: first we obtain an expression for the cross section of the 2D $S = 1/2$ Heisenberg antiferromagnet in linear spin wave theory in terms of magnon creation and annihilation operators. Then we evaluate the cross section at $T = 0$ and we also consider the low temperature case. Next, the leading correction to the cross section in the UCL approximation is calculated. Finally, we will present our conclusions.

Cross Section for Indirect RIXS on a Heisenberg AFM. Recently, Hill *et al.* [14] and Ellis *et al.* [53] observed that RIXS on the high-T_c superconductor $La_{2-x}Sr_xCuO_4$ picks up transversal spin dynamics: magnons. In the undoped regime, the RIXS intensity turns out to be highest. The same feature was observed in the related compound Nd_2CuO_4 [14]. These cuprates consist of perovskite CuO_2 layers with a hole in the Cu 3d subshell. The low energy spin dynamics of these systems are properly described by a single band Hubbard model at half filling. The strong interactions between holes in the Cu 3d subshells drive these materials into the Mott insulating regime, where the low energy excitations are the ones of the $S = 1/2$ 2D Heisenberg antiferromagnet (4.1) with $J \approx 146$ meV for nearest neighbors [83]. In the antiferromagnetic groundstate, the Hamiltonian can be bosonized in linear spin wave theory (LSWT) where $S_i^z \mapsto 1/2 - a_i^\dagger a_i$, $S_i^+ \mapsto a_i$ and $S_i^- \mapsto a_i^\dagger$ for $i \in A$ (A being the sublattice with spin-up) and $S_j^z \mapsto b_j^\dagger b_j - 1/2$, $S_j^+ \mapsto b_j^\dagger$ and $S_j^- \mapsto b_j$ for $j \in B$ (the spin-down sublattice). Note that we now introduce two boson species in a doubled unit cell, so the Brillouin zone will be twice as small as before in Sec. 4.2. A Bogoliubov transformation in reciprocal space is necessary to diagonalize the Heisenberg Hamiltonian:

$$\alpha_{\mathbf{k}} = U_{\mathbf{k}} a_{\mathbf{k}} + V_{\mathbf{k}} b^\dagger_{-\mathbf{k}}, \tag{4.30}$$

$$\beta_{\mathbf{k}} = U_{\mathbf{k}} b_{\mathbf{k}} + V_{\mathbf{k}} a^\dagger_{-\mathbf{k}} \tag{4.31}$$

with $U_{\mathbf{k}}$, $V_{\mathbf{k}}$ as in Eq. (4.18). For interactions up to third nearest neighbors we get

$$J_{\mathbf{k}} = J\left(\cos ak_x + \cos ak_y\right) \tag{4.32}$$

$$J'_{\mathbf{k}} = 2J' \cos ak_x \cos ak_y + J'' \left(\cos 2ak_x + \cos 2ak_y\right) \tag{4.33}$$

with a the lattice constant and J, J', J'' the first through third nearest neighbor couplings. The final linear spin wave Hamiltonian in terms of boson operators is

$$H_0 = \text{const} + \sum_{\mathbf{k}} \Omega_{\mathbf{k}} \left(\alpha^\dagger_{\mathbf{k}} \alpha_{\mathbf{k}} + \beta^\dagger_{\mathbf{k}} \beta_{\mathbf{k}} \right) \tag{4.34}$$

with $\Omega_{\mathbf{k}}$ as in Sec. 4.2.

Our aim is to understand how this picture changes when doing indirect RIXS. In RIXS, one uses X-rays to promote a Cu 1s electron to a 4p state. For an ultrashort time, one creates a core hole at a certain site which lowers the Coulomb repulsion U on that site with an amount U_c. As in chapter 3, we again assume that the core hole potential is local; *i.e.*, it acts only at the core hole site. This approximation is reasonable as the Coulomb potential is certainly largest on the atom where the core hole is located. Moreover, we can consider the potential generated by both the localized core hole and photo-excited electron at the same time. As this exciton is a neutral object, its monopole contribution to the potential vanishes for distances larger than the exciton radius. The multi-polar contributions that we are left with in this case are generally small and drop off quickly with distance.

The strong core hole potential in the intermediate state alters the superexchange processes between the 3d valence electrons. This causes RIXS to couple to multi-magnon excitations, as was first pointed out in Ref. [51]. The simplest microscopic mechanism for this coupling is obtained within the strong-coupling Hubbard model, in which the doubly occupied and empty virtual states shift in energy in presence of the core hole [51, 96]. Adding the amplitudes for the two possible processes shown in Fig. 4.3 leads to an exchange integral in presence of a core hole on site i of

$$J^c_{ij} = \frac{2t^2_{ij}}{U + U_c} + \frac{2t^2_{ij}}{U - U_c} = J_{ij}\,(1 + \eta) \tag{4.35}$$

where j is a site neighboring to i and $\eta = U_c^2/(U^2 - U_c^2)$. This enables us to write down the generic Hamiltonian for the intermediate states [51]:

$$H_{\text{int}} = H_0 + \eta \sum_{i,j} s_i s_i^\dagger J_{ij} \mathbf{S}_i \cdot \mathbf{S}_j \tag{4.36}$$

where s_i creates a core hole and $s_i^\dagger$ annihilates one at site i. In the Hubbard framework, one could identify U with the Coulomb energy associated with two holes in a 3d orbital, $U_d = 8.8$ eV, which together with $U_c = 7.0$ eV [97, 98] leads to $\eta = 1.7$; from $U/U_c = 2/3$, as suggested in Ref. [99], one finds $\eta = -0.8$.

The situation in the cuprates, however, is more complex and one needs to go beyond the single band Hubbard model to obtain a value of η from microscopic considerations. We will do so by considering a three-band model in the strong coupling limit. However, it should be emphasized that for the end result – the computed RIXS spectrum in the UCL approach – η just determines the overall scale of the inelastic scattering intensity. As we will show, higher order corrections in the UCL approach are determined by the value of η, because $\eta J/\Gamma$ appears as a small parameter in this expansion. As for the cuprates $J/\Gamma \approx 1/5$, such corrections are small for the relevant possible values of η.

In the three-band Hubbard model that includes also the oxygen states, two important kinds of intermediate states appear: the poorly- and well-screened ones. Because the Coulomb interaction of the core-hole with the valence electrons is large ($U_c = 7.0$ eV, compared to a charge transfer energy $\Delta = 3.0$ eV [98]), a copper hole can transfer to a neighboring oxygen to form a well-screened intermediate state. The low-energy sector now also encompasses an oxygen hole,

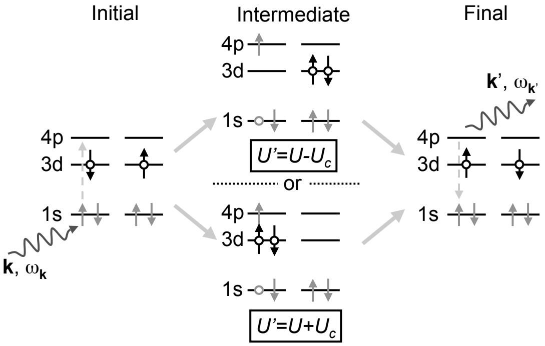
Initial
Intermediate
Final
4p
3d
1s
k, ωk
4p
3d
1s
U'=U-Uc
or
4p
3d
1s
U'=U+Uc
k', ωk'
4p
3d
1s

Figure 4.3: In RIXS, a photon tuned to the K edge of a transition metal ion creates a core hole at a certain site. The superexchange interaction between this site and a neighboring site is modified because the energy of the virtual intermediate states is changed. The same-site Coulomb repulsion U is lowered by U_c if the core hole site contains no holes and is raised by U_c if there are two holes present. Summing the amplitudes for both processes, we obtain the modified superexchange interaction [see Eq. (4.35)].

equally distributed over the ligands. We will show that, starting from a three band Hubbard model, Eq. (4.36) gives a proper description of both the well- and poorly-screened intermediate states, with η now a function of the parameters of the three band model. Before presenting these results we remark that scattering processes that scatter a well-screened state into a poorly-screened state or vice versa yield a large energy loss $\hbar\omega$. These are not important at low ω, where one will only observe scattering in the magnetic channel, not the charge one.

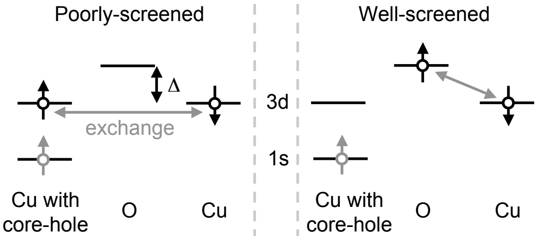
Poorly-screened
Well-screened
Δ
exchange
3d
1s
Cu with core-hole
O
Cu
Cu with core-hole
O
Cu

Figure 4.4: Modification of the superexchange interaction in the well- and poorly-screened intermediate states. In the poorly-screened state, the core hole potential U_c modifies the superexchange. For the well-screened state, however, the copper 3d hole on the core hole site is transfered to a neighboring oxygen ion, and superexchange is only of order $\mathcal{O}(t_{pd}^2)$, independent of U_c.

The magnetic scattering processes for the poorly-screened state are very similar to the single band picture: all copper ions have one hole and all oxygen ions are filled-shell. The superexchange processes are shown in Fig. (4.4). We consider the Anderson and Geertsma contributions to the superexchange [97] and find

$$\begin{aligned}\eta_{ps} =&\frac{U_d\Delta^2(U_p+2\Delta)}{2(2U_d+2\Delta+U_p)}\left(\frac{1}{(U_d-U_c)(U_c-\Delta)^2}+\frac{1}{(U_d+U_c)\Delta^2}\right.\\&\left.+\frac{[1/\Delta+1/(\Delta-U_c)]^2}{2\Delta-U_c+U_p}\right)-1,\end{aligned}\tag{4.37}$$

which results in $\eta=-0.3$ using the parameters $U_d=8.8$ eV, $U_p=6.0$ eV, $t_{pd}=1.3$ eV, $\Delta=3.0$ eV, and $U_c=7.0$ eV [97, 98], where t_{pd} is the copper-oxygen hoping integral and U_p the on-site Coulomb repulsion of two oxygen holes.

The well-screened intermediate states have a similarly modified superexchange interaction, as shown in Fig. 4.4. Because of the large core hole Coulomb interaction, an electron from the neighboring oxygen atoms moves in to screen it, or, equivalently, the copper hole is transferred to the in-plane oxygen ions. Transfer out of the plane is not considered since the Cu 3d$_{x^2-y^2}$ hole only couples to the in-plane oxygens. Because the Cu hole is transfered in the direction of one of its neighboring Cu ions, the contribution to the superexchange interaction for the well-screened state is of second order in t_{pd}, instead of fourth order between two Cu sites (see Fig. 4.4). The rotational invariance around the core-hole site of the transfered hole ensures that the intermediate state Hamiltonian of the form Eq. (4.36) gives the correct scattering amplitude. To lowest order in t_{pd} we hence find

$$\eta_{ws}=\frac{U_d(U_d+U_p)\Delta^2(U_p+2\Delta)}{2(U_d-\Delta)t_{pd}^2(2U_d+U_p+2\Delta)(U_p+\Delta)}-4,\tag{4.38}$$

which results in $\eta=-1.3$ – again restricting ourselves to superexchange of the Anderson and Geertsma type. We see that to lowest order, the core hole potential U_c does not appear in the well-screened intermediate state. From these microscopic considerations, we conclude that the intermediate state Hamiltonian Eq. (4.36) is the correct one and higher order corrections to it are small because for the cuprates η is a number of order unity.

In chapter 3, we have shown in detail how to derive the cross section for RIXS processes with a local core hole using the UCL expansion Eq. (2.49). As in chapter 3, we take the energy E_i of the initial state as a reference energy: $E_i=0$. We also measure the energy E_n of the intermediate state with respect to the resonance energy $\hbar\omega_{\text{res}}$ as before. The detuning of the incoming photon energy from $\hbar\omega_{\text{res}}$ is defined as $\hbar\omega_{\text{in}}=\hbar\omega_{\mathbf{k}}-\hbar\omega_{\text{res}}$. If $\Gamma>E_n$, we can expand the amplitude $\mathcal{F}_{fi}$ in a powerseries (2.49). We assume that the energy of the incoming photon is tuned to the resonance ($\omega_{\text{in}}=0$):

$$\mathcal{F}_{fi}=\frac{1}{i\Gamma}\sum_{l=1}^{\infty}\frac{1}{(i\Gamma)^l}\left\langle f\right|\mathcal{D}^\dagger(H_{\text{int}})^l\mathcal{D}\left|i\right\rangle.\tag{4.39}$$

Note that we left out the $l = 0$ term because it only contributes to elastic scattering. The leading order non-vanishing term in the sum is $l = 1$, since the core hole broadening is quite large compared to J. At the copper K edge, $2\Gamma \approx 1.5$ eV according to Refs. [100, 101], and $2\Gamma \approx 3$ eV for the closely related ions Mn and Ge according to Refs. [102, 103], which in either case is large compared to J. As in the three-band model $\eta = -1.3$ or -0.3 for the well- or poorly-screened intermediate state respectively, the largest value we find is $\eta J/\Gamma \approx -0.22$. Note that the UCL expansion therefore converges very well – even faster for the poorly-screened state than for the well-screened state (where $|\eta|$ is larger). It is possible to directly include a number of terms with $l \geq 2$ in the cross section by using the expansion

$$\sum_{l=1}^{\infty} \frac{(H_{\text{int}})^l}{(i\Gamma)^l} \approx \sum_{l=1}^{\infty} \left(\frac{H_0^l}{(i\Gamma)^l} + \frac{H_0^{l-1} H'}{(i\Gamma)^l} \right) + \mathcal{O}\left([\eta J/\Gamma]^2 \right) \tag{4.40}$$

with $H' = \eta \sum_{i,j} s_i s_i^\dagger J_{ij} \mathbf{S}_i \cdot \mathbf{S}_j$. Since $[H_0, \mathcal{D}] = 0$ and $H_0 |i\rangle \equiv 0$, all terms with H_0 on the right can be safely neglected. Using Eq. (4.40), $\mathcal{F}_{fi}$ simplifies to

$$\mathcal{F}_{fi} = \frac{1}{i\Gamma} \frac{\eta}{i\Gamma - \hbar\omega} \langle f | \hat{O}_{\mathbf{q}} | i \rangle \tag{4.41}$$

with the scattering operator

$$\hat{O}_{\mathbf{q}} = \sum_{i,j} e^{i\mathbf{q}\cdot\mathbf{R}_i} J_{ij} \mathbf{S}_i \cdot \mathbf{S}_j, \tag{4.42}$$

where we neglected the polarization dependence in the same way as in Eq. (3.7). The polarization dependence is discussed in more detail in Sec. 3.4.

From Eq. 4.42, we can deduce two important features. First, indirect RIXS probes a momentum dependent four-spin correlation function [51]. Second, $\hat{O}_{\mathbf{q}}$ commutes with the z component of total spin S^z, so the allowed scattering processes should leave S^z unchanged. Only an even number of magnons can be created or annihilated.

To bosonize Eq. (4.42), we split $\hat{O}_{\mathbf{q}}$ in four parts,

$$\hat{O}_{\mathbf{q}} = \sum_{i,j \in A} \cdots + \sum_{i,j \in B} \cdots + \sum_{i \in A,\, j \in B} \cdots + \sum_{i \in B,\, j \in A} \cdots \tag{4.43}$$

Next, we rewrite this expression using LSWT as introduced above. Fourier transforming the result gives

$$\begin{aligned} \hat{O}_{\mathbf{q}} = \text{const.} + S \sum_{\mathbf{k}} \Big[& \left(J'_{\mathbf{k}+\mathbf{q}/2} + J'_{\mathbf{k}-\mathbf{q}/2} - J'_{\mathbf{0}} - J'_{\mathbf{q}} + J_{\mathbf{0}} + J_{\mathbf{q}} \right) \times \\ & \left(a^\dagger_{\mathbf{k}+\mathbf{q}/2} a_{\mathbf{k}-\mathbf{q}/2} + b^\dagger_{\mathbf{k}+\mathbf{q}/2} b_{\mathbf{k}-\mathbf{q}/2} \right) + \\ & \left(J_{\mathbf{k}+\mathbf{q}/2} + J_{\mathbf{k}-\mathbf{q}/2} \right) \left(a_{\mathbf{k}-\mathbf{q}/2} b_{-\mathbf{k}-\mathbf{q}/2} + a^\dagger_{\mathbf{k}+\mathbf{q}/2} b^\dagger_{-\mathbf{k}+\mathbf{q}/2} \right) \Big], \end{aligned} \tag{4.44}$$

and we can write $\hat{O}_{\mathbf{q}}$ in terms of the magnon operators using the inverses of Eqs. (4.30) and (4.31). This leads to

$$\hat{O}_{\mathbf{q}} = \hat{O}^{(1)}_{\mathbf{q}} + \hat{O}^{(2)}_{\mathbf{q}} \tag{4.45}$$

where $\hat{O}^{(1,2)}_{\mathbf{q}}$ are lengthy expressions that contain the one- and two-magnon scattering part respectively. The next section deals with the two-magnon part $\hat{O}^{(2)}_{\mathbf{q}}$ where two magnons are created or annihilated. The one-magnon part $\hat{O}^{(1)}_{\mathbf{q}}$ (where the change in the number of magnons is zero) is treated in Sec. 4.4.

Two-Magnon Scattering at $T = 0$ K. At $T = 0$ K, the system is in its ground state, where no magnons are present: $|i\rangle = |0\rangle$. Adding conservation of S^z, the only allowed scattering processes are the ones in which two magnons are created, so we consider the two-magnon part of the scattering operator of Eq. (4.45) with $S = 1/2$:

$$\begin{aligned}\hat{O}^{(2)}_{\mathbf{q}} = \sum_{\mathbf{k}\in\mathrm{MBZ}} \Big[-\Big(J'_{\mathbf{k}+\mathbf{q}/2} + J'_{\mathbf{k}-\mathbf{q}/2} - J'_{\mathbf{0}} - J'_{\mathbf{q}} + J_{\mathbf{0}} + J_{\mathbf{q}}\Big) \times \\ \Big(U_{\mathbf{k}+\mathbf{q}/2}V_{\mathbf{k}-\mathbf{q}/2} + U_{\mathbf{k}-\mathbf{q}/2}V_{\mathbf{k}+\mathbf{q}/2}\Big) \\ + \Big(J_{\mathbf{k}+\mathbf{q}/2} + J_{\mathbf{k}-\mathbf{q}/2}\Big)\Big(U_{\mathbf{k}+\mathbf{q}/2}U_{\mathbf{k}-\mathbf{q}/2} + V_{\mathbf{k}+\mathbf{q}/2}V_{\mathbf{k}-\mathbf{q}/2}\Big)\Big] \times \\ \Big(\alpha_{\mathbf{k}-\mathbf{q}/2}\beta_{-\mathbf{k}-\mathbf{q}/2} + \alpha^{\dagger}_{\mathbf{k}+\mathbf{q}/2}\beta^{\dagger}_{-\mathbf{k}+\mathbf{q}/2}\Big)\end{aligned} \tag{4.46}$$

The two-magnon spectrum is shown in Fig. 4.5(a). Several remarkable features can be seen.

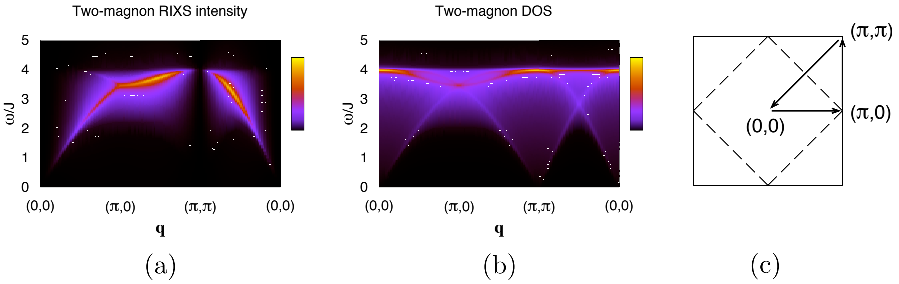

(a) (b) (c)

Figure 4.5: RIXS spectrum (a) and two-magnon DOS (b) for a nearest neighbor Heisenberg antiferromagnet with exchange interaction J as a function of transferred momentum $\mathbf{q}$ for a cut through the Brillouin zone (c). The dashed line indicates the magnetic BZ boundary.

First of all the spectral weight vanishes at $\mathbf{q} = (0,0)$ and $\mathbf{q} = (\pi,\pi)$, as can be seen in Fig. 4.6(b). This is in agreement with experimental observations [14].

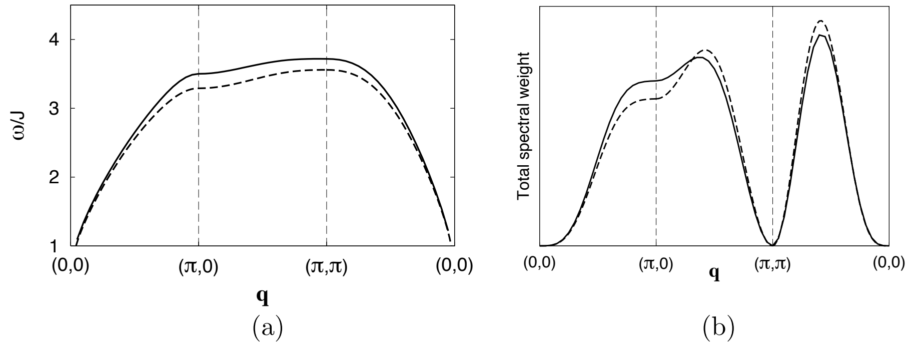

Figure 4.6: (a) First moment and (b) total spectral weight of the RIXS spectrum. The solid lines are obtained by using interaction strengths determined from neutron data (next neighbor coupling $J = 146.3$ meV, second and third neighbor couplings $J' = J'' = 2$ meV and ring exchange $J_\square = 61$ meV) [83]. The dashed lines have only nearest neighbor interaction.

The vanishing of the RIXS intensity at $\mathbf{q} = \mathbf{0}$ is obvious: from Eq. (4.42) we see that at $\mathbf{q} = \mathbf{0}$, $\hat{O}_\mathbf{q}$ reduces to $2H_0$ (the factor of 2 arises from the fact that the sum in Eq. (4.42) is over all i and j). At zero temperature, $|i\rangle = |0\rangle$ and consequently $H_0 |i\rangle = 0$ –the RIXS intensity vanishes. At nonzero temperatures, $H_0 |i\rangle = E_i |i\rangle$ and according to Eq. (4.41) only elastic scattering occurs. It is easy to show that at $\mathbf{q} = (\pi, \pi)$ the RIXS intensity always vanishes, regardless of the temperature or the form of J_{ij}. This holds because $\mathbf{q} = (\pi, \pi)$ is a reciprocal magnetic lattice vector: $e^{i\mathbf{q}\cdot\mathbf{R}_i} = 1$ if $\mathbf{R}_i$ is in sublattice A and $e^{i\mathbf{q}\cdot\mathbf{R}_i} = -1$ if $\mathbf{R}_i$ is in sublattice B (assuming that at $\mathbf{R}_i = (0, 0)$ we are in sublattice A). We obtain

$$\hat{O}_{\mathbf{q}=(\pi,\pi)} = \sum_{i\in A,j} J_{ij}\mathbf{S}_i\cdot\mathbf{S}_j - \sum_{i\in B,j} J_{ij}\mathbf{S}_i\cdot\mathbf{S}_j. \tag{4.47}$$

Adding all terms where $j \in B$ in the first term and $j \in A$ in the latter, we get zero. What remains is

$$\hat{O}_{\mathbf{q}=(\pi,\pi)} = \sum_{i,j\in A} J_{ij}\mathbf{S}_i\cdot\mathbf{S}_j - \sum_{i,j\in B} J_{ij}\mathbf{S}_i\cdot\mathbf{S}_j. \tag{4.48}$$

This operator commute with the Hamiltonian and therefore does not contribute to inelastic scattering.

The other remarkable feature of the magnetic RIXS spectrum is its strong dispersion. This is apparent from Fig. 4.5(a) and 4.6(a), showing the first moment (average peak position) of the spectrum. The calculations for the nearest neighbor Heisenberg antiferromagnet [see the dashed line in Fig. 4.6(a)] show that the magnetic scattering disperses from about $\omega \approx 0$ around $(0, 0)$ to $\omega \approx 4J$ at $(\pi, 0)$ and $(\pi/2, \pi/2)$. Longer range couplings tend to reduce (increase) the first moment of the RIXS spectrum if they weaken (reinforce) the antiferromagnetic order [see the solid line in Fig. 4.6(a)]. The observed dispersion in Fig. 4.5(a) has a twofold origin. It is in part due to the **q**-dependence of the two-magnon density of states (DOS), combined with the scattering matrix elements that tend to pronounce the low energy tails of the two-magnon DOS. In Fig. 4.5(b), it looks as if the two-magnon DOS has two branches. The most energetic one around $\mathbf{q} = \mathbf{0}$ is strongly suppressed by the matrix elements throughout the Brillouin zone (BZ).

The consistency at $\mathbf{q} = (0, 0)$ and $\mathbf{q} = (\pi, \pi)$ of the theoretical results and experimental data was already noticed, but at other wave vectors, the agreement stands out even more. The data on $\mathrm{La_2CuO_4}$ for $\mathbf{q} = (\pi, 0)$ shows a peak at around 500 meV, precisely where we find it on the basis of a nearest neighbor Heisenberg model with $J = 146$ meV – a value found by the analysis of neutron scattering data [83]. Similar agreement is found at $\mathbf{q} = (0.6\pi, 0)$ and $\mathbf{q} = (0.6\pi, 0.6\pi)$ [14]. Even better agreement is found when we take into account the second and third nearest neighbors and ring exchange according to the neutron data. The ring exchange interaction, which we treat on a mean field level, simply renormalizes first- and second-nearest neighbors exchange [83].

In Fig. 4.7, we compare the results for the two-magnon scattering intensity with experimental data [14], using the interaction strengths determined from neutron data [83], for three values of **q** in the BZ. Note that we use the wave vector independent renormalization factor Z_c here, which takes into account some of the magnon-magnon interactions [104]. This simply changes the energy scale by a factor $Z_c \approx 1.18$ but does not affect the intensity of the spectrum. Each panel shows the theoretical prediction (dashed line), the theory convoluted with the current instrumental resolution (solid line), and the experimental data. The only free parameter in the theoretical spectra is the overall scale of the scattering intensity. We find it to vary by a factor of 2.5 comparing different **q**'s, which is within the error bars of the experiment [105].

Many qualitative features such as the occurrence of intense peaks at the magnetic BZ boundary and the large dispersion characterizing the total spectrum are in accordance with our earlier results [51] and the results of Nagao and Igarashi [96]. The spectra of Ref. [96], taking two-magnon interactions partially into account, show slight quantitative differences with respect to our results: the RIXS peaks soften and broaden somewhat as a consequence of the magnon-magnon interaction, particularly for the (π,0) point. The range of the dispersion in the spectrum is therefore smaller (the mean ω/J varies between 1 and 3 instead of 1 and 4).

Finite T: single-magnon scattering. The S^z_{tot} symmetry allows scattering processes where no additional magnons are created. In the finite temperature case, an initial magnon of momentum $\mathbf{k}$ can be scattered to $\mathbf{k} + \mathbf{q}$. The one-

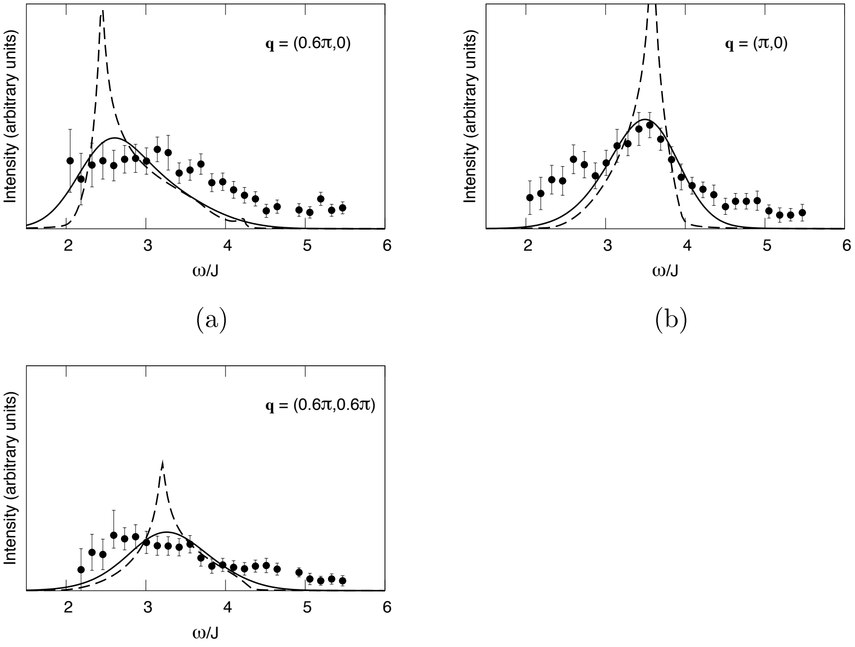

(a) (b)

(c)

Figure 4.7: RIXS intensity for various points in the BZ. Each figure contains the bare theoretical data (dashed line), the convolution with experimental resolution (solid line), and the experimental data from Ref. [14]. For these figures, we used $J = 146.3$ meV, second and third neighbor couplings $J' = J'' = 2$ meV and ring exchange $J_\square = 61$ meV. The latter contribution is evaluated theoretically using a mean field approximation. These values were found in neutron scattering experiments [83]. These experiments were analyzed using the wave vector independent renormalization factor $Z_c = 1.18$, which is also used to generate the theoretical curves. The theoretical intensity is scaled independently in each figure to match the experiment. The overall scale factors differ at most by a factor 2.5, which is comparable to experimental uncertainty in absolute intensities [105].

magnon part of the scattering operator, within LSWT, takes the following form:

$$\begin{aligned}\hat{O}^{(1)}_{\mathbf{q}} = S \sum_{\mathbf{k}\in\mathrm{MBZ}} \Big[& \left(J_{\mathbf{0}} + J_{\mathbf{q}} - J'_{\mathbf{0}} - J'_{\mathbf{q}} + J'_{\mathbf{k}} + J'_{\mathbf{k+q}}\right)\left(U_{\mathbf{k}}U_{\mathbf{k+q}} + V_{\mathbf{k}}V_{\mathbf{k+q}}\right) \\ & - \left(J_{\mathbf{k}} + J_{\mathbf{k+q}}\right)\left(U_{\mathbf{k}}V_{\mathbf{k+q}} + V_{\mathbf{k}}U_{\mathbf{k+q}}\right)\Big]\left(\alpha^\dagger_{\mathbf{k+q}}\alpha_{\mathbf{k}} + \beta^\dagger_{\mathbf{k+q}}\beta_{\mathbf{k}}\right). \end{aligned} \tag{4.49}$$

We choose to concentrate on the basic case where the only non-vanishing interaction is the nearest-neighbors coupling J, for a 2D Heisenberg antiferromagnet with $S = 1/2$.

In the low temperature regime, a few magnons of low momentum $\mathbf{k}$ are present in the system. Their energy can be approximated for $T \to 0$ by letting $\mathbf{k} \to 0$: $\Omega_{\mathbf{k}} \approx \sqrt{2}J|\mathbf{k}|$. In this limit $U_{\mathbf{k}}$ and $V_{\mathbf{k}}$ can be substituted by the following approximate expressions:

$$\begin{aligned} U_{\mathbf{k}} &\approx \tfrac{1}{\sqrt{\sqrt{2}|\mathbf{k}|}}(1 + \tfrac{\sqrt{2}}{4}|\mathbf{k}|), \\ V_{\mathbf{k}} &\approx \tfrac{1}{\sqrt{\sqrt{2}|\mathbf{k}|}}(1 - \tfrac{\sqrt{2}}{4}|\mathbf{k}|). \end{aligned} \tag{4.50}$$

In order to calculate the one-magnon contribution to the cross section, we have to evaluate the scattering amplitude expressed by Eq. (4.41). In the low temperature case we can consider a one-magnon initial state $|i\rangle = \alpha^{\dagger}_{\mathbf{k}}|0\rangle$[1]. The only contribution to $\mathcal{F}^{(1)}_{fi}$ comes from the final state with a single magnon of momentum $\mathbf{k} + \mathbf{q}$

$$\begin{aligned} \mathcal{F}^{(1)}_{fi} &= S\left[(J_{\mathbf{0}} + J_{\mathbf{q}})(U_{\mathbf{k}}U_{\mathbf{k+q}} + V_{\mathbf{k}}V_{\mathbf{k+q}}) - (J_{\mathbf{k}} + J_{\mathbf{k+q}})(U_{\mathbf{k}}V_{\mathbf{k+q}} + V_{\mathbf{k}}U_{\mathbf{k+q}})\right] \\ &\approx \frac{S}{\sqrt{2\sqrt{2}}}\,(J_{\mathbf{0}} + J_{\mathbf{q}})\,(U_{\mathbf{q}} - V_{\mathbf{q}})\sqrt{|\mathbf{k}|} \end{aligned} \tag{4.51}$$

where we used the condition $|\mathbf{k}| \ll |\mathbf{q}|$ and inserted the expressions of Eqs. (4.50) for $U_{\mathbf{k}}$ and $V_{\mathbf{k}}$, retaining the leading order term in $|\mathbf{k}|$.

These approximations allow the analytic evaluation of the scattering intensity. At finite T, the cross section is given by

$$\left.\frac{d^2\sigma^{(1)}}{d\Omega d\omega}\right|_{\text{res}} \propto \sum_{i,f} \frac{1}{e^{\beta E_i} - 1}\left|\mathcal{F}^{(1)}_{fi}\right|^2 \delta(\hbar\omega - E_f + E_i). \tag{4.52}$$

For $\mathbf{k} \approx 0$, and by taking the continuum limit, we obtain

$$\frac{d^2\sigma^{(1)}}{d\Omega d\omega} \propto P(\mathbf{q}) \int_{\text{MBZ}} dk_x dk_y \frac{|\mathbf{k}|}{e^{\beta\Omega_{\mathbf{k}}} - 1}\delta(\hbar\omega - \Omega_{\mathbf{k+q}} + \Omega_{\mathbf{k}}), \tag{4.53}$$

where we defined $P(\mathbf{q}) = S^2\,(J_{\mathbf{0}} + J_{\mathbf{q}})^2\,(U_{\mathbf{q}} - V_{\mathbf{q}})^2$. In the low temperature limit, the Bose factor goes to zero rapidly for high $|\mathbf{k}|$, so the only substantial contribution to the integral comes from $|\mathbf{k}| \approx 0$. Therefore we can extend the domain of integration to the entire k space. Replacing $\Omega_{\mathbf{k}}$ with its approximate expression in the limit of low $|\mathbf{k}|$, and assuming polar coordinates, we obtain

$$\frac{d^2\sigma^{(1)}}{d\Omega d\omega} \propto P(\mathbf{q}) \int_0^{\infty} dk \frac{k^2}{e^{\beta\sqrt{2}Jk} - 1}\delta(\hbar\omega - \Omega_{\mathbf{q}} + \sqrt{2}Jk) \tag{4.54}$$

---

[1] At finite temperature, more than one magnon can exist. This modifies the action of the $\hat{O}^{(1)}_{\mathbf{q}}$ operator in addition to the Bose factor. It is easy to show that, in the low temperature limit, the main contribution to this factor arises from $n_{\mathbf{k}} = 1$, since other terms rapidly go to zero for $\beta \to \infty$.

Note that we used the replacement $\Omega_{\mathbf{k}+\mathbf{q}} \to \Omega_{\mathbf{q}}$, which breaks down at $\mathbf{q} = \mathbf{0}$ and the BZ corners. This integral can simply evaluated to be

$$\frac{d^2\sigma^{(1)}}{d\Omega d\omega} \propto P(\mathbf{q}) \frac{\left(\hbar\omega - \Omega_{\mathbf{q}}\right)^2}{e^{-\beta(\hbar\omega - \Omega_{\mathbf{q}})} - 1} \theta\left(\Omega_{\mathbf{q}} - \hbar\omega\right), \tag{4.55}$$

and the spectral weight for $T/J \ll 1$ is

$$W_1 = \int \frac{d^2\sigma^{(1)}}{d\Omega d\omega} d\omega \propto P(\mathbf{q}) \frac{1}{(\beta J)^3}. \tag{4.56}$$

The T^3 behavior also shows up in the numerical evaluation of W_1 (without assuming $|\mathbf{k}| \ll |\mathbf{q}|$), as shown in Fig. 4.8 as a function of the transferred momentum $\mathbf{q}$, for various temperatures (dashed lines). According to the considerations discussed in the previous section, the RIXS intensity is vanishing for (π, π). The average peak position and the peak width are expected to be modified as a function of temperature. We can easily estimate these modifications by evaluating the first moment

$$\langle \hbar\omega_{\max} \rangle \approx \Omega_{\mathbf{q}} - \frac{\pi^4}{30\zeta(3)} T, \tag{4.57}$$

and the variance

$$\langle \hbar\omega_{\max} \rangle^2 - \langle \hbar\omega_{\max} \rangle^2 \propto T^2. \tag{4.58}$$

We conclude that the peak position is shifted from $\Omega_{\mathbf{q}}$ towards lower values of $\hbar\omega$, by an amount that grows linearly with T and at the same time the peak broadens proportional to T.

We now determine the relative intensity of the one- and two-magnon scattering processes. Even if a direct comparison is not possible, since the one-magnon and the two-magnon peaks occur at different lost energies $\hbar\omega$, it is useful to compare the one-magnon and the two-magnon total spectral weight for the 2D Heisenberg antiferromagnet. The latter is evaluated numerically at $T = 0$, and the former at various temperatures without making the approximation $\mathbf{k}+\mathbf{q} \approx \mathbf{q}$. In Fig. 4.8 we plot the two-magnon (solid line) and the one-magnon weight for different temperatures (dashed lines). At room temperature, the one-magnon weight is one or two orders of magnitude smaller for almost every value of $\mathbf{q}$ and is expected to decrease with decreasing T, according to Eq. (4.56). This allows us to conclude that the two-magnon scattering is the dominant process at low temperatures. A rough estimate for the temperature at which the one-magnon process becomes significant gives a value of $\sim$ 1 eV in the case of $\mathrm{La_2CuO_4}$, which is well above room temperature. These results support the conclusion that two-magnon scattering dominates the magnetic RIXS intensities in this material observed by Hill *et al.* [14] and Ellis *et al.* [53]. In other materials this of course needs not necessarily be so, depending on the temperature at which the experiments are performed. One can expect for instance interesting RIXS scattering signals from high temperature paramagnons.

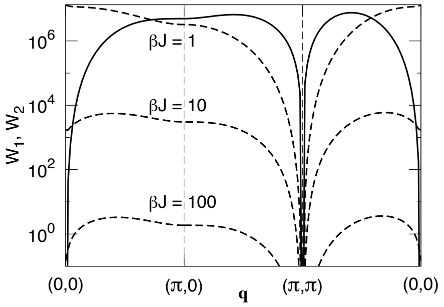

Figure 4.8: Comparison between spectral weight for single-magnon scattering W_1 (dashed lines) for various temperatures and zero temperature two-magnon scattering W_2 (solid line), all obtained numerically. The vertical scale has arbitrary units. W_1 displays the T^3 behavior from Eq. (4.56) for the single-magnon intensity. For La$_2$CuO$_4$, $J \approx$ 146 meV, and at room temperature we have $\beta_{\rm rt} J \approx 5.8$.

Leading correction to ultrashort lifetime approximation. The UCL expansion offers a systematic way of calculating the Kramers-Heisenberg equation. In this section we calculate the leading correction term to the two-magnon cross section in the UCL approximation. This is especially relevant at $\mathbf{q} = (0, 0)$ where the intensity is vanishing to first order, but non-zero to second order. The leading order correction is taken into account by including all terms up to $\mathcal{O}((\eta J/\Gamma)^2)$ in Eq. (4.40). Again we can include a number of extra correction terms by using an expansion of the type

$$\sum_{l=1}^{\infty} \frac{H_{\rm int}^l}{(i\Gamma)^l} \approx \sum_{l=1}^{\infty} \left(\frac{H_0^l}{(i\Gamma)^l} + \frac{H_0^{l-1}H'}{(i\Gamma)^l} \right) + \sum_{l=2}^{\infty} \frac{H_0^{l-2}(H')^2}{(i\Gamma)^l} + \mathcal{O}\left((\eta J/\Gamma)^3\right). \quad (4.59)$$

The contribution of the last term to the UCL scattering amplitude is

$$\frac{1}{\Gamma^2} \frac{\eta^2}{\hbar\omega - i\Gamma} \langle f | \sum_i e^{i\mathbf{q}\cdot\mathbf{R}_i} \sum_{j,k} J_{ij} J_{ik} (\mathbf{S}_i \cdot \mathbf{S}_j)(\mathbf{S}_i \cdot \mathbf{S}_k) | i \rangle \quad (4.60)$$

This scattering amplitude that corresponds to this term is non-zero at $\mathbf{q} = \mathbf{0}$, which can be easily checked in linear spin wave theory. The reason is that the resulting scattering operator at zero transferred momentum does not commute with the Hamiltonian. For the LSW analysis, we make use of the identity

$$\sum_{j,k} J_{ij} J_{ik} (\mathbf{S}_i \cdot \mathbf{S}_j)(\mathbf{S}_i \cdot \mathbf{S}_k) = \frac{1}{4} \sum_{j \neq k} J_{ij} J_{ik} \mathbf{S}_j \cdot \mathbf{S}_k - \frac{1}{2} \sum_j J_{ij}^2 \mathbf{S}_i \cdot \mathbf{S}_j + \text{const.} \quad (4.61)$$

We drop the constant because it does not contribute to inelastic scattering. For simplicity, we only take nearest neighbor interactions into account. The last term in Eq. (4.61) is proportional to the first order result for the scattering amplitude, which has already been analyzed in LSWT. The other term can be treated in LSWT too and yields a two-magnon contribution to the scattering amplitude at zero temperature of:

$$-\frac{1}{4\Gamma^2} \frac{(\eta J)^2}{\hbar\omega - i\Gamma} \sum_{\mathbf{k}} \langle f | f(\mathbf{k}, \mathbf{q}) (U_{\mathbf{k}} V_{\mathbf{k}-\mathbf{q}} + U_{\mathbf{k}-\mathbf{q}} V_{\mathbf{k}}) \alpha_{\mathbf{k}}^\dagger \beta_{-\mathbf{k}+\mathbf{q}}^\dagger | 0 \rangle \quad (4.62)$$

with $f(\mathbf{k},\mathbf{q}) = -6(\cos q_x + \cos q_y) + 4\cos k_x \cos(k_y - q_y) + 4\cos k_y \cos(k_x - q_x) + 2\cos(2k_x - q_x) + 2\cos(2k_y - q_y)$. Since the phase of the first order amplitude differs from the second order amplitude by $\pi/2$, there is no interference of these terms. The consequence is that the leading corrections to the first order scattering intensity are down by a factor $(\eta J/\Gamma)^2 \approx 0.06$ for the well-screened intermediate state. This makes the UCL expansion a viable way of computing magnetic RIXS spectra. The contribution Eq. (4.60) is shown in Fig. 4.9(a), and the full cross section in Fig. 4.9(b). Only at $\mathbf{q} = \mathbf{0}$, there is an appreciable difference from the first order result shown in Fig. 4.5 (a). At $\mathbf{q} = (\pi, \pi)$, there is again no intensity, which can be understood by the same argument as for the first order result in Sec. 4.4.

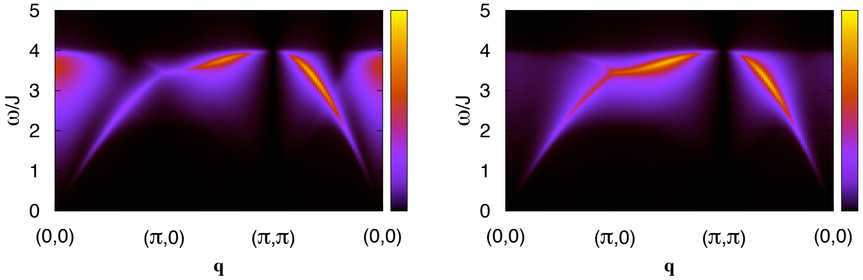

(a) (b)

Figure 4.9: The leading order correction to the scattering amplitude does not interfere with the first order. Fig. (a) shows the contribution to the cross section from Eq. (4.60). The full, corrected cross section is shown in Fig. (b). There is an appreciable correction only at $\mathbf{q} = \mathbf{0}$.

Comparison to two-magnon Raman scattering. In Raman scattering, one can select the symmetry of the two-magnon mode by selecting a certain polarization configuration. The Loudon-Fleury Raman scattering operator is [106–108]

$$\hat{O}_{\mathrm{LF}} \propto \sum_{i,\delta} P(\delta) \mathbf{S}_i \cdot \mathbf{S}_{i+\delta}. \tag{4.63}$$

The polarization configuration determines the symmetry of the scattering operator through $P(\delta) = (\boldsymbol{\delta} \cdot \boldsymbol{\epsilon}')(\boldsymbol{\delta} \cdot \boldsymbol{\epsilon})$. In two-magnon RIXS at the Cu K edge, in contrast, the polarization dependence can be disentangled from the scattering operator, and the polarization cannot be used to select the symmetry of the excitations one probes. However, RIXS has momentum dependence, with which one can obtain the same effect: the role of $P(\delta)$ is taken over by the phase factor $e^{i\mathbf{q}\cdot\mathbf{R}_i}$ in RIXS: compare Eq. (4.42) for nearest neighbors to Eq. (4.63). RIXS can also select two-magnon modes of different symmetry by tuning to specific $\mathbf{q}$'s.

The simplest case is that of A_{1g} symmetry [*i.e.*, $P(\delta)$ transforms as A_{1g} under the symmetry operations of D_{4h}, so $P_{A_{1g}}(\delta) = 1$], which corresponds to RIXS at $\mathbf{q} = \mathbf{0}$, so $e^{i\mathbf{q}\cdot\mathbf{R}_i} = 1$. In this case, both Raman and RIXS do not show inelastic weight (in theory).

For the less trivial symmetries, we rewrite the RIXS phase factor as:

$$\hat{O}_{\mathbf{q}} \propto \sum_{i,\delta} e^{i\mathbf{q}\cdot\mathbf{R}_i}\mathbf{S}_i \cdot \mathbf{S}_{i+\delta} = \sum_{i,\delta} \frac{1}{2} e^{i\mathbf{q}\cdot\mathbf{R}_i}(1 + e^{i\mathbf{q}\cdot\boldsymbol{\delta}})\mathbf{S}_i \cdot \mathbf{S}_{i+\delta}. \tag{4.64}$$

The phase factor on the right-hand side is now symmetric under the exchange of neighbors i and $i+\delta$. To probe the B_{2g} two-magnon mode (which transforms as xy), one needs

$$\frac{1}{2} e^{i\mathbf{q}\cdot\mathbf{R}_i}(1 + e^{i\mathbf{q}\cdot\boldsymbol{\delta}}) = P_{B_{2g}}(\boldsymbol{\delta}) = 0, \tag{4.65}$$

which is satisfied for all $\mathbf{R}_i$ at $\mathbf{q} = (\pi, \pi)$. Indeed, both RIXS and Raman scattering predict zero intensity for a nearest neighbor Heisenberg antiferromagnet.

For B_{1g} symmetry (x^2-y^2), the RIXS phase factor must satisfy impossible conditions:

$$\text{const.} \times e^{i\mathbf{q}\cdot\mathbf{R}_i}(1 + e^{\pm i\mathbf{q}\cdot\hat{x}}) = P_{B_{1g}}(\pm\hat{\mathbf{x}}) = +1 \tag{4.66}$$

$$\text{const.} \times e^{i\mathbf{q}\cdot\mathbf{R}_i}(1 + e^{\pm i\mathbf{q}\cdot\hat{y}}) = P_{B_{1g}}(\pm\hat{\mathbf{y}}) = -1. \tag{4.67}$$

The first condition implies $q_y = 0$, which is incompatible with the second one. Thus, Cu K edge RIXS cannot probe the B_{1g} two-magnon mode.

The only other wave vector for RIXS that we might expect to be special is $\mathbf{q} = (\pi, 0)$, but this leads to a mode that is not symmetric under, for example, rotations over 90° and therefore cannot be classified as a representation of the symmetry group D_{4h}.

We conclude that indirect RIXS on a nearest neighbor Heisenberg antiferromagnet can probe two-magnon excitations of a certain symmetry by choosing an appropriate $\mathbf{q}$, instead of choosing the polarization as in Raman scattering. Unfortunately, this is only possible for the A_{1g} and B_{2g} cases, which give no inelastic weight for both Raman and RIXS spectra, at least in theory. Comparison of any residual two-magnon feature in experimental RIXS and Raman spectra (resulting from, *e.g.*, longer range interactions [109]) is not necessarily expected to show agreement.

Conclusions. We derived the two-magnon scattering cross section which is measured in magnetic RIXS at the Cu K edge, taking advantage of a series expansion in the UCL of the intermediate state. In the context of LSWT, we calculated the magnetic RIXS spectrum for a 2D $S = 1/2$ Heisenberg antiferromagnet, in the more general case where the superexchange is not limited to nearest neighbors. Our results strongly suggest a multi-magnon scattering scenario, where two-magnon excitations are created in the system as a consequence of the modifications in the superexchange interaction induced by the core hole potential.

Our results for the two-magnon scattering agree very well with experimental data on La_2CuO_4. The vanishing of the RIXS intensity for the elastic case $\mathbf{q} = (0,0)$ and the antiferromagnetic point $\mathbf{q} = (\pi,\pi)$ is recovered. The latter feature turns out to be a consequence of an underlying symmetry property of the scattering operator and does not depend on the range of the exchange interaction. The excellent quantitative agreement between our results and experiments is testified by the occurrence of an intense peak at $\mathbf{q} = (\pi,0)$ for $\hbar\omega \approx 500$ meV. We have generalized the theory to include also finite temperature scattering, for which we find that also one-magnon processes contribute. For La_2CuO_4 at room temperature, the single-magnon spectral weight is very small compared to two-magnon scattering.

The subleading order in the UCL expansion of the cross section is shown to be of order $\mathcal{O}((\eta J/\Gamma)^2)$ smaller than the first order result. This makes the expansion a rigorous method for this case to calculate the Kramers-Heisenberg relation. The introduction of longer range interactions (according to data from neutron experiments) improves the correspondence between theory and magnetic RIXS experiments on La_2CuO_4. The generalization of the analysis to doped systems will be an interesting next step towards understanding multi-spin correlations in the spin liquid phase of the high-T_c superconductors.

Acknowledgments. We thank Michel van Veenendaal for stimulating discussions and John P. Hill for also sharing unpublished data with us. We gratefully acknowledge support from the Argonne National Laboratory Theory Institute, Brookhaven National Laboratory (DE-AC02-98CH10996) and the Dutch Science Foundation FOM. This paper was supported in part by the National Science Foundation under Grant No. PHY05-51164.

4.5 Copper L edge

4.5.1 Theory of probing single magnons in cuprates with RIXS

Published as '*Theoretical Demonstration of How the Dispersion of Magnetic Excitations in Cuprate Compounds can be Determined Using Resonant Inelastic X-Ray Scattering*' in Phys. Rev. Lett. **103**, 117003 (2009) with Giacomo Ghiringhelli, Marco Moretti Sala, Lucio Braicovich, and Jeroen van den Brink.

Abstract. *We show that in Resonant Inelastic X-ray Scattering at the copper L and M edge direct spin flip scattering is in principle allowed. We demonstrate how this possibility can be exploited to probe the dispersion of magnetic excitations, for instance magnons, of cuprates such as the high-T_c superconductors. We*

compute the relevant local and momentum dependent magnetic scattering amplitudes, which we compare to the elastic and dd excitation scattering intensities. For cuprates these theoretical results put RIXS as a technique on the same footing as neutron scattering.

Introduction. Here we show that contrary to common belief [2, 72, 73, 110], RIXS at the copper L edge is also a powerful probe of single spin flip excitations and related magnetic dispersions. The presence of this magnetic scattering channel is an important theoretical result because it puts L edge RIXS on, for instance, the high-T_c superconductors, as a technique on the same footing as neutron scattering.

Soft X-ray RIXS has been much used in transition metal oxides to study local transitions, such as dd excitations in cuprates [9, 73, 110] and spin flips [111, 112] in NiO. Although interesting in themselves, these experiments do not exploit a unique capability of RIXS: to measure the *dispersion* of excitations by determining both momentum change and energy loss of the scattered X-ray photons. This capability is far beyond the possibilities of traditional low energy optical techniques, which are constrained to essentially zero momentum transfer because, as opposed to high energy X-rays, photons in the visible range carry negligible momentum. This asset of RIXS has already been exploited to determine the momentum dependence of charge [85, 86], bimagnon [14, 51, 52, 96] and orbital excitations [54] at Cu K and L_3 edges.

In order to prove that at the Cu L edge RIXS can probe dispersion of collective magnetic excitations, we will first determine the local spin flip cross section for a copper d^9 ion in a tetragonal crystal field. This is the familiar case encountered in numerous cuprates, with one hole occupying the x^2-y^2 orbital. The important observation is that the local spin flip process can either be forbidden or allowed, depending on the spatial orientation of the copper spin. Subsequently, we calculate the momentum ($\mathbf{q}$) dependence of the magnon cross section for a spin system with a collective response. As an example we consider the Heisenberg antiferromagnet, where we find a vanishing of the magnon scattering intensity around the center of the Brillouin zone proportional to $|\mathbf{q}|$ and a strong peak at the antiferromagnetic wave vector.

Local spin flip scattering at Cu L edge. From the viewpoint of inelastic magnetic scattering, RIXS and neutron scattering appear to be very different techniques. It is easy to show, for instance, that in transition metal K edge RIXS single spin flip scattering is forbidden [51] because of the absence of spin orbit coupling in the intermediate state. Ever since the seminal work of Kuiper and coworkers [110], more than a decade ago, it is believed that also at the copper L and M edge spin flip scattering is not allowed for Cu^{2+} in a tetragonal crystal field, unless the spin flip excitation is accompanied by a dd excitation [2, 72, 73]. Based on a symmetry analysis of the wavefunction of the copper hole, Ref. [72] concludes that “the reason is that the x^2-y^2 state, a linear combination of atomic $Y_{2,2}$ and $Y_{2,-2}$ states, does not allow a direct spin flip transition.” The observation that the spin flip excitations are intrinsically entangled with dd excitations implies that mapping out momentum dependencies of magnetic excitations with L edge RIXS would be a hopeless endeavor. As will be clarified shortly, the dd-excitations act as a momentum sink, which would limit the information that can be gained from RIXS in this case to *momentum averaged properties* of the magnetic excitations, preempting the possibility to observe, *e.g.*, a single magnon dispersion.

We will show in the following, however, that the symmetry analysis on which these assertions rely [72, 73] is incomplete because it is restricted to directions of the spin moment along an axis that is orthogonal to the x^2-y^2 orbital. In fact we will show that for any other spin orientation direct spin flip scattering is allowed. This includes, in particular, Néel ordered cuprates, where the magnetic moment lies in the plane of the x^2-y^2 orbital: for example, in La_2CuO_4, $Sr_2CuO_2Cl_2$ and $(CaSr)CuO_2$ [113, 114], spins order along the $[x, y, z]$=[110] direction and in Nd_2CuO_4 along [100] and [010] in alternating planes [115].

The dependence of the direct spin flip scattering amplitude on photon polarization, scattering angle and momentum transfer can be computed from the Kramers-Heisenberg expression (2.41). At the copper L edge we are dealing with the local electronic process $2p^63d^9 \to 2p^53d^{10} \to 2p^63d^{9*}$, where $*$ denotes an excited state with a dd excitation and/or spin flip. At the L_3 resonance the intermediate states $|n\rangle$ are just the multiplets corresponding to the four $J^z = L^z + S^z$ states of the spin-orbit coupled $2p_{3/2}$ core hole.

It is easy to see that direct spin flip excitations are forbidden if the spin of the hole in the x^2-$y^2 \propto (Y_{2,2} + Y_{2,-2})/\sqrt{2}$ initial state is aligned along [001], which is the situation considered previously [72, 73]. In the first step of the RIXS process a dipole allowed 2p → 3d transition creates a core hole in a linear combination of $Y_{1,1}$ and $Y_{1,-1}$, while conserving the spin. In this intermediate state the spin-orbit coupling of the core hole $\mathbf{L} \cdot \mathbf{S} = L^zS^z + (L^+S^- + L^-S^+)/2$ can cause a spin flip S^- (or S^+) in combination with a raising (or lowering) L^+ (or L^-) of the orbital moment. In either case a $Y_{1,0}$ core hole state with reversed spin is the result [72, 73, 116]. The last step to end up in a final state with only a spin flip excitation, requires the optical decay of the $Y_{1,0}$ 2p core hole into a $(Y_{2,2} + Y_{2,-2})/\sqrt{2}$ 3d valence band hole. But this transition is dipole forbidden because it requires $\Delta L^z = 2$, which thus forbids direct spin flip scattering.

The situation changes drastically when the local magnetic moment is oriented in the xy plane: we will show that in this case direct spin flip excitations are fully allowed. This is best illustrated by a direct calculation of the RIXS amplitudes in the different channels for Cu^{2+} in a tetragonal crystal field. We consider a scattering geometry as in Fig. 4.10(a), with fixed scattering angle of 90° and π (σ) linear polarization of the incident photons parallel (perpendicular) to the scattering plane. In this geometry θ_{IN} is the azimuthal angle between incident beam and [001] axis. In Fig. 4.10(b) we show the polarization and momentum dependent RIXS matrix elements to all possible final states for the starting con-

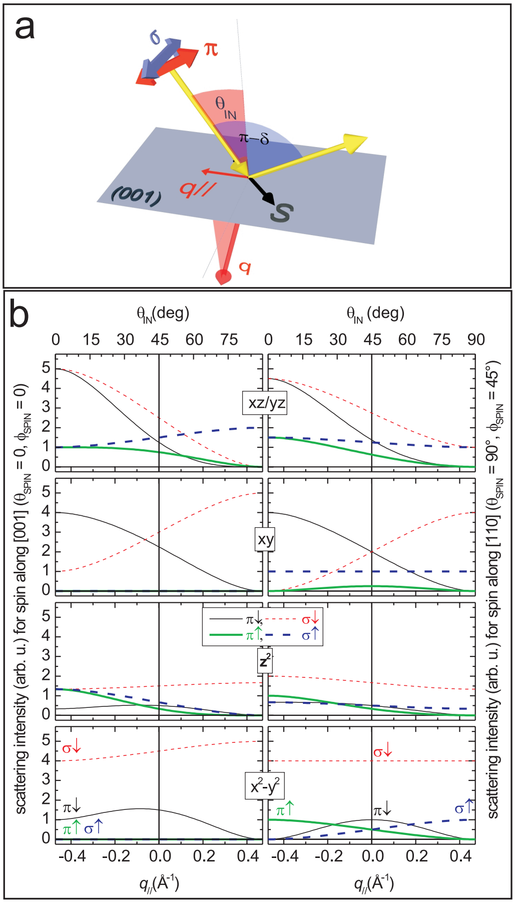

Figure 4.10: L_3 RIXS cross section for a single Cu^{2+} ion with σ and π polarization of the incident beam. (a) The geometry: the scattering plane is (100), scattering angle 90°, the incident photons impinge at an angle θ_{IN} to the [001] direction (c axis). (b) Scattering intensities to different orbital and spin orientations, starting from a $(x^2\text{-}y^2)\!\downarrow_z$ state (left panels) and a $(x^2\text{-}y^2)\!\downarrow_{xy}$ groundstate (right panels) as a function of θ_{IN} or alternatively the in-plane transferred momentum $q_{\|}$. For $\downarrow_z$, *i.e.*, spin along [001], the spin flip cross section vanishes (bottom left), not so for $\downarrow_{xy}$, with spin along [110] (right).

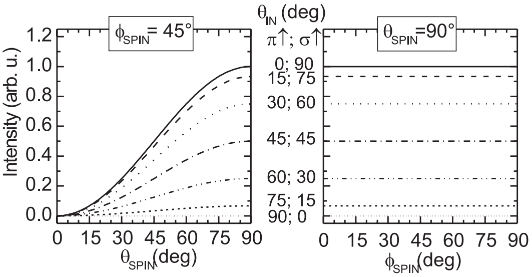

Figure 4.11: The dependence of scattering cross section for spin flip scattering to (x^2-y^2)↑ final states on the atomic spin orientation for selected cases of scattering geometry given by varying $\theta_{\rm IN}$ and fixed $\phi_{\rm IN} = 0$.

figuration of a hole in the x^2-y^2 orbital with a spin oriented either along [001] (left panels) or along [110] (right panels), denoted by $(x^2\text{-}y^2)\!\downarrow_z$ and $(x^2\text{-}y^2)\!\downarrow_{xy}$, respectively, so that (x^2-y^2)↑ is a final state with only a spin flip excitation.

Note that along the [100] direction the nuclear Brillouin zone boundary is in $q_{||} \approx 0.826$ Å^{-1} for $a = 3.8$ Å an in-plane lattice parameter that is typical for cuprates. At 90° scattering Cu L$_3$ RIXS can explore half of the reciprocal space, but going to backscattering geometry $q_{||}$ grows considerably and almost all the Brillouin zone can be covered. Fig. 4.10(b) shows that the spin flip to dd excitation intensity ratio varies from zero at the zone center to about 0.1 at the zone edge. From the lower panels in Fig. 4.10 at the left and right it is clear that for a spin along [110] the spin flip cross section is allowed for both σ and π polarizations, whereas it is in all cases forbidden for a spin along [001]. It is interesting to note that for the σ polarization the elastic peak is more than 4 times stronger than the spin flip scattering channel, whereas for π the two intensities are similar. The direct spin flip cross section for a generic spin direction, characterized by the Euler angles $(\theta_{\rm spin}, \phi_{\rm spin})$ is shown in Fig. 4.11 for a number of azimuthal angles $\theta_{\rm IN}$.

The upshot of these numerical results can easily be understood on the basis of a symmetry argument. If the spin of the x^2-y^2 hole points along the x axis, it is in the spin state $(|\!\uparrow\rangle + |\!\downarrow\rangle)/\sqrt{2}$, corresponding to $S^x = 1/2$. In the intermediate 2p$_{3/2}$ core hole state the diagonal part of the spin-orbit coupling, $L^z S^z$, causes a transition of this spin state into $(|\!\uparrow\rangle - |\!\downarrow\rangle)/\sqrt{2}$ (corresponding to $S^x = -1/2$), while the angular part of the core hole wavefunction stays in a linear combination of $Y_{1,1}$ and $Y_{1,-1}$. The transition of the core hole back into the 3d x^2-y^2 orbital is therefore dipole allowed while at the same time the spin along the x axis is flipped.

Momentum dependence of magnon cross section. We now wish to generalize the cross section from local spin flips to collective magnetic excitations, which are characterized by their momentum quantum number $\mathbf{q}$. There are several ways to compute the $\mathbf{q}$ dependence of this cross section, but a particularly transparent one is by the UCL expansion (2.49), which we will employ to zeroth order. This corresponds with summing over only the $J = 3/2$ core states in the

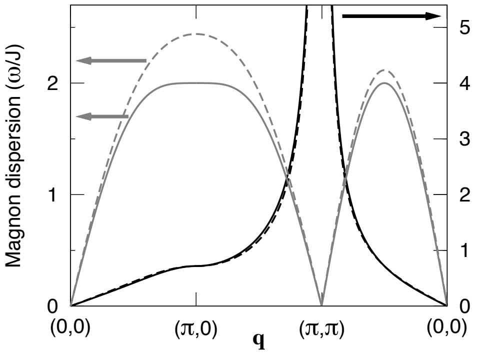

Figure 4.12: Momentum dependence of the magnetic RIXS spectral weight at the Cu L$_3$ edge (black) and the magnon dispersion (gray) for a simple 2D Heisenberg model (solid curves) and an extended model relevant for La$_2$CuO$_4$ [83] (dashed).

sum over intermediate states. The dipole operators $\mathcal{D}$ and $\mathcal{D}'^{\dagger}$ now allow for a direct creation of a spin flip upon de-excitation. The corresponding amplitude $T_{\mathrm{sf},L_3}(\boldsymbol{\epsilon}', \boldsymbol{\epsilon})$ depends on incident and outgoing polarization, as clarified above and shown in Figs. 4.10 and 4.11. We thus obtain

$$\mathcal{F}_{fg} = \frac{1}{i\Gamma} \sum_{L_3} T_{\mathrm{sf},L_3}(\boldsymbol{\epsilon}', \boldsymbol{\epsilon}) \sum_i e^{i\mathbf{q}\cdot\mathbf{R}_i} \langle f | \, \sigma_i^z \, | g \rangle \tag{4.68}$$

where the operator σ^z flips the spin when it is in the xy plane. The sum is over all intermediate core hole states of the L_3 edge, and we denote the shorthand $T_{\mathrm{sf}}(\boldsymbol{\epsilon}', \boldsymbol{\epsilon}) = \sum_{L_3} T_{\mathrm{sf},L_3}(\boldsymbol{\epsilon}', \boldsymbol{\epsilon})$.

It is instructive to compute with this generic expression the single magnon RIXS spectrum for an antiferromagnetic 2D Heisenberg model, given by Eq. 4.1. Rotating the spin operators to align the staggered magnetization along the z axis, introducing Holstein-Primakoff bosons and adopting linear spin wave theory one finds after a Fourier and a Bogoliubov transformation the magnon scattering amplitude

$$\mathcal{F}_{fg} = \sqrt{N} \frac{1}{i\Gamma} T_{\mathrm{sf}}(\boldsymbol{\epsilon}', \boldsymbol{\epsilon})(u_{\mathbf{q}} - v_{\mathbf{q}}) \langle f | \, \alpha_{-\mathbf{q}} + \alpha_{\mathbf{q}}^{\dagger} \, | g \rangle \tag{4.69}$$

with N the total number of sites. The resulting zero-temperature single magnon spectrum,

$$\frac{d^2\sigma}{d\Omega d\omega} \propto |T_{\mathrm{sf}}(\boldsymbol{\epsilon}', \boldsymbol{\epsilon})|^2 \, (u_{\mathbf{q}} - v_{\mathbf{q}})^2 \delta(\omega - \omega_{\mathbf{q}}), \tag{4.70}$$

is shown in Fig. 4.12. At $\mathbf{q} = (0, 0)$ the magnon scattering amplitude vanishes because in this situation the scattering operator is proportional to the total spin in the z direction S^z_{tot}, which does not cause inelastic processes because this operator commutes with the Heisenberg Hamiltonian. For small transferred momenta, $|\mathbf{q}| \to 0$, the magnon scattering intensity vanishes as $\omega_{\mathbf{q}}/4J$. We also observe that the magnon cross section diverges at $\mathbf{q} = (\pi, \pi)$ as $4J/\omega_{\mathbf{q}}$, similar to the neutron scattering form factor. This divergence is due to the RIXS photons scattering on spin fluctuations: at $\mathbf{q} = (\pi, \pi)$ the scattering operator is proportional to the staggered spin along the z axis S^z_{stag}, so that the total, energy integrated, scattering intensity $\int d\omega \sum_f |\mathcal{F}_{fg}|^2 \delta(\hbar\omega - E_f) \propto \left\langle (S^z_{\text{stag}})^2 \right\rangle$ and the inelastic scattering intensity is proportional to the variance $\left\langle (S^z_{\text{stag}})^2 \right\rangle - \left\langle S^z_{\text{stag}} \right\rangle^2$. We performed the same calculation for a Hamiltonian including longer-range and ring exchange terms, with a parameterization derived from neutron scattering[2]. Fig. 4.12 shows that these additional interactions cause only small changes in the momentum dependence of the magnetic scattering cross section.

Using the same formalism, we can compute the $\mathbf{q}$ dependent scattering amplitude of a spin flip entangled with a dd excitation. If the local spin flip operator is S^-_i and the operator corresponding to the dd transiton is T^+_i, the inelastic scattering amplitude is $\mathcal{F}_{fg} \propto \langle f | \sum_i e^{i\mathbf{q}\cdot\mathbf{R}_i} S^-_i T^+_i | g \rangle = \langle f | \sum_{\mathbf{k}} S^-_{\mathbf{k}} T^+_{\mathbf{k}-\mathbf{q}} | g \rangle$. Clearly part of the momentum is absorbed by the dd excitation, so that RIXS measures a momentum convolution of the two excitations. In particular, the magnetic scattering amplitude looses all $\mathbf{q}$ dependence if the dd excitation is dispersionless, exemplifying that in order to determine magnon dispersions the presence of a *direct* spin flip process is essential.

Conclusions. Depending on the spatial orientation of the copper spin, the local spin flip process for RIXS at the L_3 edge can be forbidden or allowed. This makes RIXS a very sensitive probe of the orientation of the local magnetic moment. In typical cuprates direct spin flip scattering is allowed and for this case we determined the spin flip and magnon cross section, which turns out to be strongly momentum and polarization dependent. Our theory holds at both the copper L and M edges. At the M edge ($\hbar\omega_{\mathbf{k}} \approx 75$eV) the photon momentum is small, so that only magnons in a very small portion of the Brillouin zone can be probed. But at the copper L_3 edge the X-ray photon carries a momentum $|\mathbf{q}_{\text{in}}| \sim 0.47$ Å^{-1}, which is in a typical cuprate large enough to observe magnetic excitations in almost all of the Brillouin zone. Indeed very recently high resolution soft X-ray RIXS experiments on La_2CuO_4 have for the first time resolved the single magnon dispersion, confirming our predictions [11,21]. Thus, at least for high-T_c superconductors, L edge RIXS can be placed on the same footing as neutron scattering – with the additional great advantage that for photon scattering only small sample volumes are required so that the measurement of the spin dynamics of thin films, oxide heterostructures and other nanostructures comes now within experimental reach.

Acknowledgments. We thank Michel van Veenendaal, Tom Devereaux, Maurits Haverkort, Marco Grioni and George Sawatzky for stimulating discussions. This research benefited from the RIXS collaboration supported by the Computational Materials Science Network (CMSN) program of the Division of Materials

---

[2] Next-nearest neighbor $J'/J = -0.11$, next-next-nearest neighbor $J''/J = 0.026$ and ring exchange $J_{\Box}/J = 0.41$ [83]

Science and Engineering, U. S. Department of Energy, grant number DE-FG02-08ER46540 and is supported by the Dutch Science Foundation FOM.

4.5.2 Experimental verification of the single magnon theory

Soon after the predictions of Ref. [19] for the single magnon cross section, the single magnon dispersion was measured by Braicovich *et al.* [11]. A typical RIXS spectrum is shown in Fig. 4.13, together with the dispersion found by the authors. The dispersion is obtained by tracing the peak of the low energy spectrum along the [100] direction. The agreement with the dispersion obtained by neutron scattering is excellent.

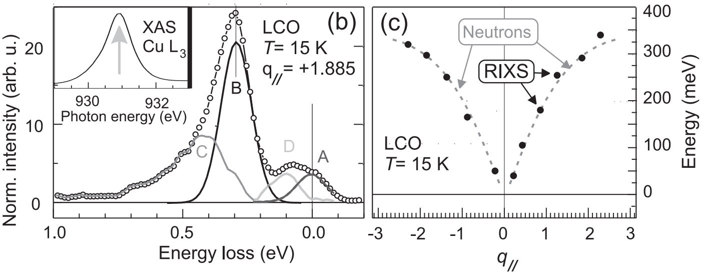

Figure 4.13: Left panel: a typical low energy RIXS spectrum of 2D cuprates. Shown here is a spectrum at the Cu L_3 edge of La_2CuO_4 at $\mathbf{q} = (0.6\pi, 0)$. The spectrum is decomposed in (A) the elastic peak, (B) a single magnon peak (by fitting a Gaussian at the spectrum's maximum), leaving (C) multiple magnon modes at higher energy and (D) optical phonons at lower energy. In the inset the L_3 X-ray Absorption Spectrum is shown, where the arrow indicates excitation energy. Tracing the maximum of the RIXS spectra at different transferred momenta along the [100] direction, RIXS can determine the single magnon dispersion, as shown in the right panel. The black dots were found by RIXS experiments [11] and the dashed, gray line by inelastic neutron scattering [83]. All RIXS measurements were done at $T = 15$ K. Figures from Ref. [11].

More data was taken by Guarise *et al.* [69], who also used the Cu L_3 edge. Their data are shown and compared to theory in Fig. 4.14. They are consistent with the results from inelastic neutron scattering on La_2CuO_4 [83], and cover for the first time the full dispersion in $Sr_2CuO_2Cl_2$ up to the boundary of the magnetic Brillouin zone. They reveal a striking 70 meV difference between the magnon energies of 310 meV at $(\pi, 0)$ and 240 meV at $(\pi/2, \pi/2)$, suggesting that further neighbor interactions are important. The large disersion along the magnetic Brillouin zone boundary can be compared with the smaller ~ 20 meV dispersion in La_2CuO_4 [83]. The dispersion along the magnetic zone boundary is also predicted by recent LDA+U theory, which, however, underestimates the energy at $\mathbf{q} = (\pi, 0)$ in $Sr_2CuO_2Cl_2$ by almost 50 meV [117].

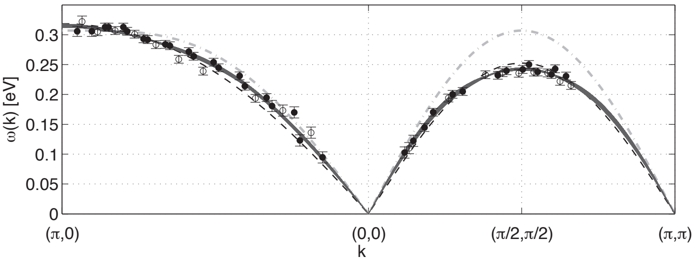

Figure 4.14: Single magnon dispersion measured at the Cu L_3 edge of $Sr_2CuO_2Cl_2$. Open and closed symbols stem from 2 independent measurements on different samples. In the [100] direction, data for both $q_x > 0$ and $q_x < 0$ are collapsed on the same $(0, 0) - (\pi, 0)$ branch. The dot-dashed line is the LSWT result (including the Oguchi correction [104]) for a nearest neighbor Heisenberg model with $J = 130$ meV. The black dashed line is a nearest-neighbor Hubbard model fit for $t = 0.261 \pm 0.004$ eV and $U = 1.59 \pm 0.04$ eV. For the gray lines, further neighbor hoppings are added to the Hubbard model. Reasonable fits can also be obtained at larger U: the thickness of the gray band is generated by taking 1.9 eV $< U <$ 4 eV, while fitting the hopping parameters. Guarise *et al.* [69] experimentally establish a relation between U and the hopping parameters. All measurements were done at $T = 15$ K. Figure from Ref. [69]

RIXS experiments have not only mapped out the magnon dispersion, they have also verified the predicted spectral weight of the magnon peak in various cuprates. Since the experimental spectral weight is sensitive to, amongst others, self-absorption, Braicovich *et al.* [21] compared the ratio of spectral weights for σ and π polarization while keeping the incident and outgoing photon directions constant – thus reducing the effect of self-absorption. The data and theory are first normalized to the spectral weight of the dd excitations, which are well-understood theoretically [19, 20]. Then, the single magnon spectral weight for σ polarization is divided by the signal for π polarization. One finds that the resulting linear dichroism ratio R of the (renormalized) theoretical intensities is

$$R = \frac{I_\sigma}{I_\pi} = \frac{\sum_{\boldsymbol{\epsilon}'} |T_{\rm sf}(\boldsymbol{\epsilon}', \boldsymbol{\epsilon}_\sigma)|^2}{\sum_{\boldsymbol{\epsilon}'} |T_{\rm sf}(\boldsymbol{\epsilon}', \boldsymbol{\epsilon}_\pi)|^2}, \tag{4.71}$$

i.e., independent of the dynamic, $\mathbf{q}$ dependent spin susceptibilities. Only the local, atomic spin flip scattering factors $T_{\rm sf}$ remain in the ratio. Fig. 4.15 shows the linear dichroism ratio, which has a clear asymmetry between $+\mathbf{q}$ and $-\mathbf{q}$. The agreement between theory and experiments is again very good.

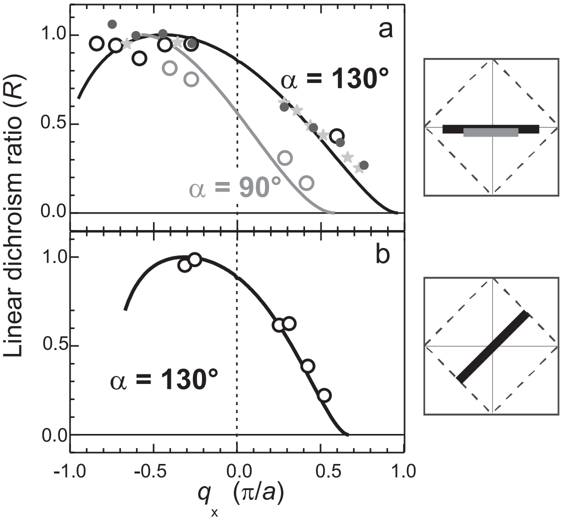

Figure 4.15: Single magnon spectral weight measured at the copper L_3 edge of various cuprates with transferred momentum along (a) the [100] direction, and (b) the [110] direction. The open circles refer to La_2CuO_4, the filled circles to (Sr,Ca)CuO_2 (prepared as a thin film on $SrTiO_3$), and the stars to strongly underdoped $NdBa_2Cu_3O_{6+\delta}$. The data were taken at $T = 15$ K. α is the scattering angle. Figures from Ref. [21].

4.5.3 Bimagnon excitations at the Cu L edge

Published in '*Dispersion of Magnetic Excitations in the Cuprate La_2CuO_4 and $CaCuO_2$ Compounds Measured Using Resonant X-Ray Scattering*', Phys. Rev. Lett. **102**, 167401 (2009) with L. Braicovich, V. Bisogni, F. Forte, C. Aruta, G. Balestrino, N. B. Brookes, G. M. De Luca, P. G. Medaglia, F. Miletto Granozio, M. Radovic, M. Salluzzo, J. van den Brink, and G. Ghiringhelli.

Next to single magnons, the Cu L edge can also exhibit bimagnon excitations [10]. Single magnons will dominate the RIXS spectrum as they arise in direct RIXS processes, but at the high energy side of the single magnon peak, a tail is observed [11]. This could well be multi-magnon excitations.

Bimagnon excitations arise in RIXS at the Cu L edge because the $3d^{10}$ configuration in the intermediate state blocks all superexchange. The spins of its neighbors reorient themselves, and this process can be described in terms of bimagnon excitations. The blocking of superexchange bonds is formalized in the intermediate state Hamiltonian

$$\bar{H} = H_0 - J \sum_{i,\delta} p_i p_i^\dagger \mathbf{S}_i \cdot \mathbf{S}_{i+\delta}, \tag{4.72}$$

where p_i annihilates a 2p core electron at site i and δ points to nearest neighbors. To first order in the UCL expansion, we find

$$\mathcal{F}_{fi} = \frac{T_{\text{el}}(\boldsymbol{\epsilon}', \boldsymbol{\epsilon})}{(i\Gamma)^2} \langle f| \sum_i e^{i\mathbf{q}\cdot\mathbf{R}_i} p_i^\dagger \bar{H} p_i \, |i\rangle \tag{4.73}$$

where the polarization dependence is the same as for elastic scattering as the Hamiltonian should excite the valence electrons in indirect RIXS. Of course, the dipole transitions can also add other excitations like dd or spin flip excitations, but we are not interested in these processes here. As Eqs. (4.72) and (4.36) have the same form, the Cu L edge bimagnon spectra have the same line shape as the bimagnon spectra at the Cu K edge [see Fig. 4.5(a)], and we therefore will not elaborate on this subject here.

4.5.4 Chemical pressure effects

Published as '*Effect of the chemical pressure on bimagnons in antiferromagnetic insulators: $CaCuO_2$ and $BaCuO_2$ studied with Cu-L_3 resonant inelastic X-ray scattering*' in Eur. Phys. J. Special Topics **169**, 141 (2009) with V. Bisogni, C. Aruta, G. Balestrino, N. B. Brookes, F. Forte, G. Ghiringhelli, P. G. Medaglia, J. van den Brink, and L. Braicovich.

When the lattice parameter of a magnetic solid is changed, the hopping amplitudes change too, and ultimately also the superexchange constant is altered. A comparison of $CaCuO_2$ with $BaCuO_2$ with Cu L_3 edge RIXS is presented by Bisogni *et al.* [118]. Ba is a bigger ion than Ca and therefore increases the lattice parameters by a factor of 1.03 in-plane, and 1.27 along the z axis, making the crystal field in $BaCuO_2$ more cubic. The increase in the in-plane lattice parameters reduces the superexchange constant. An energy shift is observed for the magnetic spectrum, implying that J is reduced by a factor of 0.67 ± 0.06 when substituting Ca by Ba.

For the dd excitations, the (average) observed scaling factor for the energy is different: 0.8 ± 0.06. This should be ascribed to the more cubic symmetry of the crystal field, which rearranges the energies of the different dd excitations.

Further, a reduction in the spectral weight of the low energy spectrum is seen of at least a factor 0.5 when the data is normalized to the total dd excitations' spectral weight. In interpreting this fact, one has to take into account that the large increase of the lattice parameter in the z direction changes the radial matrix elements. The radial parts of all the wave functions become more similar in the more cubic Ba compound, while in $CaCuO_2$, the radial parts differ substantially for the different 3d orbtals because of the D_{4h} crystal field splitting.

4.5.5 Spectral weight at the Γ point

Both the single magnon and the bimagnon spectral weight vanish at $\mathbf{q} = \mathbf{0}$. The question then arises which higher order process gives spectral weight at the Γ point. The single magnon DOS vanishes at $\mathbf{q} = \mathbf{0}$, so unless there is some mixing with other wave vectors, there cannot be any single magnon spectral weight at the Γ point. The bimagnon DOS, however, is very large at $\mathbf{q} = \mathbf{0}$ [see Fig. 4.5(b)]. In Sec. 4.4, we discussed bimagnon excitations that arise in the second order of the UCL expansion, generating spectral weight at $\mathbf{q} = \mathbf{0}$, proportional to $(J/\Gamma)^4$. This also holds at the Cu L edge, of course. Here, we consider another possible mechanism: multi-site exchange mechanisms that are not included in the simple Heisenberg model also give rise to bimagnon excitations, in particular at the Γ point.

Starting from a single-band Hubbard model, multi-site exchange processes appear in the effective spin Hamiltonian at fourth order in t/U. Such processes contribute to the scattering amplitude in two ways: first, the initial and final states are modified. Second, the intermediate state energies are modified, and in the UCL expansion, this is reflected in a modified $\bar{H}$.

The Heisenberg Hamiltonian to fourth order in t/U without a core hole is given by Eq. (4.14). The corresponding magnon (approximate) eigenstates that determine the initial and final states are given in Sec. 4.2.

The fourth order contribution to the intermediate state Hamiltonian (*i.e.*, including the core hole) is obtained through a tedious calculation using degenerate perturbation theory of the Hubbard model to fourth order [82,119]. The Hubbard Hamiltonian of the system with a core hole is written as $\bar{H} = h + V$ where h contains the Coulomb repulsion part (including the 2p-3d Coulomb energy U_c) and V contains the hopping. Turning off the hopping, the (degenerate) ground state has the core hole site doubly occupied and all other sites singly occupied. The projector on the space spanned by all these ground states is P_0. Turning on a small hopping parameter t introduces exchange interactions. The effective Hamiltonian to fourth order in t/U is [82, 119]:

$$\begin{aligned}\bar{H}^{(4)}_{\text{eff}} &= P_0VSVP_0 + P_0VSVSVSVP_0 \\ &\qquad - \frac{1}{2}\left(P_0VS^2VP_0VSVP_0 + P_0VSVP_0VS^2VP_0\right)\end{aligned} \tag{4.74}$$

where $S = (P_0 - \mathbb{1})/h$. Because of the projectors P_0, the eigenstates of the effective Hamiltonian are also eigenstates of P_0 and can be reformulated in terms of spins, see Eq. (2.14) of Ref. [82]. The first term on the right-hand side of Eq. (4.74) generates the familiar nearest neighbor exchange (which is blocked at the core hole site, however). The other terms in Eq. (4.74) involve four hops, which after two hops may [terms between parentheses in Eq. (4.74)] or may not $[P_0VSVSVSVP_0]$ return to the space of unperturbed ground states.

The details of the derivation of the low energy effective Hamiltonian $\bar{H}_{\text{eff}}$ to 4th order in $t/U_{(c)}$ can be found in appendix D. The resulting intermediate state Hamiltonian in the mean field approximation is

$$\begin{aligned}\bar{H}^{(4)}_{\text{eff}} = H_0 + \sum_i p_i p_i^\dagger \Bigg[&\sum_j^{\text{nn}} \left(\frac{64t^4}{U^3} - \frac{4t^2}{U}\right)\mathbf{S}_i\cdot\mathbf{S}_j + \sum_j^{\text{nnn}} \frac{20t^4}{U^3}\mathbf{S}_i\cdot\mathbf{S}_j \\ &+ \sum_{j\neq k}\left(\frac{4t^4}{UU_c^2} + \frac{8t^4}{U_c^2(2U_c+U)} - \frac{4t^4}{U^3}\right)\mathbf{S}_j\cdot\mathbf{S}_k +\end{aligned}$$

$$\begin{aligned}&+\sum_{\text{squares}}\left\{\left(\frac{24t^4}{U^3}-\frac{2t^4}{U_c^3}-\frac{2t^4}{UU_c^2}\right)(\mathbf{S}_j\cdot\mathbf{S}_k+\mathbf{S}_k\cdot\mathbf{S}_l)\right.\\&\left.+\left(\frac{20t^4}{U^3}-\frac{2t^4}{U_c^3}-\frac{2t^4}{UU_c^2}\right)\mathbf{S}_j\cdot\mathbf{S}_l\right\}\Bigg].\end{aligned}\tag{4.75}$$

The sums between the straight brackets are, respectively, over all nearest neighbors (nn) j of i, over all next nearest neighbors (nnn) j of i, over all pairs j,k of nearest neighbors of i, and over all squares of 2×2 sites containing i.

Eq. (4.75) is substituted in the UCL expansion. The leading inelastic order is

$$\mathcal{F}_{fi}=\frac{1}{(i\Gamma)^2}\langle f|\,\mathcal{D}^\dagger\bar{H}^{(4)}_{\text{eff}}\mathcal{D}\,|i\rangle=-\frac{T_{\text{el}}(\boldsymbol{\epsilon}',\boldsymbol{\epsilon})}{\Gamma^2}\langle f|\sum_i e^{i\mathbf{q}\cdot\mathbf{R}_i}[\ldots]\,|i\rangle\,,\tag{4.76}$$

where $[\ldots]$ represents the lengthy expression between striaght brackets in Eq. (4.75). The polarization factor for elastic scattering is the same as in Eq. (4.73).

In appendix D.2, the scattering amplitude for two-magnon creation processes at zero temperature is evaluated. The result is

$$\begin{aligned}\mathcal{F}_{fi}=&-\frac{T_{\text{el}}(\boldsymbol{\epsilon}',\boldsymbol{\epsilon})}{\Gamma^2}\sum_{\mathbf{k}}\Bigg[\Bigg\{-\left(\frac{20t^4}{U^3}-\frac{2t^4}{U_c^3}-\frac{2t^4}{UU_c^2}\right)f_b(\mathbf{k},\mathbf{q})-\frac{20t^4}{U^3}f_{\text{nnn}}(\mathbf{k},\mathbf{q})\\&-\left(\frac{4t^4}{UU_c^2}+\frac{8t^4}{U_c^2(2U_c+U)}-\frac{4t^4}{U^3}\right)f_a(\mathbf{k},\mathbf{q})-\left(\frac{64t^4}{U^3}-\frac{4t^2}{U}\right)(1+\gamma_{\mathbf{q}})\\&-\left(\frac{24t^4}{U^3}-\frac{2t^4}{U_c^3}-\frac{2t^4}{UU_c^2}\right)f_{c1}(\mathbf{q})\Bigg\}(U_{\mathbf{k}}V_{\mathbf{k}-\mathbf{q}}+U_{\mathbf{k}-\mathbf{q}}V_{\mathbf{k}})\\&+\left\{\left(\frac{64t^4}{U^3}-\frac{4t^2}{U}\right)(\gamma_{\mathbf{k}-\mathbf{q}}+\gamma_{\mathbf{k}})+\left(\frac{24t^4}{U^3}-\frac{2t^4}{U_c^3}-\frac{2t^4}{UU_c^2}\right)f_{c2}(\mathbf{k},\mathbf{q})\right\}\\&\times(U_{\mathbf{k}}U_{\mathbf{k}-\mathbf{q}}+V_{\mathbf{k}-\mathbf{q}}V_{\mathbf{k}})\Bigg]\langle f|\,\alpha^\dagger_{\mathbf{k}}\alpha^\dagger_{-\mathbf{k}+\mathbf{q}}\,|0\rangle\,.\end{aligned}\tag{4.77}$$

At $\mathbf{q}=\mathbf{0}$, the amplitude reduces to

$$\begin{aligned}\mathcal{F}_{fi}=&\frac{T_{\text{el}}(\boldsymbol{\epsilon}',\boldsymbol{\epsilon})}{\Gamma^2}\sum_{\mathbf{k}}\Bigg[\Bigg\{\left(\frac{4t^4}{UU_c^2}+\frac{8t^4}{U_c^2(2U_c+U)}-\frac{4t^4}{U^3}\right)f_a(\mathbf{k},\mathbf{0})\\&\left(\frac{30t^4}{U^3}-\frac{2t^4}{U_c^3}-\frac{2t^4}{UU_c^2}\right)f_b(\mathbf{k},\mathbf{0})\Bigg\}2U_{\mathbf{k}}V_{\mathbf{k}}\Bigg]\langle f|\,\alpha^\dagger_{\mathbf{k}}\alpha^\dagger_{-\mathbf{k}}\,|0\rangle\end{aligned}\tag{4.78}$$

with

$$f_a(\mathbf{k},\mathbf{0})=2\gamma_{2\mathbf{k}}-2+f_b(\mathbf{k},\mathbf{0}),\qquad f_b(\mathbf{k},\mathbf{0})=4\cos k_x\cos k_y-4.\tag{4.79}$$

Using the parameters (obtained by neutron scattering on La_2CuO_4) $t = 0.33$ eV, $U = 2.9$ eV [83], and $U_c = 4.1$ eV [61], one finds

$$\frac{4t^4}{UU_c^2} + \frac{8t^4}{U_c^2(2U_c + U)} - \frac{4t^4}{U^3} \approx -0.4 \text{ meV}, \tag{4.80}$$

$$\frac{30t^4}{U^3} - \frac{2t^4}{U_c^3} - \frac{2t^4}{UU_c^2} \approx 13.7 \text{ meV}. \tag{4.81}$$

We now make a rough comparison between the spectral weight coming from corrections to the Hamiltonian, and from the second order of the UCL expansion. In Sec. 4.4, it is shown that the second order of the UCL expansion (4.62) gives the following contribution at $\mathbf{q} = \mathbf{0}$:

$$\mathcal{F}_{2^{\text{nd}}UCL} = \frac{T_{\text{el}}(\boldsymbol{\epsilon}', \boldsymbol{\epsilon})}{\Gamma^2} \frac{J^2}{4i\Gamma} \sum_{\mathbf{k}} \langle f| \, f_a(\mathbf{k}, \mathbf{0}) 2U_{\mathbf{k}} V_{\mathbf{k}} \, \alpha^\dagger_{\mathbf{k}} \alpha^\dagger_{-\mathbf{k}} \, |0\rangle \, . \tag{4.82}$$

Ignoring all details in the functions f, we compare $13.7 - 0.4 = 13.3$ meV for the higher order exchange scenario with $J^2/2\Gamma \approx 15.6$ meV for the second order of the UCL expansion at the Cu L_3 edge. We conclude that both the second order of the UCL expansion and higher order exchange processes contribute significantly to the Cu L_3 RIXS intensity at the Γ point. It should be noted that the higher order exchange processes dominate the $\mathbf{q} = \mathbf{0}$ RIXS intensity when Γ is larger, as, *e.g.*, at the L_2 and K edges.

4.6 Copper L edge of doped cuprates

Now that the magnetic RIXS spectrum of the undoped cuprates is understood to a fair level of detail, the next question to be addressed is the following: how does the low energy L_3 edge RIXS spectrum evolve upon doping?

The X-ray absorption spectrum of undoped La_2CuO_4 at the Cu L_3 edge shows a single peak, corresponding (mainly) to the transition $3d^9 \rightarrow \underline{2p}_{3/2}3d^{10}$. When La_2CuO_4 is doped with holes, this peak aquires a tail at the high energy side, which is interpreted as $3d^9\underline{L} \rightarrow \underline{2p}_{3/2}3d^{10}\underline{L}$ [84]. The energy is slightly higher because one breaks up a Zhang Rice Singlet (ZRS) in the latter process, which costs some energy. From the XAS spectra, it therefore seems possible to tune X-ray photons so that they are absorbed either at the undoped or at the doped sites of $La_{2-x}Sr_xCuO_4$. These resonances are called the L_3 and L_3' edges, respectively.

We assume that the low energy physics of doped cuprates are described by the t-J model. Of course, phonons will also play a role, but the treatment of phonon excitations in RIXS is postponed to chapter 7. The Hamiltonian for the t-J model reads

$$H_0 = H_t + H_J = -t \sum_{\langle i,j \rangle, \sigma} \left(d^\dagger_{i\sigma} d_{j\sigma} + \text{h.c.} \right) + J \sum_{\langle i,j \rangle} \mathbf{S}_i \cdot \mathbf{S}_j . \tag{4.83}$$

The $d_{i\sigma}^{(\dagger)}$ operators annihilate (create) an electron on site i with spin σ, and the sums over $\langle i, j\rangle$ count each bond once. Unoccupied sites correspond to ZRS's.

4.6.1 RIXS amplitude for doped cuprates

We now consider the RIXS amplitude when the X-ray photons are tuned to the L_3 edge. As mentioned above, we assume that only sites that do not carry ZRS's are excited. This can be incorporated in the Kramers-Heisenberg equation by projecting out all intermediate states that have a ZRS at the core hole site. We write Eq. 2.41 as

$$\mathcal{F}_{fi} = \sum_{\zeta\in\{\text{el},\text{sf}\}} T_\zeta(\boldsymbol{\epsilon}', \boldsymbol{\epsilon}) \sum_i e^{i\mathbf{q}\cdot\mathbf{R}_i} \sum_n \frac{\langle f|\, d_{i\sigma'} p_{i\sigma'}^\dagger P\, |n\rangle \, \langle n|\, P\; p_{i\sigma} d_{i\sigma}^\dagger \,|i\rangle}{z - E_n} \tag{4.84}$$

where ζ indicates either a spin flip process or an elastic scattering event, and determines the spins σ and σ'. Further, $z = E_g + \hbar\omega_{\mathbf{k}} + i\Gamma$, $p_{i\sigma}$ is the 2p core electron annihilation operator and P the projection operator

$$P = \sum_{i,\sigma} p_{i\sigma} p_{i\sigma}^\dagger n_{i\uparrow} n_{i\downarrow}, \tag{4.85}$$

removing any contribution to the amplitude coming from X-ray transitions at ZRS sites. Note that $n_{i\sigma} = d_{i\sigma}^\dagger d_{i\sigma}$. We assume that the RIXS process remains a predominantly local one, *i.e.*, a local $3d^{10}$ intermediate state is created, so the polarization factors T_ζ are the same as for the undoped cuprates: at low energy loss, they either yield a spin flip or an elastic process.

At the Cu L_3 edge of the undoped compounds, the main source of low energy inelastic spectral weight is spin flip scattering. In doped cuprates, it is also possible to rearrange the charges. As will be shown below, charge scattering happens even when the intermediate state dynamics are absent, and springs from the elastic scattering channel when the Cu ions are interacting with each other. This is analogous to the spin flip cross section for single ions, which also depends strongly on the way the electrons of the system interact. We ignore the dd excitations here, because they do not affect the low energy spectra. The question now arises which channel dominates the low energy RIXS spectra of doped cuprates: magnetic or charge scattering?

4.6.2 Fast collision approximation

To answer the question which scattering channel dominates the low energy RIXS spectra of the cuprates, we first make the fast collision approximation, *i.e.*, keeping only the zeroth order of the UCL expansion.In the undoped case, the single magnon spectrum is quite accurately described by the fast collision approximation (4.68). When the system is doped and the incident energy is tuned to the sites with a spin, the sum over sites should exclude all hole sites. This is enforced in Eq. (4.84) by the projection operator P. The spin flip scattering amplitude is

$$\mathcal{F}_{fi}^{\mathrm{sf}} = \frac{T_{\mathrm{sf}}(\boldsymbol{\epsilon}', \boldsymbol{\epsilon})}{i\Gamma} \langle f| \sum_i e^{i\mathbf{q}\cdot\mathbf{R}_i} \sigma_i^z \rho_i)\, |i\rangle + \mathcal{O}(\Gamma^{-2}) \tag{4.86}$$

where we introduced the density operator $\rho_i = n_{\uparrow i} + n_{\downarrow i}$.

Calculating this correlation function within the t-J model is, of course, difficult. Compared to the undoped compounds, we expect spectral weight to leak to higher energies because of the new, higher energy scale introduced by hopping. Also, the magnon peak is expected to significantly broaden and lose weight (it loses coherence), analogous to the evolution of the two-magnon Raman spectra with doping [120]. To see how much spectral weight is in the spin flip cross section, we integrate it over energy loss and transferred momentum, and get

$$\begin{aligned}\frac{1}{N}\sum_{\mathbf{q}} \int d\omega \frac{d^2\sigma}{d\Omega d\omega} &= \frac{|T_{\mathrm{sf}}(\boldsymbol{\epsilon}', \boldsymbol{\epsilon})|^2}{\Gamma^2} \langle i| \sum_{\mathbf{q},i,j} \frac{e^{-i\mathbf{q}\cdot\mathbf{R}_j}}{N} \rho_j \sigma_j^z e^{i\mathbf{q}\cdot\mathbf{R}_i} \sigma_i^z \rho_i\, |i\rangle \\ &= \frac{|T_{\mathrm{sf}}(\boldsymbol{\epsilon}', \boldsymbol{\epsilon})|^2}{\Gamma^2} \langle i| \sum_i \rho_i (\sigma_i^z)^2 \rho_i\, |i\rangle \\ &= \frac{|T_{\mathrm{sf}}(\boldsymbol{\epsilon}', \boldsymbol{\epsilon})|^2}{\Gamma^2} \langle i| \sum_i \rho_i\, |i\rangle = \frac{|T_{\mathrm{sf}}(\boldsymbol{\epsilon}', \boldsymbol{\epsilon})|^2}{\Gamma^2} N(1-x).\end{aligned} \tag{4.87}$$

We conclude that the total spin flip intensity scales linearly with doping. This result is valid for all doping x.

Next to spin flip scattering, there is also the elastic scattering channel. Note that we mean with ‘elastic scattering channel’ that $\nu = \nu'$ in Eq. (2.42), and emphatically not that $\omega = 0$. In an ideal crystal, all intensity is pushed to the Bragg conditions $\mathbf{G}$. Upon doping, the elastic scattering channel at the L_3 edge in the fast collision approximation becomes

$$\mathcal{F}_{fi}^{\mathrm{el}} = \frac{T_{\mathrm{el}}(\boldsymbol{\epsilon}', \boldsymbol{\epsilon})}{i\Gamma} \langle f| \sum_i e^{i\mathbf{q}\cdot\mathbf{R}_i} \rho_i\, |i\rangle + \mathcal{O}(\Gamma^{-2}), \tag{4.88}$$

with $T_{\mathrm{el}}(\boldsymbol{\epsilon}', \boldsymbol{\epsilon})$ the atomic scattering factor for the elastic channel. The elastic channel thus gives rise to charge scattering.

It might appear strange that one arrives at charge scattering through the elastic scattering channel. In the case of non-interacting ions, there is no inelastic scattering: the above expression gives spectral weight at $\omega = 0$ only. The elastic peak is expected to gain intensity away from Bragg conditions upon doping as the holes constitute impurities in the crystal from the photon’s perspective. When the ions interact, the holes are allowed to move, and hole and spin sites mix.

As with the magnetic cross section, it is complicated to evaluate the exact correlation function for charge scattering in the t-J model. The total spectral weight of the elastic channel for the hole-doped cuprates is

$$\begin{aligned}\frac{1}{N}\sum_{\mathbf{q}}\int d\omega\frac{d^2\sigma}{d\Omega d\omega} &= \frac{\left|T_{\mathrm{el}}(\boldsymbol{\epsilon}',\boldsymbol{\epsilon})\right|^2}{\Gamma^2 N}\sum_{\mathbf{q}}\langle i|\,\rho_{-\mathbf{q}}\rho_{\mathbf{q}}\,|i\rangle+\mathcal{O}(\Gamma^{-3})\\ &= \frac{\left|T_{\mathrm{el}}(\boldsymbol{\epsilon}',\boldsymbol{\epsilon})\right|^2}{\Gamma^2}\langle i|\sum_{i,j}\delta_{i,j}\rho_i\rho_j\,|i\rangle = \frac{\left|T_{\mathrm{el}}(\boldsymbol{\epsilon}',\boldsymbol{\epsilon})\right|^2}{\Gamma^2}N(1-x). \qquad (4.89)\end{aligned}$$

The elastic channel is reduced as $1-x$, as expected for a decreasing number of scattering centers. It can be easily checked that the intensity of the Bragg peak reduces as $1-2x$, and it follows that the elastic scattering channel gives rise to inelastic charge scattering with intensity proportional to x.

The evaluation of the charge scattering operator is a difficult task, and the center of much effort. In the special case of very low doping, the holes in hole-doped cuprates reside around $(\pi/2,\pi/2)$, according to ARPES data. In RIXS, these holes are scattered to approximately $(\pi/2,\pi/2)+\mathbf{q}$. There are xN holes around $(\pi/2,\pi/2)$ in the initial state, so we approximate the charge intensity as

$$\left.\frac{d^2\sigma}{d\Omega d\omega}\right|_{\mathrm{charge}} \approx \frac{T_{\mathrm{el}}(\boldsymbol{\epsilon}',\boldsymbol{\epsilon})^2 xN}{\Gamma^2}\delta(\omega-\epsilon_{\mathbf{q}+(\pi/2,\pi/2)}) \qquad (4.90)$$

where $\epsilon_{\mathbf{q}}$ is the 'energy' of a hole with momentum $\mathbf{q}$. This is of course a sloppy approach: the holes are heavily dressed by, for instance, phonons, see Shen *et al.* [121]. Therefore, the hole dispersion relation is fuzzy and not a delta function[3]. The dispersion of quasiparticles in several strongly underdoped compounds is given in, for instance, Ref. [122–125]. For higher dopings (up to the overdoped, Fermi liquid phase of the t-J model), the dynamic charge and spin correlation functions are calculated in, *e.g.*, Refs. [126–129].

Although the exact magnetic and charge spectra are hard to predict, we have shown above that charge scattering scales linearly with doping, and is proportional to the elastic atomic scattering factor. Similarly, the magnetic RIXS intensity decreases linearly with doping, and stays proportional to $T_{\mathrm{sf}}(\boldsymbol{\epsilon}',\boldsymbol{\epsilon})$. Since the dynamic spin and charge correlation functions are symmetric under inversion of space, any asymmetry between spectra at $+\mathbf{q}$ and $-\mathbf{q}$ is generated by the atomic scattering factors. In particular, for $\mathbf{q}$ along the $(\pi,0)$ direction, T_{el} is also symmetric under inversion [19], and any asymmetry seen in such spectra arises through to the magnetic scattering channel. Further, in the special case of $\mathbf{q}=(0,0)$, it can be seen from Eqs. (4.86) and (4.88) that the inelastic magnetic and charge signals are zero. In the case of magnetic scattering, the scattering operator is proportional to the total spin along the z axis, which is a constant. In the case of charge scattering, the scattering operator counts the total charge, which also is a constant. In the limit of very low doping, we found that the RIXS charge cross section traces the hole dispersion.

---

[3] Note that we do not remove electrons as in ARPES. The number of holes is conserved in RIXS, and in the charge-neutral final state the coupling to phonons might be reduced compared to ARPES.

4.6.3 Experimental data

Although it is difficult to make a detailed comparison between theory and experiment because of the complicated correlation functions in the theory, recent RIXS experiments on 8.5% doped $La_{2-x}Sr_xCuO_4$ [11] can put the theory to some tests.

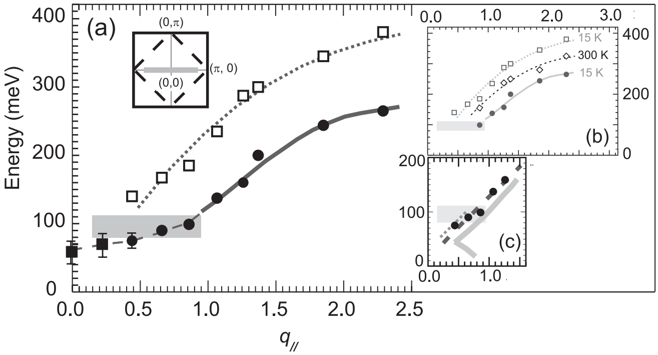

Figure 4.16: RIXS data on 8.5% doped $La_{2-x}Sr_xCuO_4$ at $T = 15$ K, *i.e.*, in the superconducting state, with transferred momentum along the $(\pi, 0)$ direction, show (a) two dispersing branches that (b) merge into a single branch at room temperature. At low energy loss, the two features are hard to resolve because of phonons. In Fig. (a), the dotted line is the magnon dispersion from the undoped compound, multiplied by 1.09. The solid line is a guide to the eye. (c) Comparison to inelastic neutron scattering data taken around $\mathbf{q} = (\pi, \pi)$ (dotted line: $x = 0.05$, dashed line: $x = 0.085$, thick line: $x = 0.16$). Note that the RIXS data is taken around the center of the Brillouin zone, and that these regions are not necessarily equivalent in a doped compound where the long range magnetic order is absent. Figure from Braicovich *et al.* [11].

First, our theory predicts that both the elastic and magnetic scattering channels give no spectral weight at the Γ point. This agrees quite well with the RIXS data of Ref. [11], which mainly shows an elastic line at $\mathbf{q} = \mathbf{0}$.

Second, at low doping, the magnetic spectral weight is reduced by only $x = 8.5\%$ relative to the undoped compound. Since the RIXS spectra of the undoped compound are magnetic in nature (there is no charge contribution there), we expect the spectra of the doped compounds to be dominated by magnetic scattering as well. Indeed, the low energy spectra from Ref. [11] are very different for $+\mathbf{q}$ and $-\mathbf{q}$, implying that the spectra are dominated by magnetic scattering, as explained above.

In the data, two dispersing branches are seen, whose dispersions are shown in Fig. 4.16. (Both are ascribed to the magnetic channel.) The lower branch is also observed with neutron scattering, the higher one not. That could be due to experimental limitations of neutron scattering. The higher branch coincides with the magnon dispersion if the latter is rescaled by a factor 1.09. However, in Raman scattering data, the two-magnon excitation is seen to go down in energy upon doping: in Fig. 9(b) of Ref. [120], the two-magnon signal moves from 3300 cm^{-1} in $\mathrm{La_2CuO_4}$ to 2700 cm^{-1} in the 8% doped compound.

4.7 Oxygen K edge

The oxygen K edge (1s → 2p) is a peculiar edge since it is in principle direct RIXS (the core electron is excited into the 2p valence bands), but the core level spin-orbit coupling is absent. Single spin flips are therefore forbidden at the O K edge, and low energy excitations can only occur via the indirect channel. Two-magnon excitations are allowed and give a strong, non-dispersive signal at high energy loss, even for small $\mathbf{q}$, as will be shown in Sec. 4.7.2.

The O K edge is a difficult edge for experiments, since in the cuprates the O ions have a filled 2p subshell. Only through hybridization with the Cu hole is it possible to excite a core electron. Usually, the Cu hole is in the $3\mathrm{d}_{x^2-y^2}$ orbital and this orbital hybridizes with the O 2p orbitals that are directed towards the lobes of the x^2-y^2 wave function: $2\mathrm{p}_x$ along the x direction and $2\mathrm{p}_y$ along the y direction. The wave function of the valence hole is therefore

$$|\psi\rangle = \cos\theta \left|3d^9\right\rangle + \sin\theta \left|3d^{10}\underline{\mathrm{L}}\right\rangle \tag{4.91}$$

where both states have $x^2 - y^2$ symmetry and θ is a small number parametrizing the hybridization. $\underline{\mathrm{L}}$ means that the hole is on the oxygen ions. The dipole matrix element $\langle\psi| \mathcal{D} |O\ 1s\rangle$ is small: it is controlled by $\sin\theta$ and the smallness of the overlap of O 1s with Cu 3d orbitals. The result is that O K edge experiments suffer from low intensity. Most of the radiative decay processes will be via the fluorescence channels, where the hole in the final state is on an O ion.

Notwithstanding this difficulty, RIXS experiments at the O K edge of $\mathrm{La_2CuO_4}$ have been successfully performed [70]. The low energy region shows spectral weight ranging from 0 to 1 eV, peaking at 0.5 eV and dispersing very little.

In this section, we discuss the magnetic excitations to be expected at the O K edge. The polarization dependence is strikingly different from the Cu edges, and will be explained in Sec. 4.7.1. Then, the expected magnetic RIXS signal will be presented in detail in Sec. 4.7.2 and compared to the present data [70]. Finally, we will consider other possible contributions to the low energy RIXS spectrum in Sec. 4.7.3.

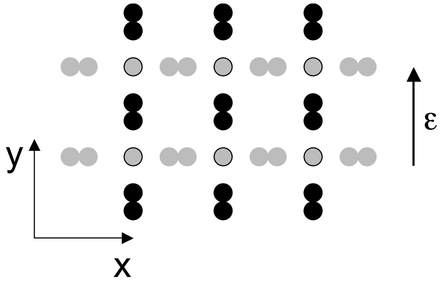

Figure 4.17: Polarization dependence of the absorption of X-rays at the O K edge. The oxygen ions with the black 2p orbitals can be excited with RIXS when the polarization is directed along the y axis, while the gray oxygen ions are then inactive. The gray circles with black borders represent the Cu ions.

4.7.1 Polarization dependence

It is assumed that only the $2p_{x,y}$ orbitals of the in-plane O ions hybridize with the Cu levels. The 2p orbitals of the out-of-plane O ions do not hybridize because of the x^2-y^2 symmetry of the hole wave function. Therefore, the out-of-plane O ions are assumed not to be active in O K edge RIXS. In that case, one finds a remarkable polarization dependence: when the polarization vector of the incoming photon is aligned along the x axis, only the O ions that connect Cu ions along the x direction are excited. When the polarization vector is aligned along the y direction, only those O ions are excited that connect Cu ions along the y direction, see Fig. 4.17. This can be easily seen by writing the dipole matrix elements as

$$\left\langle O\ 2p_{x_j}\right| \mathcal{D} \left|O\ 1s\right\rangle \propto \int d\mathbf{r}\ x_j x_i \epsilon_i \propto \epsilon_j. \tag{4.92}$$

The full dipole operator is

$$\begin{aligned}\mathcal{D} &\propto \left\langle 3d^{10}\right| \mathbf{D} \left|\psi\right\rangle \cdot \boldsymbol{\epsilon} \propto \sum_i e^{i\mathbf{k}\cdot\mathbf{R}_i} \sin\theta \left\langle 2p_x\right| x \left|1s\right\rangle \\ &\quad \times \left[\epsilon_x (e^{-i\mathbf{k}\cdot\hat{\mathbf{x}}} s_{i-\hat{\mathbf{x}}} - e^{i\mathbf{k}\cdot\hat{\mathbf{x}}} s_{i+\hat{\mathbf{x}}}) + \epsilon_y (e^{i\mathbf{k}\cdot\hat{\mathbf{y}}} s_{i+\hat{\mathbf{y}}} - e^{-i\mathbf{k}\cdot\hat{\mathbf{y}}} s_{i-\hat{\mathbf{y}}})\right], \end{aligned} \tag{4.93}$$

where $3d^{10}$ represents the Cu $3d^{10}$, O $2p^6$ intermediate state. The minus signs in front of the 1s core electron annihilation operators s_i come from the way the 2p orbitals are hybridized with the Cu x^2-y^2 orbital. The creation operators for the 2p electrons are suppressed. The vectors $\hat{\mathbf{x}}, \hat{\mathbf{y}}$ point from the central Cu ion at position $\mathbf{R}_i$ to the neighboring in-plane oxygen ions. The dipole matrix element of the O 1s core orbital with the Cu $3d_{x^2-y^2}$ orbital is neglected here, but give approximately the same polarization dependence.

The above polarization dependence introduces an anisotropy in the scattering amplitude. Magnetic scattering is therefore expected to be different from the Cu edges, where the modification of the superexchange bonds is isotropic. Now, only bonds along either the x or the y direction are modified. If the polarization vector is directed along the [110] direction, all oxygens are active, but because of the photon phase factors, we do not expect to recover the Cu results.

4.7.2 Two-magnon contribution to the RIXS spectrum

Since the direct RIXS channel is absent in oxygen, we calculate the indirect magnetic RIXS spectrum to first order in the UCL expansion. The result is a two-magnon spectrum, like at the Cu K edge, but with different RIXS matrix elements because of the different excitation processes. As can be seen in Fig. 4.5(b), most of the two-magnon states have energies around $4J$ (neglecting renormalizations due to magnon-magnon interactions). The large dispersion of the two-magnon spectrum at the Cu edges is therefore a peculiar matrix element effect. Since at the O K edge, the matrix elements are different, one would in general not expect that this peculiar effect survives. The O K edge RIXS signal would likely be more like the two-magnon DOS: peaked at high energy loss for all transferred momenta.

Since the oxygen orbitals play an important role at the O K edge, we analyze the RIXS process within the three-band Hubbard model. The photo-excited electron creates a 3d^{10} configuration on a neighboring copper ion. With two Cu-O hoppings (with amplitude t_{pd}), the 3d^{10} can be transferred to the other Cu ion neighboring the core hole site. To second order in t_{pd}, the matrix element for this process to happen is $t_{pd}^2/(\Delta + U_c)$ where Δ is the energy to transfer an electron from O to Cu and where U_c is the screening potential of the core hole. After the X-ray emission at the end of the RIXS process, the two Cu spins can be left behind interchanged. The Cu L edge superexchange blocking mechanism can be neglected here, as it is of order t_{pd}^4. To leading order, the low energy effective spin Hamiltonian is

$$H_{\text{int}} = H_0 + (J_{\text{eff}} - J) \sum_i s_{i+\delta} s^\dagger_{i+\delta} \mathbf{S}_i \cdot \mathbf{S}_{i+2\delta} \tag{4.94}$$

with $J_{\text{eff}} = \frac{2t_{pd}^2}{\Delta + U_c}$ and where δ points from a copper to an oxygen ion. The original Heisenberg Hamiltonian H_0 is modified at the core hole site. Note that the Heisenberg form of the bond is preserved.

The effective scattering operator to first order in the UCL expansion is

$$\hat{O}_{\mathbf{q}} \propto \sum_i e^{i\mathbf{q}\cdot\mathbf{R}_i} \left[\sum_{\boldsymbol{\delta}=\pm\hat{\mathbf{x}}} \epsilon'^*_x \epsilon_x e^{i\mathbf{q}\cdot\boldsymbol{\delta}} \mathbf{S}_i \cdot \mathbf{S}_{i+2\delta} + \sum_{\boldsymbol{\delta}=\pm\hat{\mathbf{y}}} \epsilon'^*_y \epsilon_y e^{i\mathbf{q}\cdot\boldsymbol{\delta}} \mathbf{S}_i \cdot \mathbf{S}_{i+2\delta} \right]. \tag{4.95}$$

In general, one would expect spectral weight at $\mathbf{q} = \mathbf{0}$ since the scattering operator does not reduce to the Hamiltonian in this case. Only when $\epsilon'^*_x \epsilon_x = \epsilon'^*_y \epsilon_y$ (and $\mathbf{q} = \mathbf{0}$) is the RIXS intensity zero.

At this point, it is instructive to make a comparison with Raman scattering. In Sec. 4.4 we established that at the Cu edges one can probe certain two-magnon modes with a definite symmetry by tuning the transferred momentum, mimicking the polarization dependence of Raman scattering. At the O K edge, however, one can also use the polarization, in addition to $\mathbf{q}$, as is clear from Eq. (4.95).

The isotropic Raman mode (A_{1g}) is obtained with RIXS at $\mathbf{q} = \mathbf{0}$ when $\epsilon_x'^*\epsilon_x = \epsilon_y'^*\epsilon_y$, as can be seen directly from Eq. (4.95) because the bonds are modified in an isotropic way. Indeed, the intensity should then vanish in RIXS, as noted above. The Raman B_{1g} mode (x^2-y^2 symmetry) can be probed by $\mathbf{q} = \mathbf{0}$ RIXS when $\epsilon_x'^*\epsilon_x = -\epsilon_y'^*\epsilon_y$. This is the case when we transfer two units of angular momentum to the sample, *e.g.*, when $\boldsymbol{\epsilon} = (1, i, 0)$ and $\boldsymbol{\epsilon}' = (1, -i, 0)$. The Raman scattering operator for the B_{2g} mode (xy symmetry) vanishes for a nearest-neighbor Heisenberg antiferromagnet, which also happens in RIXS when one chooses, for instance, $\boldsymbol{\epsilon} = (1, 0, 0)$ and $\boldsymbol{\epsilon}' = (0, 1, 0)$ at $\mathbf{q} = \mathbf{0}$.

In terms of two-magnon creation processes, the general form of the RIXS scattering operator is

$$\hat{O}_{\mathbf{q}} \propto \frac{1}{N} \sum_{\mathbf{k}} \left[\epsilon_x'^*\epsilon_x A_x + \epsilon_y'^*\epsilon_y A_y\right] \alpha^\dagger_{\mathbf{k}} \alpha^\dagger_{-\mathbf{k}+\mathbf{q}} \tag{4.96}$$

where

$$\begin{aligned} A_{x,y} = & -\cos\left(\frac{q_{x,y}}{2}\right)\left(u_{\mathbf{k}}v_{\mathbf{k}-\mathbf{q}} + u_{\mathbf{k}-\mathbf{q}}v_{\mathbf{k}}\right) + \cos\left(k_{x,y} - \frac{q_{x,y}}{2}\right) v_{\mathbf{k}}v_{\mathbf{k}-\mathbf{q}} \\ & + \frac{1}{2}\left[\cos\left(k_{x,y} - \frac{3q_{x,y}}{2}\right) + \cos\left(k_{x,y} + \frac{q_{x,y}}{2}\right)\right] u_{\mathbf{k}}u_{\mathbf{k}-\mathbf{q}}. \end{aligned} \tag{4.97}$$

One can choose to excite only half of the in-plane oxygen ions by choosing an appropriate polarization, as explained in Sec. 4.7.1. Typically, this happens for $\mathbf{q}$ directed along the [100] direction and incident π or σ polarization. For a scattering angle of 2θ, the two-magnon intensity for $\mathbf{q}$ along the [100] direction is

$$I^{(\pi)} \propto \frac{[\cos\varphi \cos(2\theta + \varphi)]^2}{N} \sum_{\mathbf{k}} A_x^2 \delta(\hbar\omega - \omega_{\mathbf{k}} - \omega_{-\mathbf{k}+\mathbf{q}}) \tag{4.98}$$

$$I^{(\sigma)} \propto \frac{1}{N} \sum_{\mathbf{k}} A_y^2 \delta(\hbar\omega - \omega_{\mathbf{k}} - \omega_{-\mathbf{k}+\mathbf{q}}) \tag{4.99}$$

for π and σ polarization respectively. φ is the angle between the incident X-rays and the normal to the CuO$_2$ planes.

The results for $2\theta = 90°$ are shown in Figs. 4.18 and 4.19. There is very little dispersion for either polarization. The intensity fluctuates, however, as one increases $\mathbf{q}$ or changes the polarization. The spectra are symmetric with respect to $+\mathbf{q} \leftrightarrow -\mathbf{q}$. Note that magnon-magnon interactions are not taken into account in these figures and all the following ones in this section. Magnon-magnon interactions would probably lower the energy by $\sim 25\%$, as in two-magnon Raman scattering [130]. The vanishing of the π polarization spectra at certain $\mathbf{q}$ is due to the vanishing of the absorption amplitudes.

Note that the angle φ is related to $\mathbf{q}$: they cannot be chosen independently. The O K edge is at an energy of around 531.2 eV [131] (and corresponding momentum of 0.269 $\hbar$Å^{-1}) which means that in a 90° scattering geometry one can

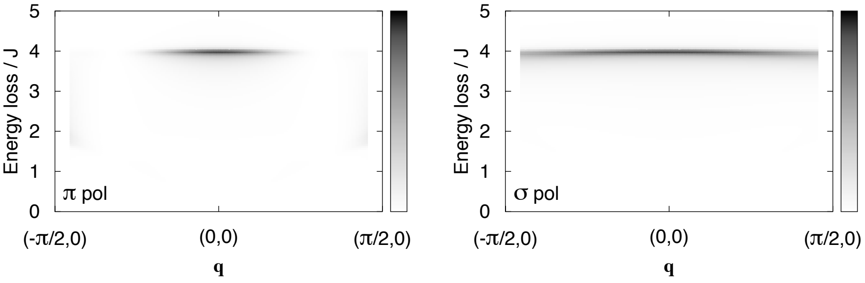

(a) (b)

Figure 4.18: Leading order two-magnon contribution to the O K edge RIXS spectra in 90° scattering geometry for **q** along the [100] direction with (a) incident π polarization and (b) incident σ polarization. The outgoing polarization is averaged over. The plots are restricted to roughly half the Brillouin zone, because this is the theoretical limit to the momentum transfer at the O K edge. The gray scales cannot be compared; for a comparison of spectral weight see Fig. 4.19(a).

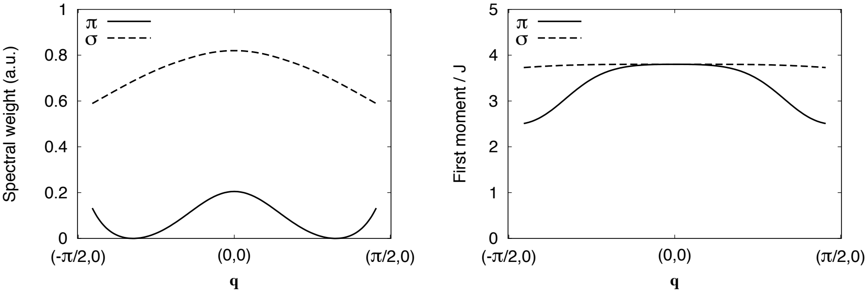

(a) (b)

Figure 4.19: (a) Comparison of the spectral weight of the two-magnon spectra in π and σ polarization along the [100] direction, obtained by integrating the spectra shown in Fig. 4.18 over energy loss. The scattering angle $2\theta = 90°$. (b) The first moment of the same spectra.

transfer a momentum of 0.380 $\hbar\text{Å}^{-1}$. The $(\pi, 0)$ point of the Brillouin zone is at 0.827 $\hbar\text{Å}^{-1}$ in La_2CuO_4, so one can in theory access momenta up to about 46% of the Brillouin zone boundary. In practice, when the crystal is cut parallel to the CuO_2 planes, it is impossible to reach more than 32% in a 90° geometry because the X-rays cannot go through the sample and its holder. (Cutting the sample in a different way circumvents this constraint [132].) This implies that the spectra of Figs. 4.18 and 4.19 cannot be probed beyond $q_x \approx \pm 0.32\pi$. These cases correspond to grazing and normal incidence, where the dipole transitions are forbidden in π polarization, explaining the zeroes in the spectral weight. In the 90° scattering geometry, the in-plane component of $\mathbf{q}$ is $q_\| = 0.380\ \hbar\text{Å}^{-1}\sin(\pi/4 - \varphi)$. Grazing incidence means $q_x < 0$, and normal incidence corresponds to $q_x > 0$.

If the polarization is directed along the diagonal of the CuO_2 plaquettes, *i.e.*, along the [110] or [−110] direction, all oxygen ions are excited. When $\boldsymbol{\epsilon}' = \boldsymbol{\epsilon}$, the cross section is proportional to $[A_x + A_y]^2$, which is equal to the effective scattering operator of the Cu K edge when $\mathbf{q}$ is along the [110] direction. Thus, for such a geometry, the scattering intensity will vanish at $\mathbf{q} = \mathbf{0}$. However, it is currently not experimentally feasible to measure the outgoing photon's polarization. The polarization-averaged cross sections for $\mathbf{q}$ along the [110] direction are

$$\begin{aligned} I^{(\pi)} \propto & \sum_{\mathbf{k}} \left(\frac{[\cos\varphi \cos(2\theta + \varphi)]^2}{4N} [A_x + A_y]^2 + \frac{\cos^2\varphi}{4N} [A_x - A_y]^2 \right) \\ & \times \delta(\hbar\omega - \omega_{\mathbf{k}} - \omega_{-\mathbf{k}+\mathbf{q}}), \qquad (4.100) \\ I^{(\sigma)} \propto & \sum_{\mathbf{k}} \left(\frac{1}{4N} [A_x + A_y]^2 + \frac{\cos^2(2\theta + \varphi)}{4N} [A_x - A_y]^2 \right) \\ & \times \delta(\hbar\omega - \omega_{\mathbf{k}} - \omega_{-\mathbf{k}+\mathbf{q}}), \qquad (4.101) \end{aligned}$$

The spectra for transferred momentum along the [110] direction in $2\theta = 90°$ scattering geometry with π and σ polarization are shown in Fig. 4.20, and the corresponding spectral weights and first moments are displayed in Fig. 4.21. As mentioned above, the spectra of Figs. 4.18 and 4.20 have non-zero intensity at $\mathbf{q} = \mathbf{0}$, which is very different from the Cu edges. Similar to the spectra of Fig. 4.18, there is very little dispersion. Only the intensity changes as one increases $\mathbf{q}$ or changes the polarization. A difference with the spectra along the [100] direction is the symmetry of $+\mathbf{q} \leftrightarrow -\mathbf{q}$: this symmetry is not present in the spectra along the [110] direction. At the Γ point, a discontinuity in the spectral weight arises when the scattering plane is rotated by 45°. This becomes clear when comparing Figs. 4.19(a) and 4.21(a).

The dip in the first moment of the σ spectrum around $\mathbf{q} = (\pi/4, \pi/4)$ in Fig. 4.21(b) is due to the $[A_x + A_y]^2$ term, which is proportional to the Cu K edge bimagnon RIXS spectrum. It is very small (but finite) at the low $\mathbf{q}$ values accessible at the O K edge. Around $\mathbf{q} = (\pi/4, \pi/4)$, the $[A_x - A_y]^2$ term is quenched and the dispersing Cu K edge bimagnon spectrum becomes visible, shifting the first moment down. For π polarization, the spectral weight does

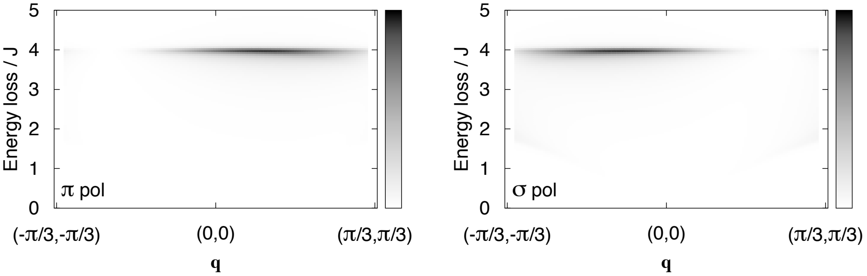

(a) (b)

Figure 4.20: The two-magnon RIXS spectra at the O K edge for 90° scattering geometry and **q** along the [110] direction, with (a) incident π polarization and (b) incident σ polarization. The outgoing polarization is averaged over. The plots are again restricted to the theoretical limit to the transferred momentum at the O K edge. In practice, the experimental geometry limits this region even further to $|q_x| < 0.23\pi$ when the crystal is cut parallel to the CuO_2 planes.

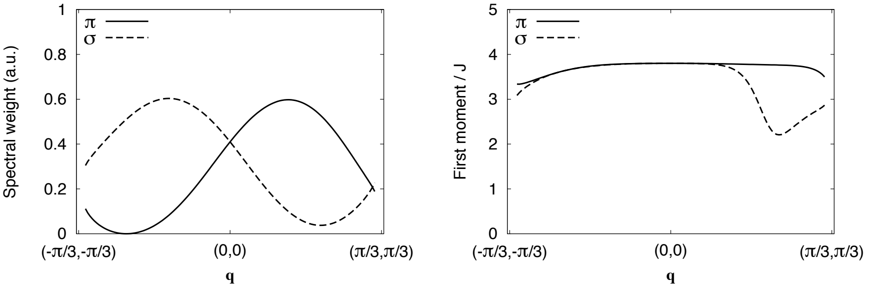

(a) (b)

Figure 4.21: (a) Comparison of the spectral weight of the two-magnon spectra for **q** along the [110] direction in 90° scattering geometry, obtained by integrating the spectra shown in Fig. 4.20 over energy loss. The scale is the same as in Fig. 4.19(a). (b) The first moment of the spectra.

completely vanish at $\phi = \pi/2$ because in that case, the absorption amplitude is zero.

The RIXS experiments at the O K edge of La_2CuO_4 reported in Ref. [70] agree on a qualitative level with our calculations, although Bisogni *et al.* use a 110° scattering angle, while the calculations presented in this section are evaluated for a 90° geometry. In the low energy region, Bisogni *et al.* observe a broad feature ranging from 0 to 1 eV, which peaks at 500 meV and disperses downward by ~ 50 meV when going from the center of the Brillouin zone to $\mathbf{q} = (0.3\pi, 0.3\pi)$ or $(0.3\pi, 0)$. This small dispersion is also seen in Fig. 4.19(b). From neutron scattering, it is found that $J \approx 120$ meV [83], and with this value we reproduce the 500 meV peak and the downward dispersion of $0.7J \approx 84$ meV in π polarization going along the [100] direction. Magnon-magnon interactions will likely make the correspondence between theory and experiment less good, as it probably decreases the theoretical peak's energy.

4.7.3 Other contributions to the low energy RIXS spectrum

In the experiments, the low energy spectral weight extends up to 1 eV. Any spectral weight above ~ 0.5 eV cannot be due to two-magnon excitations, since the two-magnon DOS is zero there. This suggests that higher order magnon excitations are also important, like four-magnon excitations.

From other work, both theoretical [82] and experimental [83], it is clear that ring exchange is quite large in the cuprates: the large numerical prefactor compensates for the smallness of the expansion parameter. At the Cu edges, ring exchange is modified or blocked by the core hole. Therefore, the effective scattering operator has a term of order t_{pd}^8, giving (amongst other things) four-magnon final states.

In contrast, at the O K edge, one can flip all four spins on a Néel ordered square of neighboring copper ions with only 6 hops (in the three-band Hubbard model), so the four-magnon contribution will contribute to the scattering amplitude proportional to something like t_{pd}^6/Δ^5, which is in principle small, but again could have a huge prefactor because of the myriad of different ways in which the four spins can be flipped. Note that, to order t_{pd}^6, one only gets four-spin terms in the effective scattering operator and not in the Hamiltonian (without core hole), because the four-spin contribution to the Hamiltonian is of order t_{pd}^8. Therefore, one obtains a four-spin contribution at the O K edge to order t_{pd}^6, but not at the Cu edges. This might explain the high energy tail of the 500 meV feature.

The (non-interacting) four-magnon DOS shows a broad peak between $4J$ and $8J$ at $\mathbf{q} = \mathbf{0}$ [130]. The dispersion is minimal: the four-magnon DOS curves from all over the BZ virtually coincide. In principle it could extend from 0 to $8J$ since the single magnon energy ranges from 0 to $2J$, but as is evident, the low energy region is virtually devoid of states. Whatever the exact form of the effective scattering operator, it is clear that the four-magnon spectrum will be 'gapped' by approximately $4J$. This value could be smaller, however: for two-magnon RIXS at the Cu edges, the low energy part of the DOS is more pronounced by the matrix elements (see Fig. 4.5). The same effect could play a role in four-magnon RIXS too.

An entirely different contribution to the O K edge might come from phonons. At the O K edge, the phonon contribution is expected to be larger than at the Cu edges because of the nature of the intermediate states. For the Cu edges, the photo-excited electron stays relatively close to the core hole: they remain on the same ion. At the O K edge, however, the core hole is on the O ion while the photo-excited electron fills the Cu 3d subshell. Because the centers of mass of the two charges are separated, there will be a relatively large attractive force between the O and the Cu ions. A strong coupling to phonons is thus expected at the O K edge.

Acknowledgements. We would like to thank L. Braicovich, G. Ghiringhelli, V. Bisogni and M. Moretti Sala for valuable discussions, and the ESRF, Grenoble, where part of this work was done, for its hospitality.

4.8 Two-magnon screening of holes in the t-J model probed by angle-resolved photoemission

Because two-magnon excitations show up so prominently in RIXS, one could ask the question if two-magnon excitations are also important in other spectroscopic techniques, or, on a more fundamental level, in the t-J model. In this section, we investigate the two-magnon screening effect on angle-resolved photoemission spectroscopy (ARPES), and calculate the contribution of two-magnon excitations to the self-energy of a hole in an antiferromagnetic background.

4.8.1 Introduction

It has been put forward that the t-J model, perhaps supplemented with phonons, captures the physics essential to high temperature superconductivity in cuprates. Yet understanding even the basic properties of this model is a hard task. Even the regime of very low doping of an antiferromagnet (AFM) is complicated because of the interplay between the hopping of holes and the antiferromagnetic background. The situation becomes tractable in the extreme limit of a single hole in a 2D AFM background, which has become a classic theory problem [123–125,133–141]. Experimentally, this regime can be probed with ARPES [121,122,142–150] and, as we will expand upon below, RIXS.

In the t-J model, the hole interacts with the spins: a moving hole rearranges the spin background, causing spin flips that correspond to single magnon excitations of the AFM. This effect is accounted for in the canonical theory approaches such as the diagrammatic self-consistent Born-approximation [123–125,133–141]. There is another channel for spin-hole scattering that is not taken into account in these approaches. A hole in an AFM reduces the number of magnetic neighbors of the surrounding spins, and these spins react to the presence of a hole. The spins thus dynamically screen any moving or static hole in the system, which is an effect that in lowest order is described by two-magnon excitations of the AFM. Precisely these two-magnon modes and their dispersions have recently been measured in the cuprates by momentum resolved RIXS at the Cu K edge [14, 52, 53] and possibly at the L edge too [70]. At the Cu M edge, zero momentum two-magnon excitations have been reported [15]. Describing the motion of holes in the t-J model in terms of screening by magnons only makes sense in the limit of very low doping, as magnons are not well-defined away from this limit.

The question arises how the coupling to these magnetic modes affects other physical properties. In this context we focus here on the quasiparticle (QP) excitation spectrum of the t-J model – experimentally accessible by ARPES. To this end we study theoretically the effect of the two-magnon modes on the magnetic dressing of mobile holes in the t-J model.

ARPES. In the limit of large S the two-magnon coupling mechanism can be neglected in the t-J model, which can be seen most easily by casting the problem into a form where the hole carries spin $S - 1/2$ [124]. However, it is a priori not obvious that this argument can be extrapolated to the $S = 1/2$ limit of the high-T_c cuprates, and two-magnon screening can in principle become important there. In particular one could speculate that the two-magnon coupling might be relevant in the context of a long standing challenge for theory posed by ARPES data: the width of the Zhang-Rice Singlet (ZRS) peak is broader than theory predicts. The peak width is approximately 0.3 eV at $\mathbf{k} = (\pi/2, \pi/2)$ for undoped cuprates at room temperature [142,143], increasing with temperature by 1.0 ± 0.3 meV/K [146, 150].

This problem has attracted considerable theoretical effort [140, 151–153]. Polaron formation appears to be the best candidate solution available [121, 154, 155]: due to the string of flipped spins left behind by a hopping hole, it is slowed down and therefore becomes more susceptible to electron-phonon interaction. The broad peak in this picture is actually the multi-phonon satellite of the quasiparticle.

In addition to contributing to slowing down the hole, the two-magnon screening of a hole in principle provides an additional mechanism to broaden the ARPES features. To settle these issues we consider the hole – two-magnon vertex quantitatively and in detail. We will first establish that the coupling of holes to two-magnon modes is independent of the hole's momentum. Subsequently we derive the resulting self-energy of the hole, and calculate the effect of two-magnon screening on the ARPES spectra. In general, we find that the effect of this interaction is small and conclude that the two-magnon screening redistributes less than 1% of the QP spectral weight.

4.8.2 Two-magnon – charge interaction

Magnetic scattering vertices. To treat the AFM t-J model on a bipartite, inversion-symmetric lattice in the (very) low doping limit, we start from a Heisenberg model and introduce Holstein-Primakoff bosons for the magnetic degrees of freedom, see Eq. (4.11) in Sec. 4.2. When holes are introduced, they couple to the spins in two ways. First, when a hole hops from one site to another, it rearranges the spins. In an AFM background, a hopping hole creates or annihilates single magnons [123, 124, 135]. This leads to an effective reduction in the bandwidth from order t to order J because, loosely speaking, the hole has to wait for the relaxation of the string of energetically unfavorable spins it left behind before the hole can continue its motion [125]. In contrast, the coupling of holes to two-magnons is unrelated to the movements of a hole. Because the spins next to a hole have one less magnetic neighbor, they evolve in a different way than in an undoped AFM. In lowest order, they screen the hole with two-magnon excitations as in the screening process the z component of the total spin is conserved.

To quantify the two-magnon screening, it is advantageous to introduce a virtual spin at every hole site. If all magnetic bonds that these virtual spins have with the physical spins are subsequently subtracted from the Hamiltonian, it is still possible to use Eq. (4.11) as a starting point and simply add the two-magnon coupling term

$$H_2 = -J \sum_{i,\delta} h_i^\dagger h_i \mathbf{S}_i \cdot \mathbf{S}_{i+\delta}, \tag{4.102}$$

where $h_i^{(\dagger)}$ is the hole annihilation (creation) operator, and δ points to nearest neighbors. We assume for simplicity that holes are surrounded only by spins, which is reasonable at low doping and certainly true for a single hole in undoped cuprates, as one encounters in the RIXS intermediate state. H_2 does not commute with H_0. Rewriting H_2 in terms of magnon operators at the linear spin wave level, one arrives at

$$\begin{aligned} H_2 = & \sum_{\mathbf{k},\mathbf{p},\mathbf{l}} g_{\mathbf{k},\mathbf{p}} h^\dagger_{\mathbf{l}-\mathbf{k}-\mathbf{p}} h_{\mathbf{l}} \, (\alpha^\dagger_{\mathbf{k}} \alpha^\dagger_{\mathbf{p}} + \alpha_{-\mathbf{k}} \alpha_{-\mathbf{p}}) + \sum_{\mathbf{k},\mathbf{p},\mathbf{l}} f_{\mathbf{k},\mathbf{p}} h^\dagger_{\mathbf{l}-\mathbf{k}-\mathbf{p}} h_{\mathbf{l}} \, \alpha^\dagger_{\mathbf{k}} \alpha_{-\mathbf{p}} \\ & + \sum_{\mathbf{l}} h^\dagger_{\mathbf{l}} h_{\mathbf{l}} \left[zJS^2 - \frac{1}{N} \sum_{\mathbf{k}} (\omega_{\mathbf{k}} - zJS) \right], \end{aligned} \tag{4.103}$$

with vertices

$$f_{\mathbf{k},\mathbf{p}} = -\frac{zJS}{N}\left[(1+\gamma_{\mathbf{k}+\mathbf{p}})(u_{\mathbf{k}}u_{\mathbf{p}}+v_{\mathbf{k}}v_{\mathbf{p}}) - (\gamma_{\mathbf{k}}+\gamma_{\mathbf{p}})(u_{\mathbf{k}}v_{\mathbf{p}}+v_{\mathbf{k}}u_{\mathbf{p}})\right], \quad (4.104)$$

$$g_{\mathbf{k},\mathbf{p}} = +\frac{zJS}{2N}\left[(1+\gamma_{\mathbf{k}+\mathbf{p}})(u_{\mathbf{k}}v_{\mathbf{p}}+v_{\mathbf{k}}u_{\mathbf{p}}) - (\gamma_{\mathbf{k}}+\gamma_{\mathbf{p}})(u_{\mathbf{k}}u_{\mathbf{p}}+v_{\mathbf{k}}v_{\mathbf{p}})\right]. \quad (4.105)$$

The vertices are independent of the hole momentum, and symmetric under the exchange of the magnon momenta $\mathbf{k}$ and $\mathbf{p}$. Furthermore, because of energy and momentum conservation for a hole producing two magnons, $g_{\mathbf{k},-\mathbf{k}} = 0$. The last term in Eq. (4.103) corresponds to the energy cost of breaking z magnetic bonds in the classical Néel state, plus quantum corrections from linear spin wave theory. It cancels the contribution of the unphysical spins to the constant in Eq. (4.11).

Although H_2 has no intrinsically small parameter, it will turn out that its effects are in all respects quite small. This comes about because of the Bogoliubov coefficients $u_{\mathbf{k}}$ and $v_{\mathbf{k}}$ that make $f_{\mathbf{k},\mathbf{p}}$ and $g_{\mathbf{k},\mathbf{p}}$ in general small. At the only momenta for which $u_{\mathbf{k}}$ and $v_{\mathbf{k}}$ diverge, *i.e.*, $\mathbf{k} = (0,0)$ and $\mathbf{k} = (\pi,\pi)$, the number of available magnon states is so small that processes involving the low energy magnons at these wave vectors do not contribute much to the hole's self-energy in the thermodynamic limit. This observation justifies a perturbation approach.

Hole self-energy and spectral function. In the following we calculate the loewst order contribution of two-magnon screening processes to the QP self-energy. The dispersion of the propagating hole is renormalized by single-magnon excitations, and the QP energy is $\sum_{\mathbf{k}} \epsilon_{\mathbf{k}} h^\dagger_{\mathbf{k}} h_{\mathbf{k}}$. The effective dispersion $\epsilon_{\mathbf{k}}$ can be obtained from a variational analysis [125] extended with (effective) second and third neighbor hopping [156], so that

$$\begin{aligned}\epsilon_{\mathbf{k}} &= 4t'\cos k_x \cos k_y + 2t''(\cos 2k_x + \cos 2k_y) \\ &\quad - \sqrt{0.44J^2 + t^2\{4.56 - 0.70(\cos k_x + \cos k_y)^2\}} + \text{const.} \end{aligned} \quad (4.106)$$

where the constant is chosen such that the minimum of $\epsilon_{\mathbf{k}}$ is 0. Further, we take $t = 3.1J$, $t' = -0.36J$, $t'' = 0.18J$ to get a best fit to data on the Mott insulator $\mathrm{Sr_2CuO_2Cl_2}$ [142, 153]. $\epsilon_{\mathbf{k}}$ is consistent with the effective QP dispersion derived in Ref. [153].

The lowest order self-energy diagram of the QP at zero temperature due to interaction with two-magnon modes is shown in Fig. 4.22(a). Expanding $g_{\mathbf{k},\mathbf{p}}$ around the singular points $\mathbf{k} \to \mathbf{0}, \boldsymbol{\pi}$ [with $\mathbf{0} = (0,0)$ and $\boldsymbol{\pi} = (\pi,\pi)$], we find that $g_{\mathbf{0},\mathbf{0}} = g_{\boldsymbol{\pi},\mathbf{0}} = g_{\boldsymbol{\pi},\boldsymbol{\pi}} \to 0$, so the holes do not couple to long wavelength magnons via H_2, regardless of the hole dispersion. Consequently, two-magnon broadening of the QP peak around the bottom of the band will vanish because of a lack of decay processes. To compute the two-magnon contribution to the QP

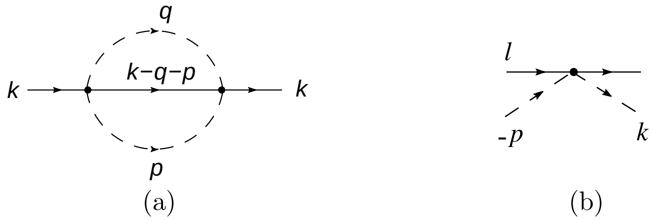

Figure 4.22: (a) Self-energy diagram for two-magnon screening of a hole with momentum **k**. The solid lines represent the hole, the dashed lines represent magnons. The vertices indicate an interaction via the $g_{\mathbf{k},\mathbf{p}}$ term of Eq. (4.103). (b) At finite temperatures, long wavelength magnons are present in the system and they can scatter off the holes via the $f_{\mathbf{k},\mathbf{p}}$ term, increasing their linewidth.

self-energy we introduce the hole and magnon Green's functions, respectively, as

$$G(\mathbf{k}, t-t') = -i \langle \psi_0 | T\{h_{\mathbf{k}}(t) h^{\dagger}_{\mathbf{k}}(t')\} | \psi_0 \rangle , \tag{4.107}$$

$$D(\mathbf{k}, t-t') = -i \langle \psi_0 | T\{\alpha_{\mathbf{k}}(t) \alpha^{\dagger}_{\mathbf{k}}(t')\} | \psi_0 \rangle \tag{4.108}$$

where $|\psi_0\rangle$ is the ground state of the perturbed system. The unperturbed Green's functions are

$$D^{(0)}(\mathbf{k}, \omega) = \int_{-\infty}^{\infty} dt\ e^{i\omega t} D^{(0)}(\mathbf{k}, t) = \frac{1}{\omega - \omega_{\mathbf{k}} + i\eta}, \tag{4.109}$$

$$G^{(0)}(\mathbf{k}, \omega) = \int_{-\infty}^{\infty} dt\ e^{i\omega t} G^{(0)}(\mathbf{k}, t) = \frac{1}{\omega - \epsilon_{\mathbf{k}} + i\eta}, \tag{4.110}$$

where η is a (very small) convergence factor. When the perturbation H_2 is turned on, the hole Green's function acquires a self-energy:

$$G(\mathbf{k}, \omega) = \frac{1}{\omega - \epsilon_{\mathbf{k}} - \Sigma(\mathbf{k}, \omega) + i\eta}. \tag{4.111}$$

To second order in the interaction, the self-energy diagram, shown in Fig. 4.22(a), is

$$\Sigma^{(2)}(\mathbf{k}, \omega) = \sum_{\mathbf{p},\mathbf{q}} \frac{2 g^2_{\mathbf{p},\mathbf{q}}}{\omega - \omega_{\mathbf{p}} - \omega_{\mathbf{q}} - \epsilon_{\mathbf{k}-\mathbf{p}-\mathbf{q}} + i\eta}. \tag{4.112}$$

The hole spectral function is by definition

$$A(\mathbf{k}, \omega) = -\frac{1}{\pi} \mathfrak{Im}\{G(\mathbf{k}, \omega)\} = \frac{1}{\pi} \frac{|\mathfrak{Im}\{\Sigma\}|}{(\omega - \epsilon_{\mathbf{k}} - \mathfrak{Re}\{\Sigma\})^2 + |\mathfrak{Im}\{\Sigma\}|^2}. \tag{4.113}$$

We evaluated the QP spectral function within the formalism above and the result is shown in Fig. 4.23. From the bottom two figures showing the spectrum with the second order self-energy, it can be seen that the QP broadening due to two-magnon screening is below about $0.1J \approx 12$ meV. For more broadening at momenta away from $(\pi/2, \pi/2)$, the bare hole dispersion would have to reach higher energies, around $4J$, where the two-magnon DOS is highest and thus the number of decay channels is maximized. This observation is reflected in $\mathfrak{Im}\{\Sigma^{(2)}\}$ peaking in this region to about $-0.12J$, broadening the peak just a little more.

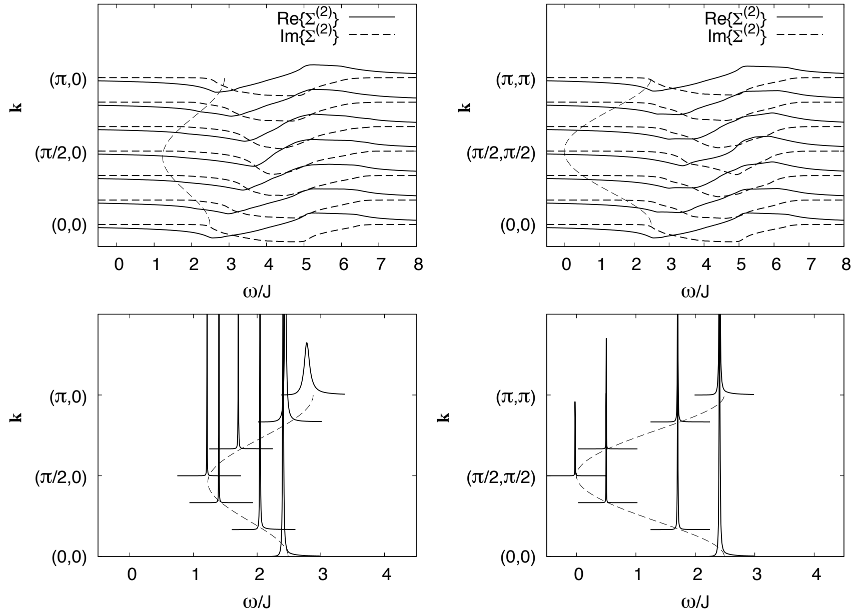

Figure 4.23: Hole self-energy to second order in H_2 (top figures) and the corresponding spectra (bottom figures). In the top figures, the solid line represents the real part of $\Sigma^{(2)}$, while the dashed line represents the imaginary part. The left figures show $\mathbf{k}$ ranging from $(0,0)$ to $(\pi,0)$, while the right figures show $(0,0)$ to (π,π). The dashed gray lines indicate the bare hole dispersion (4.106). A tiny artificial broadening of $0.02J$ is introduced for the numerical evaluation of the spectra. Around $(\pi/2,\pi/2)$, the spectrum approaches a delta function; their height is artificially limited due to the finite energy resolution of the numerical evaluation of the spectra.

Although the zero temperature mechanism we considered above does not explain the ARPES ZRS peak broadening, we can also consider finite temperature effects, where the coupling $f_{\mathbf{k},\mathbf{p}}$ becomes important. At non-zero temperatures, low energy magnons are present in the system and they can scatter off the holes via the vertex $f_{\mathbf{k},\mathbf{p}}$, as shown in Fig. 4.22(b). This decreases the lifetime of the quasiparticles. Holes at the bottom of the band can only scatter the low energy magnons into other low energy modes because of energy conservation.

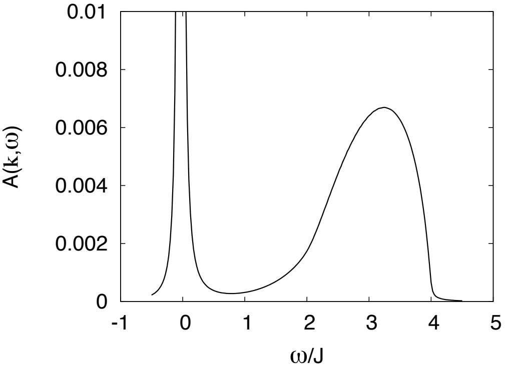

Figure 4.24: The spectrum of a static, two-magnon screened hole. The spectrum is independent of the hole's momentum. It consists of a sharp quasiparticle peak at $\omega \approx 0$ and a two-magnon incoherent feature at $\omega \approx 2-4J$.

By expanding $f_{\mathbf{k},\mathbf{p}}$ around the singular points at the center and corners of the BZ, we see that $f_{\mathbf{0},\mathbf{0}} = f_{\boldsymbol{\pi},\mathbf{0}} = f_{\boldsymbol{\pi},\boldsymbol{\pi}} \to 0$, and the amplitude for this kind of scattering process vanishes. We conclude that, even if low energy magnons are present at finite temperatures, the lifetime of quasiparticles near the bottom of the band does not increase due to single magnon scattering via H_2, and the zero temperature results are robust with respect to finite temperature effects.

To make a connection with RIXS at the Cu L edge, we calculate the spectrum for a flat band $\epsilon_{\mathbf{k}} \to$ const. This situation corresponds to RIXS since to good approximation the intermediate state is excitonic [157]: the 3d^{10} configuration is bound to the local core hole, and its dispersion is zero. Then, $\Sigma^{(2)}$ is independent of $\mathbf{k}$, and so is the spectrum $A(\mathbf{k},\omega)$. The resulting spectrum is shown in Fig. 4.24.

As is clear from Fig. 4.24, the two-magnon satellite between J and $4J$ carries approximately 1.1% of the total spectral weight. At first glance this small number might be surprising, considering that the two-magnon excitations appear so strongly in RIXS, particularly at the K edge [14, 52, 53]. We first note that in RIXS the elastic signal is (largely) pushed to the Bragg peaks and in that sense the dominating quasiparticle peak of Fig. 4.24 is absent. This argument is of course heuristic because the RIXS cross section is not directly related to the single particle spectral function $A(\mathbf{k},\omega)$, but rather given by the Kramers-Heisenberg relation (2.30). Also, at the Cu L edge, the two-magnon peak seems to be quite small compared to other magnetic features [11], which is at least qualitatively agreeing with the theoretical result presented here. It might be due to the absence of any other spectral weight that two-magnon excitations are seen so clearly in Cu K edge RIXS.

4.8.3 Conclusions

We conclude that the two-magnon screening of holes in the t-J model is a very small effect. It is by far not enough to explain the broad ARPES peaks: two-magnon screening gives a broadening of at most $0.1J \approx 12$ meV, while experimentally the peaks have a broadening of 0.3 eV. Earlier work [140] has already excluded broadening due to single magnon processes, and our results are in agreement with Ref. [143], which states that the ZRS peak broadening is probably not due to interactions with the Cu spins. Their reasoning is that at certain momenta, ARPES ejects O 2p electrons from the sample that, by symmetry, do not hybridize with the magnetic Cu ions. These ARPES peaks have exactly the same low energy line shape as the ZRS peaks that do communicate with the Cu ions. The authors therefore assume that the ZRS too owes it lineshape not to the Cu spins, but to something else.

The calculations for a dispersionless hole indicate that two-magnon excitations should show up only weakly in RIXS processes with a 3d^{10} intermediate state: we expect two-magnon excitations to be some two orders of magnitude smaller in intensity than direct RIXS processes that lead to the elastic line, single magnons and dd excitations. That a two-magnon signal is observed at the Cu K and L edges illustrates how sensitive RIXS is becoming [11, 14, 53].

4.8.4 Acknowledgements

We thank George Sawatzky, Byron Freelon and Tom Devereaux for fruitful discussions. This work is supported by the U.S. Department of Energy, Office of Basic Energy Sciences under contract DE-AC02-76SF00515 and benefited from the RIXS collaboration supported by the Computational Materials Science Network (CMSN) program under grant number DE-FG02-08ER46540. This work is supported by the Dutch ‘Stichting voor Fundamenteel Onderzoek der Materie (FOM)’.

CHAPTER 5

ORBITAL RIXS

5.1 Introduction

The orbital degree of freedom arises when the valence shell of an ion is not completely filled: the electrons can be distributed over the orbitals in different ways. For instance, a Ti^{3+} ion has one electron in the 3d subshell, making the ground state five-fold degenerate. It follows that orbitally active ions are also magnetic, although the converse is not necessarily true.

In many cases, the orbital degree of freedom is quenched by a large crystal field of low symmetry. In La_2CuO_4, for instance, the $x^2 - y^2$ orbital of Cu^{2+} is separated from the other $3d$ orbitals by more than 1.5 eV [70]. Transitions between those crystal field levels are called dd or crystal field excitations. The coupling of the Cu ions with their neighbors only introduces a small perturbation to this picture. Consequently, the crystal field excitations disperse only very little and are thus essentially local.

Much more interesting (from the point of view of orbital physics) are systems where the couplings between ions dominate over the local lattice coupling.

In general, orbital degeneracy can remain to very low temperatures in materials with highly symmetric lattices. In principle all local degeneracy can still be removed by the lattice through Jahn-Teller (JT) instabilities if the temperature is low enough [158, 159]. However, other interactions can dominate over the JT couplings, like superexchange (SE) interactions [24, 160–162] or relativistic spin-orbit coupling [25]. Lattice effects can then be regarded as only a perturbation to the orbital dynamics. In this chapter, we discuss the case where SE interactions dominate. Chapter 6 treats the case of dominant relativistic spin-orbit coupling.

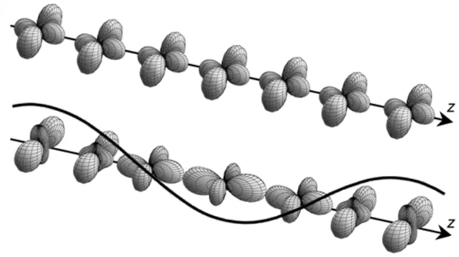

Figure 5.1: Top: a cartoon picture of an orbitally ordered ground state. Bottom: a snapshot of an orbital wave. Reprinted by permission from Macmillan Publishers Ltd: Nature **410**, 180 (2001).

When the lattice interacts strongly with the charge degree of freedom, phonons become visible in RIXS, as studied in Chapter 7.

Both the JT and SE interaction can couple neighboring orbitals and lead to orbital order. However, the excitations on top of the respective orbitally ordered ground states are very different. The lattice-dominated case yields localized dd excitations, while in SE-driven systems, collective orbital waves emerge. Fig. 5.1 shows a snapshot of such a wave, which can be crudely thought of as a dispersing dd excitation. The quanta of orbital waves are called orbitons, in analogy to spin waves and magnons.

Orbitons are a hot topic, yet they are difficult to observe in practice [163,164]. The interpretation of Raman scattering data of $\mathrm{LaMnO_3}$ in terms of orbitons remains controversial [163,165,166]. In any case, Raman scattering is hindered by the fact that it cannot show momentum dependence, which is the distinguishing feature of a collective excitation. In contrast, RIXS has enough momentum to probe their dispersion in a large part of the Brillouin zone. Also, RIXS is directly sensitive to dipole forbidden dd excitations, unlike, for instance, optical conductivity measurements.

In section 5.2 the orbital excitations will be introduced in more detail. Also, it will be discussed how they are probed with RIXS. The remainder of the chapter describes the specific cases of 2D e_g systems like $\mathrm{LaMnO_3}$ (section 5.3), and the t_{2g} system $\mathrm{YTiO_3}$ (section 5.4).

5.2 Theory

Orbitally active ions can be coupled together via JT or SE interactions. In section 5.2.1 we discuss these couplings and their implications for the excitation spectrum. How the excitation spectrum of an orbitally active system is probed with RIXS is explained in section 5.2.2.

5.2.1 Orbital excitations

Superexchange is well-known to generate magnetic interactions between spins. It relies on the presence of virtual hopping processes that, on 180° bonds, promote antiferromagnetic alignment of electron spins. In the virtual hopping processes, not only the spins of the electrons can be effectively interchanged, but also the orbitals that they occupy. These processes are described by the Kugel-Khomskii model, which can be derived by taking the low energy limit of a multi-band Hubbard model for a Mott insulator [24]. The type of orbital order promoted by SE is closely related to the magnetic order, because the hopping amplitudes depend both on the spins and orbitals involved, as stated by the Goodenough-Kanamori rules [162,167]. Fig. 5.2 shows an example of a virtual hopping process.

Kugel-Khomskii models are often frustrated because of the impossibility to optimize the superexchange bonds to a certain ion in all directions simultaneously. As a consequence, such a system often has a small orbital order parameter, or is in an orbital liquid state. In the case of an ordered ground state, a certain orbital condenses in the ground state, analogous to the Heisenberg antiferromagnet. The orbiton excitations on top of this condensate are collective, dispersing ones.

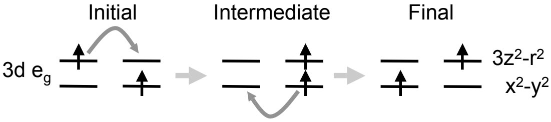

Figure 5.2: An example of a spin-orbital superexchange process on two neighboring transition metal ions with a half-filled 3d e_g subshell. The electrons usually hop via oxygen ions in between the orbitally active ions; these are omitted in the figure. The amplitude for these processes depends on the hopping integrals between the involved orbitals and the energy of the intermediate state, which involves Coulomb repulsion and Hund's rule exchange.

When JT interactions dominate over SE in orbitally active systems, the orbital dynamics are different. The lattice couples to the charge distribution of the orbitals and can mediate a cooperative JT phase transition that polarizes the orbital state. The orbital degrees of freedom are frozen out at low temperatures. Remaining degrees of freedom, *e.g.*, magnetic ones, are in a sense decoupled from the orbitals. Although the orbital pattern is fixed at low energies, the magnetic interactions are still determined by the orbital pattern, following the Goodenough-Kanamori rules [162, 167].

Orbital excitations on the JT-induced ground state are more localized in nature. Orbital excitations have to drag along lattice deformations due to the JT interaction, which reduce the orbiton band width or even localize the orbital excitations [168–170]. Another way to look at the localization is to regard the JT phonons as a bath to which the orbital degree of freedom couples. When one looks only at the orbital excitations and ignores the lattice, the orbitals constitute an open quantum system. The lattice acts as a bath and is a source of decoherence for the orbital excitations. Because of the local nature of the JT interaction, decoherence localizes the orbital excitations. In contrast, SE interactions between orbitally active ions are not mediated by another degree of freedom, and therefore do not have this intrinsic source of decoherence.

The two types of orbital interactions suppress each other. When JT distortions are large, virtual excursions of electrons to neighboring sites are suppressed because of the large energy cost of populating excited state orbitals. Vice versa, if there are large orbital fluctuations, the slower JT distortions cannot keep up with them, and the JT energy gain is lowered.

When looking for systems that exhibit orbitons, the JT coupling needs to be small. Typically, in transition-metal oxides with octahedral symmetry, the e_g orbitals are pointing towards the negatively charged oxygen ions, so they couple stronger to the lattice than the t_{2g} orbitals. On the other side, SE interactions are enhanced near the Mott transition, *i.e.*, when the hopping parameter t is large and the Hubbard U is small. From an experimental point of view, a highly symmetric lattice signals small JT couplings. Further, structural and magnetic phase transitions can be compared: because in a JT-dominated system the spin degrees of freedom can remain active after the orbital ones have frozen out, one expects the cooperative structural phase transition and the magnetic phase transition to be at different temperatures (as in $LaMnO_3$ [168, 171]). In SE-dominated systems, the spins and orbitals are entangled and order simultaneously. In $LaTiO_3$, for instance, no separate transitions have been observed. Finally, the magnetic excitation spectrum depends on the orbital physics. When lattice distortions dominate, the orbital polarization generally induces an anisotropic magnetic SE interaction through the Goodenough-Kanamori rules. The magnetic spectra of the titanates $LaTiO_3$ and $YTiO_3$ are isotropic [160].

5.2.2 Orbital RIXS

RIXS is capable of detecting the full dynamics of orbitons. Recently, astounding progress was made in the energy and momentum resolution of RIXS, allowing, for instance, the observation of magnon excitations and their dispersions in copper oxides, see Refs. [11, 14, 53] and chapter 4. The improved resolution opens the way for probing orbitons, which are predicted to exist at similar energy scales.

Ishihara and Maekawa [66] mention three types of RIXS processes.

The first one is direct RIXS: the incident X-ray photon promotes a core electron to a certain valence orbital, and an electron from a different orbital fills the core hole.

In indirect RIXS, the core hole and photo-excited electron can affect the valence electrons in two ways: first, through the potential of the core hole and the excited electron (from hereon referred to simply as core hole potential) and second, by the Pauli exclusion principle (if the electron is excited into the valence band). These interactions lead to two indirect RIXS processes: a single-site shakeup mechanism and two-site SE bond modulation. In a single-site shakeup process, the core hole potential changes the orbit of one of the valence electrons at the core hole site. Which transitions can be effected is determined by the symmetry of the potential. In two-site SE bond modulation, the core hole potential influences the SE bond strength $J \sim t^2/U$ by modifying U in the intermediate state. The orbitals on the two sites involved in the bond can flip, in analogy to bimagnon RIXS at the Cu K edge. Also, the Pauli exclusion principle may play a role in SE bond modulation, in analogy to bimagnon RIXS at the Cu L edge. Of course, there are many more channels, like non-local shakeup, three-site SE modification, etc., but these are all of higher order.

Multiplet effects, like relativistic core spin-orbit coupling and intra-ionic Coulomb interactions, drive the rapid evolution of the intermediate states and so tend to wash out any particular symmetry of the core hole potential when the core hole lifetime broadening is smaller than the multiplet energy scales. Transitions of different symmetries are expected to become equal in strength. Therefore, the shakeup channel gives low energy spectra that are very similar for different edges: the differences in the initial multiplet structures are averaged out rapidly.

The effective scattering operator can in general be expanded in the number of sites involved in the scattering process:

$$\hat{O}_{\mathbf{q}} = \sum_i e^{i\mathbf{q}\cdot\mathbf{R}_i} \left(\hat{O}_i + \hat{O}_{ij} + \ldots \right). \tag{5.1}$$

The phase factor comes from the dipole operators. Direct RIXS belongs to the single-site processes. Indirect RIXS contributes to both single- and two-site processes. The shakeup processes belong to the single-site part, while the SE bond modulation processes belong to the two-site part. One might think that the two-site part is a higher order correction to shakeup processes. However, since the core hole potential is averaged by multiplet effects, it is dominated by the isotropic part. The isotropic part of the potential does not contribute to on-site shakeup processes, but it does contribute to intersite bond modulation processes. It follows that it is a priori not clear which mechanism dominates indirect orbital RIXS.

One may distinguish two regimes for RIXS processes: in the first regime Γ is much larger than the relevant energy scales of the intermediate states, and these processes can be easily analyzed with the Ultra-short Core hole Lifetime expansion [48, 50], see section 2.5. In the other regime, Γ is small and its inverse is irrelevant as a cut-off time of the intermediate state dynamics. The lifetime broadening at the transition metal L edges, for instance, is relatively small, and the effects of the core hole on the valence electrons is averaged over many precessions of the core hole due to the large spin-orbit coupling in the core levels of transition metal ions.

5.3 RIXS spectra of 2D e_g systems

Published as '*Single and Double Orbital Excitations Probed by Resonant Inelastic X-ray Scattering*' in Phys. Rev. Lett. **101**, 106406 (2008) with Fiona Forte and

Jeroen van den Brink.

Abstract. *The dispersion of the elusive elementary excitations of orbital ordered systems, orbitons, has escaped detection so far. The recent advances in resonant inelastic x-ray scattering (RIXS) techniques have made it, in principle, a powerful new probe of orbiton dynamics. We compute the detailed traces that orbitons leave in RIXS for an e_g orbital ordered system, using the ultra-short core hole lifetime expansion for RIXS. We observe that both single- and double-orbiton excitations are allowed, where the former, at lower energy, have sharper features. The rich energy- and momentum-dependent intensity variations that we observe make clear that RIXS is an ideal method to identify and map out orbiton dispersions.*

5.3.1 Introduction

The exotic phases and phenomena exhibited by many transition metal oxides originate from the interplay of their electronic spin, charge and orbital degrees of freedom, coupled to the lattice dynamics [162, 172]. The orbital degree of freedom, originating from the unlifted or only partially lifted local orbital degeneracy of the $3d$ electrons, plays a particularly important role in for instance the physics of Colossal-Magneto-Resistence (CMR) manganites [24, 173, 174]. The orbitals also stand out because –in contrast to the other degrees of freedom– the dynamics of these elementary excitations is still far from being fully understood. The main reason is that it has proven very difficult to access orbital excitations experimentally.

The first claim of the observation of these elusive orbital excitations, orbitons, in LaMnO$_3$ by optical Raman scattering [163] is very controversial [165]. Irrespective of the interpretation of these data, however, a severe limitation of the Raman technique is its selectiveness to excitations carrying zero momentum. This method is thus intrinsically unsuitable to map out orbiton dispersions. Other evidence for the existence of orbital excitations comes from very recent optical pump-probe experiments on manganites [164]. Even if very ingenious, also these experiments cannot provide information on the momentum dependence of orbitons.

The success of theory in describing the dispersive magnetic RIXS data [51, 52, 96] and, in particular, the success of the so-called ultra-short core hole lifetime (UCL) expansion [49, 50] provide the motivation to uncover also the signatures of orbital excitations using this theoretical framework. We therefore set out to compute and predict the detailed fingerprints of the orbitons in RIXS, finding that both single- and double-orbiton excitations are allowed, with the former having sharper features, appearing at lower energy. Orbiton scattering causes characteristic energy- and momentum-dependent intensity variations in RIXS with certain selection rules. Matrix element effects also make, for instance, the two-orbiton scattering intensity very different from the bare two-orbiton density of states. This bolsters the case that from a theoretical perspective RIXS is ideally suited to map out the orbiton dispersions [66, 175].

In RIXS a material is resonantly excited by tuning the energy of incoming X-rays to an atomic absorption edge. In manganites, for instance, one can use the Mn K or L edge. At the Mn K edge the incoming photon promotes a 1s electron into the 4p state far above the Fermi energy, see Fig. 5.3. The present experimental resolution at the Mn edges is $\sim$ 100 meV. In the very near future, instrumentation with an improvement with an order of magnitude in resolution at the K edge will become feasible [176], allowing the detection of low lying orbital excitations.

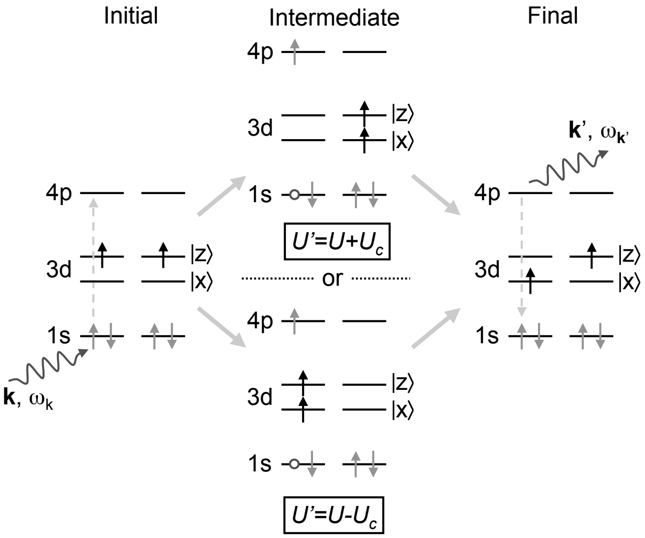

Figure 5.3: The effect of the core hole on the orbital exchange. An X-ray with energy $\hbar\omega_{\mathbf{k}}$ and momentum $\hbar\mathbf{k}$ excites the 1s electron to a 4p state. Via an intermediate state, the system reaches a final state and the core hole decays, emitting a photon of energy $\hbar\omega_{\mathbf{k}'}$ and momentum $\hbar\mathbf{k}'$. In the figure, the matrix element $\langle\downarrow_i\uparrow_j|\, H\, |\uparrow_i\uparrow_j\rangle$ is considered in presence of a core hole. There are two alternative intermediate states to reach the final state. In the upper case, the amplitude is proportional to $t^{xz}t^{xx}/(U+U_c)$ and in the lower case to $t^{xz}t^{zz}/(U-U_c)$. Adding these gives a modified exchange $J' = J\,(1+\eta)$ where η depends on U_c.

We determine the orbiton RIXS spectrum for an orbital ordered system with orbitals of e_g symmetry, but the approach that we outline can equally well be used for other orbital ordering symmetries. In order to compute the RIXS spectrum it is key to determine how the intermediate state core hole modifies the orbital-dependent superexchange processes between the $3d$ electrons. After doing so, our calculations based on the UCL expansion will show how such modifications give rise to both single- and double-orbiton features in the RIXS spectrum. The one-orbiton part turns out to carry most spectral weight. This is in stark contrast with magnetic RIXS, where only two-magnon scattering is allowed at zero temperature [51, 52]. The computed orbiton spectrum for the e_g orbital ordering of $LaMnO_3$ shows, besides the orbiton dispersions, also strong momentum dependence of scattering intensity, with, in particular, a vanishing of it at $\mathbf{q}$=(0,0) and (π,π) for all but one orbiton branch. The orbiton is also expected to have phonon sidebands [169], observable in RIXS as well.

5.3.2 Model Hamiltonian

We focus on orbital excitations in a system with staggered e_g orbital order, such as $LaMnO_3$, the mother compound of CMR manganites. The methods used below can without restriction be applied to different orbital ordered e_g or t_{2g} systems as well. In the undoped manganite, three 3d electrons occupy the Mn t_{2g} orbitals and a fourth 3d electron can be in either one of the two Mn e_g orbitals. Below 780 K, the e_g orbitals order in an antiferro-orbital fashion. At lower temperatures, the spins order in an A-type magnetic structure, where the ferromagnetic, orbital ordered planes are stacked antiferromagnetically along the c axis [175, 177, 178].

The orbital physics of $LaMnO_3$ can be cast in a simple pseudo-spin model, where the pseudo-spin represents the Mn $3d$ e_g orbital that is occupied. It is derived starting from a generic Kondo lattice Hamiltonian [179, 180], with a local Coulomb repulsion U between the electrons in the e_g subspace. In the resulting Kugel-Khomskii model [24], the orbitals of classical antiparallel spins decouple if one neglects the Hund's rule exchange compared to the on-site Coulomb repulsion. As the quantum fluctuations associated with the large Mn core spin on the A-type AFM structure are typically small, in leading order the orbital degrees of freedom effectively decouple along the c axis, simplifying the orbital dispersion to a two-dimensional one.

The orbitals in the ab-plane are described by pseudospins, where pseudospin up corresponds to the orbital $|z\rangle \sim (3r^2-z^2)/\sqrt{6}$ and down to $|x\rangle \sim (x^2-y^2)/\sqrt{2}$. The in-plane hopping integrals are $|t^{xx}| = \frac{3}{4}t$, $|t^{zz}| = \frac{1}{4}t$ and $|t^{xz}| = \frac{\sqrt{3}}{4}t$, with reference $t = |t^{zz}|$ along the z direction. After a rotation in pseudospin space over an angle $\theta = \pi/4$, the orbital model Hamiltonian is $H^0 = \frac{J}{2}\sum_{\langle ij\rangle} H^0_{ij}$ with

$$H^0_{ij} = 3T^z_iT^z_j + T^x_iT^x_j \pm \sqrt{3}\left(T^z_iT^x_j + T^x_iT^z_j\right), \tag{5.2}$$

where $J = t^2/U$ [175]. The prefactor of the $\sqrt{3}$ term is positive in the x direction and negative in the y direction. The classical ground state has electrons alternately occupying the orbitals $\frac{1}{\sqrt{2}}(|x\rangle+|z\rangle)$ and $\frac{1}{\sqrt{2}}(|x\rangle-|z\rangle)$. We introduce sublattice A with pseudospin up and B with pseudospin down and Holstein-Primakoff bosons $T^+_{i\in A} = a_i$, $T^z_{i\in A} = 1/2 - a^\dagger_i a_i$ and $T^+_{j\in B} = a^\dagger_j$, $T^z_{j\in B} = a^\dagger_j a_j - 1/2$.

To obtain the orbital excitations we retain the terms up to quadratic order in the boson operators. After Fourier transforming the Hamiltonian and a Bogoliubov transformation, the orbiton Hamiltonian is $H^0 = \text{const.} + \sum_{\mathbf{k}} \epsilon_{\mathbf{k}} \alpha^\dagger_{\mathbf{k}} \alpha_{\mathbf{k}}$ with $\epsilon_{\mathbf{k}} = 3J\sqrt{1 + \frac{1}{6}(\cos k_x + \cos k_y)}$. The orbiton spectrum is gapped: as our orbital Hamiltonian does not have a continuous symmetry, Goldstone modes are absent.

5.3.3 Modifications by core hole

In the RIXS intermediate state, a core hole is present, and the Hamiltonian becomes $H = H^0 + H^{core}$, which includes the interaction between the core hole and the orbital degrees of freedom. The main effect of the core hole potential is to lower the Coulomb repulsion U between two e_g electrons at the core hole site by an amount U_c, disrupting the superexchange processes [52]. This effect is substantial as $U_c \approx 7$ eV [181]. To calculate the matrix elements of H^{core}, we consider how the core hole changes the superexchange processes for all different pseudospin orientations. In Fig. 5.3, the two exchange paths for the specific case $\langle \downarrow_i \uparrow_j | H | \uparrow_i \uparrow_j \rangle$ are shown. The upper process involves $t^{xz}t^{xx}/U$, where U is increased in presence of a core hole with U_c. The lower process involves $t^{xz}t^{zz}/U$ and decreases the intermediate energy U by U_c. These two processes result in

$$\begin{aligned}\langle \downarrow\uparrow | H^{core}_{ij} | \uparrow\uparrow \rangle &= 2\left(\frac{t^{xz}t^{zz}}{U - U_c} - \frac{t^{xz}t^{xx}}{U + U_c}\right) \langle \downarrow\uparrow | T^-_i T^z_j | \uparrow\uparrow \rangle \\ &= \pm\frac{\sqrt{3}}{4} J' \langle \downarrow\uparrow | T^-_i T^z_j | \uparrow\uparrow \rangle \qquad (5.3)\end{aligned}$$

with $J'/J = 1 + \frac{U_c(U_c - 2U)}{U^2 - U_c^2}$. Note that J' is, in general, different for each matrix element. Collecting the matrix elements, one finds $H = H^0 + \frac{J}{2}\sum_{<i,j>} H^{\text{core}}_{ij} s_i s^\dagger_i$ with

$$H^{\text{core}}_{ij} = \eta_1 H^0_{ij} + \eta_2 \left[\left(T^x_j - T^x_i\right) \mp \sqrt{3}\left(T^z_j - T^z_i\right)\right], \qquad (5.4)$$

where s_i creates a core hole and the dimensionless coupling constants are $\eta_1 = \frac{U_c^2}{U^2 - U_c^2}$ and $\eta_2 = \frac{UU_c}{U^2 - U_c^2}$. The $\mp$ sign is $-$ for bonds along the x direction and $+$ along the y direction. The first term in H^{core}_{ij} is similar to the one encountered in magnetic RIXS scattering. Physically it is due to the fact that the core hole modifies the strength of the superexchange bonds to all neighboring sites. Its analytic form implies the selection rule that RIXS intensity vanishes for $\mathbf{q} = (0,0)$, as at zero momentum transfer the scattering operator is proportional to the Hamiltonian H^0 and thus commutes with it [51, 52]. The second term, with coefficient η_2, contains single orbital operators and is specific for core hole orbital coupling – in spin systems such a coupling is not allowed by conservation of S^z_{tot}. The presence of this term will allow the observation of single-orbiton scattering.

Figure 5.4: The indirect RIXS spectrum for a cut through the Brillouin zone. The lower two branches originate from single orbiton excitations, the upper, continuous spectrum from double orbiton scattering. Selection rules are such that at $\mathbf{q} = (0,0)$ all spectral weight vanishes and at $\mathbf{q} = (\pi,\pi)$ only one single-orbiton branch is active.

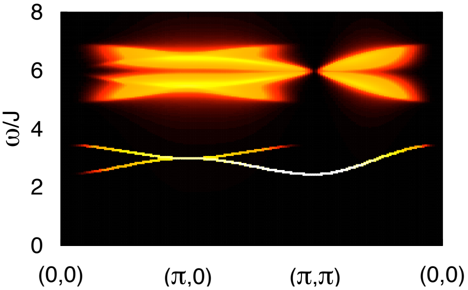

5.3.4 Scattering Cross section

Having derived the Hamiltonian, we can compute the RIXS spectrum using the ultra-short core hole lifetime (UCL) expansion [49,50], see section 2.5. The zeroth order term gives only elastic scattering and is thus omitted in the following. We can retain only the lowest order terms in $\eta_{1,2}J/\Gamma \approx 0.2$ in the expansion of $H^l = (H^0 + H^{\text{core}})^l$. This approximation is controlled by the large core hole broadening ($\Gamma \approx 0.58$ eV at the Mn K-edge, 1.3 eV at the Mn L$_1$-edge and 0.16 eV at the Mn L$_{2,3}$-edges [100]) and the values of $J \approx 25$ meV [181, 182] and $U_c/U \approx 1.1$. With this the expression for the scattering simplifies to $A_{fi} = \frac{\omega_{\text{res}}}{i\Gamma}\frac{1}{i\Gamma+\omega}\langle f|\,\hat{O}_{\mathbf{q}}\,|i\rangle$, with the effective scattering operator $\hat{O}_{\mathbf{q}} = \frac{J}{2}\sum_{<i,j>} e^{i\mathbf{q}\cdot\mathbf{R}_i} H_{ij}^{\text{core}}$. We evaluate this expression in terms of the boson creation and annihilation operators, in linear spinwave approximation. After Fourier transforming and introducing the Bogoliubov transformed orbiton operators, we obtain the single- and double-orbiton scattering operators, $\hat{O}^{(1)}_{\mathbf{q}}$ and $\hat{O}^{(2)}_{\mathbf{q}} = \sum_{\mathbf{k}} \hat{O}^{(2)}_{\mathbf{k},\mathbf{q}}$, respectively. At $T = 0$, the single-orbiton scattering operator is

$$\begin{aligned}\hat{O}^{(1)}_{\mathbf{q}} =& -\frac{\eta_1\sqrt{3N}}{8} J^-_{\mathbf{q}}\,(u_{\bar{\mathbf{q}}} - v_{\bar{\mathbf{q}}})\,\alpha^\dagger_{-\bar{\mathbf{q}}} \\ &+ \frac{\eta_2\sqrt{N}}{4}\,(J_{\mathbf{q}} - J_{\mathbf{0}})\,(u_{\mathbf{q}} - v_{\mathbf{q}})\,\alpha^\dagger_{-\mathbf{q}} \end{aligned} \tag{5.5}$$

and the double orbiton scattering operator

$$\begin{aligned}\hat{O}^{(2)}_{\mathbf{k},\mathbf{q}} =& -\frac{\eta_1}{8}\,[(6(J_{\mathbf{q}} + J_{\mathbf{0}}) + J_{\mathbf{k}} + J_{\mathbf{k}+\mathbf{q}})\,u_{\mathbf{k}}v_{\mathbf{k}+\mathbf{q}} \\ &- J_{\mathbf{k}+\mathbf{q}}\,(u_{\mathbf{k}}u_{\mathbf{k}+\mathbf{q}} + v_{\mathbf{k}}v_{\mathbf{k}+\mathbf{q}})]\,\alpha^\dagger_{\mathbf{k}}\alpha^\dagger_{-\mathbf{k}-\mathbf{q}} \\ &+ \frac{\eta_2\sqrt{3}}{2} J^-_{\mathbf{q}}\,u_{\mathbf{k}}v_{\mathbf{k}+\bar{\mathbf{q}}}\alpha^\dagger_{\mathbf{k}}\alpha^\dagger_{-\mathbf{k}-\bar{\mathbf{q}}}, \end{aligned} \tag{5.6}$$

where $u_{\mathbf{k}}$ and $v_{\mathbf{k}}$ are the coefficients of the Bogoliubov transformation, $\bar{\mathbf{q}} = \mathbf{q} + (\pi,\pi)$, $J^{x(y)}_{\mathbf{k}} = 2J\cos k_{x(y)}$, $J_{\mathbf{k}} = J^x_{\mathbf{k}} + J^y_{\mathbf{k}}$ and $J^-_{\mathbf{k}} = J^x_{\mathbf{k}} - J^y_{\mathbf{k}}$. As expected, since the z component of the total pseudospin $T^z_{\text{tot}} = \sum_i T^z_i$ is not conserved in the scattering process, we get a contribution to the scattering intensity both

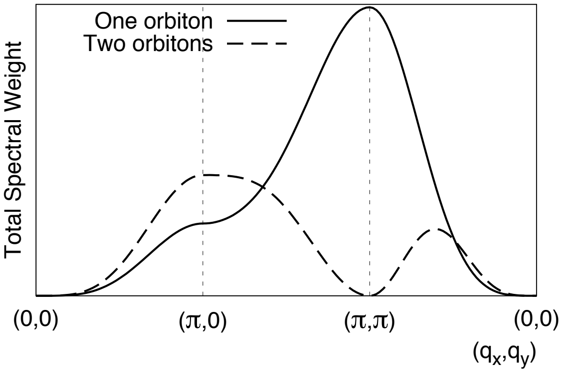

Figure 5.5: Comparison of the energy integrated spectral weight of the one- and two-orbiton RIXS spectra at fixed momentum transfer **q**.

from the one- and two-orbiton part. This is a fundamental difference with respect to magnetic RIXS spectrum, where the conservation of total S^z allows only creation/annihilation of an even number of magnons [51, 52].

The resulting RIXS spectrum is shown in Fig. 5.4. We observe that the two-orbiton spectrum vanishes not only at $\mathbf{q} = (0, 0)$ but also at the antiferro-orbital ordering wavevector (π, π). This is due to the RIXS matrix elements and not to the two-orbiton DOS, which actually peaks at (π, π). The total spectral weight of the orbiton spectrum is strongly **q**-dependent. In Fig. (5.5) we compare the spectral weights: the one-orbiton weight dominates and peaks at $\mathbf{q} = (\pi, \pi)$, where the two-orbiton spectrum vanishes. The two-orbiton spectrum has its maximum total weight at $(\pi, 0)$, where the total two-orbiton intensity actually outweighs the one-orbiton one. An exchange constant of $J \approx 25$ meV [181, 182] will put the two-orbiton spectrum around $\omega \approx 150$ meV. The one-orbiton peak at (π, π) is much more intense, but at $\omega \approx 2.4J \approx 60$ meV, might be more difficult to discern from the tail of the elastic peak.

5.3.5 Conclusion

Our calculations shown that in resonant inelastic X-ray experiments orbital excitations are distinguishable by characteristic variations in scattering amplitude as a function of both energy and momentum transfer. Both single- and double-orbiton excitations are allowed, with intensities that are of the same order. The single orbiton features are sharp and lower in energy; the double orbiton ones are higher in energy and more smeared out. At high symmetry points in the Brillouin zone, the intensity of specific orbiton branches vanishes. Our detailed predictions on the orbiton spectrum of an e_g orbital ordered system bolster the case that with RIXS it will for the first time be possible to directly probe orbiton dynamics and dispersions. The necessary energy and momentum resolution starts to come within reach of experiment. An observation of orbitons in RIXS will open the way to probe new orbital related quasiparticles, for instance, orbiton-magnon bound states for which so far only theoretical evidence exists [183].

Acknowledgements. We thank Sumio Ishihara, Giniyat Khaliullin and Jan Zaanen for stimulating discussions.

5.4 RIXS spectra of $YTiO_3$

Published as '*Theory of Raman and Resonant Inelastic X-ray Scattering from Collective Orbital Excitations in* $YTiO_3$' in Phys. Rev. B **103**, 107205 (2009) with Giniyat Khaliullin.

Abstract. *We present two different theories for Raman scattering and Resonant Inelastic X-ray Scattering (RIXS) in the low temperature ferromagnetic phase of* $YTiO_3$ *and compare this to the available experimental data. For description of the orbital ground-state and orbital excitations, we consider two models corresponding to two theoretical limits: one where the* t_{2g} *orbitals are degenerate, and the other where strong lattice distortions split them. In the former model the orbitals interact through superexchange. The resulting superexchange Hamiltonian yields an orbitally ordered ground state with collective orbital excitations on top of it – the orbitons. In the orbital-lattice model, on the other hand, distortions lead to local dd-transitions between crystal field levels. Correspondingly, the orbital response functions that determine Raman and RIXS lineshapes and intensities are of cooperative or single-ion character. We find that the superexchange model yields theoretical Raman and RIXS spectra that fit very well to the experimental data.*

5.4.1 Introduction

The titanates, with a pseudo-cubic perovskite lattice structure, are good candidates to support orbitons. The Ti ions with their $3d^1$ configuration have one electron in one of the three nearly degenerate t_{2g} orbitals. Since these orbitals are directed away from the neighboring oxygen ions, the coupling to the lattice is expected to be small. Further, it has been shown that a SE-only model explains many of the ground state properties of $YTiO_3$ [184, 185]. Also, there is experimental evidence that $LaTiO_3$ is a (SE-driven) orbital liquid [186–188]. On the other hand, local crystal field models also well reproduce some of the physical properties of the titanates [189–199]. Both models have their shortcomings as well: a JT dominated description is not able to reproduce the spin wave spectrum, which is nearly isotropic in both spin and real space, while the SE model has difficulties explaining the experimentally observed orbital polarization [196–199]. Consequently, it still remains controversial which mechanism dominates the orbitals in titanates [160].

In order to resolve this controversy, it is of crucial importance to compare recent Raman and RIXS experiments on titanates [200–202] to both of the competing theories. We analyze recent Raman and RIXS spectra [200–202] for YTiO$_3$ from the point of view of a SE-only model and the alternative extreme of a completely local, lattice distortion dominated model. We find that while the orbital-lattice model can be finetuned to capture some aspects of the observed spectra, the collective superexchange model yields a much better overall description of the Raman and RIXS data.

This section is organized as follows: Sec. 5.4.2 compactly reviews previous work on YTiO$_3$ and introduces the SE formalism and the local crystal field model. Sections 5.4.3 and 5.4.4 deal with the theory of Raman scattering and RIXS respectively, in both the SE and crystal field models.

5.4.2 Two models of YTiO$_3$

For the existence of collective excitations of orbitals, the so-called orbitons, it makes a difference whether the orbital order is driven by JT distortions or SE [24, 159]. For large JT distortions, the crystal field splitting is large and a local picture applies: the collective nature of the orbital excitations characteristic of orbitons is lost. In materials where the orbital-lattice coupling is small, the SE interactions between orbitals can dominate over crystal field splittings due to lattice distortions. The Ti ions have a 3d^1 configuration, and the octahedral crystal field induces a splitting between the higher energy e_g and lower energy t_{2g} levels. Because the t_{2g} orbitals are not directed towards neighboring oxygen ions, they are not expected to couple strongly to lattice distortions.

Building on this assumption, one can derive a superexchange Hamiltonian starting from a Hubbard model. Below, we follow Refs. [184, 185] closely. By symmetry, the hopping term connects, for instance, the zx to zx and yz to yz orbitals along the z direction (c axis) via the intermediate oxygen 2p$_\pi$ states. xy orbitals are not coupled along this direction. In the limit of large on-site Coulomb repulsion U, this leads to a SE interaction that depends on the spatial direction of a bond, and the resulting model is intrinsically frustrated: on any given ion, there is no orbital that minimizes the bond energy in all directions simultaneously.

Because YTiO$_3$ is ferromagnetic at low temperature ($T_c \approx 30$ K) [203], we restrict ourselves to the completely ferromagnetic part of the Hilbert space. Then one obtains the simple Hamiltonian

$$\hat{H}_0 = \frac{1}{2} J_{\text{orb}} \sum_{\langle i,j \rangle} \left(\hat{A}_{ij}^{(\gamma)} + \frac{n_{\gamma,i} + n_{\gamma,j}}{2} \right), \tag{5.7}$$

with the orbital exchange integral $J_{\text{orb}} = r_1 J_{SE}$, where $r_1 = 1/(1 - 3J_H/U) \approx 1.56$ parametrizing Hund's rule coupling J_H and $J_{SE} = 4t^2/U$ is the superexchange constant derived from the Hubbard model. The operator $\hat{A}_{ij}^{(\gamma)}$ depends on the direction γ of the bond ij. For example, in the z direction we have

$$\hat{A}_{ij}^{(c)} = n_{a,i} n_{a,j} + n_{b,i} n_{b,j} + a_i^\dagger b_i b_j^\dagger a_j + b_i^\dagger a_i a_j^\dagger b_j. \tag{5.8}$$

The operators $a^\dagger, b^\dagger$ and $c^\dagger$ create an electron in the yz-, zx- and xy-orbital, respectively, and $n_a = a^\dagger a$. The Hamiltonian can also be written in terms of interacting effective angular momenta $l = 1$, operating on the t_{2g} triplet. Because of the orbital frustration, these can form a myriad of different classical ground states. Refs. [184, 185] conclude that a 4-sublattice quadrupole ordered state is favored, in which the orbitals

$$|\psi_c\rangle = \frac{1}{\sqrt{3}} \left(|d_{yz}\rangle \pm |d_{zx}\rangle \pm |d_{xy}\rangle\right) \tag{5.9}$$

are condensed. The signs ± alternate between the sublattices, such that nearest-neighbor orbitals are orthogonal, supporting ferromagnetic order. On top of this condensate, two species of orbitons can be created, loosely speaking by populating either one of the two orbitals orthogonal to ψ_c. The orbiton spectrum has $3N^{1/3}$ Goldstone modes (where N is the total number of Ti ions), because the number of orbitals of a specific "color" is conserved in the plane in which it is lying. However, in $YTiO_3$ the TiO_6 octahedra are tilted. Because of this, hopping between different t_{2g} orbitals is now no longer symmetry forbidden, and the conservation of orbital "color" is violated, removing the Goldstone modes. When also some anharmonic terms of the Hamiltonian are taken into account on a mean field level, the orbiton dispersion becomes [185]

$$\begin{aligned} \omega_{1/2,\mathbf{k}} =& \sqrt{Z_\varepsilon Z_f}\, J_{\mathrm{orb}} \{1 - (1-2\varepsilon)(1-2f)(\gamma_{1,\mathbf{k}} \pm \kappa_{\mathbf{k}})^2 \\ & - 2(\varepsilon - f)(\gamma_{1,\mathbf{k}} \pm \kappa_{\mathbf{k}})\}^{1/2}, \end{aligned} \tag{5.10}$$

where we use the signs + and − for $\omega_{1,\mathbf{k}}$ and $\omega_{2,\mathbf{k}}$ respectively. Further, $\sqrt{Z_\varepsilon Z_f} \approx 1.96$, $f \approx 0.086$, $\varepsilon \approx 0.18$, $\gamma_{1,\mathbf{k}} = (c_x + c_y + c_z)/3$ and $\kappa_{\mathbf{k}} = \sqrt{\gamma_{2,\mathbf{k}}^2 + \gamma_{2,\mathbf{k}}^2}$ with $\gamma_{2,\mathbf{k}} = \sqrt{3}(c_y - c_x)/6$ and $\gamma_{3,\mathbf{k}} = (2c_z - c_x - c_y)/6$ with $c_\alpha = \cos k_\alpha$. Eq. (5.10) describes the collective orbital modes that disperse up to energies of $2J_{\mathrm{orb}}$ and have a gap of approximately J_{orb}.

In the second orbital model for $YTiO_3$ that we consider, lattice distortions dominate over superexchange interactions. Pavarini *et al.* [190, 191] did a DMFT+LDA calculation and found that lattice distortions of the $GdFeO_3$-type lift the orbital degeneracy. They also obtained four sublattices. The resulting local eigenstates of the t_{2g} system are [191]

$$|1\rangle = 0.781\,|yz\rangle - 0.073\,|zx\rangle + 0.620\,|xy\rangle \tag{5.11}$$

$$|2\rangle = -0.571\,|yz\rangle + 0.319\,|zx\rangle + 0.757\,|xy\rangle \tag{5.12}$$

$$|3\rangle = 0.253\,|yz\rangle + 0.945\,|zx\rangle - 0.207\,|xy\rangle \tag{5.13}$$

for sublattice 1, with corresponding orbital energies $\epsilon_1 = 289$ meV, $\epsilon_2 = 488$ meV and $\epsilon_3 = 620$ meV. This yields excitation energies $\omega_1 = \epsilon_2 - \epsilon_1 = 199$ meV, $\omega_2 = \epsilon_3 - \epsilon_1 = 331$ meV. The orbital states on the other sublattices can be obtained from lattice symmetry considerations [191]. Superexchange processes are treated as a perturbation in this model, broadening the states generated by lattice distortions. This picture is also supported by other theoretical work [189, 193, 204, 205].

It is possible to rotate the axes on each of the sublattices in such a way that in the new coordinates, the eigenstates are still given by Eqs. (5.11) through (5.13):

$$\text{subl. } 1 : (x, y, z) \mapsto (x, y, z) \tag{5.14}$$
$$\text{subl. } 2 : (x, y, z) \mapsto (y, x, z) \tag{5.15}$$
$$\text{subl. } 3 : (x, y, z) \mapsto (x, y, -z) \tag{5.16}$$
$$\text{subl. } 4 : (x, y, z) \mapsto (y, x, -z). \tag{5.17}$$

Correspondingly, the orbiton operators transform as follows:

$$\text{subl. } 1 : (a, b, c) \mapsto (a, b, c) \tag{5.18}$$
$$\text{subl. } 2 : (a, b, c) \mapsto (b, a, c) \tag{5.19}$$
$$\text{subl. } 3 : (a, b, c) \mapsto (-a, -b, c) \tag{5.20}$$
$$\text{subl. } 4 : (a, b, c) \mapsto (-b, -a, c). \tag{5.21}$$

5.4.3 Raman scattering

In the search for orbitons, Raman scattering has been an important tool for experimentalists. After the controversial first observation of orbitons in LaMnO$_3$ [163, 165, 166], the titanates now seem to be a more promising candidate. In addition to the reasons mentioned in previous sections, recent Raman data by Ulrich *et al.* [200] should be noted, which shows a striking temperature dependence: the spectral weight of the 235 meV peak in YTiO$_3$ increases dramatically when temperature is lowered. This can be naturally explained by collective orbitons: as temperature drops, the orbitons gain coherence and the spectral weight increases, analogous to two-magnon Raman scattering in the cuprates [206]. From the local dd-excitation point of view, temperature should not affect the intensity of local transitions between crystal field levels. Also, Ulrich *et al.* found that the polarization dependence of the spectra is hard to reconcile with the local excitation picture a result that we will reproduce below. In optical data [207], a peak is seen at the same energy and was ascribed to orbital excitations.

Earlier theoretical work on Raman scattering in the titanates [205] built on the assumption that JT-distortions determine the symmetry of the orbital order. In this paper, we investigate the Raman spectrum of YTiO$_3$ in both the lattice distortion and superexchange frameworks laid out in Sec. 5.4.2. We start out with the Loudon-Fleury effective Raman scattering operator [106, 107]

$$\hat{R} \propto \sum_{\langle i,j \rangle} (\boldsymbol{\epsilon}_i \cdot \boldsymbol{\delta}_{ij}) (\boldsymbol{\epsilon}_f \cdot \boldsymbol{\delta}_{ij}) \left(\hat{A}_{ij}^{(\gamma)} + \frac{n_{\gamma,i} + n_{\gamma,j}}{2} \right) \tag{5.22}$$

where the usual spin exchange Hamiltonian has been replaced by the orbital Hamiltonian of Eq. (5.7). $\boldsymbol{\epsilon}_{i,f}$ are the polarization vectors of the in- and outgoing light, $\boldsymbol{\delta}_{ij}$ connects nearest neighbors i and j. The physical picture is that the light induces an electric dipole transition to the intermediate state where a $3d\ t_{2g}$ electron ends up on a neighboring Ti ion, after which one of the electrons of this now doubly occupied site can hop back in another transition. In this process, the two involved electrons can end up in different orbitals, resulting in a two-orbiton excitation, in full analogy with two-magnon Raman scattering in the cuprates. As the light forces the electrons to perform a superexchange process independently of the intrinsic coupling mechanism of the orbitals, this effective Raman operator holds for the lattice distortion model too.

With this scattering operator, we calculate the Raman spectrum for the superexchange model. Similar calculations have been done before in the context of Raman scattering on orbital excitations in vanadates [208]. Adopting the geometry used in the experiment of Ref. [200], we take the polarization vectors to be in the plane parallel to the [110] and [001] directions: $\boldsymbol{\epsilon}_{i(f)} \propto (\frac{1}{\sqrt{2}}\sin\theta_{i(f)}, \frac{1}{\sqrt{2}}\sin\theta_{i(f)}, \cos\theta_{i(f)})$ where $\theta_{i(f)}$ is the angle the polarization vector makes with the c axis. Throughout this section we use a coordinate system in which the nearest neighbor Ti-Ti bonds are parallel to the coordinate axes. Substituting into Eq. (5.22) and using that $\sum_i n_{\gamma,i}$ is a conserved quantity in the superexchange model and that $\hat{H}_0 |0\rangle \propto |0\rangle$, we find for inelastic Raman scattering

$$\hat{R} \propto \left(\cos\theta_i \cos\theta_f - \frac{1}{2}\sin\theta_i \sin\theta_f\right) \sum_{\langle i,j\rangle_c} \hat{A}^{(c)}_{ij} \tag{5.23}$$

where the sum is over bonds in the c-direction only. Performing the transformations mentioned in Sec. 5.4.2, condensing ψ_c and Fourier transforming, we obtain

$$\begin{aligned}\sum_{\langle i,j\rangle_c} \hat{A}^{(c)} =& \frac{2}{3}\sum_{\mathbf{k}} \Big[(a^\dagger_{\mathbf{k}} - b^\dagger_{\mathbf{k}})(a_{\mathbf{k}} - b_{\mathbf{k}}) + \frac{c_z}{2}(a^\dagger_{\mathbf{k}} - b^\dagger_{\mathbf{k}})(a^\dagger_{-\mathbf{k}} - b^\dagger_{-\mathbf{k}}) \\ &+ \frac{c_z}{2}(a_{-\mathbf{k}} - b_{-\mathbf{k}})(a_{\mathbf{k}} - b_{\mathbf{k}})\Big]\end{aligned} \tag{5.24}$$

where only quadratic terms in the operators are retained. Linear terms do not appear. Next, this result is Bogoliubov transformed according to

$$\begin{aligned}a_{\mathbf{k}} =& u_{\mathbf{k}}\text{ch}\,\theta_{1,\mathbf{k}}\alpha_{1,\mathbf{k}} + v_{\mathbf{k}}\text{ch}\,\theta_{2,\mathbf{k}}\alpha_{2,\mathbf{k}} \\ &- u_{\mathbf{k}}\text{sh}\,\theta_{1,\mathbf{k}}\alpha^\dagger_{1,-\mathbf{k}} - v_{\mathbf{k}}\text{sh}\,\theta_{2,\mathbf{k}}\alpha^\dagger_{2,-\mathbf{k}},\end{aligned} \tag{5.25}$$

$$\begin{aligned}b_{\mathbf{k}} =& - v_{\mathbf{k}}\text{ch}\,\theta_{1,\mathbf{k}}\alpha_{1,\mathbf{k}} + u_{\mathbf{k}}\text{ch}\,\theta_{2,\mathbf{k}}\alpha_{2,\mathbf{k}} \\ &+ v_{\mathbf{k}}\text{sh}\,\theta_{1,\mathbf{k}}\alpha^\dagger_{1,-\mathbf{k}} - u_{\mathbf{k}}\text{sh}\,\theta_{2,\mathbf{k}}\alpha^\dagger_{2,-\mathbf{k}},\end{aligned} \tag{5.26}$$

where the indices $1, 2$ refer to the orbiton branch. This transformation diagonalizes $\hat{H}_0$ up to quadratic order if

$$u_{\mathbf{k}} = \sqrt{\frac{1}{2} + \frac{\gamma_{2,\mathbf{k}}}{2\kappa_{\mathbf{k}}}} \tag{5.27}$$

$$v_{\mathbf{k}} = \mathrm{sign}(\gamma_{3,\mathbf{k}})\sqrt{\frac{1}{2} - \frac{\gamma_{2,\mathbf{k}}}{2\kappa_{\mathbf{k}}}} \tag{5.28}$$

$$\tanh 2\theta_{1(2),\mathbf{k}} = \gamma_{1,\mathbf{k}} \pm \kappa_{\mathbf{k}}. \tag{5.29}$$

The effective Raman scattering operator now either produces two orbitons or scatters single orbitons already present in the initial state. At zero temperature, the initial state has no orbitons (in "linear orbital wave theory", i.e. if we neglect orbiton-orbiton interactions), so we keep only the two-orbiton creation part of $\sum_{\langle i,j \rangle_c} \hat{A}^{(c)}$ in Eq. (5.24):

$$\begin{aligned} \frac{1}{3}\sum_{\mathbf{k}} \Big[& \left\{(u+v)^2(c_z \mathrm{ch}\ 2\theta_1 - \mathrm{sh}\ 2\theta_1)\right\} \alpha^\dagger_{1,\mathbf{k}}\alpha^\dagger_{1,-\mathbf{k}} \\ & + \left\{(u-v)^2(c_z \mathrm{ch}\ 2\theta_2 - \mathrm{sh}\ 2\theta_2)\right\} \alpha^\dagger_{2,\mathbf{k}}\alpha^\dagger_{2,-\mathbf{k}} \\ & + 2\Big\{(u^2-v^2)[\mathrm{sh}\ (\theta_1+\theta_2) - c_z \mathrm{ch}\ (\theta_1+\theta_2)]\Big\} \alpha^\dagger_{1,\mathbf{k}}\alpha^\dagger_{2,-\mathbf{k}} \Big] \end{aligned} \tag{5.30}$$

where $c_z = \cos k_z$ and the index $\mathbf{k}$ is implied on every u, v, θ_1 and θ_2.

The cross section at zero temperature now is

$$\frac{d^2\sigma}{d\omega d\Omega} \propto \sum_f \left| \langle f | \hat{R} | 0 \rangle \right|^2 \delta(\omega - \omega_f) \tag{5.31}$$

with f labelling the two-orbiton final states with energy ω_f. The corresponding matrix elements are given by Eq. (5.30).

Because there are orbiton-orbiton interaction terms in the Hamiltonian which are neglected in "linear orbital wave theory", we introduce a phenomenological orbiton damping of $\gamma = 30$ meV. Also, broadening from other sources such as interaction with phonons and magnons can be mimicked this way.

The result is displayed in Fig. 5.6, compared to the data from Ref. [200]. In the superexchange model, only two-orbiton creation processes contribute to the Raman spectrum. The best fit is obtained for $J_{\mathrm{orb}} = 65$ meV, close to the value estimated in Ref. [185] from magnon data of YTiO$_3$ [209]. Including orbiton-orbiton interactions will probably reduce the peak energy (in analogy to two-magnon Raman scattering), increasing the fit parameter J_{SE}.

The local model of YTiO$_3$ also yields Raman spectra via Eq. (5.22). In this model, the orbital order makes the c-direction different from the a and b ones. Therefore, all bond directions are considered separately. For technical convenience, the rotations Eqs. (5.18) through (5.21) are first performed. Bonds

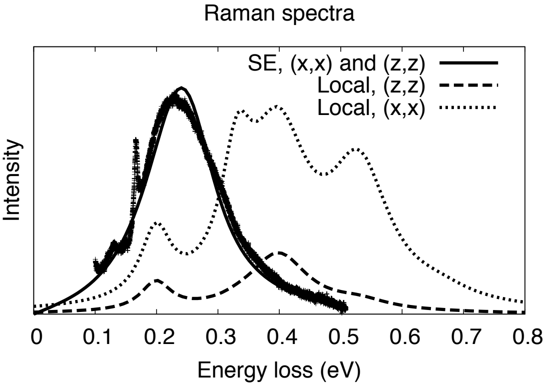

Figure 5.6: Raman spectrum of $\mathrm{YTiO_3}$ at $T = 13$ K in (z, z) geometry, taken from Ref. [200]. A background is subtracted from the data. The sharp peak around 170 meV in the data is the two-phonon Raman signal, and is not considered in our theory. The thin-solid line is the superexchange theory curve. The anisotropy of the local model is reflected in its Raman spectra: (z, z) polarization (dashed line) gives a very different spectrum from (x, x) polarization (dotted line). In the superexchange model, the xx, yy- and zz-polarizations are equivalent. It should be noted that the experimental Raman spectra are also of cubic symmetry [200].

in the c-direction connect sublattice 1 to sublattice 3, and 2 to 4. Both these bonds give the same contribution to the Raman operator:

$$\sum_{\langle i,j\rangle_c} \left(\hat{A}^{(c)}_{ij} + \frac{1}{2}\left(n_{c,i} + n_{c,j}\right) \right) =$$

$$\sum_{\langle i,j\rangle_c} \left(n_{a,i}n_{a,j} + n_{b,i}n_{b,j} + a^\dagger_i b_i b^\dagger_j a_j + b^\dagger_i a_i a^\dagger_j b_j + \frac{1}{2}\left(n_{a,i} + n_{b,j}\right) \right). \tag{5.32}$$

Note that the expression is symmetric in i, j. Similarly, for the a- and b-directions, we obtain again the same contribution for both bonds with $i \in$ sublattice 1 and $j \in$ sublattice 2, and for bonds with $i \in 3$ and $j \in 4$:

$$\sum_{\langle i,j\rangle_a} \left(n_{b,i}n_{a,j} + n_{c,i}n_{c,j} + b^\dagger_i c_i c^\dagger_j a_j + c^\dagger_i b_i a^\dagger_j c_j + \frac{1}{2}\left(n_{a,i} + n_{b,j}\right) \right), \tag{5.33}$$

$$\sum_{\langle i,j\rangle_b} \left(n_{a,i}n_{b,j} + n_{c,i}n_{c,j} + a^\dagger_i c_i c^\dagger_j b_j + c^\dagger_i a_i b^\dagger_j c_j + \frac{1}{2}\left(n_{b,i} + n_{a,j}\right) \right). \tag{5.34}$$

In general, these operators give rise to final states with one and two dd-

excitations. Using the local wave functions proposed in Ref. [204], final states with one *dd*-excitation cannot be reached in (z, z) polarization configuration, in agreement with the findings of Ref. [205]. Because the wave functions Eqs. (5.11) through (5.13) of Pavarini *et al.* are close to these states, there is little single *dd*-excitation weight (in particular in (z, z) polarization), and the spectrum is dominated by double *dd*-excitations. In the numerical calculations of the Raman spectra, the same broadening of $\gamma = 30$ meV as above is included.

The resulting Raman spectra are shown in Fig. 5.6, together with the experimental data. The experimental data peaks around 230 meV in the (z, z) polarization configuration shown here. In the experiment, other configurations give very similar line shapes, with the maximum shifting around no more than ~ 40 meV. The intensity is strongest when both in- and outgoing polarizations are directed along one of the cubic axes [200], i.e., in the zz, xx, yy polarization geometries.

Even though we have included possible orbiton-orbiton interactions only as a phenomenological damping, the superexchange model gives a very good fit to the experimental line shape: it reproduces a single peak without internal structure at approximately the right energy. The cubic isotropy of the superexchange model is in agreement with experiment, as noted in Ref. [200].

An interpretation of the Raman spectrum in terms of local crystal field excitations is problematic. Not only is the predicted strong polarization dependence of the intensity (a stark contrast between the c axis and the a, b axes) opposite of what is seen in experiment (which obeys cubic symmetry [200]), the suppression of the single dd-excitations with respect to double excitations leads to a wrong prediction of the peak energy. We tried to include corrections to the Raman operator from nondiagonal hoppings between t_{2g} orbitals but this did not improve the fit. Also, to blur the multiple peaks together into one peak, a large broadening is needed. Finally, the temperature dependence of the peak as observed in Ref. [200] is difficult to explain in the context of local dd-excitations.

5.4.4 RIXS

In the experiment [202] we analyze, the L_3 edge is used, where the 2p core electron is promoted from the spin-orbit split $j = 3/2$ state to a 3d state. The intermediate states have a complicated multiplet structure, with large spin-orbit coupling in the core levels, strong intra-ionic Coulomb interactions altered by the core potential, etc, which makes the RIXS process hard to analyze microscopically in an exact way. Fortunately, it is possible to disentangle the problem of the intermediate states from the low energy orbital transitions in the final states. Namely, since the intermediate states dynamics is much faster than that of orbital fluctuations, one can construct – based on pure symmetry grounds – a general RIXS operator describing orbital transitions between the initial and final states. In this operator, the problem of the intermediate states can be cast in the form of phenomenological matrix elements that depend only on the energy of the incident photon and its polarization factors. These martix elements can then be calculated independently, *e.g.*, by means of well developed quantum chemistry methods on small clusters. This approach is general, but can be simplified in the (physically relevant) case where the energy dependence of martix elements is smooth: they can then be regarded as effective constants at energy scales corresponding to the low frequency orbital dynamics.

RIXS spectra are described by the Kramers-Heisenberg formula, which can be written in terms of an effective scattering operator $\hat{O}_{\mathbf{q}}$:

$$A_{fi} = \langle f| \hat{D} \frac{1}{E_i - H - i\Gamma} \hat{D} |i\rangle = \langle f| \hat{O}_{\mathbf{q}} |i\rangle \tag{5.35}$$

The cross section can be written in terms of the Green's function for the effective scattering operator:

$$\frac{d^2\sigma}{d\omega d\Omega} \propto \sum_f \left| \langle f| \hat{O}_{\mathbf{q}} |i\rangle \right|^2 \delta(\omega - \omega_{fi}) = -\frac{1}{\pi} \mathfrak{Im} \left\{ G(\omega) \right\} \tag{5.36}$$

with

$$G(\omega) = -i \int_0^\infty dt e^{i\omega t} \langle i| \hat{O}^\dagger_{\mathbf{q}}(t) \hat{O}_{\mathbf{q}}(0) |i\rangle . \tag{5.37}$$

In Eq. (5.1), we neglect RIXS processes that create excitations on more than two sites in the final state, and further assume that the two-site processes are dominated by processes on nearest neighbors. Further, we assume that the titanates belong to the regime of small Γ, and that the internal dynamics of intermediate states is the fastest process in the problem. The core hole potential is then dominated by the A_{1g} component, but this only gives contributions to the Bragg peaks in the leading order (single site) of Eq. (5.1). The subleading order therefore consists of single site processes $\hat{O}_i$ of other than A_{1g} symmetries, and of two-site processes $\hat{O}_{ij}$ of A_{1g} symmetry.

The single site coupling of RIXS to the orbitals can be dubbed a "shakeup" process. If we allow the core hole potential to have a symmetry other than A_{1g}, it can locally induce an orbital flip. If the orbital ground-state is dominated by superexchange many-body interactions, a local flipped orbital will strongly interact with the neighboring sites and thus becomes a superposition of extended (multi-)orbitons. In the limit of strong crystal field splittings, however, this excitation remains a localized, on-site transition between t_{2g} levels.

Two-site processes $\hat{O}_{ij}$ may involve modulation of the superexchange bonds, analogous to two-magnon RIXS, where the superexchange constant J is effectively modified at the core hole site [10,51,52,54]. The core hole potential locally changes the Hubbard U, which in effect changes $J_{SE} = 4t^2/U$ on the Ti-Ti bonds coupled to the core hole site. Alternatively, the two-site processes can describe the lattice-mediated interaction that is altered by the presence of a core hole. The equilibrium positions and vibration frequencies of the oxygens surrounding the core hole site may change, affecting the intersite interactions. As said above, the A_{1g} component of the core hole potential is most relevant in the two-site coupling channel $\hat{O}_{ij}$.

This section is divided into three subsections. Subsection 5.4.4 deals with the single site shakeup mechanism and contains the evaluation in the superexchange model. The next subsection, 5.4.4, is devoted to the calculation of the same processes in the local model of the orbital excitations in YTiO$_3$. The final subsection 5.4.4 covers two-site processes, evaluated within the superexchange model. A detailed comparison is made of the RIXS spectra arising from the different models.

Single site processes – Superexchange model. We start out with an analysis of the single site processes. RIXS processes that involve orbital excitations on a single site are dominated by direct transitions between the t_{2g} orbitals when the core hole potential is not of A_{1g} symmetry. In a superexchange dominated system, a local flipped orbital strongly interacts with the neighboring sites and becomes a superposition of extended orbitons.

We start from the Kramers-Heisenberg equation (2.31), where we insert the polarization-dependent dipole operator $\hat{D}$ which we take to be local: $\hat{D} = \sum_i \hat{D}_i$ with

$$\begin{aligned}\hat{D}_i = &\sum_{d,m} \Big(e^{i\mathbf{k}\cdot\mathbf{R}_i} \left|m\right\rangle \left\langle m\right| \hat{\mathbf{r}} \cdot \boldsymbol{\epsilon} \left|d\right\rangle \left\langle d\right| \\ &+ e^{-i\mathbf{k}'\cdot\mathbf{R}_i} \left|d\right\rangle \left\langle d\right| \hat{\mathbf{r}} \cdot \boldsymbol{\epsilon}' \left|m\right\rangle \left\langle m\right| \Big) + \text{h.c.},\end{aligned} \tag{5.38}$$

where $|d\rangle$ denotes the state of atom i when it is not photo-excited and $|m\rangle$ denotes the system's intermediate eigenstates:

$$\hat{H} = \sum_m E_m \left|m\right\rangle \left\langle m\right|. \tag{5.39}$$

Now we consider only the single site part of the effective scattering operator in Eq. (5.1):

$$\hat{O}_i = \sum_{d,d',m} \left|d'\right\rangle \left\langle d'\right| \hat{\mathbf{r}}' \cdot \boldsymbol{\epsilon}' \left|m\right\rangle \frac{1}{E_i - E_m - i\Gamma} \left\langle m\right| \boldsymbol{\epsilon} \cdot \hat{\mathbf{r}} \left|d\right\rangle \left\langle d\right| \tag{5.40}$$

Next we decompose the operator part into terms transforming according to the rows of the irreducible representations of the octahedral group (labeled by Γ, not to be confused with the core hole lifetime broadening):

$$\left|d'\right\rangle \left\langle d\right| = \sum_\Gamma \Gamma_{d'd} \hat{\Gamma}. \tag{5.41}$$

In the second quantized picture, we need only terms that are quadratic in the creation and annihilation operators. With the irreducible representations

A_{1g}, T_{1u}, E_g and T_{2g} all possible $|d'\rangle \langle d|$ can be constructed. Therefore $\hat{\Gamma}$ assumes only the following forms:

$$A_{1g} : \hat{\Gamma} = 1 \tag{5.42}$$

$$T_{1u} : \hat{\Gamma} \in \{\hat{l}_x, \hat{l}_y, \hat{l}_z, \} \tag{5.43}$$

$$E_g : \hat{\Gamma} \in \{\hat{Q}_x, \hat{Q}_z\} \tag{5.44}$$

$$T_{2g} : \hat{\Gamma} \in \{\hat{T}_x, \hat{T}_y, \hat{T}_z\}. \tag{5.45}$$

The operators $\hat{\Gamma}$ and the corresponding 3×3 matrices $\Gamma_{d'd}$ are defined in Appendix B.1. Because A_{1g} only contributes to elastic scattering, we drop it from hereon.

Further, we also decompose the dipole matrix elements into

$$\langle d'| \hat{\beta} |m\rangle \langle m| \hat{\alpha} |d\rangle = \sum_{\Gamma} \Gamma_{\beta\alpha} M^{\Gamma}_{d'd} \tag{5.46}$$

with $\hat{\alpha}, \hat{\beta} \in \{\hat{x}, \hat{y}, \hat{z}\}$ and the $M^{\Gamma}_{d'd}$ listed in Appendix B.2: Eqs. (B.10) through (B.18). Plugging Eqs. (5.41) and (5.46) into Eq. (5.40), we obtain

$$\hat{O}_i = \sum_{d,d',m} \sum_{\Gamma'} \sum_{\alpha,\beta} \frac{\epsilon'_\beta \epsilon_\alpha \Gamma'_{\beta\alpha} M^{\Gamma'}_{d'd}}{E_i - E_m - i\Gamma} \sum_{\Gamma} \Gamma_{d'd} \hat{\Gamma}_i \tag{5.47}$$

which can be simplified using

$$\sum_{d,d'} M^{\Gamma'}_{d'd} \Gamma_{d'd} = \delta_{\Gamma,\Gamma'} \sum_{d,d'} M^{\Gamma}_{d'd} \Gamma_{d'd}. \tag{5.48}$$

This identity can be proven by interpreting M^{Γ} and Γ as matrices indexed by d and d'. Then it can be seen that $M^{\Gamma} \propto \Gamma$. We thus obtain

$$\sum_{d,d'} M^{\Gamma'}_{d'd} \Gamma_{d'd} = \mathrm{Tr}\left(M^{\Gamma'} \Gamma^T\right) \propto \mathrm{Tr}\left(\Gamma' \Gamma^T\right) \tag{5.49}$$

which is zero for $\Gamma \neq \Gamma'$, proving the above identity. We find then

$$\hat{O}_i = \sum_{\Gamma} P_{\Gamma} \mathcal{M}_{\Gamma} \hat{\Gamma}_i \tag{5.50}$$

with a polarization factor

$$P_{\Gamma} = \sum_{\alpha,\beta} \epsilon'_\beta \Gamma_{\beta\alpha} \epsilon_\alpha \tag{5.51}$$

and the matrix elements $\mathcal{M}_{\Gamma}$ depending on the multiplet effects in the intermediate state

$$\mathcal{M}_{\Gamma} = \sum_{d,d',m} \frac{M^{\Gamma}_{d'd} \Gamma_{d'd}}{E_i - E_m - i\Gamma} \ . \tag{5.52}$$

One can perform the sum over m, which yields

$$\sum_m \frac{M^{Q_x}_{d'd}}{E_i - E_m - i\Gamma} = \langle d'| \left(\hat{y} \frac{1}{E_i - H - i\Gamma} \hat{y} - \hat{x} \frac{1}{E_i - H - i\Gamma} \hat{x} \right) |d\rangle \tag{5.53}$$

and similar expressions for the other representations. As discussed above, we will assume that the intermediate state dynamics is much faster than that of t_{2g} orbitals we are interested in, and thus regard the matrix elements as phenomenological constants. Further, using that $\mathcal{M}_\Gamma$ does not depend on any coordinate and therefore must be invariant under the octahedral group, we obtain

$$\mathcal{M}_Q \equiv \mathcal{M}_{Q_x} = \mathcal{M}_{Q_z} \tag{5.54}$$

$$\mathcal{M}_T \equiv \mathcal{M}_{T_x} = \mathcal{M}_{T_y} = \mathcal{M}_{T_z} \tag{5.55}$$

$$\mathcal{M}_l \equiv \mathcal{M}_{l_x} = \mathcal{M}_{l_y} = \mathcal{M}_{l_z}. \tag{5.56}$$

The $\mathcal{M}_\Gamma$ are hard to calculate explicitly since they involve inverting H, which contains the multiplet structure. In the following, we assume $\mathcal{M}_\Gamma = \mathcal{M}$ for all Γ. This is a reasonable assumption: the core hole generates a multitude of many-body states that evolves very rapidly due to the large spin-orbit coupling and intra-ionic Coulomb interactions, and therefore its potential is averaged. Any particular symmetry is washed away; all become equal, except for the A_{1g} component, which is enhanced at the cost of the others. This is also the reason why the experiments at the t_{2g} and e_g edges are similar [202]: the different edges create different multiplet structures initially, but these differences are averaged out by the intermediate state dynamics, as far as we are concerned with t_{2g} orbital transitions at relatively low energies 0.2-0.3 eV.

Note that P_Γ and $\mathcal{M}_\Gamma$ are independent of the site i. Only $\hat{\Gamma}$ depends on i, giving

$$\hat{O}_{\mathbf{q}} = \sum_\Gamma P_\Gamma \mathcal{M}_\Gamma \sum_i e^{i\mathbf{q}\cdot\mathbf{R}_i} \hat{\Gamma}_i. \tag{5.57}$$

Most interference terms between different Γ's are zero. This comes about because of the specific ground state ordering. Transforming to the local axes (Eq. (15) in Ref. [185]), the ground state and $\hat{H}_0$ are invariant under translations, while the operators $\hat{T}_{\alpha,i}$ and $\hat{l}_{\alpha,i}$ (with $\alpha \in \{x, y, z\}$) acquire a phase upon translation to a different sublattice, which is equivalent to a momentum shift (by orbital ordering vectors) for the corresponding $\hat{\Gamma}_{\mathbf{q}}$. Therefore, many interference terms are zero, which can be seen from Eqs. (5.36) and (5.37): two operators with different momenta cannot bring the ground state (zero momentum) back to itself. The only non-vanishing interference terms are $\langle 0| \hat{Q}^\dagger_{x,\mathbf{q}}(t)\hat{Q}_{z,\mathbf{q}}(0) |0\rangle$ which do not acquire momentum shifts and $\langle 0| \hat{T}^\dagger_{\alpha,\mathbf{q}}(t)\hat{l}_{\alpha,\mathbf{q}}(0) |0\rangle$ where the momentum shifts cancel.

To compare with experiment, we calculate the polarization factors P_Γ for the experimental setup of Ref. [202], where $\mathbf{q}$ is along the [001]-direction. Only the incoming polarization is fixed, the outgoing polarization is not detected and should be averaged over. We have

$$\boldsymbol{\epsilon} = (\frac{1}{\sqrt{2}}\sin\theta, \frac{1}{\sqrt{2}}\sin\theta, \cos\theta) \tag{5.58}$$

$$\boldsymbol{\epsilon}'_H = (-\frac{1}{\sqrt{2}}\sin\theta, -\frac{1}{\sqrt{2}}\sin\theta, \cos\theta) \tag{5.59}$$

$$\boldsymbol{\epsilon}'_V = (\frac{1}{\sqrt{2}}, \frac{1}{\sqrt{2}}, 0) \tag{5.60}$$

with 2θ the scattering angle. Then, we find for the horizontal outgoing polarization $\boldsymbol{\epsilon}'_H$ (i.e. the electric field vector is in the scattering plane):

$$P_{Q_x,H} = P_{T_x,H} = P_{T_y,H} = P_{l_z,H} = 0 \tag{5.61}$$

$$P_{A_{1g},H} = \frac{1}{3}\cos 2\theta \tag{5.62}$$

$$P_{Q_z,H} = \frac{1}{2\sqrt{3}}(1+\cos^2\theta) \tag{5.63}$$

$$P_{T_z,H} = \frac{1}{2}\sin^2\theta \tag{5.64}$$

$$P_{l_x,H} = -P_{l_y,H} = -\frac{i}{\sqrt{2}}\sin\theta\cos\theta \tag{5.65}$$

and for vertical outgoing polarization $\boldsymbol{\epsilon}'_V$ (electric field vector perpendicular to the scattering plane):

$$P_{A_{1g},V} = P_{Q_z,V} = P_{T_z,V} = 0 \tag{5.66}$$

$$P_{Q_x,V} = -\frac{1}{2}\sin\theta \tag{5.67}$$

$$P_{T_x,V} = -P_{T_y,V} = \frac{1}{2\sqrt{2}}\cos\theta \tag{5.68}$$

$$P_{l_x,V} = P_{l_y,V} = -\frac{i}{2\sqrt{2}}\cos\theta \tag{5.69}$$

$$P_{l_z,V} = \frac{i}{2}\sin\theta. \tag{5.70}$$

For horizontal polarization, the polarization factors make all remaining interference terms zero.

In Appendix B.3, the one- and two-orbiton parts of the $\hat{\Gamma}_{\mathbf{q}} = \sum_i e^{i\mathbf{q}\cdot\mathbf{R}_i}\hat{\Gamma}_i$ are listed. They are obtained by performing the transformations on the orbital operators mentioned in Ref. [185]. Then, the ψ_c orbital (with corresponding annihilation operator $\tilde{c}$) is condensed:

$$n_{\tilde{c}} = |c_0|^2 + \delta n_{\tilde{c}} \tag{5.71}$$

where $\delta n_{\tilde{c}}$ is the fluctuating part. In the completely ordered state, $\langle \delta n_{\tilde{c}} \rangle = \langle n_{\tilde{a}} \rangle = \left\langle n_{\tilde{b}} \right\rangle = 0$ and $|c_0|^2 = 1$, while in the completely disordered state $\langle \delta n_{\tilde{c}} \rangle = \langle n_{\tilde{a}} \rangle = \left\langle n_{\tilde{b}} \right\rangle = 1/3$ and $|c_0|^2 = 0$. Ref. [185] obtains a finite value for the quadrupole orbital order parameter:

$$\hat{Q} = n_{\tilde{c}} - (n_{\tilde{a}} + n_{\tilde{b}})/2 \equiv \left\langle \hat{Q} \right\rangle + \delta\hat{Q} \simeq 0.19 + \delta\hat{Q} \tag{5.72}$$

with the fluctuating part averaging to zero. This fixes $|c_0|^2 \simeq 0.19$. Taking the square root of Eq. (5.71), one arrives at

$$\tilde{c} = \tilde{c}^{\dagger} = \sqrt{|c_0|^2 + \delta n_{\tilde{c}}} \approx |c_0| + \frac{1}{2\,|c_0|}\delta n_{\tilde{c}} \tag{5.73}$$

to first order in the fluctuations $\delta n_{\tilde{c}}$.

In the process of writing the $\hat{\Gamma}_{\mathbf{q}}$ in terms of orbiton operators, unphysical contributions to the intensity may appear as a result of neglecting cubic and higher order terms in the orbiton operators. When restoring all terms, these unphysical contributions should cancel by symmetry. For $\mathbf{q}$ along the [001] direction for instance, $[\hat{H}, \hat{Q}_{z,\mathbf{q}}] = 0$ if we use the untransformed forms Eqs. (5.7) and (B.5), and it is clear that there should only be an elastic contribution to the intensity. However, in terms of orbitons, this selection rule is violated if we go only up to quadratic orbiton terms. To make sure these unphysical contributions are dropped, we first calculate the commutator in the untransformed picture. If this yields zero, the commuting part of the scattering operator is dropped. Applying this procedure to the case where $\mathbf{q}$ is along the [001] direction, we find that only $\hat{Q}_{z,\mathbf{q}}$ among the operators (5.43) to (5.45) is zero while all the other channels give finite contributions.

Since we did not include explicitly the orbiton-orbiton interactions, damping of the orbitons should still be taken care of, at least on a phenomenological level. As in the case of Raman scattering calculations, we introduce by hand an energy broadening γ of the orbiton states (half-width at half maximum, HWHM) of $\gamma = 0.4\ J_{\mathrm{orb}}$. This broadening can also be used to take orbiton damping by phonons, magnons etc. into account. In addition to this, there is an experimental broadening added of 27.5 meV (HWHM) [202].

The resulting spectra are shown in Fig. 5.7. The intensity is strongly momentum-dependent (especially for $\mathbf{q}$ along the z direction), which is also seen in the experiments [202]. This dependence is mainly due to the coherent response of the exchange-coupled orbitals which enhances at large momenta, reflecting staggered orbital order in the ground state – Eq. (5.9). In Fig. 5.8, the theoretical cross section (with $\mathbf{q}$ along the z direction and horizontal incoming polarization, i.e. the electric field is in the scattering plane) is compared to the experimental data. The main features of the data [202] are reproduced: the spectral weight increases with increasing q_z and there is virtually no dispersion of the maximum of the theoretical curve (because it is determined by the two-orbiton continuum, containing an integration over the Brillouin zone).

Especially in plots (b) and (c), the one-orbiton shoulder seems a bit too large. We note here again that the weight of this shoulder is controlled by the orbital order parameter: if the orbital order melts, $|c_0|^2$ decreases and the one-orbiton peak becomes less intense. The value we used ($|c_0|^2 = 0.19$) is obtained at zero temperature, assuming that $YTiO_3$ is a fully saturated ferromagnet [184, 185]. Under realistic conditions, $|c_0|^2$ is expected to be smaller than 0.19. Indeed, the saturated ordered moment in $YTiO_3$ is actually $0.84\mu_B$, which is reduced further to approximately $0.80\mu_B$ at $T = 15$ K [203, 210]. Correspondingly, the orbital order is decreased by joint spin-orbital quantum fluctuations, suppressing the one-orbiton peak.

The best chance to see a one-orbiton contribution to the spectrum is with momentum transfer directed maximally in the [110] direction. Fig. 5.9 shows the prediction for the shakeup mechanism with $|c_0|^2 = 0.19$: the one-orbiton peak is about as strong as the two-orbiton peak.

Single site processes – Local model. Although the response functions of the local model of $YTiO_3$ are entirely different from the superexchange model, the phenomenological scattering operator Eq. (5.1) is still valid. Focusing on single site processes, Eq. (5.57) can be evaluated using the wave functions found by Pavarini *et al.*: Eqs. (5.11) through (5.13). Since the eigenstates of the local model have a very simple form, we can straightforwardly use Eqs. (B.1) through (B.8) to evaluate the RIXS spectrum. The P_Γ and $\mathcal{M}_\Gamma$ remain the same as in the collective orbiton case. The spectrum now consists of two sharp peaks at ω_1 and ω_2. These peaks can be broadened by coupling to the lattice as well as due to the SE coupling.

Because there are four sublattices which all support their own, local eigenstates, the RIXS intensity can be decomposed into four signals. From the expressions Eqs. (5.18) through (5.21), it is easily derived how the $\hat{\Gamma}_i$ transform.

So far, the analysis is similar to Sec. 5.4.4. However, in the local model, the eigenstates are local and this changes the analysis of Sec. 5.4.4 at two important points. The first one is that the momentum shifts of $\hat{\Gamma}_{\mathbf{q}}$ do not destroy interference terms: any final state $|f\rangle$ can be reached with any shift of $\mathbf{q}$. All interference terms can in principle be present. The second point to be noted is that, because the eigenstates are local, the only momentum dependence of the cross section comes in through the experimental geometry, which is reflected in the polarization factors P_Γ.

When we compare the theoretical RIXS spectrum of this model to experiment, we again have to take into account the average over the two outgoing polarizations. Assuming again $\mathcal{M}_\Gamma$ are the same for all Γ, and introducing the same broadening as before (HWHM $\gamma \approx 30$ meV phenomenological intrinsic broadening plus 27.5 meV HWHM experimental broadening), we obtain the spectra shown by the solid lines in Fig. 5.10.

It is evident that the local model yields a RIXS spectrum that does not agree

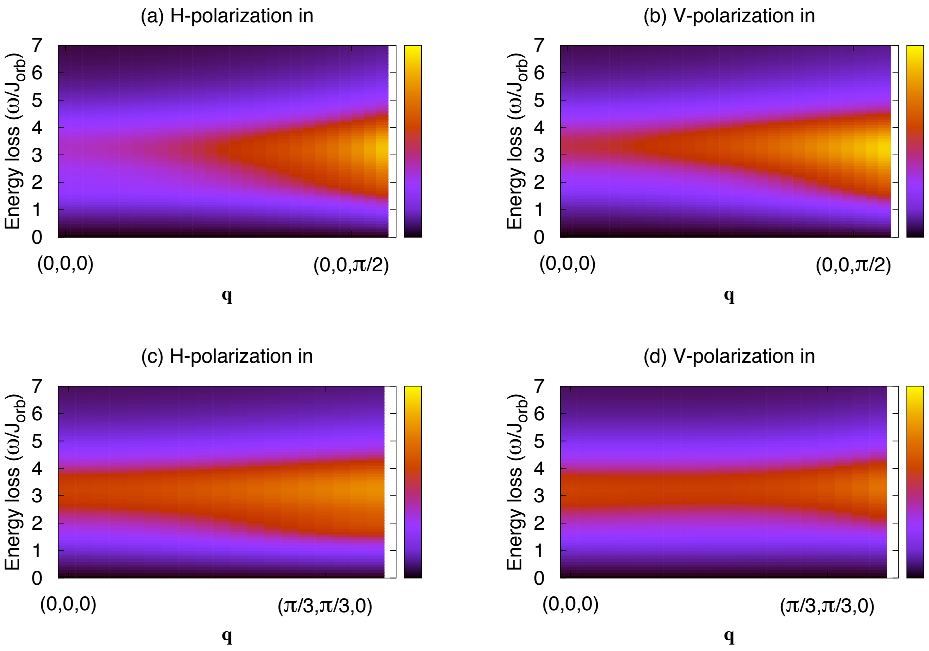

Figure 5.7: RIXS spectra for a model of superexchange-driven orbital order with RIXS coupling to orbitons only via the single site mechanism. Spectra (a) and (b) are for $\mathbf{q}$ directed along the [001] direction, and (c) and (d) for $\mathbf{q}$ along the [110] direction. Spectra (a) and (c) are for horizontal incoming polarization (electric field in the scattering plane), and (b) and (d) are for vertical incoming polarization (electric field perpendicular to the scattering plane). Note that the $\mathbf{q} = \mathbf{0}$ points are different in each spectrum because of the different experimental geometries, leading to different P_Γ. We only plotted the experimentally accessible part of the Brillouin Zone.

well with experiment. Firstly, there is no two-peak structure visible in the data. The presence of a two-peak structure in the theoretical curves does not depend on the assumption that all the $\mathcal{M}_\Gamma$ are equal. We may finetune the model to produce a better fit by changing the energy levels found in Ref. [191] so that both crystal field transitions have an energy of 240 meV, and introducing a very large intrinsic broadening of 100 meV (see the dashed lines in Fig. 5.10). But even in the artificially optimized case of degenerate levels to produce a single peak, the intensity trend remains in contradiction with experiment. Further, it is impossible to tune the energy levels to optimize simultaneously the RIXS and Raman data. Both experiments show a peak at the same energy, while the local model theory predicts the Raman spectra (with its double crystal field excitations) to peak at approximately double the RIXS peak energy.

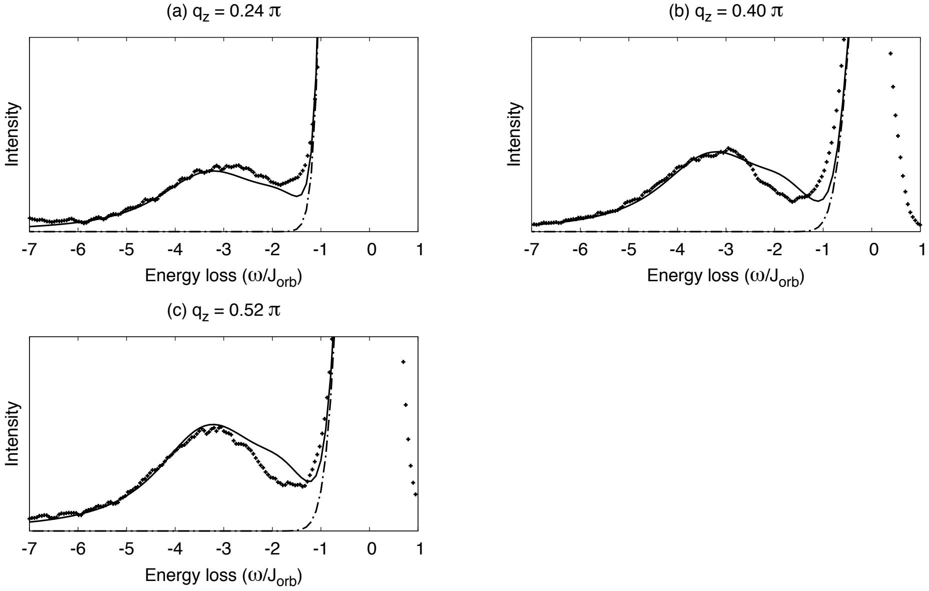

Figure 5.8: RIXS spectra for a SE-driven orbital order with RIXS coupling to orbitons only via the single site mechanism (solid line), compared to the experimental data [202]. The vector $\mathbf{q}$ is directed along the [001] direction, with q_z as indicated in the figures. We took $J_{\rm orb} = 80$ meV, and introduced a phenomenological HWHM broadening of $\gamma = 0.4\ J_{\rm orb} \approx 30$ meV for the orbitons, as well as the HWHM experimental resolution of 27.5 meV. The elastic peak is fitted with a Gaussian (dash-dotted line).

Even though we could improve the line shape by increasing γ, the intensity gain with increasing q_z cannot be reproduced in any way. In fact, the trend is the opposite: as q_z increases, the spectral weight of the theoretical spectrum decreases (see Fig. 5.10). We recall that the $\mathbf{q}$-dependence in this case is merely due to polarization factors Eqs. (5.61–5.70), since in a local picture, each Ti ion contributes independently to the cross section. This is in sharp contrast with the superexchange picture, where the intensity has an intrinsic $\mathbf{q}$-dependence because of the collective response of all the Ti ions.

Two-site processes. The second term in the expansion of the effective scattering operator, Eq. (5.1), involves two-site processes. Due to the strong multiplet effects, the core hole potential is averaged out and becomes mainly of A_{1g} symmetry. While such a potential cannot directly flip the orbitals at the core hole site, it does affect multi-site processes. In the case of the superexchange model, the core hole potential effectively changes the superexchange constant J_{SE} lo-

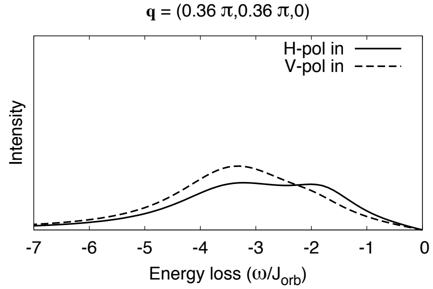

Figure 5.9: Spectra, obtained with the single site mechanism, for the largest experimentally accessible momentum transfer directed along the [110] direction. The solid line indicates the case where the incoming polarization is horizontal, the dashed line is for vertical incoming polarization. The elastic peak has been removed. In the horizontally polarized case, the single orbiton peak is quite strong and should be visible in experiments if the system is superexchange-driven and the RIXS signal is dominated by the single site mechanism.

cally as discussed earlier in the context of RIXS on magnons [10, 51, 52]. This process is illustrated in Fig. 5.11. (In principle, it is also possible that the core hole potential modifies the orbital interactions via the lattice vibrations.) In this section, we consider the superexchange modulation mechanism to illustrate two-site process in RIXS on orbital fluctuations.

The SE modification can be derived explicitly by starting from a Hubbard model

$$\begin{aligned}\tilde{H} = &- t \sum_i \left(b^\dagger_{i\pm\hat{x}} b_i + c^\dagger_{i\pm\hat{x}} c_i + a^\dagger_{i\pm\hat{y}} a_i + c^\dagger_{i\pm\hat{y}} c_i + a^\dagger_{i\pm\hat{z}} a_i + b^\dagger_{i\pm\hat{z}} b_i \right) \\ &+ U \sum_i \left(n_{b,i} n_{c,i} + n_{a,i} n_{c,i} + n_{a,i} n_{b,i} \right) \\ &- U_c \sum_i p_i p^\dagger_i \left(n_{a,i} + n_{b,i} + n_{c,i} - 1 \right) \end{aligned} \tag{5.74}$$

where the last term includes the Coulomb energy U_c of the core hole attracting the t_{2g} electrons. p_i is the annihilation operator for 2p core electrons at site i. We have taken the core hole potential to be of A_{1g} symmetry. Doing perturbation theory to second order in $t/U_{(c)}$ (U and U_c are about the same order of magnitude), we obtain the superexchange Hamiltonian

$$H = H_0 + \sum_{i,\delta} p_i p^\dagger_i \left(J_2 \hat{A}^{(\gamma)}_{i,i+\delta} - J_1 \hat{n}^{(\gamma)}_{i+\delta} + \text{const.} \right) \tag{5.75}$$

with δ pointing to nearest neighbors, $n^{(c)}_i = n_{a,i} + n_{b,i}$ (the other $n^{(\gamma)}$ can be

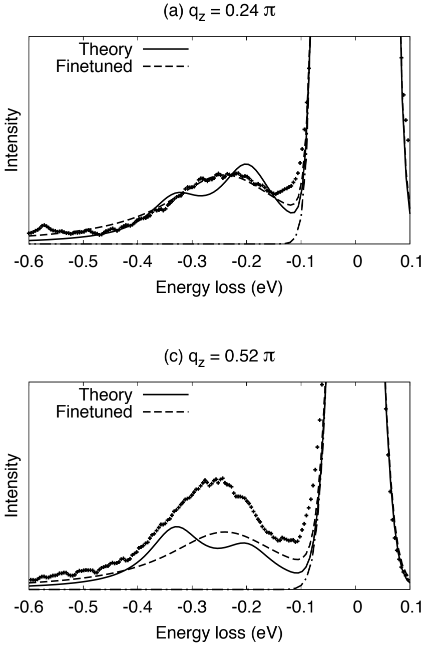

Figure 5.10: RIXS spectra for the local model (solid and dashed lines) compared to experimental data [202]. The vector $\mathbf{q}$ is directed along the [001] direction, where q_z is indicated in the figures. The dashed curve shows the artificially optimized model with degenerate crystal field levels. We introduced a phenomenological intrinsic HWHM broadening ($\gamma \approx 30$ meV [solid line] and $\gamma = 100$ meV [dashed line]) for the final states and added experimental broadening.

obtained by permuting the indices a, b, c) and

$$J_1 = \frac{t^2}{U - U_c} - \frac{t^2}{U} \qquad \text{and} \qquad J_2 = \frac{t^2}{U + U_c} + \frac{t^2}{U - U_c} - \frac{2t^2}{U} \tag{5.76}$$

so that $J_1/J_2 = (1 + U/U_c)/2$. Eq. (5.75) shows we get the unperturbed Hamiltonian plus a contribution which is active only if there is a core hole (in which case $p_i p_i^\dagger \to 1$). The J_1 term involves single site processes only, and is therefore included in the general description in Sec. 5.4.4. In the following, the J_1 term will be dropped.

For simplicity, polarization effects are neglected and we assume U_c to be independent of the specific dipole transition. We take

$$\hat{D} = \sum_i \left(e^{-i\mathbf{q}_{\text{in}} \cdot \mathbf{R}_i} p_i d_i^\dagger + e^{i\mathbf{q}_{\text{out}} \cdot \mathbf{R}_i} p_i^\dagger d_i \right) + \text{h.c.} \tag{5.77}$$

with p_i the 2p electron annihilation operator and d_i the 3d e_g electron annihilation

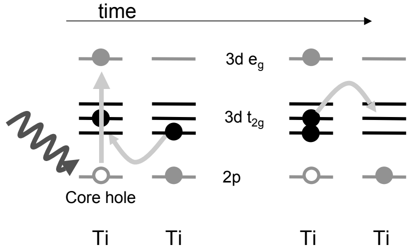

Figure 5.11: In the SE model, two-site RIXS processes locally modify the SE interaction, coupling the RIXS core hole to the t_{2g} orbitals. Shown is an orbital SE process between two neighboring Ti ions in the presence of a core hole. On the left, one of the ions is excited by an incoming x-ray photon. After that, the t_{2g} electrons undergo a SE process. On the right, the virtual state of the SE process is depicted. The presence of the core hole frustrates the SE process. Instead of the usual Hubbard U, the energy of the virtual state is lowered by the presence of the positively charged core hole. This modifies the SE constant $J_{SE} = 4t^2/U$ at the core hole site.

operator. The position of the i^{th} site is $\mathbf{R}_i$. The transfered momentum is $\mathbf{q} = \mathbf{q}_{\text{out}} - \mathbf{q}_{\text{in}}$. The neglected polarization dependence could give rise to a $\mathbf{q}$-dependent factor in the cross section, but will not affect the line shape for a specific $\mathbf{q}$.

The relevant energy scale for the excitation of orbitons in the intermediate states via superexchange bond modulation is J_2, as established above, as long as the core hole potential is of A_{1g} symmetry. This is the case when core level spin-orbit coupling and Hund's rule coupling are large compared to J_2: the core hole evolves rapidly with time and its potential's symmetry averages out to A_{1g} before any orbitons can be excited. Because the symmetry is effectively cubic, bonds in all directions are affected in the same way. The effective scattering operator must therefore be a function of $\sum_\delta \hat{A}^{(\gamma)}_{i,i+\delta}$ which is of A_{1g} symmetry. Non-linear operators like $\hat{A}^{(\gamma)}_{i,i+\delta} \hat{A}^{(\gamma)}_{i,i+\delta'}$ are excluded, they are expected to yield smaller contributions because more and more distant sites are involved. In the expansion Eq. (5.1), these come in at different orders. The only remaining candidate for the two-site effective scattering operator is therefore

$$\hat{O}_{\mathbf{q}} = \mathcal{M}_2 \sum_{i,\delta} e^{i\mathbf{q}\cdot\mathbf{R}_i} \hat{A}^{(\gamma)}_{i,i+\delta} \tag{5.78}$$

where $\mathcal{M}_2$ is an unknown phenomenological matrix element, in the same way as in Sec. 5.4.4. By construction, the two-site process matrix element $\mathcal{M}_2$ should be proportional to J_2 with a constant determined by the intermediate state dynamical susceptibilities. At this stage, without microscopical calculations of the single-site $\mathcal{M}_\Gamma$ (5.52) and two-site $\mathcal{M}_2$ matrix elements, we cannot judge which coupling process dominates the observed RIXS on orbital excitations. Instead, we calculate two-site process independently and compare it with both experimental data and the results obtained above for single-site coupling mechanism.

As it turns out, the two-site effective scattering operator (5.78) contains only two-orbiton creation terms; it does not create single orbitons because the orbitons are constructed in the first place to diagonalize the Hamiltonian: all linear contributions to $\hat{A}_{ij}^{(\gamma)}$ in Eq. (5.8) are canceled (similar to the Raman scattering calculations above).

Using again the transformations on the orbital operators mentioned in Ref. [185], condensing the ψ_c orbital and transforming to orbiton operators, we obtain for the two-orbiton creation part

$$\begin{aligned}\hat{O}_{\mathbf{q}}^{(2)} =&\mathcal{M}_2 \sum_{\mathbf{k}} \Big[f_{11}(\mathbf{k},\mathbf{q}) \alpha^{\dagger}_{1,\mathbf{k}} \alpha^{\dagger}_{1,-\mathbf{k}-\mathbf{q}} \\ &+ f_{22}(\mathbf{k},\mathbf{q}) \alpha^{\dagger}_{2,\mathbf{k}} \alpha^{\dagger}_{2,-\mathbf{k}-\mathbf{q}} + f_{12}(\mathbf{k},\mathbf{q}) \alpha^{\dagger}_{1,\mathbf{k}} \alpha^{\dagger}_{2,-\mathbf{k}-\mathbf{q}} \Big] \end{aligned} \tag{5.79}$$

where the $f_{ij}(\mathbf{k},\mathbf{q})$ are lengthy functions listed in Appendix B.4. The cross section then is

$$\begin{aligned}\frac{d^2\sigma^{(2)}}{d\omega d\Omega} &\propto \sum_f \left| \langle f | \, \hat{O}_{\mathbf{q}}^{(2)} \, |0\rangle \right|^2 \delta(\omega - \omega_{1/2,\mathbf{k}} - \omega_{1/2,\mathbf{k}+\mathbf{q}}) \\ &= \frac{1}{2} \sum_{\mathbf{k}} \Big[\left| f_{11}(\mathbf{k},\mathbf{q}) + f_{11}(-\mathbf{k}-\mathbf{q},\mathbf{q}) \right|^2 \delta(\omega - \omega_{1,\mathbf{k}} - \omega_{1,\mathbf{k}+\mathbf{q}}) \\ &+ \left| f_{22}(\mathbf{k},\mathbf{q}) + f_{22}(-\mathbf{k}-\mathbf{q},\mathbf{q}) \right|^2 \delta(\omega - \omega_{2,\mathbf{k}} - \omega_{2,\mathbf{k}+\mathbf{q}}) \\ &+ 2 \left| f_{12}(\mathbf{k},\mathbf{q}) \right|^2 \delta(\omega - \omega_{1,\mathbf{k}} - \omega_{2,\mathbf{k}+\mathbf{q}}) \Big] . \end{aligned} \tag{5.80}$$

The resulting cross section for transfered momenta along the [001] direction is shown in Fig. 5.12. As in the above sections, we introduced here by hand an energy broadening γ of the orbiton states of $\gamma = 0.4 \; J_{\text{orb}}$.

A few things should be noted. Firstly, the spectrum disappears at $\mathbf{q} = \mathbf{0}$. This is clear from Eq. (5.78): the scattering operator becomes proportional to the Hamiltonian Eq. (5.7), giving elastic scattering only.

Secondly, the spectrum shown in Fig. 5.12 is calculated without taking polarization dependence into account. That could change the relative spectral weight for different $\mathbf{q}$'s, but does not affect the line shapes.

In Fig. 5.13 we compare the calculated superexchange spectra for the specific $\mathbf{q}$ values of the experiments reported in Ref. [202]. The only free parameter (J_{orb}) gives a best fit for $J_{\text{orb}} = 75$ meV. As is evident, the increase in spectral weight is qualitatively accounted for by the theory, although the theoretical curves show a much stronger increase with increasing q_z. We note that one factor that could diminish this discrepancy is, as stated above, the polarization factor we omitted: it could change the relative weight (but not the line shape).

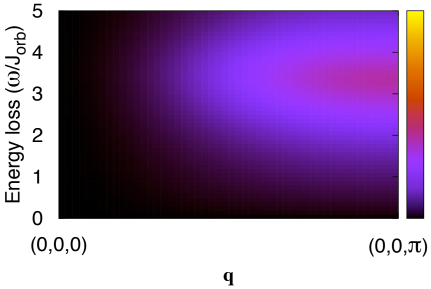

Figure 5.12: RIXS spectrum for two-site processes within the superexchange model. The color scale denotes the intensity. The figure shows $\mathbf{q}$ running from $(0, 0, 0)$ to $(0, 0, \pi)$. One-orbiton creation is not allowed for the superexchange modulation mechanism. The intrinsic energy broadening γ of the orbiton states is $\gamma = 0.4\ J_{\rm orb} \approx 30$ meV, and the added experimental resolution of 27.5 meV [202] is approximately $0.34\ J_{\rm orb}$.

Summarizing, two-site processes can capture some of the features seen in the RIXS data (the intensity trend with increasing momentum transfer, and a single peak without dispersion), but the overall fit is less satisfactory compared to the results of the single-site process shown in Fig. 5.8.

5.4.5 Conclusions

We have considered two different models, widely discussed in literature to describe orbital physics in titanites, in the context of Raman and X-ray scattering experiments. These models correspond to two limiting cases where the orbital ground state is dominated either by collective superexchange interactions among orbitals or by their coupling to lattice distortions. The models predictions, obtained within the same level of approximations, are compared to the experimental data on Raman (Fig. 5.6) and on X-ray (Figs. 5.8 and 5.10) scattering in titanites. What is evident from this comparison and our detailed analysis is that the local crystal field model of YTiO$_3$ fails to give a coherent explanation of both Raman and RIXS data taken together. There is no way one can get rid of the two-peak structure predicted for RIXS by this model without artificially finetuning its parameters. Further, once tuned to the RIXS spectra, the Raman spectra will be impossible to fit with the local model anyway, since it yields double dd excitations, different from the single crystal field excitations in RIXS. Experimentally, however, both techniques show a peak at the same energy. Also, a huge anisotropy between out-of-plane and in-plane polarizations is predicted by the local model, which is not observed in Raman data. Further, the temperature dependence of the experimental data is hard to explain from a local model: the intensity of crystal field transitions is expected to remain unchanged. Finally,

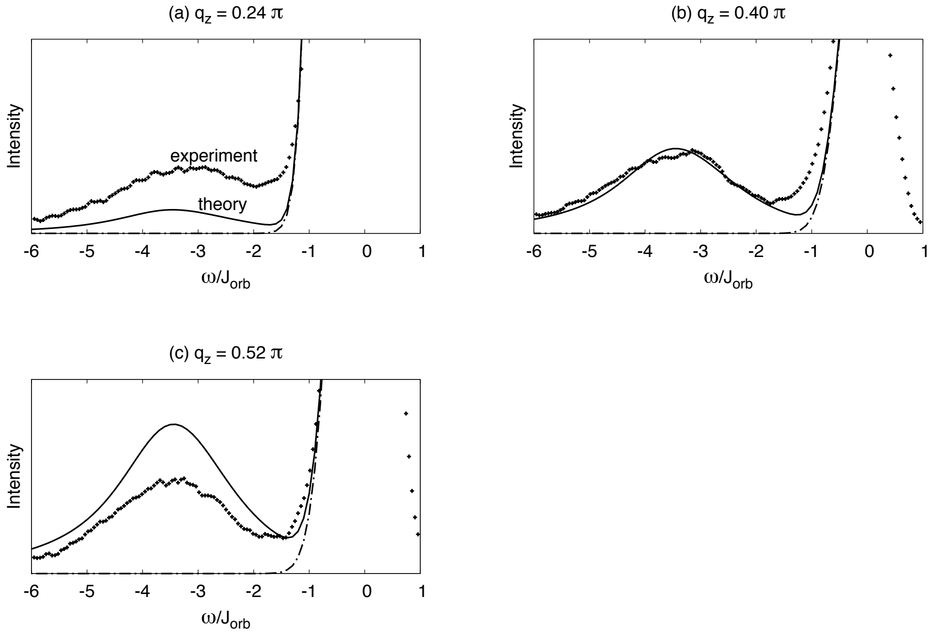

Figure 5.13: Theoretical RIXS spectra for two-site processes, calculated within the superexchange model (solid line), compared to experiment [202]. $\mathbf{q}$ is directed along the [001] direction, with q_z as indicated. We obtain a best fit for $J_{\mathrm{orb}} = 75$ meV. The solid lines are cuts from the plot of Fig. 5.12, where we added a Gaussian fit to the elastic peak (dash-dotted line). A phenomenological intrinsic orbiton broadening of $0.4\, r_1 J_{SE} \approx 30$ meV is added, as well as the experimental resolution of 27.5 meV (both HWHM) [202].

the $\mathbf{q}$ dependence of the RIXS intensity is not reproduced by the local model; in fact, the trend is opposite. We believe especially the last four points are robust evidence that the 250 meV peak seen in Raman and RIXS is not due to local *dd* excitations.

On the other side, the picture of collective excitations offers much better and broad agreement with the experimental data. The general features of both the Raman and RIXS data are reproduced by the SE model. For RIXS we presented a phenomenological scattering operator for single and two-site processes, evaluated within the SE model. Although both single and two-site processes get the general trends of the RIXS data right, the two-site processes clearly have a too strong $\mathbf{q}$-dependence of the intensity. The RIXS spectra obtained with the single site operator fit the data very well, suggesting that this process of generating orbitons might be the predominant one in the transition metal oxides. The only slight deviation from the experiments is the one-orbiton peak, which our theory overestimates. However, we note that the theoretical one-orbiton peak is decreased if we consider realistic conditions such as finite temperature and residual spin-orbital quantum fluctuations, which obstruct the orbital order and reduce $|c_0|^2$, which in its turn controls the one-orbiton spectral weight.

Ref. [202] reported that the RIXS-intensities in LaTiO$_3$ and YTiO$_3$ show different $\mathbf{q}$ dependences: While the intensity in YTiO$_3$ increases with $\mathbf{q}$, it decreases in LaTiO$_3$. On a qualitative level, this contrasting behavior can be understood from the SE picture as a manifestation of the (dynamical) Goodenough-Kanamori rules, according to which the spin and orbital correlations are complementary to each other. This implies that the spin and orbital susceptibilities are expected to behave in an opposite fashion. Since magnetic orderings in YTiO$_3$ and LaTiO$_3$ are different (ferro- and antiferromagnetic, respectively), collective response of orbitals in these coupounds are expected to be enhanced also at different portions of the Brillouin zone: at large $\mathbf{q}$ in YTiO$_3$ and, in contrast, at small $\mathbf{q}$ in LaTiO$_3$, which are complementary to the respective locations of their magnetic Bragg peaks. The SE picture suggests also that the $\mathbf{q}$-dependence of the orbiton RIXS-intensity should have cubic symmetry in both LaTiO$_3$ and YTiO$_3$, as follows from their isotropic spin-wave [186, 209] and Raman spectra [200]. Future RIXS experiments in titanites would be useful to verify these expectations.

A previous estimate [185] from neutron spin wave data [209] puts the orbital exchange constant J_{orb} at 60 meV. In close agreement with this estimate, the theoretical Raman spectrum fits best to experiment when $J_{\mathrm{orb}} = 65$ meV (vertex corrections may change this number, though). Matching to a lesser degree to the estimate, we find for the RIXS spectra $J_{\mathrm{orb}} = 75$ and 80 meV for the two-site and single site processes, respectively.

To establish the nature of the 250 meV peak, it is of great importance to search for the one-orbiton peak. In Raman scattering one-orbiton creation seems to be strongly suppressed, but in RIXS it would be possible to see a one-orbiton peak when $\mathbf{q}$ is directed maximally along the [110] direction. There the one-orbiton peak (around $\omega \approx 1.8\ J_{\mathrm{orb}} \approx 140$ meV) is about as strong as the two-orbiton continuum, assuming single site processes are the dominant RIXS channel, and provided $|c_0|^2$ is not too small.

To summarize, we may conclude that the existing Raman and RIXS data in titanites are better described by the SE model. This implies that while some polarization of orbitals by static lattice distortions must be a part of a realistic, "ultimate" model for titanites, the orbital fluctuations which are intrinsic to the t_{2g} orbital SE process [187] are not yet suppressed and strong enough to stabilize nearly isotropic charge distributions around the Ti-ions.

On the technical side, we believe that our semi-phenomenological approach to the RIXS problem which disentangles the high energy intermediate state dynamics from low energy collective excitations of orbitals and spins may serve as a simple and efficient tool in the theoretical description of Resonant Inelastic X-ray Scattering in oxides in general.

5.4.6 Acknowledgements

We would like to thank J. van den Brink for stimulating discussions that initiated this work. We also thank B. Keimer, C. Ulrich, and M. W. Haverkort for many fruitful discussions. L. A. thanks the Max-Planck-Institut FKF, Stuttgart, where most of the work was done, for its hospitality.

CHAPTER 6

RIXS IN SYSTEMS WITH STRONG SPIN-ORBIT COUPLING

Published as '*Resonant Inelastic X-ray Scattering on Spin-Orbit Coupled Insulating Iridates*', arXiv:1008.4862, with Giniyat Khaliullin and Jeroen van den Brink

6.1 Introduction

In the introduction of chapter 5, it was noted that one way to lift the ground state orbital degeneracy is by relativistic spin-orbit coupling. Relativistic spin-orbit coupling is strong in the heavier elements such as iridium – the subject of this chapter.

More specifically, we focus on compounds where the Ir ion has a charge of 4+, *i.e.*, it is in a $5d^5$ configuration. The Kramers degeneracy theorem states that the energy levels of a system with an odd number of electrons remain at least doubly degenerate in the absence of magnetic fields [211]. This implies that spin-orbit coupling cannot remove all degeneracy of the Ir^{4+} ion. As a matter of fact, as shown in Sec. 6.2, the ground state is a Kramers doublet: its two degenerate states are each other's time reversed states, and it can be represented by a pseudo-spin-1/2.

Because the two states in the Kramers doublet have exactly the same charge distribution, Jahn-Teller couplings cannot lift their degeneracy. Superexchange coupling, however, is present in the Mott insulating Ir compounds.

The strong spin-orbit interaction can cause entirely new kinds of ordering in the combined orbital-spin sector which are of a topological nature. This was recently proposed for certain iridium-oxides [212,213], members of a large family of iridium-based materials. Na_2IrO_3, for instance, is predicted to be a topological insulator exhibiting the quantum spin Hall effect at room temperature [212]. The topologically non-trivial state arises from the presence of complex hopping integrals, resulting from the unquenched iridium orbital moment. This system can also be described in terms of a Mott insulator, with interactions between the effective iridium spin-orbital degrees of freedom that are given by the Kitaev-Heisenberg model [214, 215]. In the pyrochlore iridates $A_2Ir_2O_7$ (where A is a 3+ ion), a quantum phase transition from a topological band insulator to a topological Mott insulator has been proposed as a function of the electron-electron interaction strength [213].

To establish whether and how such novel phases are realized in iridium oxides it is essential to probe and understand their spin-orbital ordering and related elementary excitations. In this context it is advantageous to consider the structurally less complicated, single-layer iridium perovskite Sr_2IrO_4. This material is in many respects the analog of the high-T_c cuprate parent compound La_2CuO_4 [214]. Structurally it is identical, with the obvious difference that the Ir $5d$ valence electrons are, as opposed to the Cu $3d$ electrons, very strongly spin-orbit coupled. The similarity cuts deeper, however, as the low energy sector of the iridates is spanned by local spin-orbit doublets with an effective spin of 1/2, which reside on a square lattice and interact via superexchange – a close analogy with the undoped cuprates. This observation motivates doping studies of Sr_2IrO_4 searching for superconductivity [216, 217]. Experimentally, however, far less is known about the microscopic ordering and excitations in iridates than in cuprates. Inelastic neutron scattering, which can in principle reveal such properties, is not possible because Ir is a strong neutron absorber and, moreover, crystals presently available tend to be tiny. As a consequence not even the interaction strength between the effective spins in the simplest iridium-oxides is established: estimates for Sr_2IrO_4, for instance, range from $\sim$50 meV [214] to $\sim$110 meV [218].

In this chapter we show that while for iridates neutron scattering falls short, RIXS fills the void: RIXS at the iridium L edge offers direct access to the excitation spectrum across the Brillouin zone, enabling one to measure the dispersion of elementary magnetic excitations. Besides the low energy magnons related to long-range order of the doublets, RIXS will also reveal the dynamics of higher energy, doublet to quartet, spin-orbit excitations. This allows to directly test theoretical models for the excitation spectra and extract accurate values of the superexchange and spin-orbit coupling constants J and λ, respectively. This chapter deals with the RIXS spectrum of insulating iridates in general, and of Sr_2IrO_4 in particular. Sec. 6.2 reviews the different models for Sr_2IrO_4 (the strong spin-orbit coupling model outlined above and the crystal field model for Ir ions in a D_{4h} crystal field). Sec. 6.3 describes the dipole operators that appear in RIXS at the Ir^{4+} L edge. In the remainder of that section, the local effective scattering operators are derived, neglecting intermediate state dynamics. The results of this section apply to all Ir^{4+} compounds with octahedral crystal fields (provided spin-orbit coupling also dominates). Then, Sec. 6.3.3 calculates the RIXS spectrum of Sr_2IrO_4 within the strong spin-orbit coupling limit. The Kramers doublet gives single- and two-pseudo-magnon excitations, while excitations from the Kramers doublet to the higher energy quartet are assumed to be local excitations.

6.2 Theory of Sr_2IrO_4

As noted in Sec. 2.2.2, the relativistic spin-orbit coupling in atoms is proportional to Z^4, where Z is the atomic number: in the heavier elements, spin-orbit coupling becomes more and more important. In iridium, the element that is studied in this chapter, the spin-orbit coupling λ is estimated to be as large as 380 meV in Ir^{4+} ions [219]. When the crystal field and superexchange interactions are small, the relativistic spin-orbit coupling can dominate the physics of materials containing Ir. Examples of such materials are Sr_2IrO_4, which will be studied in this chapter, Na_2IrO_3 [212, 214], and pyrochlore iridates $A_2Ir_2O_7$ (where A is a 3+ ion) [213].

Sr_2IrO_4 is a Mott insulator, although not a very good one: the optical gap is only ~ 0.4 eV [220]. It is a layered perovskite compound: each layer consists of a square lattice of Ir ions in a $5d^5$ configuration. The Ir ions are located in octahedra of oxygen ions, who split the d levels by ~ 3 eV into e_g and t_{2g} states [221]. This 10Dq splitting is strong enough to enforce that the lowest energy configuration is t_{2g}^5 [222, 223]. Thus, Sr_2IrO_4 can be regarded as the t_{2g} analog of La_2CuO_4 [214]. The local ground state of the hole in the t_{2g} shell could be dictated by the remaining crystal field (the octahedra are elongated along the z direction, favoring $|xy\rangle$), by superexchange interactions (as in the titanates described in chapter 5), or by the relativistic spin-orbit coupling.

The spin-orbit coupling $\lambda \approx 380$ meV [219] is much larger than intersite exchange interactions could generate. Jackeli and Khaliullin [214] derive a superexchange constant of 45 meV from the magnetic ordering temperature: an order of magnitude smaller than λ. Further, resonant X-ray scattering (RXS) data contradicts the crystal field scenario, and is in agreement with dominant spin-orbit coupling [223].

We first investigate the case that spin-orbit coupling dominates the low energy physics of the t_{2g}^5 configuration. The 10Dq splitting is larger by an order of magnitude than λ, and therefore we assume that the t_{2g} hole does not hybridize with the e_g orbitals through the spin-orbit coupling. The orbital degree of freedom of the hole is then described by an effective angular momentum $l = 1$ [25]. The true orbital angular momentum $\mathbf{L} = -\mathbf{l}$, and when the spin-orbit coupling term is projected to the t_{2g} subspace, it becomes $-\lambda \mathbf{l} \cdot \mathbf{S}$ with $\lambda > 0$. Note that electron states are considered here, instead of hole state as in Ref. [214]. The eigenstates of the spin-orbit coupling single ion Hamiltonian $H_0 = -\lambda \mathbf{l} \cdot \mathbf{S}$ are characterized by the total effective angular momentum $\mathbf{J}_{\text{eff}} = \mathbf{S} + \mathbf{l}$: $H_0 = -\lambda \left[\mathbf{J}_{\text{eff}}^2 - \mathbf{l}^2 - \mathbf{S}^2\right]/2 = -\lambda \left[J_{\text{eff}}(J_{\text{eff}}+1)/2 - 11/8\right]$. The eigenstates form a doublet with $J_{\text{eff}} = 1/2$ at energy λ and a quartet with $J_{\text{eff}} = 3/2$ at energy $-\lambda/2$. In the t_{2g}^5 ground state, the quartet is completely filled while the doublet contains a single electron.

Next, we incorporate lattice distortions in the model. They add a term $-\Delta l_z^2$ to H_0, with $\Delta > 0$ for elongation of the octahedra along the z axis. This lowers the zx and yz states in energy, relative to the xy orbital. The $J_{\text{eff}} = 1/2$ Kramers doublet remains unsplit and becomes [214]

$$\left|\tilde{\uparrow}\right\rangle = \sin\theta \left|0\uparrow\right\rangle - \cos\theta \left|+1\downarrow\right\rangle \qquad \text{and} \qquad \left|\tilde{\downarrow}\right\rangle = \sin\theta \left|0\downarrow\right\rangle - \cos\theta \left|-1\uparrow\right\rangle \tag{6.1}$$

with $\tan 2\theta = 2\sqrt{2}\lambda/(\lambda - 2\Delta)$, and where the orbital states are indexed by $l_z = -1, 0, +1$. The corresponding orbital annihilation operators $d_{-1,0,1}$ are defined by the relations

$$\begin{aligned} d_{yz} &= -\tfrac{1}{\sqrt{2}}(d_1 - d_{-1}), \\ d_{zx} &= \tfrac{i}{\sqrt{2}}(d_1 + d_{-1}), \\ d_{xy} &= d_0. \end{aligned} \tag{6.2}$$

The energy of the doublet is $E_f = \lambda/(\sqrt{2}\tan\theta)$. The $J_{\text{eff}} = 3/2$ quartet splits into two doublets: $\{\left|1\uparrow\right\rangle, \left|-1\downarrow\right\rangle\}$ at energy $E_g = -\Delta - \lambda/2$ and $\{\cos\theta\left|0\uparrow\right\rangle + \sin\theta\left|1\downarrow\right\rangle, \cos\theta\left|0\downarrow\right\rangle + \sin\theta\left|-1\uparrow\right\rangle\}$ at energy $E_h = -(\lambda\tan\theta)/\sqrt{2}$.

The three doublets are conveniently denoted by the three fermions f, g, h, where the pseudo-spin labels the two states within the doublets. We introduce their annihilation operators

$$\begin{array}{lll} f_\uparrow = \sin\theta\ d_{0\uparrow} - \cos\theta\ d_{1\downarrow}, & g_\uparrow = d_{1\uparrow}, & h_\uparrow = \cos\theta\ d_{0\uparrow} + \sin\theta\ d_{1\downarrow}, \\ f_\downarrow = \sin\theta\ d_{0\downarrow} - \cos\theta\ d_{-1\uparrow}, & g_\downarrow = d_{-1\downarrow}, & h_\downarrow = \cos\theta\ d_{0\downarrow} + \sin\theta\ d_{-1\uparrow}. \end{array} \tag{6.3}$$

Their energies were already denoted as $E_{f,g,h}$ above.

Now, we take two limits: the one suggested by Ref. [214] and supported by the RXS experiment of Ref. [223] which supposes that spin-orbit coupling dominates ($\Delta/\lambda \ll 1$), and the other limit where lattice distortions dominate ($\Delta/\lambda \gg 1$). For these limits, we find

$$\lim_{\Delta/\lambda \to 0} \tan\theta = \frac{1}{\sqrt{2}} \qquad \text{and} \qquad \lim_{\Delta/\lambda \to \pm\infty} \tan\theta = -\frac{\lambda}{\sqrt{2}\Delta}. \tag{6.4}$$

The ground state of the Ir ion is doubly degenerate in both cases. When lattice distortions are absent, J_{eff} is a good quantum number and the g and h doublets together form the $J_{\text{eff}} = 3/2$ quartet, while the hole occupies the f doublet with $J_{\text{eff}} = 1/2$ [Eq. (6.1) has $\sin\theta = \sqrt{1/3}$ and $\cos\theta = \sqrt{2/3}$ in this limit]. The energies become $E_f = \lambda$ and $E_g = E_h = -\lambda/2$, as noted above. When lattice distortions dominate, $\theta \to 0$. The hole occupies the h doublet, which becomes $\{|xy \uparrow\rangle, |xy \downarrow\rangle\}$. The energies of the doublets in this limit are $E_f = E_g = -\Delta$ and $E_h = 0$.

The RIXS experiments proposed in this chapter enable one to distinguish between the two scenario's, and so can provide complimentary evidence to existing data. But from RIXS data, one could draw more conclusions since one can probe the excitation spectrum. In the remainder of this section, the excitation spectrum of Sr_2IrO_4 is discussed.

Collective behavior of the f doublet. When spin-orbit coupling dominates, Sr_2IrO_4's excitation spectrum of the f doublet is quite remarkable: the $J_{\text{eff}} = 1/2$ levels interact via superexchange and the low energy effective Hamiltonian is of Heisenberg form, as described in, for instance, Ref. [214]. We briefly review this Hamiltonian here. Starting from the spin-orbital superexchange Hamiltonian for 1 electron in the triply degenerate t_{2g} orbitals (Eq. (3.11) from Ref. [160]), one projects on the low energy Kramers doublet and obtains a low energy effective superexchange Hamiltonian for these pseudo-spin-1/2 states:

$$H_{\text{eff}} = J_1 \tilde{\mathbf{S}}_i \cdot \tilde{\mathbf{S}}_j + J_2 (\tilde{\mathbf{S}}_i \cdot \mathbf{r}_{ij})(\mathbf{r}_{ij} \cdot \tilde{\mathbf{S}}_j) \tag{6.5}$$

where $\tilde{\mathbf{S}}$ is the pseudo-spin-1/2 operator, $\mathbf{r}_{ij}$ is the unit vector directed along the ij bond, and $J_{1,2}$ are energies determined by Hund's rule coupling J_H. For $J_H \ll U$, we get $J_1 \approx 4/9$ and $J_2 \approx 2J_H/9U$ in units of $4t^2/U$, with t the Ir-Ir hopping integral and U the same-orbital Coulomb repulsion. In this limit, the result is a Heisenberg coupling with weak dipolar anisotropy [214].

Next, the rotation of the octahedra (by an angle $\alpha \approx 11°$) are taken into account, resulting in a Dzyaloshinsky-Moriya (DM) interaction. The DM interaction rotates the spins by an angle $\phi \approx 8°$. The difference between α and ϕ is controlled by the distortion along the z axis. In the limit of no distortion along the z axis, $\alpha = \phi$. The Hamiltonian on the bond ij with $J_H = 0$ but non-zero DM interaction is

$$H_{ij} = J \tilde{\mathbf{S}}_i \cdot \tilde{\mathbf{S}}_j + J_z \tilde{S}_i^z \tilde{S}_j^z + \mathbf{D} \cdot \tilde{\mathbf{S}}_i \times \tilde{\mathbf{S}}_j \tag{6.6}$$

where $\mathbf{D} = (0, 0, -D)$ (which flips sign on alternating bonds) and the energies J, J_z and D are defined in terms of the octahedron rotation angle α and the distortion parameter θ as in Ref. [214]. The DM interaction term can be transformed away by rotating the spin operators around the z axis over the spin canting angle $\pm\phi$ (alternating with sublattice) with $\tan 2\phi = -D/J$. We define the unitary transformation $U(\phi) = \otimes_i \exp\{-i(\pm 1)^i \phi S_i^z\}$ where $(\pm)^i = 1$ on the sublattice A, where the octahedron are rotated over $+\alpha$, and -1 on sublattice B $(-\alpha)$. The transformed Hamiltonian is

$$\tilde{H} = U(\phi) H U^{-1}(\phi) = \tilde{J} \tilde{\mathbf{S}}_i \cdot \tilde{\mathbf{S}}_j, \tag{6.7}$$

where $\tilde{J} = J + J_z$. Note that the isotropic form is only retreived when there is a special relation between J, J_z and D. When $J_H/U = 0$, the degeneracy of the ground state is not lifted by the DM interaction[1]. A more extended version including Hund's rule exchange is given in Ref. [214].

It is remarkable that Sr_2IrO_4 is not only structurally identical to La_2CuO_4, it also has the same low energy excitation spectrum. However, the physical form and origin of these excitations are are not at all similar.

Local behavior of the *g* and *h* doublets. Excitations to the g and h doublets are very interesting because it is conjectured that Sr_2IrO_4 is a Mott insulator only because of the large spin-orbit coupling [222,224]. The $J_{\text{eff}} = 1/2$ doublet consists of small orbitals, which have small hopping amplitudes, therefore confining the charges and making the system Mott insulating. The $J_{\text{eff}=3/2}$ quartet consists of larger orbitals with larger hopping amplitudes, which would perhaps be enough to form metallic bands. If that picture is correct, then the g and h excitations should be very broad in RIXS: the excited electrons come from all the occupied g and h bands, and the spectrum is a convolution over all these widely dispersing states. In contrast, if Sr_2IrO_4 is a conventional Mott insulator, the g and h excitations will be localized and have more sharply defined energies. Since J is small compared to λ, these excitations will disperse very little. They have an energy slightly larger than the Mott gap, and decay via electron-hole pairs reduces their lifetime. Also, superexchange processes will often result in decay to $J_{\text{eff}} = 1/2$ states. In practice, this will make it very hard to distinguish between the two theories for the insulating behavior. On the other hand, the coupling of the inter-spin-orbit multiplet excitations to charge modes enables RIXS to also probe the latter.

6.3 Iridium L edge cross section

The spin-orbital degrees of freedom can be probed with direct RIXS at the Ir L edge. This process involves two (dipole) transitions connecting the 2p core states to the 5d valence ones. Here, we consider the case that the incident photons are tuned to excite a core electron into the empty t_{2g} state.

The intermediate state (5d t_{2g}^6) has a filled shell. The dominant multiplet effect comes from the core orbital's spin-orbit coupling Λ: the 2p core states split into $J = 1/2$ (the L_2 edge) and $J = 3/2$ states (the L_3 edge), like at the Cu L edge. Since the L_2 and L_3 edge are separated by 1.6 keV [223], their interfere is negligible, given the much smaller lifetime broadening (a few eV [100]).

---

[1] This can be understood as follows: the $J_{\text{eff}} = 1/2$ Kramers doublet states are each others' time-reversed states. This implies that their charge distributions are the same, and therefore also the hopping amplitudes to the neighboring oxygens (possibly up to a sign, although this sign cannot be affected by a continous rotation of the octahedra). By symmetry, rotation of the octahedra does not change the equality of the hopping amplitudes. This means there cannot be a preferential state and preferential direction, and thus no anisotropy.

The lifetime broadening at the Ir L edge is still quite large compared to the dynamics of the 5d electrons. Therefore, the UCL expansion should work quite well. We employ the UCL expansion to zeroth order. To obtain the cross section, one only needs the dipole operators.

6.3.1 Dipole operators

We introduce the electron annihilation operators for the 2p orbital angular momentum eigenstates

$$\begin{aligned} p_x &= -\tfrac{1}{\sqrt{2}}(p_1 - p_{-1}) \\ p_y &= \tfrac{i}{\sqrt{2}}(p_1 + p_{-1}) \\ p_z &= p_0, \end{aligned} \tag{6.8}$$

analogous to Eqs. (6.2). The core electron eigenstates are easily obtained from Sec. 6.2, because both the valence and the core electrons are spin-orbit coupled and have orbital angular momentum 1. The $J = 1/2$ states are lowest in energy, which means that the L_2 edge is higher in energy than the L_3 edge. In analogy to the valence electrons, we introduce the 2p electron annihilation operators $F_{\uparrow,\downarrow}$ for the L_2 wave functions and $G_{\uparrow,\downarrow}, H_{\uparrow,\downarrow}$ for the L_3 ones. For symmetry of notation, we introduce a tetragonal distortion δ for the core levels too, which splits the $J = 3/2$ quartet into two doublets G and H. We find, in analogy to Eqs. (6.3),

$$\begin{aligned} F_\uparrow &= \sin\Theta\; p_{0\uparrow} - \cos\Theta\; p_{1\downarrow}, \qquad & G_\uparrow &= p_{1\uparrow}, \qquad & H_\uparrow &= \cos\Theta\; p_{0\uparrow} + \sin\Theta\; p_{1\downarrow}, \\ F_\downarrow &= \sin\Theta\; p_{0\downarrow} - \cos\Theta\; p_{-1\uparrow}, \qquad & G_\downarrow &= p_{-1\downarrow}, \qquad & H_\downarrow &= \cos\Theta\; p_{0\downarrow} + \sin\Theta\; p_{-1\uparrow}, \end{aligned} \tag{6.9}$$

where $\tan 2\Theta = 2\sqrt{2}\Lambda/(\Lambda - 2\delta)$.

Now, we calculate the dipole matrix elements for the Ir L edge. We write the dipole operator in second quantization ($p_x^\dagger$ creates a $2p_x$ electron, $d_{xy}^\dagger$ creates a $5d_{xy}$ electron, etc.), and use the octahedral symmetry of Sr_2IrO_4 to simplify the expression:

$$\begin{aligned} \mathbf{x}\cdot\boldsymbol{\epsilon} &= \sum_{i,j,k,\sigma} d_{k\sigma}^\dagger \langle 5d_k|\, x_i\, |2p_j\rangle\, \epsilon_i p_{j\sigma} + \text{h.c.} \\ &= \sum_\sigma d_{yz\sigma}^\dagger \langle 5d_{yz}| \Big(y\, |2p_z\rangle\, \epsilon_y p_{z\sigma} + z\, |2p_y\rangle\, \epsilon_z p_{y\sigma} \Big) + ..zx.. + ..xy.. + \text{h.c.} \\ &= -i\, \langle 5d_{yz}|\, y\, |2p_z\rangle \sum_\sigma \Big[\epsilon_+ (d_{-1}^\dagger p_0 - d_0^\dagger p_1) + \epsilon_- (d_1^\dagger p_0 - d_0^\dagger p_{-1}) \\ &\quad + \epsilon_z (d_1^\dagger p_{-1} - d_{-1}^\dagger p_1) \Big] + \text{h.c.} = (D_2 + D_3) + \text{h.c.} \end{aligned} \tag{6.10}$$

where $\epsilon_\pm = (\epsilon_x \pm i\epsilon_y)/\sqrt{2}$, and the spin label σ is suppressed in the last lines but implied for every electron operator. The dipole operators for the L_2 and L_3

edge, respectively, are

$$\begin{aligned}
D_2 = -i \langle 5d_{yz}|\, y\, |2p_z\rangle \Big[\epsilon_+ \Big(\Big\{(ss'+cc')h^\dagger_\downarrow + (sc'-cs')f^\dagger_\downarrow\Big\} F_\uparrow + s' g^\dagger_\downarrow F_\downarrow\Big) \\
+ \epsilon_- \Big(\Big\{(ss'+cc')h^\dagger_\uparrow + (sc'-cs')f^\dagger_\uparrow\Big\} F_\downarrow + s' g^\dagger_\uparrow F_\uparrow\Big) \\
+\epsilon_z c' \Big(g^\dagger_\downarrow F_\uparrow - g^\dagger_\uparrow F_\downarrow\Big)\Big], \qquad (6.11) \\
D_3 = -i \langle 5d_{yz}|\, y\, |2p_z\rangle \Big[\epsilon_+ \Big(c' g^\dagger_\downarrow H_\downarrow + \Big\{(sc'-cs')h^\dagger_\downarrow - (ss'+cc')f^\dagger_\downarrow\Big\} H_\uparrow \\
- \Big\{s f^\dagger_\uparrow + c h^\dagger_\uparrow\Big\} G_\uparrow\Big) + \epsilon_- \Big(c' g^\dagger_\uparrow H_\uparrow + \Big\{(sc'-cs')h^\dagger_\uparrow - (ss'+cc')f^\dagger_\uparrow\Big\} H_\downarrow \\
- \Big\{s f^\dagger_\downarrow + c h^\dagger_\downarrow\Big\} G_\downarrow\Big) + \epsilon_z \Big(s' g^\dagger_\uparrow H_\downarrow + \Big\{s h^\dagger_\uparrow - c f^\dagger_\uparrow\Big\} G_\downarrow - \Big\{s h^\dagger_\downarrow - c f^\dagger_\downarrow\Big\} G_\uparrow \\
-s' g^\dagger_\downarrow H_\uparrow\Big)\Big] \qquad (6.12)
\end{aligned}$$

where we abbreviated $\sin\Theta = s'$ and $\sin\theta = s$ (and similar for the cosines).

6.3.2 Local RIXS scattering operator

The expressions for the dipole operators at the $L_{2,3}$ edges [Eqs. (6.11) and (6.12)] can be inserted in Eq. (2.41), and give, to zeroth order in the UCL expansion,

$$\mathcal{F}_{fi} = \frac{1}{i\Gamma} \sum_i e^{i\mathbf{q}\cdot\mathbf{R}_i} \langle f|\, (D^\dagger_{2,3})_i (D_{2,3})_i \,|i\rangle \qquad (6.13)$$

We define the single site RIXS scattering operators $O_{2,3} = D^\dagger_{2,3} D_{2,3}$ (the site index is suppressed in the following). Projecting out the core hole degrees of freedom, these become

$$\begin{aligned}
O_2 = \sin(\theta-\Theta) \sum_{\sigma\in\{\uparrow,\downarrow\}} \Big[\epsilon'^*_{\bar\sigma}\epsilon_{\bar\sigma} \sin(\theta-\Theta) f_\sigma f^\dagger_\sigma + \epsilon'^*_\sigma \epsilon_{\bar\sigma} s' g_{\bar\sigma} f^\dagger_\sigma \\
-(-1)^\sigma \epsilon'^*_z \epsilon_{\bar\sigma} c' g_\sigma f^\dagger_\sigma + \epsilon'^*_{\bar\sigma}\epsilon_{\bar\sigma} \cos(\theta-\Theta) h_\sigma f^\dagger_\sigma\Big] \qquad (6.14)
\end{aligned}$$

at the L_2 edge. The factor $|\langle 5d_{yz}|\, y\, |2p_z\rangle|^2$, which is just a positive number, is dropped. We define $(-1)^\sigma$ to be 1 for $\sigma = \uparrow$ and -1 for $\sigma = \downarrow$. Further, $\epsilon_\uparrow = \epsilon_+$ and $\epsilon_\downarrow = \epsilon_-$. Note that $\epsilon'^*_+ = (\epsilon'_x + i\epsilon'_y)^*/\sqrt{2}$. For the L_3 edge,

$$O_3 = \sum_{\sigma\in\{\uparrow,\downarrow\}} \Big[\Big\{\epsilon'^*_\sigma \epsilon_\sigma s^2 + \epsilon'^*_{\bar\sigma}\epsilon_{\bar\sigma} \cos^2(\theta-\Theta) + \epsilon'^*_z \epsilon_z c^2\Big\} f_\sigma f^\dagger_\sigma +$$

$$\begin{aligned}
&+ \left\{(-1)^{\sigma}(\epsilon'^{*}_{\bar\sigma}\epsilon_z - \epsilon'^{*}_{z}\epsilon_\sigma)sc\right\} f_{\bar\sigma} f^\dagger_\sigma \\
&- \Big\{(-1)^{\sigma}\epsilon'^{*}_{z}\epsilon_{\bar\sigma}s'\cos(\theta-\Theta)\Big\} g_\sigma f^\dagger_\sigma - \epsilon'^{*}_{\sigma}\epsilon_{\bar\sigma}c'\cos(\theta-\Theta) g_{\bar\sigma} f^\dagger_\sigma \\
&+ \left\{(\epsilon'^{*}_{\sigma}\epsilon_\sigma - \epsilon'^{*}_{z}\epsilon_z)\frac{1}{2}\sin 2\theta - \epsilon'^{*}_{\bar\sigma}\epsilon_{\bar\sigma}\frac{1}{2}\sin 2(\theta-\Theta)\right\} h_\sigma f^\dagger_\sigma \\
&+ \left\{(-1)^{\sigma}(\epsilon'^{*}_{z}\epsilon_\sigma s^2 + \epsilon'^{*}_{\bar\sigma}\epsilon_z c^2)\right\} h_{\bar\sigma} f^\dagger_\sigma \Big] . \qquad (6.15)
\end{aligned}$$

When spin-orbit coupling dominates, $\theta = \Theta$ and the inelastic scattering intensity at the L_2 edge completely vanishes, in addition to the vanishing elastic intensity [223]. In the presence of a large crystal field, this no longer holds: the core electrons are much less affected by the crystal field than the 5d ones. In the following, we split the local scattering operator into three parts that create excitations in the f, g and h doublets.

Excitations within the *f* doublet. When $\lambda \gg \Delta$, excitations within the $J_{\mathrm{eff}} = 1/2$ doublet are lowest in energy. The single site RIXS scattering operator for intra-f doublet excitations can be written in terms of Pauli matrices that act on the pseudo-spin of the f fermion. At the L_2 edge,

$$O_2^{(f)} = \frac{1}{2}\sin^2(\theta-\Theta)\left[\left(P_{A_{1g}} + \frac{1}{\sqrt{3}}Q_3\right)\mathbb{1}_2 - P_z\sigma_z\right], \qquad (6.16)$$

and at the L_3 edge

$$\begin{aligned}
O_3^{(f)} = &\left[\frac{1}{6}\cos^2(\theta-\Theta)\left(3P_{A_{1g}} + \sqrt{3}Q_3\right) + \frac{3}{2}P_{A_{1g}} - \frac{\sqrt{3}}{6}(2c^2 - s^2)Q_3\right]\mathbb{1}_2 \\
&- \frac{1}{2}\left(\cos^2(\theta-\Theta) - s^2\right)P_z\sigma_z + \frac{\sin 2\theta}{2\sqrt{2}}(P_x\sigma_x + P_y\sigma_y), \qquad (6.17)
\end{aligned}$$

where we introduced polarization factors

$$\begin{aligned}
P_x &= i\left(\epsilon'^{*}_{y}\epsilon_z - \epsilon'^{*}_{z}\epsilon_y\right), & T_x &= \epsilon'^{*}_{y}\epsilon_z + \epsilon'^{*}_{z}\epsilon_y, & P_{A_{1g}} &= \tfrac{2}{3}\left(\epsilon'^{*}_{x}\epsilon_x + \epsilon'^{*}_{y}\epsilon_y + \epsilon'^{*}_{z}\epsilon_z\right), \\
P_y &= i\left(\epsilon'^{*}_{z}\epsilon_x - \epsilon'^{*}_{x}\epsilon_z\right), & T_y &= \epsilon'^{*}_{x}\epsilon_z + \epsilon'^{*}_{z}\epsilon_x, & Q_2 &= \epsilon'^{*}_{y}\epsilon_y - \epsilon'^{*}_{x}\epsilon_x, \qquad (6.18) \\
P_z &= i\left(\epsilon'^{*}_{x}\epsilon_y - \epsilon'^{*}_{y}\epsilon_x\right), & T_z &= \epsilon'^{*}_{x}\epsilon_y + \epsilon'^{*}_{y}\epsilon_x, & Q_3 &= \tfrac{1}{\sqrt{3}}\left(\epsilon'^{*}_{x}\epsilon_x + \epsilon'^{*}_{y}\epsilon_y - 2\epsilon'^{*}_{z}\epsilon_z\right).
\end{aligned}$$

The polarization factors are chosen such that they are normalized as $\mathrm{Tr}(\Gamma^2) = 2$, where the matrices Γ are defined by the polarization factors P as $P = \epsilon'^{*}_{i}\Gamma_{ij}\epsilon_j$.

In the cubic limit, O_2 vanishes, while at the L_3 edge one finds

$$O_3^{(f)} = P_{A_{1g}}\mathbb{1}_2 + \frac{1}{3}(P_x\sigma_x + P_y\sigma_y - P_z\sigma_z). \qquad (6.19)$$

This is not a scalar product, which might be surprising because of the octahedral symmetry. However, the 5d t_{2g} orbitals do not transform as a vector: they have effective angular momentum $\mathbf{l} = -\mathbf{L}$. The Zeeman energy $\mathbf{B}\cdot\mathbf{S}$, projected on the f doublet, transforms in a similar way:

$$\mathbf{B}\cdot\mathbf{S} = \cos 2\theta\; B_z\sigma_z - s^2(B_x\sigma_x + B_y\sigma_y) \xrightarrow{\Delta\to 0} -\frac{1}{3}\left(B_x\sigma_x + B_y\sigma_y - B_z\sigma_z\right) \quad (6.20)$$

These combinations become scalar products when we flip the sign of either $f_\uparrow$ or $f_\downarrow$ in Eq. (6.3). Note that the Hamiltonians (6.5) and (6.6) are invariant under such a sign change. In the following, we will flip the sign of $f_\downarrow$. The inelastic parts of the scattering operators become

$$O_2^{(f)} \xrightarrow{\Delta\to 0} 0, \quad (6.21)$$

$$O_3^{(f)} \xrightarrow{\Delta\to 0} -\frac{1}{3}\left(P_x\sigma_x + P_y\sigma_y + P_z\sigma_z\right). \quad (6.22)$$

Excitation of g and h doublets. For the L_2 edge,

$$\begin{aligned} O_2^{(g)} &= \sin(\theta-\Theta)\left[\frac{is'}{2}\left(Q_2\sigma_y^{(g)} + T_z\,\sigma_x^{(g)}\right) - \frac{c'}{2\sqrt{2}}(T_y - iP_y)\mathbb{1}_2^{(g)}\right.\\ &\qquad\left. + \frac{ic'}{2\sqrt{2}}(T_x + iP_x)\sigma_z^{(g)}\right], \qquad (6.23)\\ O_2^{(h)} &= \frac{1}{4}\sin 2(\theta-\Theta)\left[\left(P_{A_{1g}} + \tfrac{1}{\sqrt{3}}Q_3\right)\sigma_z^{(h)} - P_z\,\mathbb{1}_2^{(h)}\right], \qquad (6.24) \end{aligned}$$

where, for instance, $\sigma_z^{(h)} = h_\uparrow f_\uparrow^\dagger - h_\downarrow f_\downarrow^\dagger$, and where the sign flip on $f_\downarrow$ discussed above is incorporated.

At the L_3 edge,

$$\begin{aligned} O_3^{(g)} &= \cos(\theta-\Theta)\left[-\frac{s'}{2\sqrt{2}}(T_y - iP_y)\mathbb{1}_2^{(g)} + \frac{is'}{2\sqrt{2}}(T_x + iP_x)\sigma_z^{(g)}\right.\\ &\qquad\left. - \frac{ic'}{2}Q_2\sigma_y^{(g)} + \frac{ic'}{2}T_z\,\sigma_x^{(g)}\right], \qquad (6.25)\\ O_3^{(h)} &= \frac{1}{4}\left[\sqrt{3}\sin 2\theta\; Q_3 - \sin 2(\theta-\Theta)\left(P_{A_{1g}} + \tfrac{1}{\sqrt{3}}Q_3\right)\right]\sigma_z^{(h)}\\ &\quad + \frac{i}{4}\left[\sin 2\theta + \sin 2(\theta-\Theta)\right]P_z\mathbb{1}_2^{(h)} + \frac{1}{2\sqrt{2}}\left[T_y + i\cos 2\theta\; P_y\right]\sigma_x^{(h)}\\ &\quad + \frac{1}{2\sqrt{2}}\left[T_x - i\cos 2\theta\; P_x\right]\sigma_y^{(h)}. \qquad (6.26) \end{aligned}$$

In the cubic limit, one obtains

$$O_2^{(g)} = O_2^{(h)} = 0 \quad (6.27)$$

$$O_3^{(g)} = \frac{1}{\sqrt{6}}\left[-\frac{1}{2}(T_y - iP_y)\mathbb{1}_2^{(g)} + \frac{i}{2}(T_x + iP_x)\sigma_z^{(g)} - iQ_2\sigma_y^{(g)} + iT_z\sigma_x^{(g)}\right] \quad (6.28)$$

$$\begin{aligned} O_3^{(h)} = \frac{1}{3\sqrt{2}}\Big[& iP_z\mathbb{1}_2^{(h)} + \sqrt{3}Q_3\sigma_z^{(h)} + \frac{3}{2}\left(T_y\sigma_x^{(h)} + T_x\sigma_y^{(h)}\right) \\ & + \frac{i}{2}\left(P_y\sigma_x^{(h)} - P_x\sigma_y^{(h)}\right)\Big]. \end{aligned} \quad (6.29)$$

6.3.3 Iridium L edge RIXS cross section

Up to this point, the discussion is general and applies to all materials with an Ir^{4+} ion in an octahedral crystal field, including Kitaev-Heisenberg model compounds. To obtain the RIXS cross sections for a certain material from the scattering operators $O_{2,3}$ is straightforward once the Hamilonian governing the interactions between the Ir ions in that material is given.

In the remainder of this chapter, we specify to the case of $\mathrm{Sr_2IrO_4}$. As laid out in Sec. 6.2, we distinguish between the low energy Kramers doublet, which shows collective behavior in the limit of strong spin-orbit coupling, and the high energy quartet, which does not.

Cross section of intra- *f* doublet excitations. It should be noted that the local scattering operators $O_{2,3}$ are derived in the local axes of a rotated octahedron. The Hamiltonian (6.6), however, is written in global coordinates. Therefore, the polarization and spin vectors should be rotated back over an angle α to obtain the scattering operator in global coordinates too. Reserving primes for the local axes, one gets

$$\begin{aligned} &P'_x = \cos\alpha\ P_x + \sin\alpha\ P_y, && T'_x = \cos\alpha\ T_x - \sin\alpha\ T_y, \\ &P'_y = \cos\alpha\ P_y - \sin\alpha\ P_x, && T'_y = \cos\alpha\ T_y + \sin\alpha\ T_x, \\ &P'_z = P_z, && T'_z = \sin 2\alpha\ Q_2 + \cos 2\alpha\ T_z, \\ &Q'_2 = \cos 2\alpha\ Q_2 - \sin 2\alpha\ T_z, && Q'_3 = Q_3, \quad P'_{A_{1g}} = P_{A_{1g}}, \end{aligned} \quad (6.30)$$

for the polarization factors. α flips sign on sublattice B, which is rotated in the opposite direction. The rotated spin operators are

$$\begin{aligned} S_i'^x &= U(-\alpha)S^xU^{-1}(-\alpha) = \cos\alpha\ S^x - (\pm 1)^i \sin\alpha\ S^y, \\ S_i'^y &= U(-\alpha)S^yU^{-1}(-\alpha) = \cos\alpha\ S^y + (\pm 1)^i \sin\alpha\ S^x, \\ S_i'^z &= U(-\alpha)S^zU^{-1}(-\alpha) = S_i^z, \end{aligned} \quad (6.31)$$

where $(\pm 1)^i$ is 1 on sublattice A and -1 on sublattice B. After this rotation, the spins are transformed by $U(\phi)$ to the basis in which the Hamiltonian is of Heisenberg type. Since $\alpha \approx \phi$, the unitary transformation nearly cancels the rotation over α. For $\alpha = \phi$, the cancellation is complete. In the following, we work in the cubic limit, so $\alpha = \phi$, and obtain for the complete, multi-site, inelastic scattering operator:

$$\begin{aligned} O_{\mathbf{q}} = \sum_i e^{i\mathbf{q}\cdot\mathbf{R}_i} (O_3^{(f)})_i = -\frac{1}{3} \sum_i \Big[& \sin\alpha \; e^{i(\mathbf{q}+\mathbf{Q})\cdot\mathbf{R}_i} \, (P_y\sigma_x - P_x\sigma_y) \\ & + e^{i\mathbf{q}\cdot\mathbf{R}_i} \, (\cos\alpha \, \{P_x\sigma_x + P_y\sigma_y\} + P_z\sigma_z) \Big] \end{aligned} \tag{6.32}$$

where $\mathbf{Q} = (\pi, \pi)$. Following Eq. (6.13), the RIXS cross section is then

$$\frac{d^2\sigma}{d\Omega d\omega} \propto \sum_f |\langle f| \, O_{\mathbf{q}} \, |g\rangle|^2 \, \delta(\hbar\omega - \hbar\omega_f), \tag{6.33}$$

where $\hbar\omega_f$ is the energy of the final state $|f\rangle$.

To describe the pseudo-spin flip excitation spectrum of the pseudo-spin Heisenberg model, Holstein-Primakoff bosons are introduced, in analogy to the magnetic Heisenberg model in Sec. 4.2. The reference state is taken to be the Néel state with ordering direction [110] [223], and accordingly, the vectors $\hat{\mathbf{n}}_1 = (-1, 1, 0)/\sqrt{2}$, $\hat{\mathbf{n}}_2 = (0, 0, 1)$, $\hat{\mathbf{n}}_3 = (1, 1, 0)/\sqrt{2}$ are introduced. The scattering operator becomes

$$\begin{aligned} O_{\mathbf{q}} = -\frac{1}{3} \sum_i \Bigg[& \frac{\sin\alpha}{\sqrt{2}} e^{i(\mathbf{q}+\mathbf{Q})\cdot\mathbf{R}_i} \, \{(P_y - P_x)\hat{\mathbf{n}}_3 \cdot \boldsymbol{\sigma}_i - (P_x + P_y)\hat{\mathbf{n}}_1 \cdot \boldsymbol{\sigma}_i\} \\ & + e^{i\mathbf{q}\cdot\mathbf{R}_i} \left(\frac{\cos\alpha}{\sqrt{2}} \{(P_x + P_y)\hat{\mathbf{n}}_3 \cdot \boldsymbol{\sigma}_i + (P_y - P_x)\hat{\mathbf{n}}_1 \cdot \boldsymbol{\sigma}_i\} + P_z \hat{\mathbf{n}}_2 \cdot \boldsymbol{\sigma}_i \right) \Bigg] . \end{aligned} \tag{6.34}$$

The Holstein-Primakoff bosons are naturally introduced in the new coordinate frame spanned by $\hat{\mathbf{n}}_1, \hat{\mathbf{n}}_2$ and $\hat{\mathbf{n}}_3$:

$$\sum_i e^{i\mathbf{q}\cdot\mathbf{R}_i} \hat{\mathbf{n}}_1 \cdot \boldsymbol{\sigma}_i = \sqrt{N}(u_{\mathbf{q}} - v_{\mathbf{q}})(\alpha^\dagger_{\mathbf{q}} + \alpha_{-\mathbf{q}}) \tag{6.35}$$

$$\sum_i e^{i\mathbf{q}\cdot\mathbf{R}_i} \hat{\mathbf{n}}_2 \cdot \boldsymbol{\sigma}_i = i\sqrt{N}(u_{\mathbf{q}} - v_{\mathbf{q}})(\alpha^\dagger_{\mathbf{q}+\mathbf{Q}} - \alpha_{-\mathbf{q}-\mathbf{Q}}) \tag{6.36}$$

$$\begin{aligned} \sum_i e^{i\mathbf{q}\cdot\mathbf{R}_i} \hat{\mathbf{n}}_3 \cdot \boldsymbol{\sigma}_i = \delta_{\mathbf{q},\mathbf{Q}} \left(N - 2\sum_{\mathbf{k}} v_{\mathbf{k}}^2 \right) + 2\sum_{\mathbf{k}} \Big[& u_{\mathbf{k}+\mathbf{q}} v_{\mathbf{k}} \Big(\alpha^\dagger_{\mathbf{k}+\mathbf{q}+\mathbf{Q}} \alpha^\dagger_{-\mathbf{k}} \\ & + \alpha_{\mathbf{k}} \alpha_{-\mathbf{k}-\mathbf{q}-\mathbf{Q}} \Big) + (v_{\mathbf{k}} v_{\mathbf{k}+\mathbf{q}} - u_{\mathbf{k}} u_{\mathbf{k}+\mathbf{q}}) \alpha^\dagger_{\mathbf{k}+\mathbf{q}+\mathbf{Q}} \alpha_{\mathbf{k}} \Big] \end{aligned} \tag{6.37}$$

with $u_{\mathbf{k}}$ and $v_{\mathbf{k}}$ defined as in Eq. (4.10). The ground state is approximated by the (pseudo-)magnon vacuum $|0\rangle$. The scattering operator consists of a single-magnon part

$$\begin{aligned}O^{(1)}_{\mathbf{q}} = \frac{\sqrt{N}}{3}\Bigg[&\frac{\sin\alpha}{\sqrt{2}}(P_x + P_y)(u_{\mathbf{q}} + v_{\mathbf{q}})\left(\alpha^{\dagger}_{\mathbf{q}+\mathbf{Q}} + \alpha_{-\mathbf{q}-\mathbf{Q}}\right)\\ &+\frac{\cos\alpha}{\sqrt{2}}(P_x - P_y)(u_{\mathbf{q}} - v_{\mathbf{q}})\left(\alpha^{\dagger}_{\mathbf{q}} + \alpha_{-\mathbf{q}}\right)\\ &-iP_z(u_{\mathbf{q}} - v_{\mathbf{q}})\left(\alpha^{\dagger}_{\mathbf{q}+\mathbf{Q}} - \alpha_{-\mathbf{q}-\mathbf{Q}}\right)\Bigg]\end{aligned} \tag{6.38}$$

and a double-magnon part

$$\begin{aligned}O^{(2)}_{\mathbf{q}} = -\frac{\sqrt{2}}{3}\sum_{\mathbf{k}} u_{\mathbf{k}+\mathbf{q}}v_{\mathbf{k}}\Big[&\sin\alpha\ (P_y - P_x)\left(\alpha^{\dagger}_{\mathbf{k}+\mathbf{q}}\alpha^{\dagger}_{-\mathbf{k}} + \alpha_{\mathbf{k}}\alpha_{-\mathbf{k}-\mathbf{q}}\right)\\ &+\cos\alpha\ (P_x + P_y)\left(\alpha^{\dagger}_{\mathbf{k}+\mathbf{q}+\mathbf{Q}}\alpha^{\dagger}_{-\mathbf{k}} + \alpha_{\mathbf{k}}\alpha_{-\mathbf{k}-\mathbf{q}-\mathbf{Q}}\right)\Big]\,.\end{aligned} \tag{6.39}$$

The part of the scattering operator that does not change the number of magnons is not considered here.

The single-magnon intensity then becomes

$$\begin{aligned}I^{(1)} \propto \frac{N}{9}\Bigg[&\left|\frac{\sin\alpha}{\sqrt{2}}(P_x + P_y)(u_{\mathbf{q}} + v_{\mathbf{q}}) - iP_z(u_{\mathbf{q}} - v_{\mathbf{q}})\right|^2\\ &+\frac{1}{2}\cos^2\alpha\ \left|P_x - P_y\right|^2(u_{\mathbf{q}} - v_{\mathbf{q}})^2\Bigg]\,\delta(\omega - \omega_{\mathbf{q}}),\end{aligned} \tag{6.40}$$

and the two-magnon intensity

$$\begin{aligned}I^{(2)} \propto \frac{2}{9}\sum_{\mathbf{k}}\Big[&\sin^2\alpha\,|P_x - P_y|^2\,(u_{\mathbf{k}+\mathbf{q}}v_{\mathbf{k}} + u_{\mathbf{k}}v_{\mathbf{k}+\mathbf{q}})^2\\ &+\cos^2\alpha\,|P_x + P_y|^2\,(u_{\mathbf{k}+\mathbf{q}}v_{\mathbf{k}} - u_{\mathbf{k}}v_{\mathbf{k}+\mathbf{q}})^2\Big]\,\delta(\omega - \omega_{\mathbf{k}+\mathbf{q}} - \omega_{\mathbf{k}}).\end{aligned} \tag{6.41}$$

Note that for non-zero α there will be single-magnon weight at $\mathbf{q} = \mathbf{0}$, in contrast to our calculations for the cuprates, where the rotation of the octahedra was not included.

Cross section of g and h excitations. For the g and h excitations, one only has to consider the polarization dependence, because in a Mott insulating state there is no collective behavior expected. The excitations decay rapidly via particle-hole excitations and through superexchange coupling to, amongst others, the f doublet on neighboring sites. Rapid decay eliminates collective behavior, and therefore all $\mathbf{q}$ dependence. In a metallic state, the g and h excitations will be broad convolutions over the bands they form, and are thus also $\mathbf{q}$-independent. Both excitations will be broadened quite strongly.

For local excitations, it is convenient to express the RIXS intensity in terms of Green's functions:

$$I \propto \sum_f |\langle f| O_{\mathbf{q}} |g\rangle|^2 \delta(\omega - \omega_{fi}) = -\frac{1}{\pi}\mathfrak{Im}\{G_{\mathbf{q}}(\omega)\} \tag{6.42}$$

with

$$G_{\mathbf{q}}(\omega) = -i\int_0^\infty dt e^{i\omega t} \langle g| O^\dagger_{\mathbf{q}}(t) O_{\mathbf{q}}(0) |g\rangle, \tag{6.43}$$

where $|g\rangle$ is the ground state. In the case of local excitations, $G(\omega)$ is a quite simple quantity. For instance, for g excitations one gets

$$\begin{aligned} G^{(g)}_{\mathbf{q}}(\omega) &= -i\int_0^\infty dt e^{i(\omega-\omega_g)t} \langle g| \sum_j e^{-i\mathbf{q}\cdot\mathbf{R}_j} O^\dagger_j \sum_i e^{i\mathbf{q}\cdot\mathbf{R}_i} O_i |g\rangle & (6.44)\\ &= \lim_{\eta\to 0} \frac{1}{\omega - \omega_g + i\eta} \sum_i \langle g| O^\dagger_i O_i |g\rangle & (6.45)\end{aligned}$$

where $\hbar\omega_g = \lambda/\sqrt{2}\tan\theta - (-\Delta - \lambda/2)$ (the energy splitting between the local ground state and a hole in the g states). We also define $\hbar\omega_h = \lambda/\sqrt{2}\tan\theta - (-\lambda\tan\theta)/\sqrt{2}$ for the h excitations. For simplicity, we have neglected the superexchange coupling for the f states so that the energy of the g and h excitations are given by the local considerations of Sec. 6.2, i.e., without corrections for the broken superexchange bonds between neighboring f holes, etc. Also, we neglect the rotation of the octahedra.

We note that

$$\begin{aligned} &\langle g| \mathbb{1}_2^{(g,h)\dagger}\mathbb{1}_2^{(g,h)} |g\rangle = \langle g| \sigma_a^{(g,h)\dagger}\sigma_a^{(g,h)} |g\rangle = \langle g| \mathbb{1}_2^{(f)} |g\rangle, \\ &\langle g| \sigma_a^{(g,h)\dagger}\sigma_b^{(g,h)} |g\rangle = i\epsilon_{abc}\langle g| \sigma_c^{(f)} |g\rangle = 0, \\ &\langle g| \mathbb{1}_2^{(g,h)\dagger}\sigma_a^{(g,h)} |g\rangle = \langle g| \sigma_a^{(f)} |g\rangle = 0, \end{aligned} \tag{6.46}$$

where $\{a,b,c\} = \{x,y,z\}$ and $\sigma_z^{(f)} = f_\uparrow f_\uparrow^\dagger - f_\downarrow f_\downarrow^\dagger$ etc. Writing the scattering operator as the inner product $(A_0, A_1, A_2, A_3)\cdot(\mathbb{1}_2^{(g,h)}, \sigma_x^{(g,h)}, \sigma_y^{(g,h)}, \sigma_z^{(g,h)})$ with appropriate complex numbers A, and using Eqs. (6.46), one obtains for the correlation function:

$$\begin{aligned} O^\dagger O = &\left(|A_0|^2 + \sum_i |A_i|^2\right)\mathbb{1}_2^{(f)} \\ &+ \sum_i \left(\{A_0^* A_i + A_0 A_i^*\} + i\sum_{j,k}\epsilon_{ijk}A_j^* A_k\right)\sigma_i^{(f)}. \end{aligned} \tag{6.47}$$

Since the $\sigma_{x,y,z}$ are summed over all sites and the order is alternating, the only contribution that is left is from the $\mathbb{1}_2$ term. What remains is

$$
\begin{aligned}
G_{L_2}^{(g)} &= N\frac{\sin^2(\theta-\Theta)}{\omega-\omega_g+i\eta}\left[\frac{c'^2}{8}(|T_y-iP_y|^2+|T_x+iP_x|^2)+\frac{s'^2}{2}(|T_z|^2+|Q_2|^2)\right], \\
G_{L_2}^{(h)} &= \frac{N}{16}\frac{\sin^2 2(\theta-\Theta)}{\omega-\omega_h+i\eta}\left(|P_z|^2+\frac{1}{3}\left|\sqrt{3}P_{A_{1g}}+Q_3\right|^2\right), \\
G_{L_3}^{(g)} &= N\frac{\cos^2(\theta-\Theta)}{\omega-\omega_g+i\eta}\left[\frac{s'^2}{8}(|T_y-iP_y|^2+|T_x+iP_x|^2)+\frac{c'^2}{4}(|Q_2|^2+|T_z|^2)\right], \\
G_{L_3}^{(h)} &= \frac{N}{8}\frac{1}{\omega-\omega_h+i\eta}\left[\frac{1}{2}(\sin 2\theta+\sin 2(\theta-\Theta))^2|P_z|^2\right. \\
&\quad +|T_y+i\cos 2\theta\ P_y|^2+|T_x-i\cos 2\theta\ P_x|^2 \\
&\quad \left.+\frac{1}{2}\left|\sqrt{3}\sin 2\theta\ Q_3-\sin 2(\theta-\Theta)\left(P_{A_{1g}}+\tfrac{1}{\sqrt{3}}Q_3\right)\right|^2\right].
\end{aligned}
\tag{6.48}
$$

In the cubic limit, this reduces to

$$
\begin{aligned}
G_{L_2}^{(g)} &= G_{L_2}^{(h)} = 0, \\
G_{L_3}^{(g)} &= \frac{N}{6}\frac{1}{\omega-\omega_g+i\eta}\left[\frac{1}{4}(|T_y-iP_y|^2+|T_x+iP_x|^2)+(|Q_2|^2+|T_z|^2)\right], \qquad (6.49) \\
G_{L_3}^{(h)} &= N\frac{1}{\omega-\omega_h+i\eta}\left[\frac{1}{6}\left(\frac{1}{3}|P_z|^2+|Q_3|^2\right)+\frac{1}{8}\left|T_y+\frac{i}{3}P_y\right|^2+\frac{1}{8}\left|T_x-\frac{i}{3}P_x\right|^2\right].
\end{aligned}
$$

In the limit of strong spin-orbit coupling, the g and h doublets have the same energy. Because quite some broadening is expected for these high energy excitations even in the Mott insulating state (as discussed in Sec. 6.2), the two peaks are probably not resolvable and merge into one big peak. In that case, it is more interesting to study the total spectral weight of the g and h excitations.

The total spectral weight is obtained by integrating the cross sections of the g and h excitations over energy loss, and adding them up. In the formula for the cross section, the imaginary part of the Green's function yields

$$
-\frac{1}{\pi}\lim_{\eta\to 0}\mathfrak{Im}\{\frac{1}{\omega-\omega_g+i\eta}\} = -\frac{1}{\pi}\lim_{\eta\to 0}\frac{-\eta}{(\omega-\omega_g)^2+\eta^2} = \delta(\omega-\omega_g). \tag{6.50}
$$

In the cubic limit with unrotated octahedra, one finds

$$
I_{L_3}^{(g+h)} = \frac{N}{6}\left[\sum_{i\in\{x,y,z\}}\left(|T_i|^2+\frac{1}{3}|P_i|^2\right)+|Q_2|^2+|Q_3|^2\right]. \tag{6.51}
$$

The polarization factors nicely group together, yielding the O_h invariants

$$\sum_i |T_i|^2 = 1 - 2\sum_j \epsilon_j^* \epsilon_j \epsilon_j'^* \epsilon_j' + |\boldsymbol{\epsilon} \cdot \boldsymbol{\epsilon}'|^2, \tag{6.52}$$

$$\sum_i |P_i|^2 = 1 - |\boldsymbol{\epsilon} \cdot \boldsymbol{\epsilon}'|^2, \tag{6.53}$$

$$\sum_i |Q_i|^2 = 2\sum_j \epsilon_j^* \epsilon_j \epsilon_j'^* \epsilon_j' - \frac{2}{3} |\boldsymbol{\epsilon}'^* \cdot \boldsymbol{\epsilon}|^2, \tag{6.54}$$

which add up to

$$I^{(g+h)}(\boldsymbol{\epsilon}', \boldsymbol{\epsilon}) = \frac{N}{9}\left[2 + |\boldsymbol{\epsilon}' \cdot \boldsymbol{\epsilon}|^2 - |\boldsymbol{\epsilon}'^* \cdot \boldsymbol{\epsilon}|^2\right]. \tag{6.55}$$

In case of linear incoming or outgoing polarization, the intensity is independent of the polarization vectors. This entails that when the outgoing polarization is not measured, as is the case in all RIXS experiments done so far, the intensity is independent of the polarization vectors[2]. A non-trivial polarization dependence can only arise when both incoming and outgoing X-rays are circularly polarized.

6.3.4 Iridium L edge cross section – Special cases

We now specialize the cross sections obtained above to some geometries often used in experiments. We consider transferred momenta along the $\Gamma - M$ and $\Gamma - X$ directions [$\Gamma = (0,0)$, $X = (\pi, 0)$ and $M = (\pi, \pi)$], and take the scattering angle to be 90°. The incoming polarization is chosen to be linear, while the outgoing polarization is not detected. Along the $\Gamma - X$ path through the BZ, the polarization vectors are

$$\boldsymbol{\epsilon}_\pi = \begin{pmatrix} \cos\varphi \\ 0 \\ \sin\varphi \end{pmatrix}, \quad \boldsymbol{\epsilon}_\sigma = \begin{pmatrix} 0 \\ 1 \\ 0 \end{pmatrix}, \quad \boldsymbol{\epsilon}'_\pi = \begin{pmatrix} -\sin\varphi \\ 0 \\ \cos\varphi \end{pmatrix}, \quad \boldsymbol{\epsilon}'_\sigma = \boldsymbol{\epsilon}_\sigma. \tag{6.56}$$

π and σ mean, respectively, polarization parallel and perpendicular to the scattering plane. φ is the angle of the incoming X-rays with the normal to the IrO_2 planes. Along the $\Gamma - M$ path,

$$\boldsymbol{\epsilon}_\pi = \begin{pmatrix} \frac{1}{\sqrt{2}}\cos\varphi \\ \frac{1}{\sqrt{2}}\cos\varphi \\ \sin\varphi \end{pmatrix}, \quad \boldsymbol{\epsilon}_\sigma = \frac{1}{\sqrt{2}}\begin{pmatrix} -1 \\ 1 \\ 0 \end{pmatrix}, \quad \boldsymbol{\epsilon}'_\pi = \begin{pmatrix} -\frac{1}{\sqrt{2}}\sin\varphi \\ -\frac{1}{\sqrt{2}}\sin\varphi \\ \cos\varphi \end{pmatrix}, \quad \boldsymbol{\epsilon}'_\sigma = \boldsymbol{\epsilon}_\sigma. \tag{6.57}$$

The angle φ is related to $\mathbf{q}$. In 90° scattering geometry, the total transferred momentum (at an incident energy of 11.2 keV at the L_3 edge [223]) is ≈ 8.05 Å^{-1}

---

[2] This can be seen as follows: when the outgoing photon's polarization is not measured, it is summed over. One can choose to sum over two orthogonal linear polarization vectors, which makes $\boldsymbol{\epsilon}'^* = \boldsymbol{\epsilon}'$, and the polarization vectors cancel in Eq. (6.55).

while the X-point is at ≈ 0.808 Å^{-1} [223]. The X-rays carry an order of magnitude more momentum than needed to probe the BZ. It is therefore reasonable to approximate $\varphi \approx 45°$ as constant: it varries 5.7° around 45° (assuming one stays in the first 2D Brillouin zone). This fact greatly diminishes the asymmetry effects between $+\mathbf{q}$ and $-\mathbf{q}$ that are so important in the cuprates (see Secs. 4.5.2 and 4.6.2).

Note that the integrated weight of the $J_{\text{eff}} = 3/2$ excitations are polarization-independent for linearly polarized light: $I^{(g+h)} = 2N/9$. For the $J_{\text{eff}} = 1/2$ excitations, we calculate 4 different cases: $\mathbf{q}$ towards X and M, and incoming π and σ polarization. Abbreviating $\cos\alpha = c_\alpha$ etc, the single- and two-magnon intensity in each case is

$$I^{(1)}_{X\pi} \propto \frac{N}{18}\left[\frac{s^2_\alpha}{2}(1+s^2_\varphi)(u_\mathbf{q}+v_\mathbf{q})^2 + \frac{c^2_\alpha}{2}(1+s^2_\varphi)(u_\mathbf{q}-v_\mathbf{q})^2 + c^2_\varphi(u_\mathbf{q}-v_\mathbf{q})^2\right] \times \delta(\omega-\omega_\mathbf{q}), \tag{6.58}$$

$$I^{(2)}_{X\pi} \propto \frac{1}{9}(1+s^2_\varphi)\sum_\mathbf{k}\left[s^2_\alpha\left(u_{\mathbf{k}+\mathbf{q}}v_\mathbf{k} + u_\mathbf{k}v_{\mathbf{k}+\mathbf{q}}\right)^2 + c^2_\alpha\left(u_{\mathbf{k}+\mathbf{q}}v_\mathbf{k} - u_\mathbf{k}v_{\mathbf{k}+\mathbf{q}}\right)^2\right] \times \delta(\omega-\omega_{\mathbf{k}+\mathbf{q}}-\omega_\mathbf{k}), \tag{6.59}$$

$$I^{(1)}_{X\sigma} \propto \frac{N}{18}\left[\frac{s^2_\alpha}{2}c^2_\varphi(u_\mathbf{q}+v_\mathbf{q})^2 + \frac{c^2_\alpha}{2}c^2_\varphi(u_\mathbf{q}-v_\mathbf{q})^2 + s^2_\varphi(u_\mathbf{q}-v_\mathbf{q})^2\right]\delta(\omega-\omega_\mathbf{q}), \tag{6.60}$$

$$I^{(2)}_{X\sigma} \propto \frac{1}{9}c^2_\varphi\sum_\mathbf{k}\left[s^2_\alpha\left(u_{\mathbf{k}+\mathbf{q}}v_\mathbf{k} + u_\mathbf{k}v_{\mathbf{k}+\mathbf{q}}\right)^2 + c^2_\alpha\left(u_{\mathbf{k}+\mathbf{q}}v_\mathbf{k} - u_\mathbf{k}v_{\mathbf{k}+\mathbf{q}}\right)^2\right] \times \delta(\omega-\omega_{\mathbf{k}+\mathbf{q}}-\omega_\mathbf{k}), \tag{6.61}$$

$$I^{(1)}_{M\pi} \propto \frac{N}{18}\left[s^2_\alpha s^2_\varphi(u_\mathbf{q}+v_\mathbf{q})^2 + c^2_\varphi(u_\mathbf{q}-v_\mathbf{q})^2 + c^2_\alpha(u_\mathbf{q}-v_\mathbf{q})^2\right]\delta(\omega-\omega_\mathbf{q}), \tag{6.62}$$

$$I^{(2)}_{M\pi} \propto \frac{2}{9}\sum_\mathbf{k}\left[s^2_\alpha\left(u_{\mathbf{k}+\mathbf{q}}v_\mathbf{k} + u_\mathbf{k}v_{\mathbf{k}+\mathbf{q}}\right)^2 + c^2_\alpha s^2_\varphi\left(u_{\mathbf{k}+\mathbf{q}}v_\mathbf{k} - u_\mathbf{k}v_{\mathbf{k}+\mathbf{q}}\right)^2\right] \times \delta(\omega-\omega_{\mathbf{k}+\mathbf{q}}-\omega_\mathbf{k}), \tag{6.63}$$

$$I^{(1)}_{M\sigma} \propto \frac{N}{18}\left[s^2_\alpha c^2_\varphi(u_\mathbf{q}+v_\mathbf{q})^2 + s^2_\varphi(u_\mathbf{q}-v_\mathbf{q})^2\right]\delta(\omega-\omega_\mathbf{q}), \tag{6.64}$$

$$I^{(2)}_{M\sigma} \propto \frac{2}{9}c^2_\alpha c^2_\varphi\sum_\mathbf{k}\left(u_{\mathbf{k}+\mathbf{q}}v_\mathbf{k} - u_\mathbf{k}v_{\mathbf{k}+\mathbf{q}}\right)^2\delta(\omega-\omega_{\mathbf{k}+\mathbf{q}}-\omega_\mathbf{k}). \tag{6.65}$$

The resulting spectra are displayed in Fig. 6.1, assuming $\varphi \approx 45°$ and $\alpha = 8°$. The (pseudo-)magnon results are very similar to the cuprates: the single-magnon intensity peaks strongly at the antiferromagnetic ordering vector (π, π). Also, the two-magnon intensity at $(0, 0)$ is suppressed while the two-magnon DOS is highest there [see Fig. 4.5(b)]. The doublet to quartet excitations have an energy of $(3/2)\lambda$. Although λ is measured to be around 380 meV, the exact ratio of λ

to J is not known. The rough theoretical estimate $J \approx 45$ meV [214] would put $(3/2)\lambda/J$ at 12.7, but that could well be off by 50% or more. High resolution RIXS experiments would be a much better way to precisely determine this ratio. We therefore regard the ratio as a free parameter in our theory, and put it at 8 for the moment. In Fig. 6.2, spectra at several transferred momenta are shown. These figures are vertical cuts through Fig. 6.1. The spectral weight of the different types of excitations is compared in Fig. 6.3.

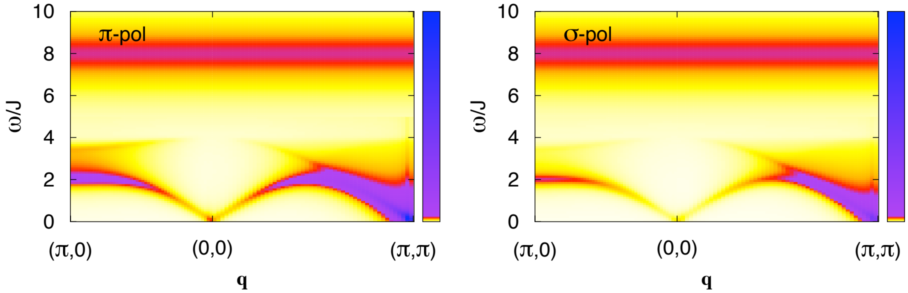

Figure 6.1: RIXS spectra of Sr_2IrO_4 at the Ir L_3 t_{2g} edge, including single- and two-magnon $J_{\text{eff}} = 1/2$ excitations and $J_{\text{eff}} = 3/2$ excitations. The latter are put at an energy of $8J$ with a phenomenological broadening of J (half-width at half-max). We have assumed that the system is dominated by 5d spin-orbit coupling, $\varphi = 45°$ and $\alpha = 8°$. The left panel shows the spectrum for incoming π polarization, and the right one for incoming σ polarization.

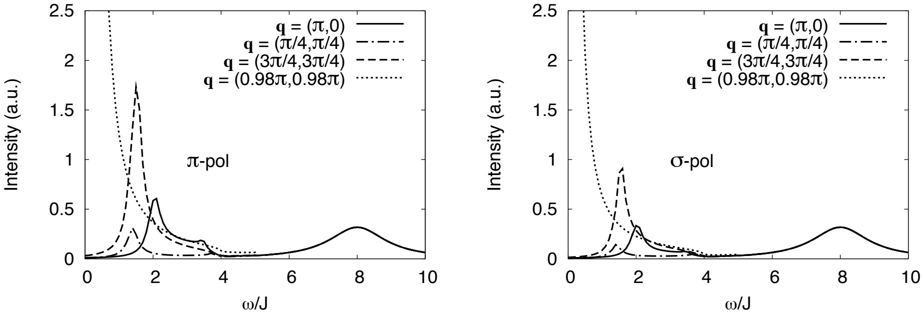

Figure 6.2: RIXS spectra of Sr_2IrO_4 at the Ir L_3 t_{2g} edge, including single- and two-magnon $J_{\text{eff}} = 1/2$ excitations and $J_{\text{eff}} = 3/2$ excitations. These spectra are vertical cuts through Fig. 6.1. The left panel shows several spectra for incoming π polarization, and the right one for incoming σ polarization.

A very striking feature of dominating spin-orbit coupling is the absence of

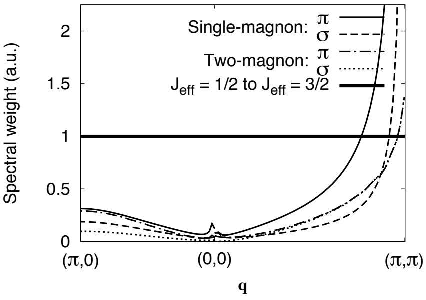

Figure 6.3: RIXS spectral weight of Sr_2IrO_4 at the Ir L_3 t_{2g} edge, obtained by integrating the different features of the spectra of Fig. 6.1 over energy loss. The units on the vertical axis are chosen such that the $J_{\text{eff}} = 1/2$ to $J_{\text{eff}} = 3/2$ excitations have spectral weight 1.

excitations in L_2 edge spectra. Looking at the L_3 edge with low energy resolution ($\sim$ 0.6 eV), it is impossible to see any details of the L_3 excitation spectra of Figs. 6.1 and 6.2 except for the total spectral weight. As is clear from Fig. 6.3, the total spectral weight strongly peaks at $\mathbf{q} = (\pi, \pi)$ and is lowest (but non-zero) at $\mathbf{q} = (0, 0)$. With a better energy resolution, one might be able to see the dispersion of the magnon excitations: at $\mathbf{q} = (\pi, \pi)$, the intense single-magnon peak disperses down to zero energy loss, from about $2J \approx 90$ meV at $\mathbf{q} = (\pi, 0)$ and $(\pi/2, \pi/2)$. RIXS can determine the values of λ and J up to the energy resolution of the experiment.

The results obtained in this chapter can easily be applied to other Ir compounds with octahedral crystal fields, such as the hexagonal Kitaev-Heisenberg model compounds A_2IrO_3 (A = Li, Na) [214, 215]. The collective response will be different, but the local scattering operators derived in Sec. 6.3.2 still apply.

Chapter 7

Phonon RIXS

Unpublished work. *Determining the Electron-Phonon Coupling Strength in Correlated Electron Systems from Resonant Inelastic X-ray Scattering*, with Michel van Veenendaal and Jeroen van den Brink.

7.1 Introduction

Often novel electronic properties of materials can be understood by systematically unravelling the interaction between its electrons and phonons. Tunable electric transport properties in molecular crystals, for instance, are explained by the presence of a strong electron-phonon (e-p) coupling [225]. The dressing of electrons by phonons is also responsible for the colossal magnetoresistance effect in manganites [226]. More delicate is the role that the e-p interaction plays in high-T_c superconducting cuprates, which is the topic of a hot, persisting debate [227–229]. The lack of a technique to measure the e-p coupling strength perpetuates this controversy. Here we show that high resolution RIXS fills this void and can provide direct, element-specific and momentum-resolved information on the coupling between electrons and phonons. We provide the theoretical framework required to distill e-p interaction strengths from RIXS, particularly in strongly correlated transition metal oxides such as the high-T_c cuprates.

The state-of-the-art resolution of RIXS experiments is such that photon energy loss features on an energy scale of 25 meV can be distinguished at a copper or nickel L_3 edge [11,112]. This resolution has brought phonons within the energy window of observation and indeed this year the first glimpses of phonons were resolved in RIXS [11, 230]. To put this achievement in perspective, one should realize that the incident photons at the Cu L edge have an energy of around 930 eV, implying experiments have a resolving power of about $4 \cdot 10^4$. Developments in instrumentation are driving this already impressive figure further up [3]. Here we show how the progress in accuracy will allow the extraction of a number of characteristics of the e-p interaction directly from RIXS, including spatial information on the e-p coupling strength. No other experimental technique has access to such e-p characteristics, particularly in strongly correlated 3d transition metal oxides.

RIXS couples to phonons because the intermediate state in the RIXS process has an altered charge distribution, which influences the lattice. Most core holes decay very rapidly, and there is not enough time for the lattice to fully adjust to the transient charge distribution. Therefore, the final states of the RIXS process contain only few phonons; multi-phonon excitations are suppressed by the large lifetime broadening Γ.

The advantage of RIXS is that X-ray photons carry an appreciable momentum. This allows RIXS to sample the Brillouin zone and hence the phonon dispersion. In contrast, Raman scattering in the optical range is restricted to zero momentum transfer. Using Raman or neutron scattering, one can measure the broadening of phonon peaks. Because of e-p coupling, the phonon decays for instance in an electron-hole pair and consequently the lifetime of the phonon is decreased. This adds to the broadening of the phonon peaks. Allen's formula [231] gives the connection between this broadening and the e-p coupling constant. However, in the absence of low energy electron-hole excitations, like in Mott insulators, this decay channel does not exist. Other methods to measure the e-p interaction also do not have access to momentum-dependent information. Electron tunneling for instance, has no momentum-dependence and thus cannot probe how strong an electron couples to a particular phonon at a particular wavevector. Moreover, it is intrinsically surface sensitive and suffers from the practical difficulty to make good yet partially transparent barriers [232–234]. Another asset of RIXS is its element-specificity: in a cuprate not only the copper-related phonons can in principle be accessed at the Cu L edge, but also the oxygen-related ones at the O K edge – resolution permitting.

Measuring phonon dispersions is a promising new utilization of RIXS but as a technique it is up against inelastic neutron scattering and (non-resonant) inelastic X-ray scattering, well-established experimental methods with the same capacity. Here we make the case that what really sets RIXS apart is the way phonons are excited, leading to the capability to measure momentum dependent e-p couplings.

This chapter is organized as follows: Sec. 7.2 reviews the general e-p coupling Hamiltonian and how it relates to RIXS. In Sec. 7.3, the cross sections for Einstein phonons and dispersive phonons are derived. These yield complicated expressions, which simplify tremendously in the UCL expansion, as explained in Sec. 7.3.1.

7.2 Electron-phonon coupling

As an introduction to phonon scattering in RIXS, we start with a summary of e-p coupling, closely following chapter 1.3.2 in Ref. [62]. Then we discuss how the e-p Hamiltonian relates to the RIXS process, where the core hole and the photo-excited electron form a potential that perturbs the lattice.

7.2.1 Theory of electron-phonon coupling

We will assume that the core hole binds the photo-excited electron (which is a very good approximation at the Cu L edge [157]). The electron-phonon Hamiltonian for electrons localized at positions $\mathbf{R}_i$ is [62]

$$H = \sum_{\mathbf{k},\lambda} \left[\omega_{\mathbf{k}\lambda} b^\dagger_{\mathbf{k},\lambda} b_{\mathbf{k},\lambda} + \sum_i \left(b_{\mathbf{k},\lambda} + b^\dagger_{-\mathbf{k},\lambda} \right) e^{i\mathbf{k}\cdot\mathbf{R}_i} \sum_{\mathbf{G}} \mathcal{M}_{\mathbf{k}+\mathbf{G},\lambda} \eta(\mathbf{k}+\mathbf{G}) e^{i\mathbf{G}\cdot\mathbf{R}_i} \right] \tag{7.1}$$

The free phonon dynamics is governed by the first term. The second term of the Hamiltonian couples the electrons to phonons with momentum $\hbar\mathbf{k}$ and branch index λ, which are created by the operator $b^\dagger_{\mathbf{k}\lambda}$. Note that we have chosen units such that $\hbar = 1$. Further, we have

$$\mathcal{M}_{\mathbf{k}+\mathbf{G},\lambda} = -(\mathbf{k}+\mathbf{G}) \cdot \boldsymbol{\xi}_{\mathbf{k}\lambda} \sqrt{\frac{\hbar}{2\rho\mathcal{V}\omega_{\mathbf{k}\lambda}}} V_{ei}(\mathbf{k}+\mathbf{G}) \tag{7.2}$$

$$\eta(\mathbf{k}+\mathbf{G}) = \int d\mathbf{r} e^{i(\mathbf{k}+\mathbf{G})\cdot\mathbf{r}} \Delta\rho(\mathbf{r}) \tag{7.3}$$

with $\Delta\rho(\mathbf{r})$ the change in the charge distribution due to the electron (centered at $\mathbf{r} = \mathbf{0}$), $\mathcal{V}$ the volume of the crystal and ρ its density. $\boldsymbol{\xi}_{\mathbf{k}\lambda}$ is the phonon polarization. $V_{ei}(\mathbf{k})$ is the Fourier transform of the potential of an ion placed at the origin. For an ion with a point-potential, $V_{ei}(\mathbf{k}) \propto 1/\mathbf{k}^2$.

We assume that the crystal has inversion symmetry: $\omega_{\mathbf{k}\lambda} = \omega_{-\mathbf{k},\lambda}$ and $\boldsymbol{\xi}_{\mathbf{k}\lambda} = -\boldsymbol{\xi}^*_{-\mathbf{k},\lambda}$. Since the Hamiltonian should be Hermitian, we obtain the condition $\mathcal{M}^*_{-\mathbf{k}-\mathbf{G},\lambda}\eta^*(-\mathbf{k}-\mathbf{G}) = \mathcal{M}_{\mathbf{k}+\mathbf{G},\lambda}\eta(\mathbf{k}+\mathbf{G})$, which is indeed satisfied if $V^*_{ei}(-\mathbf{k}-\mathbf{G}) = V_{ei}(\mathbf{k}+\mathbf{G})$: V_{ei} is invariant under inversion too.

Next, we assume that there is only one electronic excitation during the RIXS process, as is the case in RIXS if we neglect the electronic intermediate state dynamics. The unit cell is chosen such that the core hole is located at its center ($\mathbf{R}\cdot\mathbf{G} = 0$).

The electronic degree of freedom can be written in second quantization, using $e^{i\mathbf{k}\cdot\mathbf{R}} = \sum_i d^\dagger_i d_i e^{i\mathbf{k}\cdot\mathbf{R}_i}$ where d_i annihilates the photo-excited electron at site i. In momentum space, the Hamiltonian is

$$H = \sum_{\mathbf{k},\lambda} \left[\omega_{\mathbf{k}\lambda} b^\dagger_{\mathbf{k}\lambda} b_{\mathbf{k}\lambda} + M_{\mathbf{k}\lambda} \sum_{\mathbf{p}} d^\dagger_{\mathbf{p}} d_{\mathbf{p}-\mathbf{k}} \left(b_{\mathbf{k}\lambda} + b^\dagger_{-\mathbf{k},\lambda} \right) \right] \tag{7.4}$$

with

$$M_{\mathbf{k}\lambda} = \sum_{\mathbf{G}} \mathcal{M}_{\mathbf{k}+\mathbf{G},\lambda}\eta(\mathbf{k}+\mathbf{G}). \tag{7.5}$$

Because of inversion symmetry $M^*_{\mathbf{k},\lambda} = M_{-\mathbf{k},\lambda}$.

7.2.2 Electron-phonon coupling in RIXS

To understand the capacity of RIXS to measure the momentum dependence of the e-p interaction, we start with the e-p coupling Hamiltonian (7.4). For definiteness we focus on the high-T_c cuprates which have all their Cu 3d orbitals filled apart from a single hole in the x^2-y^2 orbitals, but our analysis is general. In the Cu L edge RIXS process, the x^2-y^2 state is transiently occupied as an electron from the core is launched into it. The change in the charge density $\Delta\rho(\mathbf{r})$ is given by the shape of the x^2-y^2 orbital and the core hole. As mentioned before, the filled x^2-y^2 state is very short-lived. There is then a certain probability that during the lifetime of the core hole a phonon is excited and left behind in the final state. Obviously this probability is related to the coupling of the x^2-y^2 electron to this particular phonon. Note that the presence of the core hole ensures that the intermediate state is locally charge neutral. Thus the phonons that couple to the 3d x^2-y^2 state with its characteristic quadrupolar charge distribution light up in L edge RIXS.

One might object that the phonons react to the core hole as well as to the photo-excited electron. The contribution of the core hole to the electric potential outside the Cu ion is very small, however, as can be seen from a multipole expansion of the potential of the core hole plus photo-excited electron (see, for instance, Ref. [235], page 148):

$$\begin{aligned} V(\mathbf{r}) = \frac{1}{4\pi\epsilon_0}\Bigg[\frac{1}{r}\int d\mathbf{r}'\ \rho(\mathbf{r}') + \frac{1}{r^2}\int(\hat{\mathbf{r}}\cdot\mathbf{r}')\rho(\mathbf{r}') \\ +\frac{1}{2r^3}\int d\mathbf{r}'[3(\hat{\mathbf{r}}\cdot\mathbf{r}')^2 - \mathbf{r}'^2]\rho(\mathbf{r}') + \ldots\Bigg] \end{aligned} \tag{7.6}$$

where $\mathbf{r} = |\mathbf{r}|\hat{\mathbf{r}} = r\hat{\mathbf{r}}$ and $\rho(\mathbf{r}) = e\,|\langle\mathbf{r}|\,2p\rangle|^2 - e\,|\langle\mathbf{r}|\,3d\rangle|^2$, with $|2p\rangle$ and $|3d\rangle$ the states of the core hole and the photo-excited electron, respectively. Since the core orbitals have a very small radius compared to the valence orbitals, a first order approximation would be $|\langle\mathbf{r}|\,2p\rangle|^2 \approx \delta(\mathbf{r})$, and the core hole only contributes to the monopole of the potential. Outside the Cu ion, the total monopole contribution vanishes. Within this approximation, the only contributions to the electric potential outside the Cu ion come from the 3d valence orbitals. Further, the dipole contributions are zero by symmetry. We conclude that the lattice couples mainly to the quadrupole potential of the photo-excited electron, and not to the core hole. At the Cu K-edge, in contrast, the main contribution to the potential comes from the core hole.

7.3 RIXS cross section for phonons

To understand how the electron-phonon coupling is precisely reflected in the RIXS intensity, we evaluate the RIXS amplitude for phonon scattering $\mathcal{F}$ in the Kramers-Heisenberg equation (2.30). The polarization factor (2.42) describing processes where only phonons are excited, is well approximated by the elastic process, as the phonons modify the electronic states of the system only slightly. Consequently, the dipole transition amplitudes are also marginally affected. In the case of Cu L edge RIXS at the cuprates, the photo-excited electron fills the only available hole, *i.e.*, the hole in the 3d$_{x^2-y^2}$ orbital. The polarization factor for elastic processes and phonon scattering is given by

$$T_\psi(\boldsymbol{\epsilon}', \boldsymbol{\epsilon}) = \langle\psi|\, \boldsymbol{\epsilon}'^* \cdot \mathbf{r} \left|3d_{x^2-y^2}\right\rangle \left\langle 3d_{x^2-y^2}\right| \boldsymbol{\epsilon} \cdot \mathbf{r}\, |\psi\rangle \tag{7.7}$$

where ψ is one of the resonant core states, see, *e.g.*, Sec. 4.3.1. Since the lattice (approximately) does not react to the core hole, the latter can be integrated out from the scattering amplitude:

$$\mathcal{F}_{fi} = \sum_\psi T_\psi(\boldsymbol{\epsilon}', \boldsymbol{\epsilon}) \sum_i e^{i\mathbf{q}\cdot\mathbf{R}_i} \sum_n \frac{\langle f|\, d_i\, |n\rangle \langle n|\, d_i^\dagger\, |i\rangle}{E_i + \hbar\omega_{\mathbf{k}} - E_n + i\Gamma}. \tag{7.8}$$

The sum over ψ can be performed and gives the atomic scattering factor for elastic scattering $T_{\text{el}}(\boldsymbol{\epsilon}', \boldsymbol{\epsilon}) = \sum_\psi T_\psi(\boldsymbol{\epsilon}', \boldsymbol{\epsilon})$.

Due to the presence of the intermediate states, it is in general impossible to evaluate RIXS scattering intensities exactly, even in model systems. One therefore often resorts to finite size cluster calculations to compute RIXS spectra [2,73]. The e-p problem at hand, however, is an exception. We have solved the RIXS phonon spectrum exactly by means of a canonical transformation. The fact that one is dealing with harmonic bosons allows for this solution.

Einstein phonons. In analyzing the general solution, it is instructive to consider the Einstein model, which comprises a single non-dispersive phonon per site of frequency ω_0 with a coupling strength M. The e-p Hamiltonian reduces to

$$H = \sum_i \omega_0 b_i^\dagger b_i + M d_i^\dagger d_i (b_i^\dagger + b_i). \tag{7.9}$$

This Hamiltonian can be diagonalized by a canonical transformation $\bar{H} = e^S H e^{-S}$ [62], with $S = \sum_i d_i^\dagger d_i S_i$ where

$$S_i = \frac{M}{\omega_0}(b_i^\dagger - b_i). \tag{7.10}$$

As there is a single core hole present, this results in

$$\bar{H} = \sum_i \omega_0 b_i^\dagger b_i - \frac{M^2}{\omega_0}, \tag{7.11}$$

where the last term merely shifts the energy at which the resonance occurs. The eigenstates of $\bar{H}$ are all the possible occupations $\{n_i\}$ of the phonon states, indexed by m, with energies $E_m = \sum_i n_i(m)\omega_0 - M^2/\omega_0$. The transformation can be thought of as shifting the origin of the lattice coordinate to the new equilibrium position of the lattice: zero phonons in a transformed state describes the lattice at rest in the new equilibrium position. The eigenstates $\left|\bar{\psi}_m\right\rangle$ of $\bar{H}$ are related to the eigenstates $|\psi_m\rangle$ of H by $|\psi_m\rangle = e^{-S}\left|\bar{\psi}_m\right\rangle$. Inserting this transformation in the scattering amplitude (7.8) gives

$$\begin{aligned}\mathcal{F}_{fi} &= T_{\mathrm{el}}(\boldsymbol{\epsilon}', \boldsymbol{\epsilon}) \sum_i e^{i\mathbf{q}\cdot\mathbf{R}_i} \sum_m \frac{\langle f|\, d_i e^{-S} \left|\bar{\psi}_m\right\rangle \left\langle\bar{\psi}_m\right| e^{S} d_i^\dagger \,|i\rangle}{E_i + \hbar\omega_{\mathbf{k}} - E_m + i\Gamma} \\ &= T_{\mathrm{el}}(\boldsymbol{\epsilon}', \boldsymbol{\epsilon}) \sum_i e^{i\mathbf{q}\cdot\mathbf{R}_i} \sum_{n_i=0}^{\infty} \frac{\langle n_i'|\, e^{-S_i} \,|n_i\rangle \langle n_i|\, e^{S_i} \left|n_i^0\right\rangle}{z + M^2/\omega_0 - n_i\omega_0}, \qquad (7.12)\end{aligned}$$

where in the last step the photo-excited electron degree of freedom is integrated out. We defined $z = \hbar\omega_{\mathbf{k}} - E_{\mathrm{res}} + i\Gamma$, where E_{res} is the peak energy of the phonon-broadened XAS spectrum (see page 226 of Ref. [62]). n_i^0, n_i, and n_i' are the occupations in the initial, intermediate, and final states, respectively. In the local model, the final states are indexed by the local phonon numbers $\{n_i'\}$. Note that final states where the phonon number has been changed at multiple sites cannot be reached: phonons can only be created and annihilated at the core hole site, and only contributions from this site remain in the numerator of Eq. (7.12).

The evaluation of the scattering amplitude is given in appendix C; the zero temperature result is

$$\mathcal{F}_{fg} = T_{\mathrm{el}}(\boldsymbol{\epsilon}', \boldsymbol{\epsilon}) \sum_i e^{i\mathbf{q}\cdot\mathbf{R}_i} \left[\sum_{n=0}^{n_i'} \frac{B_{n_i' n}(g) B_{n0}(g)}{z + (g-n)\omega_0} + \sum_{n=n_i'+1}^{\infty} \frac{B_{n n_i'}(g) B_{n0}(g)}{z + (g-n)\omega_0} \right], \qquad (7.13)$$

with $g = M^2/\omega_0^2$. The Franck-Condon (FC) factors in the numerator are

$$B_{ab}(g) = \sqrt{e^{-g} a! b!} \sum_{l=0}^{b} \frac{(-1)^a (-g)^l \sqrt{g}^{\,a-b}}{(b-l)!\, l!\, (a-b+l)!}. \qquad (7.14)$$

The zero temperature RIXS cross section is obtained by squaring the amplitude. As argued above, final states where the phonon number has changed at multiple sites cannot be reached with local phonons, so the sum over final states in the Kramers-Heisenberg equation is $\sum_i \sum_{n_i'=0}^{\infty}$. We get for the cross section

$$\begin{aligned}\frac{d^2\sigma}{d\Omega d\omega} \propto \sum_f \left|\mathcal{F}_{fg}\right|^2 \delta(\omega - n'\omega_0) = N \left|T_{\mathrm{el}}(\boldsymbol{\epsilon}', \boldsymbol{\epsilon})\right|^2 \sum_{n'=0}^{\infty} \Bigg| \sum_{n=0}^{n'} \frac{B_{n'n}(g) B_{n0}(g)}{z + (g-n)\omega_0} \\ + \sum_{n=n'+1}^{\infty} \frac{B_{nn'}(g) B_{n0}(g)}{z + (g-n)\omega_0} \Bigg|^2 \delta(\omega - n'\omega_0) \qquad (7.15)\end{aligned}$$

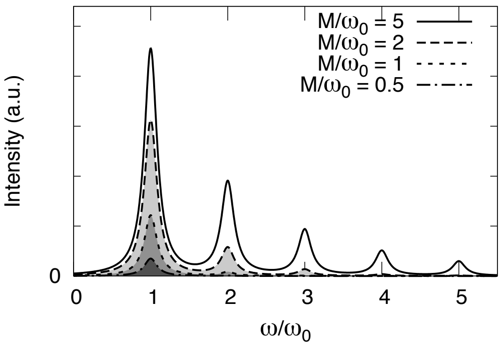

Figure 7.1: RIXS phonon cross section for Einstein phonons with energy ω_0, for different electron-phonon couplings M. We take $\Gamma/\omega_0 = 5$ (a typical value at the copper L edge), and an incident energy corresponding to the maximum in the XAS signal. The polarization dependence is omitted in this plot, as well as the zero loss peak, which shifts to the Bragg peaks in an ideal crystal.

Note that the **q** dependence is lost, because of the local nature of the Einstein phonons.

The resulting RIXS spectra for a typical weak, intermediate and strong coupling case are shown in Fig. 7.1. It is clear that for stronger e-p interactions, a larger number of multi-phonon satellites carry appreciable weight.

However, the first important observation is that the intensity of the zero loss peak is dominant even in the strong e-p coupling regime, as is clear from Figs. 7.2 and 7.3. Its spectral weight is larger than the weight of all phonon loss peaks combined when $M/\Gamma \lesssim 1.5$. As at the Cu L$_3$ edge $\Gamma = 280$ meV [100], this corresponds to the physical situation. This observation is empirically supported by the fact that a dispersion of magnon [11, 19, 21] and bimagnon [14, 51–53] excitations has been observed in L and K edge RIXS. Such dispersion would be absent if these magnetic excitations were always accompanied by (multiple) phonons, see Sec. 7.4.

It is interesting to note that in the case of an infinitely fast scattering process ($\Gamma \to \infty$), the lattice has no time to react to the transient electronic excitation, and no phonons are excited in the final state.

The exact intensity for exciting a single phonon in the RIXS process is

$$I^{(1)} = N \left|T_{\rm el}(\boldsymbol{\epsilon}', \boldsymbol{\epsilon})\right|^2 \frac{e^{-2g}}{g} \left| \sum_{n=0}^{\infty} \frac{g^n (n-g)}{n!(z + (g-n)\omega_0)} \right|^2 , \qquad (7.16)$$

In leading order in the e-p coupling g this is $I^{(1)} \approx N|T_{\rm el}(\boldsymbol{\epsilon}', \boldsymbol{\epsilon})|^2 M^2/|z|^4$ so that in this limit the single-phonon RIXS scattering intensity is directly proportional to the dimensionless e-p coupling constant g, see Fig. 7.3. Increasing z by tuning away from the absorption edge reduces the single-phonon scattering intensity.

Even when the e-p coupling g is not small, we can obtain the RIXS amplitude in approximate form by using the fact that the timescale of a typical phonon (80 meV $\sim$ 52 fs) is much slower than the ultrashort RIXS timescale (1.6 eV $\sim$ 2.6 fs at the Cu K edge). This separation of timescales suggests that the scattering

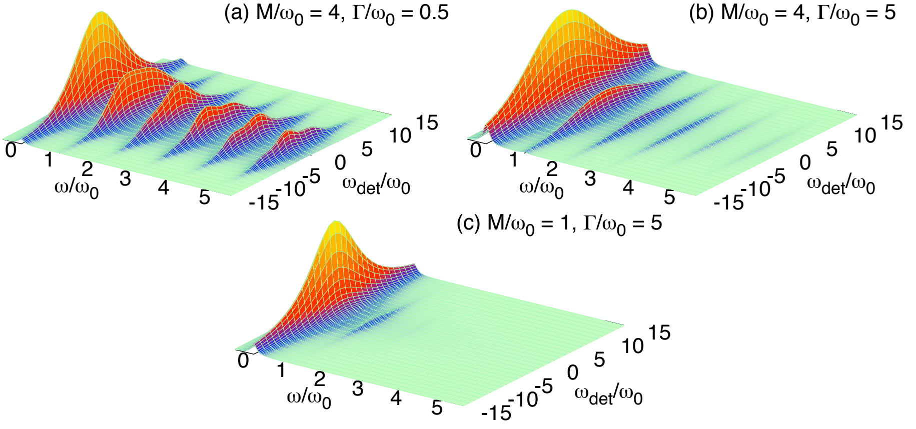

Figure 7.2: Calculated RIXS intensities for phonon loss as a function of loss energy ω and detuning from the maximum of the absorption spectrum $\omega_{\text{det}} = \mathfrak{Re}\{z\}$ in the case of (a) strong coupling and very long core-hole lifetime, (b) strong e-p coupling and (c) intermediate/weak e-p coupling.

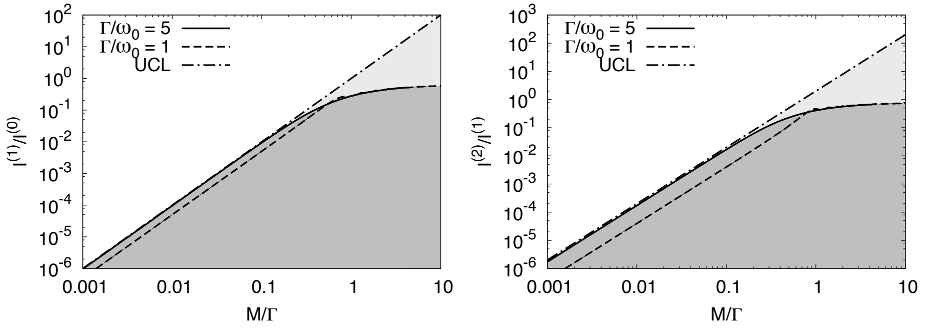

Figure 7.3: Relation of the multiple phonon RIXS cross section to the electron-phonon coupling strength M on an absolute energy scale. The ratio of the single-phonon $I^{(1)}$ to zero-phonon $I^{(0)}$ cross section is shown in the left panel. The right panel shows the two-phonon to single-phonon cross section ratio. The curves are universal in the sense that they do not depend on the phonon frequency ω_0 as long as $\Gamma \gg \omega_0$ (for instance, $\Gamma/\omega_0 = 5$). The UCL expansion (straight line) gives accurate results for $M/\Gamma \lesssim 0.2$ and $\Gamma/\omega_0 \gg 1$, *i.e.*, when Γ is the dominant energy scale. This corresponds to the physical regime of the e-p interaction at the Cu K edge ($\Gamma \approx 1.5$ eV) and to the intermediate and weak e-p coupling regime at the Cu L edge ($\Gamma \approx 280$) meV.

process contains a viable expansion parameter, which is small even for a fast phonon. The UCL expansion (see Sec. 2.5) formalizes this observation, and the result, obtained in Sec. 7.3.1, is $\mathcal{F}^{(1)}_{\text{UCL}} = T_{\text{el}}(\boldsymbol{\epsilon}', \boldsymbol{\epsilon})\frac{M}{z^2}\langle f|\sum_i e^{i\mathbf{q}\cdot\mathbf{R}_i}(b_i^\dagger + b_i)|i\rangle$. So, also in this limit, the single-phonon intensity is proportional to g.

Dispersive phonons. The exact solution of the cross section for Einstein phonons can be generalized to the case of several dispersive phonon branches λ. The e-p coupling is given by Eq. (7.4). Again we use the canonical transformation [62] $\bar{H} = e^S H e^{-S}$ with $S = \sum_{i,\mathbf{k},\lambda} S_{i\mathbf{k}\lambda}$, where

$$S_{i\mathbf{k}\lambda} = d_i^\dagger d_i \frac{M_{\mathbf{k}\lambda} e^{i\mathbf{k}\cdot\mathbf{R}_i}}{\omega_{\mathbf{k}\lambda}} (b^\dagger_{-\mathbf{k},\lambda} - b_{\mathbf{k}\lambda}). \tag{7.17}$$

so that now

$$\bar{H} = \sum_{\mathbf{k},\lambda} \omega_{\mathbf{k}\lambda} \left(b^\dagger_{\mathbf{k}\lambda} b_{\mathbf{k}\lambda} - g_{\mathbf{k}\lambda} \right), \tag{7.18}$$

with $g_{\mathbf{k}\lambda} = |M_{\mathbf{k}\lambda}/\omega_{\mathbf{k}\lambda}|^2$, and where we assumed that there is a single core hole present. Note that this transformation does not diagonalize the kinetic term for the electrons. However, this is no problem at excitonic edges, where the photo-excited electron is not itinerant, and at the Cu K-edge, where the coupling is mediated by the core hole. In close analogy with Eq. (7.12) for the Einstein phonon, this transformation can be inserted in the scattering amplitude:

$$\mathcal{F}_{fi} = T_{\text{el}}(\boldsymbol{\epsilon}', \boldsymbol{\epsilon}) \sum_i e^{i\mathbf{q}\cdot\mathbf{R}_i} \sum_m \frac{\prod_{\mathbf{k},\lambda} \langle n'_{\mathbf{k}\lambda}| e^{-S_{i\mathbf{k}\lambda}} |n_{\mathbf{k}\lambda}(m)\rangle \langle n_{\mathbf{k}\lambda}(m)| e^{S_{i\mathbf{k}\lambda}} |n^0_{\mathbf{k}\lambda}\rangle}{z + \sum_{\mathbf{k},\lambda}[g_{\mathbf{k}\lambda} - n_{\mathbf{k}\lambda}(m)]\omega_{\mathbf{k}\lambda}}, \tag{7.19}$$

where $n^0_{\mathbf{k}\lambda}$, $n_{\mathbf{k}\lambda}$, and $n'_{\mathbf{k}\lambda}$ are the occupation numbers of the modes indexed by $\mathbf{k}$ and λ in the ground, intermediate, and final states, respectively. Together with the FC factors this is an exact, closed expression for the RIXS response.

We can simplify this expression by assuming that the initial state is close to the ground state, which is a good approximation up to temperatures of the order of 80 meV ≈ 930 K for optical phonons in cuprates. Since the FC overlap between the ground and intermediate states follows a Poisson distribution with mean $g_{\mathbf{k}\lambda}$, the scattering channels with largest overlap have small $n_{\mathbf{k}\lambda}(m) - g_{\mathbf{k}\lambda}$. Effectively, we replace

$$z + \sum_{\mathbf{k},\lambda}[g_{\mathbf{k}\lambda} - n_{\mathbf{k}\lambda}(m)]\omega_{\mathbf{k}\lambda} \approx z \prod_{\mathbf{k},\lambda}(1 - [n_{\mathbf{k}\lambda}(m) - g_{\mathbf{k}\lambda}]\omega_{\mathbf{k}\lambda}/z) \tag{7.20}$$

and obtain

$$\mathcal{F}_{fg} \approx \frac{T_{\text{el}}(\boldsymbol{\epsilon}', \boldsymbol{\epsilon})}{z} \sum_i e^{i\mathbf{q}\cdot\mathbf{R}_i} \prod_{\mathbf{k},\lambda} \sum_{n_{\mathbf{k}\lambda}=0}^{\infty} \frac{\langle n'_{\mathbf{k}\lambda}| e^{-S_{i\mathbf{k}\lambda}} |n_{\mathbf{k}\lambda}\rangle \langle n_{\mathbf{k}\lambda}| e^{S_{i\mathbf{k}\lambda}} |n^0_{\mathbf{k}\lambda}\rangle}{1 - (n_{\mathbf{k}\lambda} - g_{\mathbf{k}\lambda})\omega_{\mathbf{k}\lambda}/z}. \tag{7.21}$$

The matrix elements can be evaluated analytically using the displaced harmonic oscillator transformation, resulting in (we suppress the branch index λ)

$$\mathcal{F}_{fg} \approx T_{\mathrm{el}}(\boldsymbol{\epsilon}', \boldsymbol{\epsilon}) \frac{\delta_{\mathbf{q}, \sum_{\mathbf{k}} n'_{\mathbf{k}} \mathbf{k}}}{z} \prod_{\mathbf{k}} \left(\sum_{n=0}^{n'_{\mathbf{k}}} \frac{B_{n'_{\mathbf{k}} n}(g_{\mathbf{k}}) B_{n0}(g_{\mathbf{k}})}{1 - (n - g_{\mathbf{k}})\omega_{\mathbf{k}}/z} + \sum_{n=n'_{\mathbf{k}}+1}^{\infty} \frac{B_{n n'_{\mathbf{k}}}(g_{\mathbf{k}}) B_{n0}(g_{\mathbf{k}})}{1 - (n - g_{\mathbf{k}})\omega_{\mathbf{k}}/z} \right) . \tag{7.22}$$

7.3.1 UCL expansion of the phonon scattering amplitude

The UCL expansion can be employed to obtain a very compact, approximate expression that is also valid at finite (but low) temperatures. We start from the general case of a dispersive phonon, whose approximate low temperature scattering amplitude (7.21) is expanded as

$$\begin{aligned} \mathcal{F}_{fi} \approx \frac{T_{\mathrm{el}}(\boldsymbol{\epsilon}', \boldsymbol{\epsilon})}{z} \sum_{i} e^{i\mathbf{q}\cdot\mathbf{R}_i} \prod_{\mathbf{k}} \sum_{n_{\mathbf{k}}=0}^{\infty} \langle n'_{\mathbf{k}} | \, e^{-S_{i\mathbf{k}}} \, | n_{\mathbf{k}} \rangle \langle n_{\mathbf{k}} | \, e^{S_{i\mathbf{k}}} \, | n^0_{\mathbf{k}} \rangle \\ \times \sum_{l=0}^{\infty} \left[(n_{\mathbf{k}} - g_{\mathbf{k}}) \omega_{\mathbf{k}}/z \right]^l , \end{aligned} \tag{7.23}$$

which is only valid for $n_{\mathbf{k}}\omega_{\mathbf{k}} < |z|$. For $n_{\mathbf{k}}\omega_{\mathbf{k}} > |z|$, the sum over l diverges independently of the Franck-Condon quenching of the amplitude. Clearly, such a divergence is unphysical: for $n_{\mathbf{k}}$ large, the amplitude should vanish. To avoid this problem, we only retain terms up to the first order in l. For high $n_{\mathbf{k}}$, the vanishing Franck-Condon overlap removes any contribution, while for low $n_{\mathbf{k}}$ cutting the expansion is a natural approximation. We get

$$\begin{aligned} \mathcal{F}_{fi} &\approx \frac{T_{\mathrm{el}}(\boldsymbol{\epsilon}', \boldsymbol{\epsilon})}{z} \sum_{i} e^{i\mathbf{q}\cdot\mathbf{R}_i} \prod_{\mathbf{k}} \langle n'_{\mathbf{k}} | \, e^{-S_{i\mathbf{k}}} \left[1 + \frac{\omega_{\mathbf{k}}}{z} \left(b^\dagger_{\mathbf{k}} b_{\mathbf{k}} - g_{\mathbf{k}} \right) \right] e^{S_{i\mathbf{k}}} \, | n^0_{\mathbf{k}} \rangle \\ &\approx T_{\mathrm{el}}(\boldsymbol{\epsilon}', \boldsymbol{\epsilon}) \frac{M_{\mathbf{q}\lambda}}{z^2} \langle f | \left(b^\dagger_{\mathbf{q}\lambda} + b_{-\mathbf{q},\lambda} \right) | i \rangle \end{aligned} \tag{7.24}$$

to first order in $M_{\mathbf{k}\lambda}/z$, where we neglected terms giving rise to elastic scattering. Again, multi-phonon contributions to $\mathcal{F}_{fi}$ are suppressed as $M_{\mathbf{k}\lambda}/\Gamma$.

This result implies that *momentum dependent RIXS harbors the potential to directly map out the* $\mathbf{q}$ *dependence of the e-p coupling strength* $M_{\mathbf{q}\lambda}$. With this information one can determine, for instance, the spatial range of the e-p interaction $M_{\mathbf{r}\lambda}$: it is simply the Fourier transform of $M_{\mathbf{q}\lambda}$.

Although we showed that the single Einstein phonon cross section is proportional to g in the limit of small g and in the limit of large Γ, it is in practice near-impossible to measure the absolute RIXS intensity. However, RIXS provides the means to determine the e-p coupling strength M on an absolute energy scale in another way. From the UCL expansion one finds that the ratio of the one and two-phonon loss amplitude directly reflects the e-p coupling constant: $\mathcal{F}^{(2)}/\mathcal{F}^{(1)} = \sqrt{2}M/z$ in the Einstein phonon case, where we assumed $\Gamma \gg \omega_0, M$. This result is confirmed by the exact solution, see Fig. 7.3. The figure shows the exact curves that relate the (multi-)phonon scattering intensities $I^{(2)}/I^{(1)}$ to the e-p interaction strength M/Γ for arbitrary M. This method to determine the e-p coupling on an absolute energy scale is particularly powerful in the case of weakly dispersive optical phonons, for instance the much debated phonon modes around 80 meV in the high-T_c cuprates [236–238].

7.4 dd excitations dressed by phonons

Hancock *et al.* [239] find that the charge transfer excitation in the zero-dimensional cuprate CuB_2O_4 (which is at 6.8 eV) is screened by phonons, explaining the Gaussian line shape of the spectra and yielding a dependence of the charge transfer peak position on the incident energy. In close analogy to their approach, we calculate here the RIXS spectrum of dd excitations that couple to phonons.

Because the scattering process itself is very fast, the lattice has little time to adjust in the intermediate state (as shown in Sec. 7.3) and will approximately be in the same state before and after the scattering process. This is certainly true for small e-p couplings or large core hole lifetime broadenings. The main difference with the preceding sections of this chapter is that the final state has a different charge distribution than the initial state. Therefore, the RIXS process has a lasting influence on the lattice, instead of the transient force when the system returns to its electronic ground state after scattering the photon. The final state corresponds to a displaced oscillator, and the overlap of the initial lattice state with the displaced final states is given by the Franck-Condon factors.

Our starting point is the simple Hamiltonian for a single phonon coupled to a dd excitation (from orbital ν' to ν[1]):

$$H = \sum_{\mathbf{k}} \left[\omega_{\mathbf{k}} b^{\dagger}_{\mathbf{k}} b_{\mathbf{k}} + \sum_{i} d^{\dagger}_{i\nu} d_{i\nu} d_{i\nu'} d^{\dagger}_{i\nu'} e^{i\mathbf{k}\cdot\mathbf{R}_i} M_{\mathbf{k}} \left(b_{\mathbf{k}} + b^{\dagger}_{-\mathbf{k}} \right) \right] \tag{7.25}$$

We consider RIXS processes where the final state has a single dd excitation, which gets dressed by phonons. The Hamiltonian can be diagonalized as done for dispersive phonons in Sec. 7.3: using $S_{i\mathbf{k}} = d^{\dagger}_{i\nu} d_{i\nu} d_{i\nu'} d^{\dagger}_{i\nu'} \frac{M_{\mathbf{k}}}{\omega_{\mathbf{k}}} e^{i\mathbf{k}\cdot\mathbf{R}_i} (b^{\dagger}_{-\mathbf{k}} - b_{\mathbf{k}})$, we obtain $\bar{H} = \sum_{\mathbf{k}} \omega_{\mathbf{k}} (b^{\dagger}_{\mathbf{k}} b_{\mathbf{k}} - g_{\mathbf{k}})$.

The RIXS cross section is given by the finite temperature Kramers-Heisenberg equation (2.41). In accordance with the idea that the lattice has no time to respond to the transient charge distribution in the intermediate state, we use the

---

[1] Each dd excitation has its own e-p coupling $M_{\mathbf{k}} \rightarrow M_{\nu'\nu,\mathbf{k}}$. For simplicity, we only consider a single dd excitation here.

UCL expansion to zeroth order:

$$\frac{d^2\sigma}{d\omega d\Omega} \approx \frac{|T_{\rm dd}(\boldsymbol{\epsilon}', \boldsymbol{\epsilon})|^2}{\Gamma^2} \sum_{f,i} e^{-\beta E_i} \left| \langle f| \sum_j e^{i\mathbf{q}\cdot\mathbf{R}_j} d_{j\nu'} d^\dagger_{j\nu} |i\rangle \right|^2 \delta(\omega - E_f + E_i) \quad (7.26)$$

where $T_{\rm dd}(\boldsymbol{\epsilon}', \boldsymbol{\epsilon})$ is the polarization factor (2.42) corresponding to exciting the specific dd excitation ($\nu' \to \nu$) by two consecutive dipole transitions. The core hole is integrated out. By retaining only the zeroth order of the UCL expansion, the incident energy dependence is lost, and this is different from the work of Hancock *et al.* [239]. In the case of copper 3d^9, ν can only assume one value: the photo-excited electron fills the 3d$_{x^2-y^2}$ hole and creates a 3d^{10} intermediate state. The similarity to the non-resonant inelastic X-ray scattering cross section is striking.

Based on the findings of Ref. [239], we expect the dd excitation to excite many phonons, and consequently we do not care if the initial state has a few phonons already present. For simplicity, we therefore set $T = 0$. For optical phonons, this is in any case a good approximation. Then, we find

$$\langle f| d_{j\nu'} d^\dagger_{j\nu} |i\rangle = \left(\prod_{\mathbf{k}} \langle n'_{\mathbf{k}}, {\rm dd}| \right) e^S d_{j\nu'} d^\dagger_{j\nu} |0\rangle = \prod_{\mathbf{k}} e^{-g_{\mathbf{k}}/2} \frac{\left(\frac{M_{\mathbf{k}} e^{-i\mathbf{k}\cdot\mathbf{R}_j}}{\omega_{\mathbf{k}}} \right)^{n'_{\mathbf{k}}}}{\sqrt{n'_{\mathbf{k}}!}}, \quad (7.27)$$

where $n'_{\mathbf{k}}$ is the number of phonons in the final state with wave vector $\mathbf{k}$, and dd indicates that a dd excitation is present at site j in the final state. Because the final state dd excitation is local, the sum over j in Eq. (7.26) has only one non-zero term, and the $\mathbf{q}$ dependence is lost.

Now we obtain the zero temperature cross section,

$$\begin{aligned} \frac{d^2\sigma}{d\omega d\Omega} &\approx \frac{|T_{\rm dd}(\boldsymbol{\epsilon}', \boldsymbol{\epsilon})|^2}{\Gamma^2} \sum_{f=j,\{n'_{\mathbf{k}}\}} \left| e^{i\mathbf{q}\cdot\mathbf{R}_j} \prod_{\mathbf{k}} \frac{e^{-g_{\mathbf{k}}/2}}{\sqrt{n'_{\mathbf{k}}!}} \left(\frac{M_{\mathbf{k}} e^{-i\mathbf{k}\cdot\mathbf{R}_j}}{\omega_{\mathbf{k}}} \right)^{n'_{\mathbf{k}}} \right|^2 \delta(\omega - E_f) \\ &\approx \frac{N\,|T_{\rm dd}(\boldsymbol{\epsilon}', \boldsymbol{\epsilon})|^2}{\Gamma^2} \prod_{\mathbf{k}} \sum_{n'_{\mathbf{k}}=0}^{\infty} \left(e^{-g_{\mathbf{k}}} \frac{g_{\mathbf{k}}^{n'_{\mathbf{k}}}}{n'_{\mathbf{k}}!} \right) \delta(\omega - E_f) \end{aligned} \quad (7.28)$$

where the final state energy E_f is the dd excitation energy E_{dd} plus the phonon contribution $\sum_{\mathbf{k}} n'_{\mathbf{k}} \omega_{\mathbf{k}}$.

The calculation is easily repeated for local phonons. The result is

$$\frac{d^2\sigma}{d\omega d\Omega} \approx \frac{N\,|T_{\rm dd}(\boldsymbol{\epsilon}', \boldsymbol{\epsilon})|^2}{\Gamma^2} e^{-g} \sum_{n'=0}^{\infty} \frac{g^{n'}}{n'!} \delta(\omega - E_{dd} - n'\omega_0), \quad (7.29)$$

which is a Poisson distribution with phonon number average $g = (M_{dd}/\omega_0)^2$ and variance $\sigma^2 = g$. M_{dd} is the coupling of the dd excitation to phonons. In the limit of large g, it is approximated by a Gaussian distribution. We conclude that the width of the RIXS spectra of dd excitations yields M_{dd} once the phonon energy is known (with an extremely high energy resolution, ω_0 can be measured with RIXS).

In the cuprates, one could study, for instance, the $3z^2$-r^2 to x^2-y^2 dd excitation, which is an intra-e_g transition. The splitting of these levels is partly due to the crystal field of the layered structure, and partly to Jahn-Teller (JT) distortions. Above, we found that the JT contribution is $E_{\mathrm{JT}} = 2M_{dd}$. If we assume that the dd peak broadening is only due to phonons, then the full width at half maximum of the peak directly gives E_{JT}. This way, we can determine what part of the dd excitation energy can be attributed to the JT effect and what part cannot. In practice, other factors also might contribute to the peak width, such as superexchange interactions, and the peak width thus gives only an upper bound to E_{JT} and M_{dd}.

7.5 Conclusions

In the analysis above we concentrated on transition metal L edge RIXS, which has the advantage of a photo-electron launched directly into the 3d state. A certain 3d orbital can be selected by choosing the polarization of incident and outgoing X-rays [110], so that the e-p characteristics related to this particular 3d orbital can be measured, as long as the 3d orbital is not fully occupied in the ground state. We extended the theory to include final state dd excitations coupling to the lattice [169], which is of great importance in the study of Jahn-Teller polarons. Also oxygen related phonons can be probed at the O K edge, but as this edge is at lower energy, the photons have less momentum and a smaller part of the BZ can be probed, which is also true for the Cu M edges. As hard X-ray transition metal K edges do not suffer this disadvantage, they provide an even more potent method to measure e-p interactions [230].

The theoretical analysis that we advance here bestows on RIXS the unique potential to provide direct, element-specific and momentum-resolved information on the interaction between electrons and phonons *on an absolute scale.* In weakly correlated electron systems these properties can be computed with modern *ab initio* electronic structure methods, for instance in the newly discovered iron pnictide superconductors [240], and our framework to distill them from RIXS allows a direct comparison. In strongly correlated materials, particularly the high-T_c cuprates, these assets make high resolution RIXS a unique tool to unravel the interaction between its electrons and phonons.

Acknowledgements. We thank Lucio Braicovich, Giacomo Ghiringhelli, Tom Devereaux, Brian Moritz and Steven Johnston for fruitful discussions. This work is supported by the U.S. Department of Energy, Office of Basic Energy Sciences under contract DE-AC02-76SF00515 and benefited from the RIXS collaboration supported by the Computational Materials Science Network (CMSN) program under grant number DE-FG02-08ER46540. This work is supported by the Dutch "Stichting voor Fundamenteel Onderzoek der Materie (FOM).

MvV was supported by the U.S. Department of Energy (DOE), No. DE-FG02-03ER46097. Work at Argonne National Laboratory was supported by the U.S. DOE, Office of Basic Energy Sciences (BES), under contract No. DE-AC02-06CH11357. This research benefited from the RIXS collaboration supported by the Computational Materials Science Network (CMSN), BES, DOE under grant number DE-FG02-08ER46540.

CHAPTER 8

OUTLOOK – X-RAY FREE ELECTRON LASERS

RIXS is now beginning to become a mainstream technique of condensed matter physics. Due to the tremendous progress in energy resolution and intensity, the energy scale of excitations accessible to RIXS has moved down from several eV in the late 1990's to several tens of eV now. If this progress continues at the same pace, it will soon be possible to probe excitations at even lower energy scales. This will not only bring more of the same materials within the range of RIXS experiments (for instance, materials with a lower superexchange constant), but it will also enable experimentalists to access excitations not seen before with RIXS. A very interesting prospect would be to map out the dispersion of excitations across the superconducting gap.

Not only the energy resolution is improving. The very recent availability of ultra-short and ultra-bright X-ray pulses generated by free electron lasers such as FLASH at DESY and the Linac Coherent Light Source (LCLS) at SLAC National Accelerator Laboratory offers unique opportunities for X-ray science, in particular time-resolved experiments, see, *e.g.*, Ref. [241]. In the remainder of this chapter, we discuss some implications of these X-ray Free Electron Lasers (XFEL's) for regular X-ray scattering, focussing on the bosonic enhancement of absorption and emission due to the enormous occupation number of the incident mode.

8.1 Bosonic enhancement in an XFEL

A Free Electron Laser populates a certain mode with a huge number of photons. This mode will be in a superposition of states with different, large occupation numbers n. Typically, when the mode is populated with a linear Hamiltonian, meaning $H \propto (a + a^\dagger)$ with a the photon annihilation operator, the result is a coherent state $|z\rangle = e^{-\frac{|z|^2}{2}} \sum_{n=0}^{\infty} \frac{z^n}{\sqrt{n!}} |n\rangle$ with z a complex number with huge modulus. The number of photons in the mode follows a Poisson distribution with mean $|z|^2$. The other modes of the electromagnetic field are, ideally, empty.

In deriving the RIXS cross section in chapter 2, we assumed that there is a single photon in the incident mode, which is reasonable for synchrotrons. The outlandish XFEL field state however, has enormous occupation numbers. When the field operator $\mathbf{A}$ acts on this state, it generates large boson factors $\sqrt{n}$. Processes involving multiple $\mathbf{A}$'s are therefore enhanced in an XFEL, in contrast to synchrotrons. Note that these multiple $\mathbf{A}$'s should pick up the incident mode to get the Boson enhancement factor: that does not happen for the empty outgoing modes.

As an example of this enhancement, we consider the absorption of two photons from the heavily populated incident mode of momentum $\mathbf{k}$ and polarization $\boldsymbol{\epsilon}$ through the $\mathbf{A}^2$ term of Eq. (2.22). From Eq. (2.24), we retain only the two-photon absorption and emission for the beam mode, and get

$$\mathbf{A}(\mathbf{r})^2 \sim \frac{\hbar}{2\mathcal{V}\epsilon_0\omega_{\mathbf{k}}} \left(\boldsymbol{\epsilon} \cdot \boldsymbol{\epsilon} \; a_{\mathbf{k},\boldsymbol{\epsilon}}^2 e^{i2\mathbf{k}\cdot\mathbf{r}} + \text{h.c.} \right). \tag{8.1}$$

For a highly populated incident mode, $a_{\mathbf{k},\boldsymbol{\epsilon}}^2$ produces the average occupation number, which is projected to be of the order of 10^9 for the LCLS [31]. Two things can be concluded here. First, for linear polarization, the $\mathbf{A}^2$ term is independent of polarization because $\boldsymbol{\epsilon} \cdot \boldsymbol{\epsilon} = 1$. For circular polarization, $\boldsymbol{\epsilon} \cdot \boldsymbol{\epsilon} = 0$, and the process is forbidden: these two-photon processes cannot transfer more than one unit of angular momentum to the solid. Second, these two-photon processes are (mainly) dipole transitions. This can be seen by expanding the exponential $e^{i2\mathbf{k}\cdot\mathbf{r}}$ for small $\mathbf{k} \cdot \mathbf{r}$. To zeroth order, no transitions can be made. To first order, dipole transitions appear.

Before discussing specific scattering processes, we make an estimate of the size of (the matrix elements of) $\mathbf{A}$. The coherent volume $\mathcal{V}$ is projected to be $\sim 3 \cdot 10^{-13}$ m^3 for the LCLS [31]. We thus get

$$\langle \mathbf{A} \rangle \sim \sqrt{\frac{\hbar}{2\mathcal{V}\epsilon_0 c}} \left\langle \sqrt{n}\mathbf{r} \right\rangle \sim (3 \cdot 10^{-10} \text{ Js/Cm}^2) \left\langle \sqrt{n}\mathbf{r} \right\rangle. \tag{8.2}$$

8.2 X-ray scattering with an XFEL

There are several interesting aspects of the bosonic enhancement for X-ray scattering. Multi-photon processes are enhanced, and one could either stimulate the

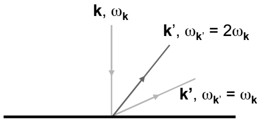
$\mathbf{k}$, $\omega_{\mathbf{k}}$
$\mathbf{k}'$, $\omega_{\mathbf{k}'} = 2\omega_{\mathbf{k}}$
$\mathbf{k}'$, $\omega_{\mathbf{k}'} = \omega_{\mathbf{k}}$

Figure 8.1: If X-rays at half the resonance energy are incident perpendicular to the sample surface (taking a simple cubic lattice, cut perpendicular to one of the cubic axes), the truely elastic Bragg peaks (light gray, $\omega_{\mathbf{k}'} = \omega_{\mathbf{k}}$) are pushed away from the surface normal. The 'elastic' line emitted at twice the incident X-ray energy has different Bragg conditions (dark gray): the first Bragg peak is closer to the surface normal.

absorption or the emission process. Enhancing both would require two XFEL beams.

Enhanced absorption. An interesting way to lose the non-resonant contributions to the spectrum is to excite the system with X-rays of half the resonance energy via the $\mathbf{A}^2$ term. Non-resonant X-ray scattering with matrix elements $\langle f | \mathbf{A}^2 | i \rangle$ produces outgoing X-rays with an energy of about half the resonance energy. Resonant scattering, however, mainly comes from the $\mathbf{A} \cdot \mathbf{p}$ term, creating X-ray photons with double that energy, *i.e.*, close to the resonance energy. The Kramers-Heisenberg equation becomes

$$\mathcal{F}_{fi} \propto \sum_n \frac{\langle f | \mathbf{A} \cdot \mathbf{p} | n \rangle \langle n | \mathbf{A}^2 | i \rangle}{E_i + 2\hbar\omega_{\mathbf{k}} - E_n + i\Gamma}. \tag{8.3}$$

This could be of use for resonant X-ray scattering: one can completely eliminate the non-resonant contributions. They remain at half the energy.

The theoretical treatment of RIXS also simplifies, because the polarization dependence of the absorption is trivial, as shown in Sec. 8.1.

Further, the Bragg conditions are interesting because the wavelength of the outgoing X-rays is halved with respect to the incident ones. Thus, there will be two sets of Bragg peaks: one set of truely elastic peaks at the regular angles, and one set at double the incident energy, arising through the resonant process of Eq. (8.3). The latter peaks are closer together: there are more Bragg peaks, as shown in Fig. 8.1. In resonant X-ray scattering, the elastic peaks arising from some ordering of the solid also appears at twice the incident energy and at outgoing wave vectors where no truely elastic ordering peaks appear.

Enhanced emission. Another interesting effect is stimulated emission. Not only the absorption can be enhanced by the boson factor, but also the consequent emission into the XFEL mode is boosted. This enhances forward scattering ($\mathbf{k}' = \mathbf{k}$): during the core hole's lifetime, which is much shorter than the pulse duration[1], elastic decay into the beam mode is stimulated. Forward scattering is enhanced by a factor $\langle n \rangle$. Note that this is not a shift of spectral weight away from other Bragg peaks or inelastic features: extra spectral weight is generated because one stimulates extra scattering events.

---

[1] At the LCLS, the X-ray pulses are projected to be 230 fs long [31], compared to $\hbar/\Gamma \sim 1$ fs.

This effect is interesting because it allows for experimental control of the lifetime of the core hole: it is decreased by stimulated emission. To determine how much this is, we have to know the resonant contribution to the spectral weight of a Bragg peak, multiply it by $\langle n \rangle$ and see if this number is a sizeable fraction of the total number of decay processes (including Auger decay etc.). The resonant contribution to the spectral weight of a Bragg peak can in principle be determined by the resonant X-ray scattering method dicussed above, where the non-resonant contribution is quenched.

Appendices

APPENDIX A

QED

This appendix contains some details of the derivation of the higher-order electron-photon coupling Hamiltonian.

A.1 H_Ψ to second order

Below the components of $H_\Psi = \Omega H_\alpha \Omega^{-1} + i\hbar(\partial_t\Omega)\Omega^{-1}$ are calculated. First,

$$\Omega H_\alpha \Omega^{-1} = H_\alpha + \frac{1}{2}\left[\tilde{D}^2, H_\alpha\right] = H_\alpha + \frac{1}{2}\left[\tilde{D}^2, -e\phi\right]. \tag{A.1}$$

where in the last step only terms up to $\mathcal{O}(m^{-2})$ are kept, and where

$$\begin{aligned}(2mc)^2\left[\tilde{D}^2, \phi\right] &= \sigma^i\sigma^j\left(D_iD_j\phi - \phi D_iD_j\right) = \sigma^i\sigma^j\left(D_i(\partial_j\phi) + D_i\phi D_j - \phi D_iD_j\right)\\ &= \sigma^i\sigma^j\left(\partial_i(\partial_j\phi) + (\partial_j\phi)D_i + (\partial_i\phi)D_j\right) = \partial_i^2\phi + 2(\partial_i\phi)D_i\\ &= -\rho/\epsilon_0 + \frac{2i}{\hbar}(\nabla\phi)\cdot(\mathbf{p} + e\mathbf{A}).\end{aligned} \tag{A.2}$$

Second,

$$\begin{aligned}i\hbar\partial_t\Omega &= \frac{i\hbar}{2(2mc)^2}\partial_t\left[(\mathbf{p} + e\mathbf{A})^2 + e\hbar\boldsymbol{\sigma}\cdot\mathbf{B}\right]\\ &= \frac{ie\hbar}{2(2mc)^2}\left[(\partial_t\mathbf{A})\cdot(\mathbf{p} + e\mathbf{A}) + (\mathbf{p} + e\mathbf{A})\cdot(\partial_t\mathbf{A}) + \hbar\boldsymbol{\sigma}\cdot(\partial_t\mathbf{B})\right]\\ &= \frac{ie\hbar}{2(2mc)^2}\left[2(\partial_t\mathbf{A})\cdot(\mathbf{p} + e\mathbf{A}) + \hbar\boldsymbol{\sigma}\cdot(\partial_t\mathbf{B})\right]\end{aligned} \tag{A.3}$$

Putting things together, one finds

$$\begin{aligned}H_\Psi &= H_\alpha - \frac{1}{2}\frac{e\hbar^2\rho}{(2mc)^2\epsilon_0} - \frac{ie\hbar}{(2mc)^2}\mathbf{E}\cdot(\mathbf{p}+e\mathbf{A}) + \frac{ie\hbar^2}{2(2mc)^2}\boldsymbol{\sigma}\cdot(\partial_t\mathbf{B})\\ &= \frac{(\mathbf{p}+e\mathbf{A})^2}{2m} + \frac{e\hbar}{2m}\boldsymbol{\sigma}\cdot\mathbf{B} - e\phi + \frac{e\hbar}{(2mc)^2}\boldsymbol{\sigma}\cdot\mathbf{E}\times(\mathbf{p}+e\mathbf{A}) + \frac{1}{2}\frac{e\hbar^2\rho}{(2mc)^2\epsilon_0}\\ &\quad - \frac{ie\hbar}{2(2mc)^2}\hbar\boldsymbol{\sigma}\cdot(\partial_t\mathbf{B}). \qquad (A.4)\end{aligned}$$

Note that the $\mathbf{E}\times\mathbf{p}$ term is not Hermitian for dynamic fields, because $\mathbf{E}$ and $\mathbf{p}$ do not commute in that case. The 'imaginary term' in H_Ψ solves this issue: it can be rewritten as

$$\begin{aligned}-\frac{ie\hbar}{2(2mc)^2}\hbar\sigma^k(\partial_t B^k) &= \frac{ie\hbar^2}{2(2mc)^2}\epsilon^{ijk}\sigma^k(\partial_i E^j) = \frac{ie\hbar^2}{2(2mc)^2}\epsilon^{ijk}\sigma^k(\partial_i E^j - E^j\partial_i)\\ &= -\frac{e\hbar}{2(2mc)^2}\epsilon^{ijk}\sigma^k(-i\hbar\partial_i E^j + E^i(-i\hbar)\partial_j)\\ &= -\frac{e\hbar}{2(2mc)^2}\boldsymbol{\sigma}\cdot(\mathbf{p}\times\mathbf{E} + \mathbf{E}\times\mathbf{p}) \qquad (A.5)\end{aligned}$$

With this substitution, H_Ψ assumes the form of Eq. (2.22).

A.2 H_Ψ to third order

This section contains the derivation of H_Ψ to order $\mathcal{O}(m^{-3})$.

Starting point is Eq. (2.7):

$$\beta(x) = \tilde{D}\alpha(x) + \tilde{D}_0\tilde{D}\alpha(x) + \tilde{D}_0^2\tilde{D}\alpha(x). \qquad (A.6)$$

Substitution in Eq. (2.5) gives the equation for $\alpha(x)$:

$$\tilde{D}_0\alpha(x) + \tilde{D}\left(1 + \tilde{D}_0 + \tilde{D}_0^2\right)\tilde{D}\alpha(x) = 0. \qquad (A.7)$$

Every $\tilde{D}_0$ is commuted to the right:

$$\begin{aligned}0 &= \left[\tilde{D}_0 + \tilde{D}^2 + \tilde{D}\left(1+\tilde{D}_0\right)\left(\tilde{D}\tilde{D}_0 + \frac{ie\hbar}{(2mc)^2c}\sigma^i E^i\right)\right]\alpha(x)\\ &= \left[\tilde{D}_0 + \tilde{D}^2 + \tilde{D}\left(\tilde{D}\tilde{D}_0 + \frac{ie\hbar}{(2mc)^2c}\sigma^i E^i\right)\right.\\ &\quad \left. + \tilde{D}\left(\left(\tilde{D}\tilde{D}_0 + \frac{ie\hbar}{(2mc)^2c}\sigma^i E^i\right)\tilde{D}_0 + \tilde{D}_0\frac{ie\hbar}{(2mc)^2c}\sigma^i E^i\right)\right]\alpha(x) \qquad (A.8)\end{aligned}$$

Using

$$\left[\tilde{D}_0, E^i\right] = \frac{-i\hbar}{2mc}(\partial_0 E^i), \qquad (A.9)$$

one obtains

$$\begin{aligned}-\tilde{D}_0\alpha(x) = \Big[&\tilde{D}^2\left(1+\tilde{D}_0+\tilde{D}_0^2\right)+\tilde{D}\frac{ie\hbar}{(2mc)^2c}\sigma^iE^i\left(1+2\tilde{D}_0\right)\\ &+\tilde{D}\frac{e\hbar^2\sigma^i(\partial_0E^i)}{(2mc)^3c}\Big]\,\alpha(x).\end{aligned}\tag{A.10}$$

$\tilde{D}_0\alpha(x)$ is replaced by the second order Schrödinger equation, and only terms that contribute to the Schrödinger equation at order $\mathcal{O}(m^{-3})$ are considered:

$$-\tilde{D}_0\alpha(x) = \left[\tilde{D}^2\left(1-\tilde{D}^2\right)+\tilde{D}\frac{ie\hbar}{(2mc)^2c}\sigma^iE^i+\tilde{D}\frac{e\hbar^2\sigma^i(\partial_0E^i)}{(2mc)^3c}\right]\alpha(x). \tag{A.11}$$

The normalization condition becomes

$$\int d^3x\,\left[\alpha(x)^\dagger\alpha(x)+\left\{\left(1+\tilde{D}_0+\tilde{D}_0^2\right)\tilde{D}\alpha(x)\right\}^\dagger\left\{\left(1+\tilde{D}_0+\tilde{D}_0^2\right)\tilde{D}\alpha(x)\right\}\right]=1. \tag{A.12}$$

Up to order $\mathcal{O}(m^{-3})$, this is

$$\begin{aligned}1 &= \int d^3x\,\left[\alpha(x)^\dagger+\alpha(x)^\dagger\tilde{D}^2+\left\{\tilde{D}_0\tilde{D}\alpha(x)\right\}^\dagger\tilde{D}+\alpha(x)^\dagger\tilde{D}\tilde{D}_0\tilde{D}\right]\alpha(x)\\ &= \int d^3x\,\Bigg[\alpha(x)^\dagger+\alpha(x)^\dagger\tilde{D}^2+\left\{\left(\tilde{D}\tilde{D}_0+\frac{ie\hbar}{(2mc)^2c}\sigma^iE^i\right)\alpha(x)\right\}^\dagger\tilde{D}\\ &\quad+\alpha(x)^\dagger\tilde{D}\left(\tilde{D}\tilde{D}_0+\frac{ie\hbar}{(2mc)^2c}\sigma^iE^i\right)\Bigg]\alpha(x)\\ &= \int d^3x\,\alpha(x)^\dagger\left[1+\tilde{D}^2+\left(\frac{ie\hbar}{(2mc)^2c}\sigma^iE^i\right)^\dagger\tilde{D}+\tilde{D}\frac{ie\hbar}{(2mc)^2c}\sigma^iE^i\right]\alpha(x)\\ &= \int d^3x\,\alpha(x)^\dagger\left[1+\tilde{D}^2+\frac{e\hbar}{(2mc)^2c}\left[\tilde{D},i\sigma^iE^i\right]\right]\alpha(x),\end{aligned}\tag{A.13}$$

where the commutator

$$\left[\tilde{D},i\sigma^iE^i\right]=\frac{\hbar}{2mc}\left(\sigma^i\sigma^j(\partial_iE^j)-2i\epsilon^{ijk}\sigma^kE^iD_j\right)\tag{A.14}$$

is hermitian. The renormalization operator becomes

$$\Omega(x)=1+\frac{1}{2}\left(\tilde{D}^2+\frac{e\hbar}{(2mc)^2c}\left[\tilde{D},i\sigma^iE^i\right]\right)=\Omega(x)^\dagger,\tag{A.15}$$

so that to order $\mathcal{O}(m^{-3})$

$$\Omega(x)^{-1}=1-\frac{1}{2}\left(\tilde{D}^2+\frac{e\hbar}{(2mc)^2c}\left[\tilde{D},i\sigma^iE^i\right]\right).\tag{A.16}$$

With this renormalization operator, one can obtain the Schrödinger equation for the normalized wave function $\Psi(x)$. Its Hamiltonian H_Ψ consists of the parts

$$\begin{aligned} i\hbar(\partial_t\Omega)\Omega^{-1} &= \frac{ie\hbar}{2(2mc)^2}\left\{2(\partial_t\mathbf{A})\cdot(\mathbf{p}+e\mathbf{A})+\hbar\boldsymbol{\sigma}\cdot(\partial_t\mathbf{B})\right\} \\ &\quad + \frac{e}{2c}\left(\frac{-i\hbar}{2mc}\right)^3\left(\sigma^i\sigma^j(\partial_t\partial_i E^j)-2i\epsilon^{ijk}\sigma^k(\partial_t E^i D_j)\right) \end{aligned} \tag{A.17}$$

and

$$\begin{aligned} \Omega H_\alpha\Omega^{-1} &= 2mc^2\left(-\frac{e\phi}{2mc^2}+\tilde{D}^2-\tilde{D}^4+\tilde{D}\frac{ie\hbar}{(2mc)^2c}\sigma^i E^i+\tilde{D}\frac{e\hbar^2\sigma^i(\partial_0 E^i)}{(2mc)^3c}\right) \\ &\quad + \left[\frac{1}{2}\left(\tilde{D}^2+\frac{e\hbar}{(2mc)^2c}\left[\tilde{D},i\sigma^i E^i\right]\right),-e\phi+2mc^2\tilde{D}^2\right] \\ &= -e\phi+\frac{(\mathbf{p}+e\mathbf{A})^2}{2m}+\frac{e\hbar}{2m}\boldsymbol{\sigma}\cdot\mathbf{B}-\frac{1}{2mc^2}\left(\frac{(\mathbf{p}+e\mathbf{A})^2}{2m}+\frac{e\hbar}{2m}\boldsymbol{\sigma}\cdot\mathbf{B}\right)^2 \\ &\quad - e\left(\frac{-i\hbar}{2mc}\right)^2\sigma^j\sigma^i D_j E^i - e\left(\frac{-i\hbar}{2mc}\right)^3\sigma^j\sigma^i D_j(\partial_0 E^i) \\ &\quad - \left(\frac{-i\hbar}{2mc}\right)^2\frac{e}{2}\left(\partial_i^2\phi+2(\partial_i\phi)D_i\right)-\frac{e^2\hbar}{2(2mc)^2c}\left[\left[\tilde{D},i\sigma^i E^i\right],\phi\right], \end{aligned} \tag{A.18}$$

where the commutator is

$$\begin{aligned} \left[\left[\tilde{D},i\sigma^i E^i\right],\phi\right] &= -\left[\phi,\tilde{D}i\sigma^i E^i\right]+\left[\phi,i\sigma^i E^i\tilde{D}\right] \\ &= -\left[\phi,\tilde{D}\right]i\sigma^i E^i-\tilde{D}\left[\phi,i\sigma^i E^i\right]+\left[\phi,i\sigma^i E^i\right]\tilde{D}+i\sigma^i E^i\left[\phi,\tilde{D}\right] \\ &= -\left[\phi,\tilde{D}\right]i\sigma^i E^i+i\sigma^i E^i\left[\phi,\tilde{D}\right]=\frac{\hbar}{2mc}\left(\sigma^j\sigma^i-\sigma^i\sigma^j\right)E^i(\partial_j\phi) \\ &= \frac{\hbar}{2mc}i2\epsilon^{jik}\sigma^k E^i(\partial_j\phi)=\frac{-i\hbar}{2mc}2\ \boldsymbol{\sigma}\cdot\mathbf{E}\times(\nabla\phi), \end{aligned} \tag{A.19}$$

so that

$$\begin{aligned} \Omega H_\alpha\Omega^{-1} &= -e\phi+\frac{(\mathbf{p}+e\mathbf{A})^2}{2m}+\frac{e\hbar}{2m}\boldsymbol{\sigma}\cdot\mathbf{B}-\frac{1}{2mc^2}\left(\frac{(\mathbf{p}+e\mathbf{A})^2}{2m}+\frac{e\hbar}{2m}\boldsymbol{\sigma}\cdot\mathbf{B}\right)^2 \\ &\quad - e\left(\frac{-i\hbar}{2mc}\right)^2\sigma^j\sigma^i D_j E^i - e\left(\frac{-i\hbar}{2mc}\right)^3\sigma^j\sigma^i D_j(\partial_0 E^i) \\ &\quad - \left(\frac{-i\hbar}{2mc}\right)^2\frac{e}{2}\left(\partial_i^2\phi+2(\partial_i\phi)D_i\right)+\frac{ie^2\hbar^2}{(2mc)^3c}\boldsymbol{\sigma}\cdot\mathbf{E}\times(\nabla\phi). \end{aligned} \tag{A.20}$$

Putting the $\mathcal{O}(m^{-3})$ term of H_Ψ together, one obtains

$$-\frac{1}{2mc^2}\left(\frac{(\mathbf{p}+e\mathbf{A})^2}{2m}+\frac{e\hbar}{2m}\boldsymbol{\sigma}\cdot\mathbf{B}\right)^2-e\left(\frac{-i\hbar}{2mc}\right)^3\sigma^j\sigma^i D_j(\partial_0 E^i)+$$

$$
\begin{aligned}
&+\frac{ie^2\hbar^2}{(2mc)^3c}\boldsymbol{\sigma}\cdot\mathbf{E}\times(\nabla\phi)+\frac{e}{2c}\left(\frac{-i\hbar}{2mc}\right)^3\left(\sigma^i\sigma^j(\partial_t\partial_i E^j)-2i\epsilon^{ijk}\sigma^k(\partial_t E^i D_j)\right)\\
&=\frac{1}{(2mc)^3}\Bigg[-c\left((\mathbf{p}+e\mathbf{A})^2+e\hbar\boldsymbol{\sigma}\cdot\mathbf{B}\right)^2+\frac{ie^2\hbar^2}{c}\boldsymbol{\sigma}\cdot\mathbf{E}\times(\nabla\phi)\\
&\quad-\frac{e}{2c}(-i\hbar)^3\sigma^j\sigma^i\left\{(\partial_j\partial_t E^i)+(\partial_t E^i)D_j+D_j(\partial_t E^i)\right\}\\
&\quad+\frac{e(-i\hbar)^3}{2c}\left(\sigma^i\sigma^j(\partial_t\partial_i E^j)-2i\epsilon^{ijk}\sigma^k\left\{(\partial_t E^i)D_j+\frac{ie}{\hbar}E^i(\partial_t A^j)\right\}\right)\Bigg]\\
&=\frac{1}{(2mc)^3}\Bigg[-c\left((\mathbf{p}+e\mathbf{A})^2+e\hbar\boldsymbol{\sigma}\cdot\mathbf{B}\right)^2+\frac{e(-i\hbar)^3}{2c}\left(-2i\epsilon^{ijk}\sigma^k(\partial_t E^i)D_j\right)\\
&\quad-\frac{e}{2c}(-i\hbar)^3\sigma^j\sigma^i\left\{(\partial_t E^i)D_j+D_j(\partial_t E^i)\right\}-\frac{ie^2\hbar^2}{c}\boldsymbol{\sigma}\cdot\mathbf{E}\times\mathbf{E}\Bigg]\\
&=\frac{1}{(2mc)^3}\Bigg[-c\left((\mathbf{p}+e\mathbf{A})^2+e\hbar\boldsymbol{\sigma}\cdot\mathbf{B}\right)^2\\
&\quad-\frac{e\,(-i\hbar)^3}{2c}\left\{(\partial_t E^i)D_i+D_i(\partial_t E^i)-i\epsilon^{ijk}\sigma^k(\partial_t\partial_j E^i)\right\}\Bigg],
\end{aligned}
\tag{A.21}
$$

giving Eq. (2.23).

Appendix B

YTiO$_3$

This appendix contains some of the lengthy expressions involved in calculating the RIXS spectra of YTiO$_3$ (section 5.4).

B.1 RIXS – Single site processes

The angular momentum $\hat{l}$ and quadrupole operators $\hat{Q}, \hat{T}$ in Eqs. (5.43–5.45) are defined as follows:

$$\hat{l}_x = i(c^\dagger b - b^\dagger c) \tag{B.1}$$

$$\hat{l}_y = i(a^\dagger c - c^\dagger a) \tag{B.2}$$

$$\hat{l}_z = i(b^\dagger a - a^\dagger b) \tag{B.3}$$

$$\hat{Q}_x = \hat{l}_x^2 - \hat{l}_y^2 = n_b - n_a \tag{B.4}$$

$$\hat{Q}_z = \frac{1}{\sqrt{3}}(\hat{l}_x^2 + \hat{l}_y^2 - 2\hat{l}_z^2) = \frac{1}{\sqrt{3}}(2n_c - n_a - n_b) \tag{B.5}$$

$$\hat{T}_x = \hat{l}_y\hat{l}_z + \hat{l}_z\hat{l}_y = -(b^\dagger c + c^\dagger b) \tag{B.6}$$

$$\hat{T}_y = \hat{l}_x\hat{l}_z + \hat{l}_z\hat{l}_x = -(c^\dagger a + a^\dagger c) \tag{B.7}$$

$$\hat{T}_z = \hat{l}_x\hat{l}_y + \hat{l}_y\hat{l}_x = -(a^\dagger b + b^\dagger a) \tag{B.8}$$

which are normalized by $\mathrm{Tr}\left(\hat{\Gamma}^2\right) = 2$. The corresponding matrices $\Gamma_{d'd}$ in Eq. (5.41) are

$$\Gamma^{Q_x} = \frac{1}{2}\begin{pmatrix}-1 & 0 & 0\\ 0 & 1 & 0\\ 0 & 0 & 0\end{pmatrix}, \qquad \Gamma^{Q_z} = \tfrac{1}{2\sqrt{3}}\begin{pmatrix}-1 & 0 & 0\\ 0 & -1 & 0\\ 0 & 0 & 2\end{pmatrix},$$
$$\Gamma^{T_x} = -\frac{1}{2}\begin{pmatrix}0 & 0 & 0\\ 0 & 0 & 1\\ 0 & 1 & 0\end{pmatrix}, \qquad \Gamma^{T_y} = -\tfrac{1}{2}\begin{pmatrix}0 & 0 & 1\\ 0 & 0 & 0\\ 1 & 0 & 0\end{pmatrix},$$
$$\Gamma^{T_z} = -\frac{1}{2}\begin{pmatrix}0 & 1 & 0\\ 1 & 0 & 0\\ 0 & 0 & 0\end{pmatrix}, \qquad \Gamma^{l_x} = \tfrac{1}{2}\begin{pmatrix}0 & 0 & 0\\ 0 & 0 & i\\ 0 & -i & 0\end{pmatrix},$$
$$\Gamma^{l_y} = \frac{1}{2}\begin{pmatrix}0 & 0 & -i\\ 0 & 0 & 0\\ i & 0 & 0\end{pmatrix}, \qquad \Gamma^{l_z} = \tfrac{1}{2}\begin{pmatrix}0 & i & 0\\ -i & 0 & 0\\ 0 & 0 & 0\end{pmatrix} \tag{B.9}$$

with the indices $d, d' = (yz, zx, xy)$ (or for polarization dependence: $\alpha, \beta = (x, y, z)$).

B.2 Multiplet factors

For the multiplet effect factors in Eq. (5.46), we have

$$M^{A_{1g}}_{d'd} = \sqrt{\frac{2}{3}}\left(\langle d'|\,\hat{x}\,|m\rangle\,\langle m|\,\hat{x}\,|d\rangle + \langle d'|\,\hat{y}\,|m\rangle\,\langle m|\,\hat{y}\,|d\rangle + \langle d'|\,\hat{z}\,|m\rangle\,\langle m|\,\hat{z}\,|d\rangle\right) \tag{B.10}$$

$$M^{Q_x}_{d'd} = \left(\langle d'|\,\hat{y}\,|m\rangle\,\langle m|\,\hat{y}\,|d\rangle - \langle d'|\,\hat{x}\,|m\rangle\,\langle m|\,\hat{x}\,|d\rangle\right) \tag{B.11}$$

$$M^{Q_z}_{d'd} = \frac{1}{\sqrt{3}}\left(2\,\langle d'|\,\hat{z}\,|m\rangle\,\langle m|\,\hat{z}\,|d\rangle - \langle d'|\,\hat{x}\,|m\rangle\,\langle m|\,\hat{x}\,|d\rangle - \langle d'|\,\hat{y}\,|m\rangle\,\langle m|\,\hat{y}\,|d\rangle\right) \tag{B.12}$$

$$M^{T_x}_{d'd} = -\left(\langle d'|\,\hat{y}\,|m\rangle\,\langle m|\,\hat{z}\,|d\rangle + \langle d'|\,\hat{z}\,|m\rangle\,\langle m|\,\hat{y}\,|d\rangle\right) \tag{B.13}$$

$$M^{T_y}_{d'd} = -\left(\langle d'|\,\hat{z}\,|m\rangle\,\langle m|\,\hat{x}\,|d\rangle + \langle d'|\,\hat{x}\,|m\rangle\,\langle m|\,\hat{z}\,|d\rangle\right) \tag{B.14}$$

$$M^{T_z}_{d'd} = -\left(\langle d'|\,\hat{x}\,|m\rangle\,\langle m|\,\hat{y}\,|d\rangle + \langle d'|\,\hat{y}\,|m\rangle\,\langle m|\,\hat{x}\,|d\rangle\right) \tag{B.15}$$

$$M^{l_x}_{d'd} = -i\left(\langle d'|\,\hat{y}\,|m\rangle\,\langle m|\,\hat{z}\,|d\rangle - \langle d'|\,\hat{z}\,|m\rangle\,\langle m|\,\hat{y}\,|d\rangle\right) \tag{B.16}$$

$$M^{l_y}_{d'd} = -i\left(\langle d'|\,\hat{z}\,|m\rangle\,\langle m|\,\hat{x}\,|d\rangle - \langle d'|\,\hat{x}\,|m\rangle\,\langle m|\,\hat{z}\,|d\rangle\right) \tag{B.17}$$

$$M^{l_z}_{d'd} = -i\left(\langle d'|\,\hat{x}\,|m\rangle\,\langle m|\,\hat{y}\,|d\rangle - \langle d'|\,\hat{y}\,|m\rangle\,\langle m|\,\hat{x}\,|d\rangle\right) \tag{B.18}$$

Note that the position operators act on the core electrons, not the t_{2g} ones. Both the core and t_{2g} electrons are implied in the states $|d\rangle\,, |d'\rangle$.

B.3 The operators $\hat{\mathbf{\Gamma}}$ in terms of orbitons

In terms of the orbiton operators, we obtain the one-orbiton creation part of $\hat{\Gamma}_{\mathbf{q}} = \sum_i e^{i\mathbf{q}\cdot\mathbf{r}_i}\hat{\Gamma}_i$ to be

$$\begin{aligned}\hat{l}^{(1)}_{x,\mathbf{q}-\mathbf{q}_1} &= \frac{i\,|c_0|}{2}\sqrt{\frac{N}{3}}\Big[\Big\{(1-\sqrt{3})u_{\mathbf{q}} + (1+\sqrt{3})v_{\mathbf{q}}\Big\}(\text{sh}\;\theta_{1,\mathbf{q}} + \text{ch}\;\theta_{1,\mathbf{q}})\alpha^{\dagger}_{1,-\mathbf{q}} \\ &\quad + \Big\{(-1-\sqrt{3})u_{\mathbf{q}} + (1-\sqrt{3})v_{\mathbf{q}}\Big\}(\text{sh}\;\theta_{2,\mathbf{q}} + \text{ch}\;\theta_{2,\mathbf{q}})\alpha^{\dagger}_{2,-\mathbf{q}}\Big]\end{aligned} \tag{B.19}$$

$$\begin{aligned}\hat{l}^{(1)}_{y,\mathbf{q}-\mathbf{q}_2} &= \frac{i\,|c_0|}{2}\sqrt{\frac{N}{3}}\Big[\Big\{(1+\sqrt{3})u_{\mathbf{q}} + (1-\sqrt{3})v_{\mathbf{q}}\Big\}(\text{sh}\;\theta_{1,\mathbf{q}} + \text{ch}\;\theta_{1,\mathbf{q}})\alpha^{\dagger}_{1,-\mathbf{q}} \\ &\quad + \Big\{(-1+\sqrt{3})u_{\mathbf{q}} + (1+\sqrt{3})v_{\mathbf{q}}\Big\}(\text{sh}\;\theta_{2,\mathbf{q}} + \text{ch}\;\theta_{2,\mathbf{q}})\alpha^{\dagger}_{2,-\mathbf{q}}\Big]\end{aligned} \tag{B.20}$$

$$\begin{aligned}\hat{l}^{(1)}_{z,\mathbf{q}-\mathbf{q}_3} &= -i\,|c_0|\sqrt{\frac{N}{3}}\Big[(u_{\mathbf{q}} + v_{\mathbf{q}})(\text{sh}\;\theta_{1,\mathbf{q}} + \text{ch}\;\theta_{1,\mathbf{q}})\alpha^{\dagger}_{1,-\mathbf{q}} \\ &\quad + (v_{\mathbf{q}} - u_{\mathbf{q}})(\text{sh}\;\theta_{2,\mathbf{q}} + \text{ch}\;\theta_{2,\mathbf{q}})\alpha^{\dagger}_{2,-\mathbf{q}}\Big]\end{aligned} \tag{B.21}$$

$$\begin{aligned}\hat{T}^{(1)}_{x,\mathbf{q}-\mathbf{q}_1} &= \frac{|c_0|}{6}\sqrt{N}\Big[\Big\{(1+\sqrt{3})u_{\mathbf{q}} + (-1+\sqrt{3})v_{\mathbf{q}}\Big\}(\text{ch}\;\theta_{1,\mathbf{q}} - \text{sh}\;\theta_{1,\mathbf{q}})\alpha^{\dagger}_{1,-\mathbf{q}} \\ &\quad + \Big\{(1-\sqrt{3})u_{\mathbf{q}} + (1+\sqrt{3})v_{\mathbf{q}}\Big\}(\text{ch}\;\theta_{2,\mathbf{q}} - \text{sh}\;\theta_{2,\mathbf{q}})\alpha^{\dagger}_{2,-\mathbf{q}}\Big]\end{aligned} \tag{B.22}$$

$$\begin{aligned}\hat{T}^{(1)}_{y,\mathbf{q}-\mathbf{q}_2} &= \frac{|c_0|}{6}\sqrt{N}\Big[\Big\{(1-\sqrt{3})u_{\mathbf{q}} + (-1-\sqrt{3})v_{\mathbf{q}}\Big\}(\text{ch}\;\theta_{1,\mathbf{q}} - \text{sh}\;\theta_{1,\mathbf{q}})\alpha^{\dagger}_{1,-\mathbf{q}} \\ &\quad + \Big\{(1+\sqrt{3})u_{\mathbf{q}} + (1-\sqrt{3})v_{\mathbf{q}}\Big\}(\text{ch}\;\theta_{2,\mathbf{q}} - \text{sh}\;\theta_{2,\mathbf{q}})\alpha^{\dagger}_{2,-\mathbf{q}}\Big]\end{aligned} \tag{B.23}$$

$$\begin{aligned}\hat{T}^{(1)}_{z,\mathbf{q}-\mathbf{q}_3} &= -\frac{|c_0|}{3}\sqrt{N}\Big[(u_{\mathbf{q}} - v_{\mathbf{q}})(\text{ch}\;\theta_{1,\mathbf{q}} - \text{sh}\;\theta_{1,\mathbf{q}})\alpha^{\dagger}_{1,-\mathbf{q}} \\ &\quad + (u_{\mathbf{q}} + v_{\mathbf{q}})(\text{ch}\;\theta_{2,\mathbf{q}} - \text{sh}\;\theta_{2,\mathbf{q}})\alpha^{\dagger}_{2,-\mathbf{q}}\Big]\end{aligned} \tag{B.24}$$

$$\begin{aligned}\hat{Q}^{(1)}_{x,\mathbf{q}} &= |c_0|\sqrt{\frac{N}{3}}\Big[-(u_{\mathbf{q}} + v_{\mathbf{q}})(\text{ch}\;\theta_{1,\mathbf{q}} - \text{sh}\;\theta_{1,\mathbf{q}})\alpha^{\dagger}_{1,-\mathbf{q}} \\ &\quad + (u_{\mathbf{q}} - v_{\mathbf{q}})(\text{ch}\;\theta_{2,\mathbf{q}} - \text{sh}\;\theta_{2,\mathbf{q}})\alpha^{\dagger}_{2,-\mathbf{q}}\Big]\end{aligned} \tag{B.25}$$

$$\begin{aligned}\hat{Q}^{(1)}_{z,\mathbf{q}} &= -\,|c_0|\sqrt{\frac{N}{3}}\Big[(u_{\mathbf{q}} - v_{\mathbf{q}})(\text{ch}\;\theta_{1,\mathbf{q}} - \text{sh}\;\theta_{1,\mathbf{q}})\alpha^{\dagger}_{1,-\mathbf{q}} \\ &\quad + (u_{\mathbf{q}} + v_{\mathbf{q}})(\text{ch}\;\theta_{2,\mathbf{q}} - \text{sh}\;\theta_{2,\mathbf{q}})\alpha^{\dagger}_{2,-\mathbf{q}}\Big]\end{aligned} \tag{B.26}$$

with $\mathbf{q}_1 = (\pi, 0, \pi)$, $\mathbf{q}_2 = (\pi, \pi, 0)$, $\mathbf{q}_3 = (0, \pi, \pi)$. The expressions for the two-orbiton creation part of $\hat{\Gamma}_{\mathbf{q}} = \sum_i e^{i\mathbf{q}\cdot\mathbf{r}_i}\hat{\Gamma}_i$ are

$$\hat{l}^{(2)}_{x,\mathbf{q}} = \frac{i}{\sqrt{3}}\sum_{\mathbf{k}}\Big[(vu' - uv')\text{ch}\;\theta_1\;\text{sh}\;\theta'_1\;\alpha^{\dagger}_{1,\mathbf{k}}\alpha^{\dagger}_{1,-\mathbf{k}-\mathbf{q}_1-\mathbf{q}} +$$

$$
\begin{aligned}
&+ (vu' - uv')\text{ch}\ \theta_2\ \text{sh}\ \theta_2'\ \alpha^\dagger_{2,\mathbf{k}}\alpha^\dagger_{2,-\mathbf{k}-\mathbf{q}_1-\mathbf{q}} \\
&+ (uu' + vv')(\text{ch}\ \theta_1\ \text{sh}\ \theta_2' - \text{sh}\ \theta_1\ \text{ch}\ \theta_2')\alpha^\dagger_{1,\mathbf{k}}\alpha^\dagger_{2,-\mathbf{k}-\mathbf{q}_1-\mathbf{q}}\Big]
\end{aligned} \tag{B.27}
$$

with $u, v, \theta_1, \theta_2 = u_\mathbf{k}, v_\mathbf{k}, \theta_{1,\mathbf{k}}, \theta_{2,\mathbf{k}}$ and primed quantities $u', v', \theta_1', \theta_2' = u_{\mathbf{k}+\mathbf{q}_1+\mathbf{q}}$, $v_{\mathbf{k}+\mathbf{q}_1+\mathbf{q}}$, $\theta_{1,\mathbf{k}+\mathbf{q}_1+\mathbf{q}}$, $\theta_{2,\mathbf{k}+\mathbf{q}_1+\mathbf{q}}$. Further, $\hat{l}^{(2)}_{y,\mathbf{q}}$ and $\hat{l}^{(2)}_{z,\mathbf{q}}$ have the same form as $\hat{l}^{(2)}_{x,\mathbf{q}}$ but with $\mathbf{q}_1$ replaced by $\mathbf{q}_2$ and $\mathbf{q}_3$ respectively. Next,

$$
\begin{aligned}
\hat{T}^{(2)}_{x,\mathbf{q}} =& \sum_\mathbf{k} \Bigg[\left\{-(uu'+vv') + \frac{uu'-vv'}{\sqrt{3}} + \frac{uv'+vu'}{3}\right\}\text{ch}\ \theta_1\ \text{sh}\ \theta_1'\ \alpha^\dagger_{1,\mathbf{k}}\alpha^\dagger_{1,-\mathbf{k}-\mathbf{q}_1-\mathbf{q}} \\
&+ \left\{-(uu'+vv') - \frac{uu'-vv'}{\sqrt{3}} - \frac{uv'+vu'}{3}\right\}\text{ch}\ \theta_2\ \text{sh}\ \theta_2'\ \alpha^\dagger_{2,\mathbf{k}}\alpha^\dagger_{2,-\mathbf{k}-\mathbf{q}_1-\mathbf{q}} \\
&+ \left\{-(uv'-vu') - \frac{uv'+vu'}{\sqrt{3}} - \frac{uu'-vv'}{3}\right\}(\text{ch}\ \theta_1\ \text{sh}\ \theta_2' + \text{sh}\ \theta_1\ \text{ch}\ \theta_2')\times \\
&\alpha^\dagger_{1,\mathbf{k}}\alpha^\dagger_{2,-\mathbf{k}-\mathbf{q}_1-\mathbf{q}}\Bigg]
\end{aligned} \tag{B.28}
$$

$$
\begin{aligned}
\hat{T}^{(2)}_{y,\mathbf{q}} =& \sum_\mathbf{k} \Bigg[\left\{-(uu'+vv') - \frac{uu'-vv'}{\sqrt{3}} + \frac{uv'+vu'}{3}\right\}\text{ch}\ \theta_1\ \text{sh}\ \theta_1'\ \alpha^\dagger_{1,\mathbf{k}}\alpha^\dagger_{1,-\mathbf{k}-\mathbf{q}_2-\mathbf{q}} \\
&+ \left\{-(uu'+vv') + \frac{uu'-vv'}{\sqrt{3}} - \frac{uv'+vu'}{3}\right\}\text{ch}\ \theta_2\ \text{sh}\ \theta_2'\ \alpha^\dagger_{2,\mathbf{k}}\alpha^\dagger_{2,-\mathbf{k}-\mathbf{q}_2-\mathbf{q}} \\
&+ \left\{-(uv'-vu') + \frac{uv'+vu'}{\sqrt{3}} - \frac{uu'-vv'}{3}\right\}(\text{ch}\ \theta_1\ \text{sh}\ \theta_2' + \text{sh}\ \theta_1\ \text{ch}\ \theta_2')\times \\
&\alpha^\dagger_{1,\mathbf{k}}\alpha^\dagger_{2,-\mathbf{k}-\mathbf{q}_2-\mathbf{q}}\Bigg]
\end{aligned} \tag{B.29}
$$

where in the expression for $\hat{T}^{(2)}_{y,\mathbf{q}}$ we replaced $\mathbf{q}_1$ by $\mathbf{q}_2$: $u', v', \theta_1', \theta_2' = u_{\mathbf{k}+\mathbf{q}_2+\mathbf{q}}$, $v_{\mathbf{k}+\mathbf{q}_2+\mathbf{q}}$, $\theta_{1,\mathbf{k}+\mathbf{q}_2+\mathbf{q}}$, $\theta_{2,\mathbf{k}+\mathbf{q}_2+\mathbf{q}}$.

$$
\begin{aligned}
\hat{T}^{(2)}_{z,\mathbf{q}} =& \sum_\mathbf{k} \Bigg[\left\{-\frac{2}{3}(uv'+vu') - (uu'+vv')\right\}\text{ch}\ \theta_1\ \text{sh}\ \theta_1'\ \alpha^\dagger_{1,\mathbf{k}}\alpha^\dagger_{1,-\mathbf{k}-\mathbf{q}_3-\mathbf{q}} \\
&+ \left\{\frac{2}{3}(uv'+vu') - (uu'+vv')\right\}\text{ch}\ \theta_2\ \text{sh}\ \theta_2'\ \alpha^\dagger_{2,\mathbf{k}}\alpha^\dagger_{2,-\mathbf{k}-\mathbf{q}_3-\mathbf{q}} \\
&+ \left\{\frac{2}{3}(uu'-vv') - (uv'-vu')\right\}(\text{ch}\ \theta_1\ \text{sh}\ \theta_2' + \text{sh}\ \theta_1\ \text{ch}\ \theta_2')\alpha^\dagger_{1,\mathbf{k}}\alpha^\dagger_{2,-\mathbf{k}-\mathbf{q}_3-\mathbf{q}}\Bigg]
\end{aligned} \tag{B.30}
$$

where we replaced $\mathbf{q}_1$ by $\mathbf{q}_3$: $u', v', \theta_1', \theta_2' = u_{\mathbf{k}+\mathbf{q}_3+\mathbf{q}}$, $v_{\mathbf{k}+\mathbf{q}_3+\mathbf{q}}$, $\theta_{1,\mathbf{k}+\mathbf{q}_3+\mathbf{q}}$, $\theta_{2,\mathbf{k}+\mathbf{q}_3+\mathbf{q}}$. Finally,

$$
\begin{aligned}
\hat{Q}^{(2)}_{x,\mathbf{q}} = -\frac{1}{\sqrt{3}}\sum_\mathbf{k}\Big[&-(uu'-vv')\text{ch}\ \theta_1\ \text{sh}\ \theta_1'\ \alpha^\dagger_{1,\mathbf{k}}\alpha^\dagger_{1,-\mathbf{k}-\mathbf{q}} \\
&+ (uu'-vv')\text{ch}\ \theta_2\ \text{sh}\ \theta_2'\ \alpha^\dagger_{2,\mathbf{k}}\alpha^\dagger_{2,-\mathbf{k}-\mathbf{q}} +
\end{aligned}
$$

$$+\,(uv'+vu')(\mathrm{ch}\,\theta_1\ \mathrm{sh}\,\theta_2'+\mathrm{sh}\,\theta_1\ \mathrm{ch}\,\theta_2')\alpha^\dagger_{1,\mathbf{k}}\alpha^\dagger_{2,-\mathbf{k}-\mathbf{q}}\Big] \tag{B.31}$$

$$\begin{aligned}\hat{Q}^{(2)}_{z,\mathbf{q}} = \frac{1}{\sqrt{3}}\sum_{\mathbf{k}}\Big[&(uv'+vu')\mathrm{ch}\,\theta_1\ \mathrm{sh}\,\theta_1'\ \alpha^\dagger_{1,\mathbf{k}}\alpha^\dagger_{1,-\mathbf{k}-\mathbf{q}}\\ &-(uv'+vu')\mathrm{ch}\,\theta_2\ \mathrm{sh}\,\theta_2'\ \alpha^\dagger_{2,\mathbf{k}}\alpha^\dagger_{2,-\mathbf{k}-\mathbf{q}}\\ &-\,(uu'-vv')(\mathrm{ch}\,\theta_1\ \mathrm{sh}\,\theta_2'+\mathrm{sh}\,\theta_1\ \mathrm{ch}\,\theta_2')\alpha^\dagger_{1,\mathbf{k}}\alpha^\dagger_{2,-\mathbf{k}-\mathbf{q}}\Big]\end{aligned} \tag{B.32}$$

where in both equations we replaced $\mathbf{q}_1$ by $\mathbf{0}$: $u', v', \theta_1', \theta_2' = u_{\mathbf{k}+\mathbf{q}}$, $v_{\mathbf{k}+\mathbf{q}}$, $\theta_{1,\mathbf{k}+\mathbf{q}}$, $\theta_{2,\mathbf{k}+\mathbf{q}}$.

B.4 RIXS – two-site processes with superexchange model

Functions f_{11}, f_{22} and f_{12} in Eqs. (5.79–5.80) are:

$$\begin{aligned}f_{11}(\mathbf{k},\mathbf{q}) = {}&[-\gamma_{3,\mathbf{q}}(uv'+u'v)-\gamma_{2,\mathbf{q}}(uu'-vv')-(1+\gamma_{1,\mathbf{q}})(uu'+vv')]\times\\ &(\mathrm{ch}\,\theta_1\ \mathrm{sh}\,\theta_1'+\mathrm{sh}\,\theta_1\ \mathrm{ch}\,\theta_1')\\ &+2\,[\gamma_1'(uu'+vv')+\gamma_2'(uu'-vv')+\gamma_3'(uv'+u'v)]\times\\ &(\mathrm{sh}\,\theta_1\ \mathrm{sh}\,\theta_1'+\mathrm{ch}\,\theta_1\ \mathrm{ch}\,\theta_1')\end{aligned} \tag{B.33}$$

$$\begin{aligned}f_{22}(\mathbf{k},\mathbf{q}) = {}&[\gamma_{3,\mathbf{q}}(uv'+u'v)+\gamma_{2,\mathbf{q}}(uu'-vv')-(1+\gamma_{1,\mathbf{q}})(uu'+vv')]\times\\ &(\mathrm{ch}\,\theta_2\ \mathrm{sh}\,\theta_2'+\mathrm{sh}\,\theta_2\ \mathrm{ch}\,\theta_2')\\ &+2\,[\gamma_1'(uu'+vv')-\gamma_2'(uu'-vv')-\gamma_3'(uv'+u'v)]\times\\ &(\mathrm{sh}\,\theta_2\ \mathrm{sh}\,\theta_2'+\mathrm{ch}\,\theta_2\ \mathrm{ch}\,\theta_2')\end{aligned} \tag{B.34}$$

$$\begin{aligned}f_{12}(\mathbf{k},\mathbf{q}) = {}&2\,[\gamma_{3,\mathbf{q}}(uu'-vv')+\gamma_{2,\mathbf{q}}(uv'+u'v)-(1+\gamma_{1,\mathbf{q}})(uv'-u'v)]\times\\ &(\mathrm{ch}\,\theta_1\ \mathrm{sh}\,\theta_2'+\mathrm{sh}\,\theta_1\ \mathrm{ch}\,\theta_2')\\ &+4\,[\gamma_1'(uv'-u'v)+\gamma_2'(uv'+u'v)-\gamma_3'(uu'-vv')]\times\\ &(\mathrm{sh}\,\theta_1\ \mathrm{sh}\,\theta_2'+\mathrm{ch}\,\theta_1\ \mathrm{ch}\,\theta_2')\end{aligned} \tag{B.35}$$

where we shortened notation by writing $\theta_{1/2} = \theta_{1/2,\mathbf{k}}$, $\theta'_{1/2} = \theta_{1/2,\mathbf{k}+\mathbf{q}}$, $u(') = u_{\mathbf{k}(+\mathbf{q})}$, $v(') = v_{\mathbf{k}(+\mathbf{q})}$ and $\gamma_i' = \gamma_{i,\mathbf{k}+\mathbf{q}}$.

APPENDIX C

PHONON RIXS

This appendix contains the lengthy derivations involved in calculating the Einstein phonon RIXS spectra of chapter 7. In the following, we evaluate the scattering amplitude (7.8). We use (see Mahan [62], section 4.3.2)

$$
\begin{aligned}
\langle n| e^{\frac{M}{\omega_0}(b^\dagger - b)} \left|n^0\right\rangle &= e^{-g/2} \langle n|\, e^{\frac{M}{\omega_0} b^\dagger} e^{-\frac{M}{\omega_0} b} \left|n^0\right\rangle \\
&= e^{-g/2} \sum_{k=0}^{n} \sum_{l=0}^{n^0} \langle n-k| \, \frac{(M/\omega_0)^k}{k!} \left[\frac{n!}{(n-k)!}\right]^{\frac{1}{2}} \frac{(-M/\omega_0)^l}{l!} \left[\frac{n^0!}{(n^0-l)!}\right]^{\frac{1}{2}} \left|n^0 - l\right\rangle \\
&= e^{-g/2} \sum_{k=0}^{n} \sum_{l=0}^{n^0} \frac{(M/\omega_0)^k}{k!} \left[\frac{n! n^0!}{(n-k)!(n^0-l)!}\right]^{\frac{1}{2}} \frac{(-M/\omega_0)^l}{l!} \delta_{n^0-l, n-k} \\
&= \begin{cases} e^{-g/2} \sum_{l=0}^{n^0} \frac{(M/\omega_0)^{l-n^0+n}}{(l-n^0+n)!} \left[\frac{n! n^0!}{(n-(l-n^0+n))!(n^0-l)!}\right]^{\frac{1}{2}} \frac{(-M/\omega_0)^l}{l!} & \text{for } n > n^0 \\ e^{-g/2} \sum_{k=0}^{n} \frac{(M/\omega_0)^k}{k!} \left[\frac{n! n^0!}{(n-k)!(n^0-(n^0-n+k))!}\right]^{\frac{1}{2}} \frac{(-M/\omega_0)^{n^0-n+k}}{(n^0-n+k)!} & \text{for } n \le n^0 \end{cases} \\
&= \begin{cases} e^{-g/2} \sum_{l=0}^{n^0} \frac{(-1)^l (M/\omega_0)^{2l-n^0+n}}{l!(l-n^0+n)!} \frac{\sqrt{n! n^0!}}{(n^0-l)!} & \text{for } n > n^0 \\ e^{-g/2} \sum_{l=0}^{n} \frac{(-1)^{l+n^0-n} (M/\omega_0)^{2l+n^0-n}}{l!(l+n^0-n)!} \frac{\sqrt{n! n^0!}}{(n-l)!} & \text{for } n \le n^0 \end{cases}
\end{aligned}
\tag{C.1}
$$

with $g = m^2/\omega_0^2$. For simplicity, we assume the system is initially in its ground state: $n^0 = 0$. In that case, the above expression simplifies to

$$
\langle n|\, e^{\frac{M}{\omega_0}(b^\dagger - b)} |0\rangle = e^{-g/2} \frac{(M/\omega_0)^n}{\sqrt{n!}}. \tag{C.2}
$$

These expressions are inserted in the Kramers-Heisenberg equation (7.12):

$$\mathcal{F}_{fg} = T_{\text{el}}(\boldsymbol{\epsilon}', \boldsymbol{\epsilon}) \sum_i e^{i\mathbf{q}\cdot\mathbf{R}_i} F_i \tag{C.3}$$

with

$$\begin{aligned} F_i &= e^{-g} \sum_{n=0}^{n_i'} \sum_{l=0}^{n} \frac{(-1)^{l+n_i'-n} \, (M/\omega_0)^{2l+n_i'}}{l!(l+n_i'-n)!} \frac{\sqrt{n_i'!}}{(n-l)!} \frac{1}{z+(g-n)\omega_0} \\ &+ e^{-g} \sum_{n=n_i'+1}^{\infty} \sum_{l=0}^{n_i'} \frac{(-1)^{l} \, (M/\omega_0)^{2l-n_i'+2n}}{l!(l-n_i'+n)!} \frac{\sqrt{n_i'!}}{(n_i'-l)!} \frac{1}{z+(g-n)\omega_0}. \end{aligned} \tag{C.4}$$

APPENDIX D

MAGNETIC SPECTRAL WEIGHT AT THE Γ POINT IN 2D CUPRATES

This appendix contains the calculational details from Sec. 4.5.5, where the leading magnetic contribution to the $\mathbf{q} = \mathbf{0}$ RIXS spectra at the Cu L edge is established.

D.1 $\bar{H}_{\text{eff}}^{(4)}$ to fourth order in t/U

In this section we evaluate Eq. (4.74) in the presence of a core hole.

The first term of Eq. (4.74) changes the Hamiltonian to

$$\bar{H}_{\text{eff}}^{(4)} = H_0 - \frac{4t^2}{U} \sum_i p_i p_i^\dagger \sum_\delta \mathbf{S}_i \cdot \mathbf{S}_{i+\delta} + \dots \tag{D.1}$$

where $p_i^\dagger$ creates a core electron, δ points to nearest neighbors, and the dots indicate the corrections to H_0 due to the four hop terms.

To handle the four hop terms systematically, we categorize all terms according to the 'connections' between sites. With a 'connection' is meant that one or more hops occur between the sites in question. For example, only the sites i and j, and j and k are connected if we select the following four hoppings from the V's:

$$t_{ij} \sum_\sigma (c_{i\sigma}^\dagger c_{j\sigma} + c_{j\sigma}^\dagger c_{i\sigma}) \times \dots \times t_{jk} \sum_{\sigma'} (c_{j\sigma'}^\dagger c_{k\sigma'} + c_{j\sigma'}^\dagger c_{k\sigma'}) \times \dots \times t_{ij}(\dots) \times \dots \times t_{jk}(\dots), \tag{D.2}$$

but also processes with a different hopping order like $t_{ij}t_{ij}t_{jk}t_{jk}$ and $t_{jk}t_{ij}t_{ij}t_{jk}$, etc., have the same connections and are thus categorized together. We will therefore represent the category comprising all these processes by $t_{ij}^2 t_{jk}^2$. The order of the t's is not important, only the number of times a certain hop occurs is important for indicating the category.

We now establish the different categories. The most general string of t's is $t_{ij}t_{kl}t_{mn}t_{pq}$. A lot of these processes change the occupancy of one of the sites. These terms vanish because of the P_0's at the beginning and end of every four hop term. This imposes a restriction on the indices i, j, k, l, m, n, p, q: if an index appears an odd number of times, the occupancy is changed and the process does not contribute to $H_{\text{eff}}^{(4)}$. We are left with the following categories: **(a)** t_{ij}^4, **(b)** $t_{ij}^2 t_{kl}^2 (i, j \neq k, l)$, **(c)** $t_{ij}^2 t_{jk}^2 (i \neq k)$, and **(d)** $t_{ij}t_{jk}t_{kl}t_{li}$ (i, j, k, l form a square). If there is no core hole present at any of the sites involved, we can just copy-paste the results from Ref. [82]. Below we analyze the processes where there is a core hole present.

Processes in category (**a**) do not flip any spins. The doublon (the doubly occupied site) hops 4 times between site i and j, where i is the core hole site. We obtain the (**a**) contribution:

$$H_{\text{eff}}^{(4)} = \cdots + p_i p_i^\dagger \frac{t^4}{U_c^3} P_0 \sum_\sigma c_{i\sigma}^\dagger c_{j\sigma} c_{j\sigma}^\dagger c_{i\sigma} P_0 \, c_{i\sigma}^\dagger c_{j\sigma} c_{j\sigma}^\dagger c_{i\sigma} P_0 \, , \tag{D.3}$$

where the dots indicate other fourth order terms. At the core hole site, $c_{i\sigma}^\dagger c_{i\sigma} = 1$, and we use the projected spins as defined in Eq. (2.14) of Ref. [82] to get

$$H_{\text{eff}}^{(4)} = \cdots + p_i p_i^\dagger \frac{t^4}{U_c^3} \left(\{\frac{1}{2}(1 - \sigma_j^z)\}^2 + \{\frac{1}{2}(1 + \sigma_j^z)\}^2 \right) = \cdots + p_i p_i^\dagger \frac{t^4}{U_c^3} \mathbb{1}. \tag{D.4}$$

The corresponding part of H_0 is

$$H_0 = \cdots - \frac{16t^4}{U^3} \mathbf{S}_i \cdot \mathbf{S}_j \tag{D.5}$$

which should be replaced by Eq. (D.4). Dropping the constant term, this gives

$$\bar{H}_{\text{eff}}^{(4)} = H_0 + \sum_i p_i p_i^\dagger \sum_\delta \frac{16t^4}{U^3} \mathbf{S}_i \cdot \mathbf{S}_{i+\delta} + \ldots \tag{D.6}$$

Processes in category **(b)** do not appear in the fourth order expansion of the half-filled Hubbard model. If we add one doubly occupied site (namely, the core hole site i), there still is no contribution to $\bar{H}_{\text{eff}}^{(4)}$. The only matrix elements for which this is not a priori clear, involve configurations pictured in Fig. D.1.

If the spins at k and l are parallel, the corresponding matrix element is obviously zero. Working out the other matrix elements (12 pathways for interchanging anti-parallel k and l, and 12 pathways for leaving anti-parallel k and l invariant),

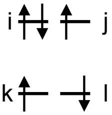

Figure D.1: The processes of category **(b)** involve $t_{ij}^2 t_{kl}^2$, connecting i to j and k to l.

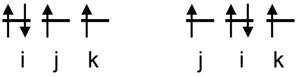

Figure D.2: The processes of category **(c)** are subdivided into two cases: the core hole site is connected to one other site (left), or the core hole site is connected to two other sites (right).

it turns out that all pathways interfere to give 0, just as in the half-filled case. Therefore, H_0 is not modified by category **(b)** processes.

Processes in category **(c)** connect three sites i, j and k. They can be subdivided into two cases: in the first one, the core hole site i is connected to one other site, and the second one, the core hole site i is connected to two other sites. Starting with the first case, we have for the following matrix elements:

$$\uparrow_j\uparrow_k\to\uparrow_j\uparrow_k \text{ and } \downarrow_j\downarrow_k\to\downarrow_j\downarrow_k: \quad \bar{H}^{(4)}_{\text{eff}} = \cdots - p_i p_i^\dagger \frac{t^4}{U_c^3}\left(\frac{1}{2}\mathbb{1} + 2S_j^z S_k^z\right), \tag{D.7}$$

$$\uparrow_j\downarrow_k\to\uparrow_j\downarrow_k \text{ and } \downarrow_j\uparrow_k\to\downarrow_j\uparrow_k: \quad \bar{H}^{(4)}_{\text{eff}} = \cdots - p_i p_i^\dagger \frac{t^4}{U_c^3}\left(\frac{1}{2}\mathbb{1} - 2S_j^z S_k^z\right), \tag{D.8}$$

$$\uparrow_j\downarrow_k\to\downarrow_j\uparrow_k \text{ and } \downarrow_j\uparrow_k\to\uparrow_j\downarrow_k: \quad \bar{H}^{(4)}_{\text{eff}} = \cdots + 0. \tag{D.9}$$

Adding these contributions and dropping the constants yields

$$\bar{H}^{(4)}_{\text{eff}} = \cdots + 0. \tag{D.10}$$

The second case gives

$$\uparrow_j\uparrow_k\to\uparrow_j\uparrow_k \text{ and } \downarrow_j\downarrow_k\to\downarrow_j\downarrow_k: \quad \bar{H}^{(4)}_{\text{eff}} = \cdots + p_i p_i^\dagger \frac{2t^4}{U_c^3}\left(\frac{1}{2}\mathbb{1} + 2S_j^z S_k^z\right), \tag{D.11}$$

$$\begin{aligned}\uparrow_j\downarrow_k\to\uparrow_j\downarrow_k \text{ and } \downarrow_j\uparrow_k\to\downarrow_j\uparrow_k: \quad \bar{H}^{(4)}_{\text{eff}} &= \cdots - p_i p_i^\dagger \left(\frac{2t^4}{UU_c^2} + \frac{4t^4}{U_c^2(2U_c+U)}\right. \\ &\left. -\frac{2t^4}{U_c^3}\right)\left(\frac{1}{2}\mathbb{1} - 2S_j^z S_k^z\right),\end{aligned} \tag{D.12}$$

$$\begin{aligned}\uparrow_j\downarrow_k\to\downarrow_j\uparrow_k \text{ and } \downarrow_j\uparrow_k\to\uparrow_j\downarrow_k: \quad \bar{H}^{(4)}_{\text{eff}} &= \cdots + p_i p_i^\dagger \left(\frac{2t^4}{UU_c^2} + \frac{4t^4}{U_c^2(2U_c+U)}\right) \\ &\times\left(S_j^+ S_k^- + S_j^- S_k^+\right).\end{aligned} \tag{D.13}$$

Adding the contributions and dropping the constants yields

$$\bar{H}^{(4)}_{\text{eff}} = \cdots + p_i p_i^\dagger \left(\frac{4t^4}{UU_c^2} + \frac{8t^4}{U_c^2(2U_c+U)}\right)\mathbf{S}_j\cdot\mathbf{S}_k. \tag{D.14}$$

The corresponding part of H_0 (including the second neighbor terms from category (**d**))[1] is

$$H_0 = \cdots + \sum_{j\neq k} \frac{4t_{ij}^2 t_{ik}^2}{U^3}\mathbf{S}_j \cdot \mathbf{S}_k \tag{D.15}$$

and it is replaced by

$$\bar{H}_{\text{eff}}^{(4)} = H_0 + \sum_i p_i p_i^\dagger \sum_{j\neq k}\left(\frac{4t^4}{UU_c^2} + \frac{8t^4}{U_c^2(2U_c+U)} - \frac{4t^4}{U^3}\right)\mathbf{S}_j \cdot \mathbf{S}_k + \dots \tag{D.16}$$

where the sum over $j \neq k$ is over all pairs of neighbors j, k of i.

Finally, the processes of category **(d)** are

$$\begin{matrix}\uparrow_j & d_i\\ \uparrow_k & \uparrow_l\end{matrix} \rightarrow \begin{matrix}\uparrow_j & d_i\\ \uparrow_k & \uparrow_l\end{matrix} + \text{flipped}:$$

$$\bar{H}_{\text{eff}}^{(4)} = \cdots - p_i p_i^\dagger \frac{2t^4}{U_c^3}\left(\frac{1}{4}\mathbb{1} + S_j^z S_k^z + S_k^z S_l^z + S_j^z S_l^z\right), \tag{D.17}$$

$$\begin{matrix}\uparrow_j & d_i\\ \downarrow_k & \uparrow_l\end{matrix} \rightarrow \begin{matrix}\uparrow_j & d_i\\ \downarrow_k & \uparrow_l\end{matrix} + \text{flipped}:$$

$$\bar{H}_{\text{eff}}^{(4)} = \cdots + p_i p_i^\dagger \frac{2t^4}{UU_c^2}\left(\frac{1}{4}\mathbb{1} - S_j^z S_k^z - S_k^z S_l^z + S_j^z S_l^z\right), \tag{D.18}$$

$$\begin{matrix}\downarrow_j & d_i\\ \uparrow_k & \uparrow_l\end{matrix} \rightarrow \begin{matrix}\downarrow_j & d_i\\ \uparrow_k & \uparrow_l\end{matrix} + \text{flip} + j \leftrightarrow l:$$

$$\bar{H}_{\text{eff}}^{(4)} = \cdots + p_i p_i^\dagger \frac{2t^4}{UU_c^2}\left(\frac{1}{2}\mathbb{1} - 2S_j^z S_l^z\right), \tag{D.19}$$

$$\begin{matrix}\downarrow_j & d_i\\ \uparrow_k & \uparrow_l\end{matrix} \rightarrow \begin{matrix}\uparrow_j & d_i\\ \downarrow_k & \uparrow_l\end{matrix} + \text{flip} + j \leftrightarrow l:$$

$$\begin{aligned}\bar{H}_{\text{eff}}^{(4)} &= \cdots - p_i p_i^\dagger \left(\frac{t^4}{U_c^3} + \frac{t^4}{UU_c^2}\right)\left(S_j^+ S_k^- + S_j^- S_k^+\right.\\ &\qquad \left. + S_k^+ S_l^- + S_k^- S_l^+\right),\end{aligned} \tag{D.20}$$

$$\begin{matrix}\downarrow_j & d_i\\ \uparrow_k & \uparrow_l\end{matrix} \rightarrow \begin{matrix}\uparrow_j & d_i\\ \uparrow_k & \downarrow_l\end{matrix} + \text{flip} + j \leftrightarrow l:$$

$$\bar{H}_{\text{eff}}^{(4)} = \cdots - p_i p_i^\dagger \left(\frac{t^4}{U_c^3} + \frac{t^4}{UU_c^2}\right)\left(S_j^+ S_l^- + S_j^- S_l^+\right). \tag{D.21}$$

where we have labeled the sites as shown in Fig. D.3, with d_i the doubly occupied core hole site.

---

[1] We do this because, first, it simplifies notation: the second and third neighbor terms in the sum get the same prefactor. Second, Coldea also does this, and following him makes it easy to compare to his mean field result for the ring exchange terms.

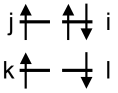

Figure D.3: The processes of category **(d)** $(t_{ij}t_{jk}t_{kl}t_{li})$ describe ring exchange.

Dropping constants, the final result for processes of category **(d)** is

$$H_{\text{eff}}^{(4)} = \cdots - \sum_{i,\text{squares at } i} p_i p_i^\dagger \left(\frac{2t^4}{UU_c^2} + \frac{2t^4}{U_c^3} \right) (\mathbf{S}_j \cdot \mathbf{S}_k + \mathbf{S}_k \cdot \mathbf{S}_l + \mathbf{S}_j \cdot \mathbf{S}_l) . \qquad \text{(D.22)}$$

The corresponding terms in H_0 (minus the second neighbor terms, which were absorbed in the correction to H_0 due to category (**c**)) are

$$H_0 = \cdots - \frac{8t^4}{U^3} \sum_{\langle i,j \rangle} \mathbf{S}_i \cdot \mathbf{S}_j + \frac{80t^4}{U^3} \sum_{\text{squares}} [(\mathbf{S}_i \cdot \mathbf{S}_j)(\mathbf{S}_k \cdot \mathbf{S}_l) + (\mathbf{S}_i \cdot \mathbf{S}_l)(\mathbf{S}_j \cdot \mathbf{S}_k) - (\mathbf{S}_i \cdot \mathbf{S}_k)(\mathbf{S}_j \cdot \mathbf{S}_l)] . \qquad \text{(D.23)}$$

The mean field result is easily obtained [82, 83]:

$$H_0 = \cdots - \frac{48t^4}{U^3} \sum_{\langle i,j \rangle} \mathbf{S}_i \cdot \mathbf{S}_j - \frac{20t^4}{U^3} \sum_{i,k} \mathbf{S}_i \cdot \mathbf{S}_k , \qquad \text{(D.24)}$$

where the sum over i, k is over all pairs of next nearest neighbors. Then, at the mean field, the intermediate state Hamiltonian for processes of category (**d**) becomes

$$\begin{aligned} \bar{H}_{\text{eff}}^{(4)} = H_0 + \sum_i p_i p_i^\dagger \sum_{\text{squares at } i} \Bigg[& \frac{24t^4}{U^3} (\mathbf{S}_i \cdot \mathbf{S}_j + \mathbf{S}_j \cdot \mathbf{S}_k + \mathbf{S}_k \cdot \mathbf{S}_l + \mathbf{S}_l \cdot \mathbf{S}_i) \\ & + \frac{20t^4}{U^3} (\mathbf{S}_i \cdot \mathbf{S}_k + \mathbf{S}_j \cdot \mathbf{S}_l) \\ & - \left(\frac{2t^4}{UU_c^2} + \frac{2t^4}{U_c^3} \right) (\mathbf{S}_j \cdot \mathbf{S}_k + \mathbf{S}_k \cdot \mathbf{S}_l + \mathbf{S}_j \cdot \mathbf{S}_l) \Bigg] + \ldots \qquad \text{(D.25)} \end{aligned}$$

Adding all contributions from all categories, we obtain

$$\begin{aligned} \bar{H}_{\text{eff}}^{(4)} = H_0 + \sum_i p_i p_i^\dagger \Bigg\{ & \sum_j \left(\frac{16t^4}{U^3} - \frac{4t^2}{U} \right) \mathbf{S}_i \cdot \mathbf{S}_j + \sum_{j \neq k} \Bigg(\frac{4t^4}{UU_c^2} + \frac{8t^4}{U_c^2(2U_c + U)} \\ & - \frac{4t^4}{U^3} \Bigg) \mathbf{S}_j \cdot \mathbf{S}_k + \sum_{\text{squares}} \Bigg[\frac{24t^4}{U^3} (\mathbf{S}_i \cdot \mathbf{S}_j + \mathbf{S}_j \cdot \mathbf{S}_k + \mathbf{S}_k \cdot \mathbf{S}_l + \mathbf{S}_l \cdot \mathbf{S}_i) \\ & + \frac{20t^4}{U^3} (\mathbf{S}_i \cdot \mathbf{S}_k + \mathbf{S}_j \cdot \mathbf{S}_l) - \left(\frac{2t^4}{UU_c^2} + \frac{2t^4}{U_c^3} \right) (\mathbf{S}_j \cdot \mathbf{S}_k + \mathbf{S}_k \cdot \mathbf{S}_l \\ & + \mathbf{S}_j \cdot \mathbf{S}_l) \Bigg] \Bigg\} . \qquad \text{(D.26)} \end{aligned}$$

The sums between the curly brackets are, respectively, over all nearest neighbors j of i, over all pairs of nearest neighbors j,k of i, and over all squares of 2×2 sites containing i. Grouping the different neighbor interactions, we finally get Eq. (4.75).

D.2 Scattering amplitude to fourth order in t/U

Once the intermediate state Hamiltonian is obtained to fourth order in t/U, it is straightforward and tedious to derive the RIXS scattering amplitude to this order. Below, we go through this expression term by term, where each term groups the interactions between certain neighbors.

The nearest neighbors term gives

$$\begin{aligned}\sum_i e^{i\mathbf{q}\cdot\mathbf{R}_i}\sum_j^{\mathrm{nn}}\mathbf{S}_i\cdot\mathbf{S}_j\left|0\right\rangle = \sum_{\mathbf{k}} & \left[-\left(1+\gamma_{\mathbf{q}}\right)\left(U_{\mathbf{k}-\mathbf{q}}V_{\mathbf{k}}+U_{\mathbf{k}}V_{\mathbf{k}-\mathbf{q}}\right)\right.\\ & \left.+\left(\gamma_{\mathbf{k}-\mathbf{q}}+\gamma_{\mathbf{k}}\right)\left(U_{\mathbf{k}-\mathbf{q}}U_{\mathbf{k}}+V_{\mathbf{k}-\mathbf{q}}V_{\mathbf{k}}\right)\right]\alpha^{\dagger}_{\mathbf{k}}\alpha^{\dagger}_{-\mathbf{k}+\mathbf{q}}\left|0\right\rangle \end{aligned} \tag{D.27}$$

as before.

For the next nearest neighbor term, we find

$$\sum_i e^{i\mathbf{q}\cdot\mathbf{R}_i}\sum_j^{\mathrm{nnn}}\mathbf{S}_i\cdot\mathbf{S}_j\left|0\right\rangle = -\sum_{\mathbf{k}} f_{\mathrm{nnn}}(\mathbf{k},\mathbf{q})\left(U_{\mathbf{k}-\mathbf{q}}V_{\mathbf{k}}+U_{\mathbf{k}}V_{\mathbf{k}-\mathbf{q}}\right)\alpha^{\dagger}_{\mathbf{k}}\alpha^{\dagger}_{-\mathbf{k}+\mathbf{q}}\left|0\right\rangle . \tag{D.28}$$

where

$$f_{\mathrm{nnn}}(\mathbf{k},\mathbf{q}) = \cos(k_x-q_x)\cos(k_y-q_y)+\cos k_x\cos k_y-1-\cos q_x\cos q_y. \tag{D.29}$$

The next term (with $j\neq k$ nearest neighbors of i) is

$$\sum_i e^{i\mathbf{q}\cdot\mathbf{R}_i}\sum_{j\neq k}\mathbf{S}_j\cdot\mathbf{S}_k\left|0\right\rangle = -\sum_{\mathbf{k}} f_a(\mathbf{k},\mathbf{q})(U_{\mathbf{k}}V_{\mathbf{k}-\mathbf{q}}+U_{\mathbf{k}-\mathbf{q}}V_{\mathbf{k}})\alpha^{\dagger}_{\mathbf{k}}\alpha^{\dagger}_{-\mathbf{k}+\mathbf{q}}\left|0\right\rangle , \tag{D.30}$$

with

$$\begin{aligned} f_a(\mathbf{k},\mathbf{q}) = f_a(-\mathbf{k}-\mathbf{q},\mathbf{q}) = 2\gamma_{2\mathbf{k}-\mathbf{q}}-6\gamma_{\mathbf{q}}+2\cos k_x\cos(k_y-q_y)\\ +2\cos k_y\cos(k_x-q_x). \end{aligned} \tag{D.31}$$

In the sum over squares, we have for the $\mathbf{S}_j\cdot\mathbf{S}_l$ term in the square sum:

$$\sum_i e^{i\mathbf{q}\cdot\mathbf{R}_i}\sum_{\delta,\delta'}\mathbf{S}_{i+\delta}\cdot\mathbf{S}_{i+\delta'}\left|0\right\rangle = -\sum_{\mathbf{k}}(U_{\mathbf{k}}V_{\mathbf{k}-\mathbf{q}}+U_{\mathbf{k}-\mathbf{q}}V_{\mathbf{k}})f_b(\mathbf{k},\mathbf{q})\alpha^{\dagger}_{\mathbf{k}}\alpha^{\dagger}_{-\mathbf{k}+\mathbf{q}}\left|0\right\rangle \tag{D.32}$$

where the sum over δ, δ' is over the 4 pairs of orthogonal vectors that point to nearest neighbors of site i (they indicate $\mathbf{S}_j$ and $\mathbf{S}_l$), and

$$f_b(\mathbf{k},\mathbf{q}) = 2\left[-2\gamma_{\mathbf{q}} + \cos k_x \cos(k_y - q_y) + \cos k_y \cos(k_x - q_x)\right]. \tag{D.33}$$

For the square terms $\mathbf{S}_j \cdot \mathbf{S}_k + \mathbf{S}_k \cdot \mathbf{S}_l$ we find

$$\begin{aligned}\sum_{i,j,k} e^{i\mathbf{q}\cdot\mathbf{R}_i} \mathbf{S}_j \cdot \mathbf{S}_k \left|0\right\rangle = \sum_{\mathbf{k}} \Big(& -(U_{\mathbf{k}-\mathbf{q}} V_{\mathbf{k}} + U_{\mathbf{k}} V_{\mathbf{k}-\mathbf{q}}) f_{c1}(\mathbf{q}) \\ & + (U_{\mathbf{k}} U_{\mathbf{k}-\mathbf{q}} + V_{\mathbf{k}} V_{\mathbf{k}-\mathbf{q}}) f_{c2}(\mathbf{k},\mathbf{q}) \Big) \alpha^\dagger_{\mathbf{k}} \alpha^\dagger_{-\mathbf{k}+\mathbf{q}} \left|0\right\rangle \end{aligned} \tag{D.34}$$

with j pointing to nearest neighbors of i, k to next nearest neighbors of i that are also nearest neighbors of j, and

$$\begin{aligned} f_{c1}(\mathbf{q}) &= 2\gamma_{\mathbf{q}} + 2\cos q_x \cos q_y, && \text{(D.35)} \\ f_{c2}(\mathbf{k},\mathbf{q}) &= \cos k_x \cos q_y + \cos k_y \cos q_x \\ &\quad + \cos(k_x - q_x)\cos q_y + \cos(k_y - q_y)\cos q_x. && \text{(D.36)} \end{aligned}$$

Putting all parts together, we obtain the total scattering amplitude (4.77).

BIBLIOGRAPHY

[1] K. Ishii, S. Ishihara, Y. Murakami, K. Ikeuchi, K. Kuzushita, T. Inami, K. Ohwada, M. Yoshida, I. Jarrige, N. Tatami, S. Niioka, D. Bizen, Y. Ando, J. Mizuki, S. Maekawa, and Y. Endoh, arXiv:1008.0682 (2010).

[2] A. Kotani and S. Shin, Rev. Mod. Phys. **73**, 203 (2001).

[3] L. J. P. Ament, M. van Veenendaal, T. P. Devereaux, J. P. Hill, and J. van den Brink, arXiv:1009.3630 (2010), submitted to Rev. Mod. Phys.

[4] G. Chabot-Couture, J. N. Hancock, P. K. Mang, D. M. Casa, T. Gog, and M. Greven, Phys. Rev. B **82**, 035113 (2010).

[5] Y.-J. Kim, J. P. Hill, S. Wakimoto, R. J. Birgeneau, F. C. Chou, N. Motoyama, K. M. Kojima, S. Uchida, D. Casa, and T. Gog, Phys. Rev. B **76**, 155116 (2007).

[6] F. de Groot and A. Kotani, *Core Level Spectroscopy of Solids* (CRC Press, 2008).

[7] K. Ichikawa, K. Jouda, S. Tanaka, K. Soda, M. Matsumoto, Y. Taguchi, T. Katsumi, O. Aita, H. Maezawa, Y. Azuma, and H. Kitazawa, J. Electron Spectr. Rel. Phenom. **78**, 183 (1996).

[8] L.-C. Duda, J. Nordgren, G. Dräger, S. Bocharov, and T. Kirchner, J. Electron Spectr. Rel. Phenom. **110-111**, 275 (2000).

[9] G. Ghiringhelli, N. B. Brookes, E. Annese, H. Berger, C. Dallera, M. Grioni, L. Perfetti, A. Tagliaferri, and L. Braicovich, Phys. Rev. Lett. **92**, 117406 (2004).

[10] L. Braicovich, L. J. P. Ament, V. Bisogni, F. Forte, C. Aruta, G. Balestrino, N. B. Brookes, G. M. De Luca, P. G. Medaglia, F. Miletto Granozio, M. Radovic, M. Salluzzo, J. van den Brink, and G. Ghiringhelli, Phys. Rev. Lett. **102**, 167401 (2009).

[11] L. Braicovich, J. van den Brink, V. Bisogni, M. Moretti Sala, L. J. P. Ament, N. B. Brookes, G. M. De Luca, M. Salluzzo, T. Schmitt, V. N. Strocov, and G. Ghiringhelli, Phys. Rev. Lett. **104**, 077002 (2010).

[12] S. E. Schnatterly, Solid State Phys. **34**, 275 (1979).

[13] R. Schuster, S. Pyon, M. Knupfer, J. Fink, M. Azuma, M. Takano, H. Takagi, and B. Büchner, Phys. Rev. B **79**, 214517 (2009).

[14] J. P. Hill, G. Blumberg, Y.-J. Kim, D. S. Ellis, S. Wakimoto, R. J. Birgeneau, S. Komiya, Y. Ando, B. Liang, R. L. Greene, D. Casa, and T. Gog, Phys. Rev. Lett. **100**, 097001 (2008).

[15] B. Freelon, P. G. Medaglia, A. Tebano, G. Balestrino, K. Okada, A. Kotani, F. Vernay, T. P. Devereaux, P. A. Glans, T. Learmonth, K. E. Smith, A. L. D. Kilcoyne, B. Rude, I. Furtado, and J.-H. Guo, arXiv:0806.4432 (2008).

[16] H. Yavaş, private communication (2008).

[17] J. Als-Nielsen and D. McMorrow, *Elements of modern X-ray physics* (Wiley, 2001).

[18] P. Debye, Ann. d. Phys. **348**, 49 (1913).

[19] L. J. P. Ament, G. Ghiringhelli, M. Moretti Sala, L. Braicovich, and J. van den Brink, Phys. Rev. Lett. **103**, 117003 (2009).

[20] M. Moretti Sala, V. Bisogni, L. Braicovich, C. Aruta, G. Balestrino, H. Berger, N. B. Brookes, G. De Luca, D. Di Castro, M. Grioni, M. Guarise, P. G. Medaglia, F. Miletto Granozio, M. Minola, M. Radovic, M. Salluzzo, T. Schmitt, and G. Ghiringhelli, arXiv:1009.4882 (2010).

[21] L. Braicovich, M. Moretti Sala, L. J. P. Ament, V. Bisogni, M. Minola, G. Balestrino, D. Di Castro, G. M. De Luca, M. Salluzzo, G. Ghiringhelli, and J. van den Brink, Phys. Rev. B **81**, 174533 (2010).

[22] J. Zaanen, G. A. Sawatzky, and J. W. Allen, Phys. Rev. Lett. **55**, 418 (1985).

[23] C. Castelnovo, R. Moessner, and S. L. Sondhi, Nature **451**, 42 (2008).

[24] K. I. Kugel and D. I. Khomskii, Sov. Phys. Usp. **25**, 231 (1982).

[25] J. Kanamori, Prog. Theor. Phys. **17**, 177 & 197 (1957).

[26] J. Luo, G. T. Trammell, and J. P. Hannon, Phys. Rev. Lett. **71**, 287 (1993).

[27] L. L. Foldy and S. A. Wouthuysen, Phys. Rev. **78**, 29 (1950).

[28] M. E. Peskin and D. V. Schroeder, *An Introduction to Quantum Field Theory* (Addison-Wesley Publishing Co., 1996).

[29] A. Messiah, *Quantum mechanics, vol. 2* (North Holland Publishing Company, Amsterdam, 1962).

[30] Y. B. Zeldovich and V. S. Popov, Sov. Phys. Usp. **14**, 673 (1972).

[31] J. Arthur *et al.*, LCLS Conceptual Design Report, 2002.

[32] J. J. Sakurai, *Advanced Quantum Mechanics* (Addison Wesley, 1967).

[33] M. Blume, J. Appl. Phys. **57**, 3615 (1985).

[34] W. Schülke, *Electron Dynamics by Inelastic X-Ray Scattering* (Oxford University Press, Oxford, 2007).

[35] F. A. Blum, Phys. Rev. B **1**, 1125 (1970).

[36] G. A. Mourou, T. Tajima, and S. V. Bulanov, Rev. Mod. Phys. **78**, 309 (2006).

[37] J. P. Hill, private communication (2009).

[38] P. M. Platzman and E. D. Isaacs, Phys. Rev. B **57**, 11107 (1998).

[39] J.-P. Rueff and A. Shukla, Rev. Mod. Phys. **82**, 847 (2010).

[40] J. J. Sakurai, *Modern Quantum Mechanics, revised edition* (Addison Wesley, 1994).

[41] H. A. Kramers and W. Heisenberg, Z. Phys. **31**, 681 (1925).

[42] M. V. Klein, *Light scattering in Solids I* (Springer-Verlag, Berlin, 1983), Vol. 8, p. 147.

[43] G. Döring, C. Sternemann, A. Kaprolat, A. Mattila, K. Hämäläinen, and W. Schülke, Phys. Rev. B **70**, 085115 (2004).

[44] P. Abbamonte, C. A. Burns, E. D. Isaacs, P. M. Platzman, L. L. Miller, S. W. Cheong, and M. V. Klein, Phys. Rev. Lett. **83**, 860 (1999).

[45] T. Nomura and J. Igarashi, J. Phys. Soc. Jpn. **73**, 1677 (2004).

[46] T. Nomura and J.-I. Igarashi, Phys. Rev. B **71**, 035110 (2005).

[47] R. S. Markiewicz and A. Bansil, Phys. Rev. Lett. **96**, 107005 (2006).

[48] J. van den Brink and M. van Veenendaal, J. Phys. Chem. Solids **66**, 2145 (2005).

[49] J. Van den Brink and M. van Veenendaal, Europhys. Lett. **73**, 121 (2006).

[50] L. J. P. Ament, F. Forte, and J. van den Brink, Phys. Rev. B **75**, 115118 (2007).

[51] J. van den Brink, Europhys. Lett. **80**, 47003 (2007).

[52] F. Forte, L. J. P. Ament, and J. van den Brink, Phys. Rev. B **77**, 134428 (2008).

[53] D. S. Ellis, J. Kim, J. P. Hill, S. Wakimoto, R. J. Birgeneau, Y. Shvyd'ko, D. Casa, T. Gog, K. Ishii, K. Ikeuchi, A. Paramekanti, and Y.-J. Kim, Phys. Rev. B **81**, 085124 (2010).

[54] F. Forte, L. J. P. Ament, and J. van den Brink, Phys. Rev. Lett. **101**, 106406 (2008).

[55] P. M. Platzman and N. Tzoar, Phys. Rev. **182**, 510 (1969).

[56] T. Tohyama, H. Onodera, K. Tsutsui, and S. Maekawa, Phys. Rev. Lett. **89**, 257405 (2002).

[57] K. Tsutsui, T. Tohyama, and S. Maekawa, Phys. Rev. Lett. **91**, 117001 (2003).

[58] M. van Veenendaal, P. Carra, and B. T. Thole, Phys. Rev. B **54**, 16010 (1996).

[59] O. Gunnarsson and K. Schönhammer, Phys. Rev. B **28**, 4315 (1983).

[60] A. Kotani, H. Mizuta, T. Jo, and J. C. Parlebas, Solid State Comm. **53**, 805 (1985).

[61] J. Zaanen, C. Westra, and G. A. Sawatzky, Phys. Rev. B **33**, 8060 (1986).

[62] G. D. Mahan, *Many-particle physics, 3rd ed.* (Kluwer Academic/Plenum Publishers, 2000).

[63] T. P. Devereaux, G. E. D. McCormack, and J. K. Freericks, Phys. Rev. Lett. **90**, 067402 (2003).

[64] T. P. Devereaux, G. E. D. McCormack, and J. K. Freericks, Phys. Rev. B **68**, 075105 (2003).

[65] H. Kondo, S. Ishihara, and S. Maekawa, Phys. Rev. B **64**, 014414 (2001).

[66] S. Ishihara and S. Maekawa, Phys. Rev. B **62**, 2338 (2000).

[67] J. Kim, D. S. Ellis, H. Zhang, Y.-J. Kim, J. P. Hill, F. C. Chou, T. Gog, and D. Casa, Phys. Rev. B **79**, 094525 (2009).

[68] G. Shirane, S. M. Shapiro, and J. M. Tranquada, *Neutron scattering with a Triple-axis spectrometer* (Cambridge University Press, Cambridge, 2002).

[69] M. Guarise, B. Dalla Piazza, M. Moretti Sala, G. Ghiringhelli, L. Braicovich, H. Berger, J. N. Hancock, D. van der Marel, T. Schmitt, V. N. Strocov, L. J. P. Ament, J. van den Brink, P.-H. Lin, P. Xu, H. M. Rønnow, and M. Grioni, arXiv:1004.2441, Phys. Rev. Lett., in press (2010).

[70] V. Bisogni, Ph.D. thesis, Politecnico di Milano, 2010.

[71] Y. Harada, K. Okada, R. Eguchi, A. Kotani, H. Takagi, T. Takeuchi, and S. Shin, Phys. Rev. B **66**, 165104 (2002).

[72] F. M. F. De Groot, P. Kuiper, and G. A. Sawatzky, Phys. Rev. B **57**, 14584 (1998).

[73] M. Van Veenendaal, Phys. Rev. Lett. **96**, 117404 (2006).

[74] M. W. Haverkort, arXiv:0911.0706 (2009).

[75] P. W. Anderson, Phys. Rev. **86**, 694 (1952).

[76] P. W. Anderson, Phys. Rev. **115**, 2 (1959).

[77] T. Thio, T. R. Thurston, N. W. Preyer, P. J. Picone, M. A. Kastner, H. P. Jenssen, D. R. Gabbe, C. Y. Chen, R. J. Birgeneau, and A. Aharony, Phys. Rev. B **38**, 905 (1988).

[78] M. A. Kastner, R. J. Birgeneau, G. Shirane, and Y. Endoh, Rev. Mod. Phys. **70**, 897 (1998).

[79] T. Holstein and H. Primakoff, Phys. Rev. **58**, 1098 (1940).

[80] A. Klein and E. R. Marshalek, Rev. Mod. Phys. **63**, 375 (1991).

[81] E. R. Marshalek, Nucl. Phys. A **161**, 401 (1971).

[82] M. Takahashi, J. Phys. C **10**, 1289 (1977).

[83] R. Coldea, S. M. Hayden, G. Aeppli, T. G. Perring, C. D. Frost, T. E. Mason, S.-W. Cheong, and Z. Fisk, Phys. Rev. Lett. **86**, 5377 (2001).

[84] C. T. Chen, L. H. Tjeng, J. Kwo, H. L. Kao, P. Rudolf, F. Sette, and R. M. Fleming, Phys. Rev. Lett. **68**, 2543 (1992).

[85] M. Z. Hasan, E. D. Isaacs, Z.-X. Shen, L. L. Miller, K. Tsutsui, T. Tohyama, and S. Maekawa, Science **288**, 1811 (2000).

[86] Y.-J. Kim, J. P. Hill, C. A. Burns, S. Wakimoto, R. J. Birgeneau, D. Casa, T. Gog, and C. T. Venkataraman, Phys. Rev. Lett. **89**, 177003 (2002).

[87] J. P. Hill, C.-C. Kao, W. A. L. Caliebe, M. Matsubara, A. Kotani, J. L. Peng, and R. L. Greene, Phys. Rev. Lett. **80**, 4967 (1998).

[88] E. D. Isaacs, P. M. Platzman, P. Metcalf, and J. M. Honig, Phys. Rev. Lett. **76**, 4211 (1996).

[89] C.-C. Kao, W. A. L. Caliebe, J. B. Hastings, and J.-M. Gillet, Phys. Rev. B **54**, 16361 (1996).

[90] T. Inami, T. Fukuda, J. Mizuki, S. Ishihara, H. Kondo, H. Nakao, T. Matsumura, K. Hirota, Y. Murakami, S. Maekawa, and E. Y., Phys. Rev. B **67**, 045108 (2003).

[91] G. Döring, C. Sternemann, A. Kaprolat, A. Mattila, K. Hämäläinen, and W. Schülke, Phys. Rev. B **70**, 085115 (2004).

[92] S. Suga, S. Imada, A. Higashiya, A. Shigemoto, S. Kasai, M. Sing, H. Fujiwara, A. Sekiyama, A. Yamasaki, C. Kim, T. Nomura, J. Igarashi, M. Yabashi, and T. Ishikawa, Phys. Rev. B **72**, 081101(R) (2005).

[93] S. Wakimoto, Y.-J. Kim, H. Kim, H. Zhang, T. Gog, and R. J. Birgeneau, Phys. Rev. B **72**, 224508 (2005).

[94] E. Collart, A. Shukla, J. P. Rueff, P. Leininger, H. Ishii, I. Jarrige, Y. Q. Cai, S.-W. Cheong, and G. Dhalenne, Phys. Rev. Lett. **96**, 157004 (2006).

[95] J. W. Seo, K. Yang, D. W. Lee, Y. S. Roh, J. H. Kim, H. Eisaki, H. Ishii, I. Jarrige, Y. Q. Cai, D. L. Feng, and C. Kim, Phys. Rev. B **73**, 161104(R) (2006).

[96] T. Nagao and J. Igarashi, Phys. Rev. B **75**, 214414 (2007).

[97] F. Barriquand and G. A. Sawatzky, Phys. Rev. B **50**, 16649 (1994).

[98] K. Okada and A. Kotani, J. Phys. Soc. Jpn. **75**, 044702 (2006).

[99] K. Tsutsui, T. Tohyama, and S. Maekawa, Phys. Rev. Lett. **83**, 3705 (1999).

[100] M. O. Krause and J. H. Oliver, J. Phys. Chem. Ref. Data **8**, 329 (1979).

[101] K. Hämäläinen, S. Manninen, P. Suortti, S. P. Collins, M. J. Cooper, and D. Laundy, J. Phys.: Condens. Matter **1**, 5955 (2010).

[102] Q. Shen, I. S. Elfimov, P. Fanwick, Y. Tokura, T. Kimura, K. Finkelstein, R. Colella, and G. A. Sawatzky, Phys. Rev. Lett. **96**, 246405 (2006).

[103] I. S. Elfimov, N. A. Skorikov, V. I. Anisimov, and G. A. Sawatzky, Phys. Rev. Lett. **88**, 015504 (2002).

[104] T. Oguchi, Phys. Rev. **117**, 117 (1960).

[105] J. P. Hill, private communication (2008).

[106] P. A. Fleury and R. Loudon, Phys. Rev. **166**, 514 (1968).

[107] R. J. Elliott and R. Loudon, Phys. Lett. **3**, 189 (1963).

[108] T. P. Devereaux and R. Hackl, Rev. Mod. Phys. **79**, 175 (2007).

[109] B. S. Shastry and B. I. Shraiman, Int. J. Mod. Phys. B **5**, 365 (1991).

[110] P. Kuiper, J.-H. Guo, C. Såthe, L.-C. Duda, J. Nordgren, J. J. M. Pothuizen, F. M. F. de Groot, and G. A. Sawatzky, Phys. Rev. Lett. **80**, 5204 (1998).

[111] S. G. Chiuzbăian, G. Ghiringhelli, C. Dallera, M. Grioni, P. Amann, X. Wang, L. Braicovich, and L. Patthey, Phys. Rev. Lett. **95**, 197402 (2005).

[112] G. Ghiringhelli, A. Piazzalunga, C. Dallera, T. Schmitt, V. N. Strocov, J. Schlappa, L. Patthey, X. Wang, H. Berger, and M. Grioni, Phys. Rev. Lett. **102**, 027401 (2009).

[113] D. Vaknin, S. K. Sinha, D. E. Moncton, D. C. Johnston, J. M. Newsam, C. R. Safinya, and H. E. King, Phys. Rev. Lett. **58**, 2802 (1987).

[114] D. Vaknin, E. Caignol, P. K. Davies, J. E. Fischer, D. C. Johnston, and D. P. Goshorn, Phys. Rev. B **39**, 9122 (1989).

[115] S. Skanthakumar, H. Zhang, T. W. Clinton, W.-H. Li, J. W. Lynn, Z. Fisk, and S.-W. Cheong, Physica C **160**, 124 (1989).

[116] M. van Veenendaal, private communication (2009).

[117] X. Wan, T. A. Maier, and S. Y. Savrasov, Phys. Rev. B **79**, 155114 (2009).

[118] V. Bisogni, L. J. P. Ament, C. Aruta, G. Balestrino, N. B. Brookes, F. Forte, G. Ghiringhelli, P. G. Medaglia, J. van den Brink, and L. Braicovich, Eur. Phys. J. Special Topics **169**, 141 (2009).

[119] T. Kato, Progress of Theoretical Physics **4**, 514 (1949).

[120] S. Sugai, H. Suzuki, Y. Takayanagi, T. Hosokawa, and N. Hayamizu, Phys. Rev. B **68**, 184504 (2003).

[121] K. M. Shen, F. Ronning, D. H. Lu, W. S. Lee, N. J. C. Ingle, W. Meevasana, F. Baumberger, A. Damascelli, N. P. Armitage, L. L. Miller, Y. Kohsaka, M. Azuma, M. Takano, H. Takagi, and Z.-X. Shen, Phys. Rev. Lett. **93**, 267002 (2004).

[122] A. Damascelli, Z. Hussain, and Z.-X. Shen, Rev. Mod. Phys. **75**, 473 (2003).

[123] S. Schmitt-Rink, C. M. Varma, and A. E. Ruckenstein, Phys. Rev. Lett. **60**, 2793 (1988).

[124] C. L. Kane, P. A. Lee, and N. Read, Phys. Rev. B **39**, 6880 (1989).

[125] O. P. Sushkov, Solid State Comm. **83**, 303 (1992).

[126] G. Khaliullin and P. Horsch, Physica C **282-287**, 1751 (1997).

[127] T. Tohyama, P. Horsch, and S. Maekawa, Phys. Rev. Lett. **74**, 980 (1995).

[128] G. Khaliullin and P. Horsch, Phys. Rev. B **54**, R9600 (1996).

[129] R. Eder, Y. Ohta, and S. Maekawa, Phys. Rev. Lett. **74**, 5124 (1995).

[130] C. M. Canali and S. M. Girvin, Phys. Rev. B **45**, 7127 (1992).

[131] L. Braicovich, private communication (2010).

[132] G. Ghiringhelli, private communication (2010).

[133] P. A. Lee, N. Nagaosa, and X.-G. Wen, Rev. Mod. Phys. **78**, 17 (2006).

[134] E. Dagotto, Rev. Mod. Phys. **66**, 763 (1994).

[135] B. I. Shraiman and E. D. Siggia, Phys. Rev. Lett. **61**, 467 (1988).

[136] O. P. Sushkov, Phys. Rev. B **49**, 1250 (1994).

[137] V. I. Belinicher, A. L. Chernyshev, A. V. Dotsenko, and O. P. Sushkov, Phys. Rev. B **51**, 6076 (1995).

[138] O. P. Sushkov, Phys. Rev. B **54**, 9988 (1996).

[139] D. N. Sheng, Y. C. Chen, and Z. Y. Weng, Phys. Rev. Lett. **77**, 5102 (1996).

[140] J. van den Brink and O. P. Sushkov, Phys. Rev. B **57**, 3518 (1998).

[141] Z.-H. Dong and S.-W. Gu, Phys. Rev. B **63**, 224501 (2001).

[142] B. O. Wells, Z. X. Shen, A. Matsuura, D. M. King, M. A. Kastner, M. Greven, and R. J. Birgeneau, Phys. Rev. Lett. **74**, 964 (1995).

[143] J. J. M. Pothuizen, R. Eder, N. T. Hien, M. Matoba, A. A. Menovsky, and G. A. Sawatzky, Phys. Rev. Lett. **78**, 717 (1997).

[144] F. Ronning, C. Kim, D. L. Feng, D. S. Marshall, A. G. Loeser, L. L. Miller, J. N. Eckstein, I. Bozovic, and Z.-X. Shen, Science **282**, 2067 (1998).

[145] N. P. Armitage, D. H. Lu, C. Kim, A. Damascelli, K. M. Shen, F. Ronning, D. L. Feng, P. Bogdanov, Z.-X. Shen, Y. Onose, Y. Taguchi, Y. Tokura, P. K. Mang, N. Kaneko, and M. Greven, Phys. Rev. Lett. **87**, 147003 (2001).

[146] C. Kim, F. Ronning, A. Damascelli, D. L. Feng, Z.-X. Shen, B. O. Wells, Y. J. Kim, R. J. Birgeneau, M. A. Kastner, L. L. Miller, H. Eisaki, and S. Uchida, Phys. Rev. B **65**, 174516 (2002).

[147] F. Ronning, T. Sasagawa, Y. Kohsaka, K. M. Shen, A. Damascelli, C. Kim, T. Yoshida, N. P. Armitage, D. H. Lu, D. L. Feng, L. L. Miller, H. Takagi, and Z.-X. Shen, Phys. Rev. B **67**, 165101 (2003).

[148] K. M. Shen, F. Ronning, D. H. Lu, F. Baumberger, N. J. C. Ingle, W. S. Lee, W. Meevasana, Y. Kohsaka, M. Azuma, M. Takano, H. Takagi, and Z.-X. Shen, Science **307**, 901 (2005).

[149] K. Tanaka, W. S. Lee, D. H. Lu, A. Fujimori, T. Fujii, Risdiana, I. Terasaki, D. J. Scalapino, T. P. Devereaux, Z. Hussain, and Z.-X. Shen, Science **314**, 1910 (2006).

[150] K. M. Shen, F. Ronning, W. Meevasana, D. H. Lu, N. J. C. Ingle, F. Baumberger, W. S. Lee, L. L. Miller, Y. Kohsaka, M. Azuma, M. Takano, H. Takagi, and Z.-X. Shen, Phys. Rev. B **75**, 075115 (2007).

[151] A. Nazarenko, K. J. E. Vos, S. Haas, E. Dagotto, and R. J. Gooding, Phys. Rev. B **51**, 8676 (1995).

[152] J. Bała, A. M. Oleś, and J. Zaanen, Phys. Rev. B **52**, 4597 (1995).

[153] O. P. Sushkov, G. A. Sawatzky, R. Eder, and H. Eskes, Phys. Rev. B **56**, 11769 (1997).

[154] A. S. Mishchenko and N. Nagaosa, Phys. Rev. Lett. **93**, 036402 (2004).

[155] V. Cataudella, G. De Filippis, A. S. Mishchenko, and N. Nagaosa, Phys. Rev. Lett. **99**, 226402 (2007).

[156] C. Kim, P. J. White, Z.-X. Shen, T. Tohyama, Y. Shibata, S. Maekawa, B. O. Wells, Y. J. Kim, R. J. Birgeneau, and M. A. Kastner, Phys. Rev. Lett. **80**, 4245 (1998).

[157] M. Haverkort, Ph.D. thesis, Universität zu Köln, 2005.

[158] H. A. Jahn and E. Teller, Proc. R. Soc. Lond. A **161**, 220 (1937).

[159] G. A. Gehring and K. A. Gehring, Rep. Prog. Phys. **38**, 1 (1975).

[160] G. Khaliullin, Prog. Theor. Phys. Suppl. **160**, 155 (2005).

[161] J. van den Brink, G. Khaliullin, and D. Khomskii, in *Orbital effects in manganites*, *Colossal Magnetoresistive Manganites* (Kluwer Academic Publishers, Dordrecht, 2004), Chap. 6, p. 263.

[162] Y. Tokura and N. Nagaosa, Science **288**, 462 (2000).

[163] E. Saitoh, S. Okamoto, K. T. Takahashi, K. Tobe, K. Yamamoto, T. Kimura, S. Ishihara, S. Maekawa, and Y. Tokura, Nature **410**, 180 (2001).

[164] D. Polli, M. Rini, S. Wall, R. W. Schoenlein, Y. Tomioka, Y. Tokura, G. Cerullo, and A. A. Cavalleri, Nature Materials **6**, 643 (2007).

[165] M. Grüninger, R. Rückamp, M. Windt, P. Reutler, C. Zobel, T. Lorenz, A. Freimuth, and A. Revcolevschi, Nature **418**, 39 (2002).

[166] E. Saitoh, S. Okamoto, K. Tobe, K. Yamamoto, T. Kimura, S. Ishihara, S. Maekawa, and Y. Tokura, Nature **418**, 40 (2002).

[167] J. B. Goodenough, *Magnetism and the chemical bond* (John Wiley & Sons, 1963).

[168] P. B. Allen and V. Perebeinos, Phys. Rev. Lett. **83**, 4828 (1999).

[169] J. van den Brink, Phys. Rev. Lett. **87**, 217202 (2001).

[170] K. P. Schmidt, M. Grüninger, and G. S. Uhrig, Phys. Rev. B **76**, 075108 (2007).

[171] J. Rodríguez-Carvajal, M. Hennion, F. Moussa, A. H. Moudden, L. Pinsard, and A. Revcolevschi, Phys. Rev. B **57**, 3189(R) (1998).

[172] M. Imada, A. Fujimori, and Y. Tokura, Rev. Mod. Phys. **70**, 1039 (2000).

[173] J. B. Goodenough, Phys. Rev. **100**, 564 (1955).

[174] J. van den Brink, G. Khaliullin, and D. I. Khomskii, in *Colossal Magnetoresistive Manganites*, edited by T. Chatterji (Kluwer Academic Publishers, 2004).

[175] J. van den Brink, P. Horsch, F. Mack, and A. M. Oleś, Phys. Rev. B **59**, 6795 (1999).

[176] H. Yavaş and E. Alp, Private communication, 2008.

[177] S. Ishihara, Y. Murakami, T. Inami, K. Ishii, J. Mizuki, K. Hirota, S. Maekawa, and Y. Endoh, New J. Phys. **7**, 119 (2005).

[178] M. B. Salamon and M. Jaime, Rev. Mod. Phys. **73**, 583 (2001).

[179] P. Horsch, J. Jaklič, and F. Mack, Phys. Rev. B **59**, 6217 (1999).

[180] J. van den Brink, New J. Phys. **6**, 201 (2004).

[181] S. Ishihara and S. Maekawa, Phys. Rev. Lett. **80**, 3799 (1998).

[182] J. van den Brink, P. Horsch, and A. M. Oleś, Phys. Rev. Lett. **85**, 5174 (2000).

[183] J. van den Brink, W. Stekelenburg, D. I. Khomskii, G. A. Sawatzky, and K. I. Kugel, Phys. Rev. B **58**, 10276 (1998).

[184] G. Khaliullin and S. Okamoto, Phys. Rev. Lett. **89**, 167201 (2002).

[185] G. Khaliullin and S. Okamoto, Phys. Rev. B **68**, 205109 (2003).

[186] B. Keimer, D. Casa, A. Ivanov, J. W. Lynn, M. V. Zimmermann, J. P. Hill, D. Gibbs, Y. Taguchi, and Y. Tokura, Phys. Rev. Lett. **85**, 3946 (2000).

[187] G. Khaliullin and S. Maekawa, Phys. Rev. Lett. **85**, 3950 (2000).

[188] J.-G. Cheng, Y. Sui, J.-S. Zhou, J. B. Goodenough, and W. H. Su, Phys. Rev. Lett. **101**, 087205 (2008).

[189] M. Mochizuki and M. Imada, Phys. Rev. Lett. **91**, 167203 (2003).

[190] E. Pavarini, S. Biermann, A. Poteryaev, A. I. Lichtenstein, A. Georges, and O. K. Andersen, Phys. Rev. Lett. **92**, 176403 (2004).

[191] E. Pavarini, A. Yamasaki, J. Nuss, and O. K. Andersen, New J. Phys. **7**, 188 (2005).

[192] M. Cwik, T. Lorenz, J. Baier, R. Müller, G. André, F. Bourée, F. Lichtenberg, A. Freimuth, R. Schmitz, E. Müller-Hartmann, and M. Braden, Phys. Rev. B **68**, 060401(R) (2003).

[193] R. Schmitz, O. Entin-Wohlman, A. Aharony, A. B. Harris, and E. Müller-Hartmann, Phys. Rev. B **71**, 144412 (2005).

[194] M. W. Haverkort, Z. Hu, A. Tanaka, G. Ghiringhelli, H. Roth, M. Cwik, T. Lorenz, C. Schüßler-Langeheine, S. V. Streltsov, A. S. Mylnikova, V. I. Anisimov, C. de Nadai, N. B. Brookes, H. H. Hsieh, H.-J. Lin, C. T. Chen, T. Mizokawa, Y. Taguchi, Y. Tokura, D. I. Khomskii, and L. H. Tjeng, Phys. Rev. Lett. **94**, 056401 (2005).

[195] I. V. Solovyev, Phys. Rev. B **74**, 054412 (2006).

[196] J. Akimitsu, H. Ichikawa, N. Eguchi, T. Miyano, M. Nishi, and K. Kakurai, J. Phys. Soc. Jpn. **70**, 3475 (2001).

[197] T. Kiyama and M. Itoh, Phys. Rev. Lett. **91**, 167202 (2003).

[198] M. Kubota, H. Nakao, Y. Murakami, Y. Taguchi, M. Iwama, and Y. Tokura, Phys. Rev. B **70**, 245125 (2004).

[199] T. Kiyama, H. Saitoh, M. Itoh, K. Kodama, H. Ichikawa, and J. Akimitsu, J. Phys. Soc. Jpn. **74**, 1123 (2005).

[200] C. Ulrich, A. Gössling, M. Grüninger, M. Guennou, H. Roth, M. Cwik, T. Lorenz, G. Khaliullin, and B. Keimer, Phys. Rev. Lett. **97**, 157401 (2006).

[201] C. Ulrich, G. Ghiringhelli, A. Piazzalunga, L. Braicovich, N. B. Brookes, H. Roth, T. Lorenz, and B. Keimer, Phys. Rev. B **77**, 113102 (2008).

[202] C. Ulrich, L. J. P. Ament, G. Ghiringhelli, L. Braicovich, M. Moretti Sala, N. Pezzotta, T. Schmitt, G. Khaliullin, J. van den Brink, H. Roth, T. Lorenz, and B. Keimer, Phys. Rev. Lett. **103**, 107205 (2009).

[203] J. P. Goral, J. E. Greedan, and D. A. MacLean, J. Solid State Chem. **43**, 244 (1982).

[204] T. Mizokawa and A. Fujimori, Phys. Rev. B **54**, 5368 (1996).

[205] S. Ishihara, Phys. Rev. B **69**, 075118 (2004).

[206] P. Knoll, C. Thomsen, M. Cardona, and P. Murugaraj, Phys. Rev. B **42**, 4842(R) (1990).

[207] R. Rückamp, E. Benckiser, M. W. Haverkort, H. Roth, T. Lorenz, A. Freimuth, L. Jongen, A. Möller, G. Meyer, P. Reutler, B. Büchner, A. Revcolevschi, S.-W. Cheong, C. Sekar, G. Krabbes, and M. Grüninger, New J. Phys. **7**, 144 (2005).

[208] S. Miyasaka, S. Onoda, Y. Okimoto, J. Fujioka, M. Iwama, N. Nagaosa, and Y. Tokura, Phys. Rev. Lett. **94**, 076405 (2005).

[209] C. Ulrich, G. Khaliullin, S. Okamoto, M. Reehuis, A. Ivanov, H. He, Y. Taguchi, Y. Tokura, and B. Keimer, Phys. Rev. Lett. **89**, 167202 (2002).

[210] J. D. Garrett, J. E. Greedan, and D. A. MacLean, Mater. Res. Bull. **16**, 145 (1981).

[211] H. Kramers, Proc. R. Acad. Sci. Amsterdam **33**, 959 (1930).

[212] A. Shitade, H. Katsura, J. Kuneš, X.-L. Qi, S.-C. Zhang, and N. Nagaosa, Phys. Rev. Lett. **102**, 256403 (2009).

[213] D. Pesin and L. Balents, Nature Physics **6**, 376 (2010).

[214] G. Jackeli and G. Khaliullin, Phys. Rev. Lett. **102**, 017205 (2009).

[215] J. Chaloupka, G. Jackeli, and G. Khaliullin, Phys. Rev. Lett. **105**, 027204 (2010).

[216] C. Cosio-Castaneda, G. Tavizon, A. Baeza, P. de la Mora, and R. Escudero, J. Phys. Cond. Mat. **19**, 446210 (2007).

[217] Y. Klein and I. Terasaki, J. Phys. Cond. Mat. **20**, 295201 (2008).

[218] S. Fujiyama, H. Ohsumi, S. Niitaka, T. Komesu, S. Takeshita, B. J. Kim, T. Arima, , and H. Takagi, unpublished.

[219] O. F. Schirmer, A. Förster, H. Hesse, M. Wöhlecke, and S. Kapphan, J. Phys. C **17**, 1321 (1984).

[220] S. J. Moon, H. Jin, W. S. Choi, J. S. Lee, S. S. A. Seo, J. Yu, G. Cao, T. W. Noh, and Y. S. Lee, Phys. Rev. B **80**, 195110 (2009).

[221] S. J. Moon, M. W. Kim, K. W. Kim, Y. S. Lee, J.-Y. Kim, J.-H. Park, B. J. Kim, S.-J. Oh, S. Nakatsuji, Y. Maeno, I. Nagai, S. I. Ikeda, G. Cao, and T. W. Noh, Phys. Rev. B **74**, 113104 (2006).

[222] B. J. Kim, H. Jin, S. J. Moon, J.-Y. Kim, B.-G. Park, C. S. Leem, J. Yu, T. W. Noh, C. Kim, S.-J. Oh, J.-H. Park, V. Durairaj, G. Cao, and E. Rotenberg, Phys. Rev. Lett. **101**, 076402 (2008).

[223] B. J. Kim, H. Ohsumi, T. Komesu, S. Sakai, T. Morita, H. Takagi, and T. Arima, Science **323**, 1329 (2009).

[224] S. J. Moon, H. Jin, K. W. Kim, W. S. Choi, Y. S. Lee, J. Yu, G. Cao, A. Sumi, H. Funakubo, C. Bernhard, and T. W. Noh, Phys. Rev. Lett. **101**, 226402 (2008).

[225] I. N. Hulea, S. Fratini, H. Xie, C. L. Mulder, N. N. Iossad, G. Rastelli, S. Ciuchi, and A. F. Morpurgo, Nature Mater. **5**, 982 (2006).

[226] A. J. Millis, P. B. Littlewood, and B. I. Shraiman, Phys. Rev. Lett. **74**, 5144 (1995).

[227] A. Lanzara, P. V. Bogdanov, X. J. Zhou, S. A. Kellar, D. L. Feng, E. D. Lu, T. Yoshida, H. Eisaki, A. Fujimori, K. Kishio, J.-I. Shimoyama, T. Noda, S. Uchida, Z. Hussain, and Z.-X. Shen, Nature **412**, 510 (2001).

[228] F. Giustino, M. L. Cohen, and S. G. Louie, Nature **452**, 975 (2008).

[229] D. Reznik, G. Sangiovanni, O. Gunnarsson, and T. P. Devereaux, Nature **455**, E6 (2008).

[230] H. Yavaş, M. van Veenendaal, J. van den Brink, L. J. P. Ament, A. Alatas, B. M. Leu, M.-O. Apostu, N. Wizent, G. Behr, W. Sturhahn, E. E. Alp, and H. Sinn, arXiv:1009.4356 (2010).

[231] P. B. Allen, Phys. Rev. B **6**, 2577 (1972).

[232] J. R. Kirtley and F. Tafuri, in *Handbook of High-Temperature Superconductivity*, edited by J. R. Schrieffer (Springer, New York, 2007), p. 19.

[233] P. B. Allen, in *Handbook of Superconductivity*, edited by C. P. Poole Jr. (Academic Press, San Diego, 2000).

[234] J. P. Carbotte, Rev. Mod. Phys. **62**, 1027 (1990).

[235] D. J. Griffiths, *Introduction to Electrodynamics, 3rd ed.* (Prentice Hall, 1999).

[236] M. d'Astuto, P. K. Mang, P. Giura, A. Shukla, P. Ghigna, A. Mirone, M. Braden, M. Greven, M. Krisch, and F. Sette, Phys. Rev. Lett. **88**, 167002 (2002).

[237] W. J. Padilla, M. Dumm, and D. N. Basov, Phys. Rev. B **72**, 205101 (2002).

[238] L. Pintschovius, Physica Status Solidi (B) **242**, 30 (2005).

[239] J. N. Hancock, G. Chabot-Couture, and M. Greven, New J. Phys. **12**, 033001 (2010).

[240] L. Boeri, O. V. Dolgov, and A. A. Golubov, Phys. Rev. Lett. **101**, 026403 (2008).

[241] U. Harbola and S. Mukamel, Phys. Rev. B **79**, 085108 (2009).

SAMENVATTING

Dit proefschrift gaat over resonante inelastische Röntgenverstrooiing ('RIXS', voor het Engelse *Resonant Inelastic X-ray Scattering*). RIXS is een techniek waarmee men, onder andere, de eigenschappen van materialen kan onderzoeken. Dit gebeurt door een soort Röntgenfoto te maken in een synchrotron. Dat is een gigantische, ringvormige deeltjesversneller met een omtrek van honderden meters die zeer intense Röntgenstraling produceert. Deze Röntgenfoto wordt vervolgens vergeleken met berekeningen op basis van verschillende modellen van het materiaal. Zo kan men modellen voor een materiaal falsificeren.

Een belangrijke categorie materialen die vaak onderzocht wordt met RIXS is die van de sterk gecorreleerde elektronmaterialen. Een voorbeeld hiervan zijn de supergeleiders met een hoge kritische temperatuur, zoals $La_{2-x}Sr_xCuO_4$, die een stroom geleiden zonder weerstand als ze worden gekoeld beneden de zogenaamde kritische temperatuur, ver onder nul graden Celsius. In dit proefschrift komen een aantal sterk gecorreleerde elektronmaterialen aan bod, elk met zijn eigen bijzondere eigenschappen.

RIXS

RIXS is een 'foton in - foton uit' techniek, wat betekent dat men het materiaal bestookt met Röntgenstralingsfotonen, die vervolgens verstrooien en gemeten worden. Meer specifiek meet men de energie en impuls van de fotonen. De energie en impuls die het foton verloren heeft, zijn overgedragen aan het materiaal. Met RIXS kan men dus excitaties maken in het materiaal met een bepaalde energie en impuls. Daarom heet RIXS *inelastisch*.

Wat RIXS onderscheid van gewone inelastische Röntgenverstrooiing is het verstrooiingsproces. In RIXS wordt het inkomende foton geabsorbeerd door een elektron in een van de binnenste schillen van een atoom. Het elektron wordt daardoor in een lege baan (a) boven het Ferminiveau geschoten, een gat in een kernschil (kerngat) achterlatend. Daarom heet RIXS 'resonant': de energie van het inkomende foton moet precies genoeg zijn om een elektron uit de kernschil in baan a te schieten. Nu kunnen er twee dingen gebeuren. Bij *directe* RIXS valt een ander elektron uit de valentieband (baan b) terug naar het kerngat. Deze transitie produceert een nieuw, uitgaand Röntgenfoton. Er blijft in de valentieband een excitatie achter: effectief gaat er een elektron van baan b naar baan a. Bij *indirecte* RIXS valt hetzelfde elektron (uit baan a) terug in het kerngat. Er kunnen echter op een indirecte manier excitaties ontstaan omdat het kerngat (eventueel in samenwerking met het elektron in baan a) de valentieelektronen opschudt. Deze interactie is meestal het resultaat van de Coulombkracht, maar kan ook ontstaan doordat het elektron in baan a de beweging van de valentieelektronen blokkeert. De resonantie zorgt ervoor dat RIXS zeer efficient is: er worden veel meer fotonen geabsorbeerd (en vervolgens verstrooid) dan in niet-resonante inelastische Röntgenverstrooiing.

Een voorbeeld van directe RIXS op $\mathrm{La_2CuO_4}$ is als men de inkomende fotonen een energie van 931 eV geeft. Dit correspondeert met de overgang van een 2p elektron van het koper ion naar de 3d schil. Het Cu^{2+} ion heeft maar één vrij 3d orbitaal: $3\mathrm{d}_{x^2-y^2}$. Dit orbitaal wordt gevuld door het elektron. Nu kan een ander 3d elektron, bijvoorbeeld $3\mathrm{d}_{3z^2-r^2}$ terugvallen naar het 2p kerngat. Als men de energie van de inkomende fotonen verhoogt tot 8993 eV, wordt een 1s elektron naar een 4p orbitaal geschoten, ver boven het Ferminiveau. Dit is indirecte RIXS: het 1s kerngat schudt de valentieelektronen op en wordt vervolgens gevuld door het 4p elektron. Natuurlijk kan er ook een ander elektron terugvallen (bijvoorbeeld een 3p elektron), maar deze transitie heeft een veel lagere energie. Door alleen te kijken naar energieën rond de 8993 eV kijkt men alleen naar 4p → 1s transities.

Het kerngat speelt een belangrijke rol in RIXS: het bepaalt het welke transities toegestaan zijn en dus welke excitaties gemaakt kunnen worden. Door het kerngat is de theorie van RIXS bijzonder ingewikkeld. Het kerngat heeft een ingewikkeld effect op de valentieelektronen en de eigentoestanden van dit systeem zijn niet exact te berekenen. In dit proefschrift wordt vaak gebruik gemaakt van een benadering van de dwarsdoorsnede van RIXS die gebruik maakt van de zeer korte levensduur van het kerngat. Het kerngat bestaat maar voor een heel korte tijd omdat het door vele elektronen gevuld kan worden. Omdat het kerngat maar een korte tijd bestaat, hebben de valentieelektronen niet veel tijd om te reageren op de aanwezigheid ervan. De reeksontwikkeling in de levensduur van het kerngat (de zogenaamde UCL reeksontwikkeling) versimpelt de formule voor de dwarsdoorsnede (de Kramers-Heisenbergvergelijking) aanzienlijk.

Excitaties

De meeste materialen die in dit proefschrift worden bestudeerd zijn Mott-isolatoren. Dit zijn materialen waar de elektronen elkaar zeer sterk afstoten via de Coulombkracht. Daardoor ontstaat er de zogenaamde Mott-isolatortoestand waarin elk elektron zijn eigen plaats heeft: een elektron kan niet naar een naburige plaats bewegen omdat daar al een ander elektron is. De gelokaliseerde elektronen zorgen in deze toestand voor lokale vrijheidsgraden: de spin van het elektron en de orbitaal die het bezet.

Hoofdstuk 3 gaat over ladingsexcitaties: het verplaatsen van een elektron van een ion naar een andere. In Mott-isolatoren moet het elektron in kwestie de Coulombafstoting overwinnen van een naburig elektron. Dit kost veel energie: typisch een paar eV. Wanneer een Mott-isolator gedoteerd wordt, ontstaat een situatie waarin niet alle ionen bezet zijn. De elektronen kunnen dus beperkt bewegen. Het resultaat van hoofdstuk 3 voor een Hubbard model met fermionen zonder spin in één band is dat RIXS de dynamische structuurfactor $S(\mathbf{q},\omega)$ meet van de ladingsdragers. Dit is met name interessant voor de hoge kritische temperatuur supergeleider $La_{2-x}Sr_xCuO_4$ omdat zijn ladingsdragers maar één orbitaal bezetten (de x^2-y^2 orbitaal van koper, gehybridiseerd met de zuurstofionen). De spin van de elektronen is irrelevant als dubbele bezetting van ionen niet voorkomt.

In ongedoteerde Mott-isolatoren kost een ladingsexcitatie een energie U voor het dubbel bezetten van een orbitaal. Onder deze energie U zijn er meestal ook excitaties mogelijk. Een elektron kan bijvoorbeeld zijn spin draaien, zonder bij een ander elektron in de buurt te komen. In hoofdstuk 4 worden de magnetische excitaties beschouwd van La_2CuO_4. Dit materiaal is een tweedimensionale Heisenberg antiferromagneet. Met directe RIXS kan men een elektronspin omdraaien, wat in de antiferromagnetische achtergrond een excitatie met een energie tot 350 meV is. De omgedraaide spin beïnvloedt de naburige spins via de superexchange interactie, en hierdoor verspreidt de excitatie zich als een golf door het materiaal. Het kwantum van een spingolf wordt een magnon genoemd. Directe RIXS kan de dispersie van magnonen in kaart brengen. Bij indirecte RIXS is het omdraaien van een enkele spin verboden. Wel kunnen twee elektronen met tegengestelde spin van plaats wisselen, wat voor een dubbele magnonexcitatie zorgt.

Naast magnetische excitaties kan RIXS ook orbitaalexcitaties creëren met een energie kleiner dan U: een elektron gaat naar een andere orbitaal op hetzelfde ion. De energie die hiermee gemoeid is, wordt bepaald door het kristalveld of door superexchange processen. Zowel directe als indirecte RIXS kan een elektron (effectief) van baan doen veranderen. In hoofdstuk 5 wordt het RIXS-spectrum van $YTiO_3$ bestudeerd. Dit materiaal heeft 1 elektron in de Ti 3d schil. RIXS kan dit elektron naar een andere orbitaal exciteren. In hoofdstuk 5 rekenen we twee verschillende modellen door die de wisselwerking van de orbitalen van naburige ionen beschrijven. We concluderen dat experimentele data van Ramanverstrooiing en RIXS aan $YTiO_3$ het best beschreven worden door een superexchangemodel.

In hoofdstukken 4 en 5 keken we naar materialen waar de spin- en orbitaalvrijheidsgraden gescheiden zijn – ze wisselwerken niet met elkaar. Zwaardere ionen zoals iridium hebben wel een sterke spin-orbitaalkoppeling. We bestuderen dit soort materialen (Sr_2IrO_4 in het bijzonder) in hoofdstuk 6. In dit geval maakt RIXS gecombineerde spin-orbitaalexcitaties. Deze aangeslagen toestanden kunnen door superexchange-interacties collectief gedrag ontwikkelen, net als de spingolven en orbitaalgolven van de voorgaande hoofdstukken.

Naast spin- en orbitaalvrijheidsgraden zijn er nog meer excitaties mogelijk bij energiën onder U. Het rooster kan bijvoorbeeld gaan trillen. De kwanta van een dergelijke trilling zijn fononen. RIXS kan fononen creëren door de verandering in de ladingsstructuur in de korte tijd tussen de absorptie en emissie van het Röntgenfoton. De ionen van het rooster reageren op deze ladingsverandering door te gaan trillen. Hoofdstuk 7 onderzoekt hoe het RIXS-spectrum van verschillende typen fononen eruitziet. Niet alleen kan RIXS de dispersie van fononen meten, het is ook mogelijk om de elektron-fononkoppeling te meten door de intensiteit te vergelijken van de 1- en 2-fononpieken. Ook is de impulsafhankelijkheid van de elektron-fononkoppeling uit RIXS-spectra af te leiden.

Als de snelle vooruitgang die RIXS de laatste paar jaar geboekt heeft, doorzet, zal het in de nabije toekomst mogelijk worden om excitaties bij zeer lage energie waar te nemen, zoals excitaties op de schaal van de *gap* in supergeleiders. Ook komen er nu nieuwe Röntgenstralingsbronnen in werking: de zogenaamde *X-ray Free Electron Lasers* die Röntgenstraling met een extreem hoge intensiteit produceren. XFEL's maken nieuwe processen mogelijk die met de huidige synchrotrons ondenkbaar zijn, zoals 2-fotonabsorptie.

PUBLICATIONS

1. L. J. P. Ament, G. Khaliullin, and J. van den Brink, *Resonant Inelastic X-ray Scattering on Spin-Orbit Coupled Insulating Iridates*, arxiv:1008.4862 (2010) [Chapter 6].
2. H. Yavaş, M. van Veenendaal, J. van den Brink, L. J. P. Ament, A. Alatas, B. M. Leu, M.-O. Apostu, N. Wizent, G. Behr, W. Sturhahn, H. Sinn, and E. E. Alp, *Observation of phonons with resonant inelastic x-ray scattering*, arXiv:1009.4356 (2010) [Chapter 7].
3. L. J. P. Ament, M. van Veenendaal, T. P. Devereaux, J. P. Hill, and J. van den Brink, *Resonant Inelastic X-ray Scattering Studies of Elementary Excitations*, arXiv:1009.3630 (2010), submitted to Rev. Mod. Phys.
4. L. Braicovich, M. Moretti Sala, L. J. P. Ament, V. Bisogni, M. Minola, G. Balestrino, D. Di Castro, G. M. De Luca, M. Salluzzo, G. Ghiringhelli, and J. van den Brink, *Momentum and polarization dependence of single-magnon spectral weight for Cu L_3-edge resonant inelastic x-ray scattering from layered cuprates*, Phys. Rev. B **81**, 174533 (2010) [Chapter 4].
5. M. Guarise, B. Dalla Piazza, M. Moretti Sala, G. Ghiringhelli, L. Braicovich, H. Berger, J. N. Hancock, D. van der Marel, T. Schmitt, V. N. Strocov, L. J. P. Ament, J. van den Brink, P.-H. Lin, P. Xu, H. M. Rønnow, M. Grioni, *High-energy magnon dispersion demonstrates extended interactions in undoped cuprates*, arXiv:1004.2441, Phys. Rev. Lett., in press [Chapter 4].
6. L. J. P. Ament, J. van den Brink, *Strong Three-magnon Scattering in Cuprates by Resonant X-rays*, arXiv:1002.3773 (2010).
7. L. Braicovich, J. van den Brink, V. Bisogni, M. Moretti Sala, L. J. P. Ament, N. B. Brookes, G. M. De Luca, M. Salluzzo, T. Schmitt, and G. Ghiringhelli, *Magnetic Excitations and Phase Separation in the Underdoped $La_{2-x}Sr_xCuO_4$ Superconductor Measured by Resonant Inelastic X-Ray Scattering*, Phys. Rev. Lett. **104**, 077002 (2010) [Chapter 4].
8. L. J. P. Ament and G. Khaliullin, *Theory of Raman and Resonant Inelastic X-ray Scattering from Collective Orbital Excitations in $YTiO_3$*, Phys. Rev. B **81**, 125118 (2010) [Chapter 5].

9. L. J. P. Ament, G. Ghiringhelli, M. Moretti Sala, L. Braicovich, and J. van den Brink, *Theoretical Demonstration of How the Dispersion of Magnetic Excitations in Cuprate Compounds can be Determined Using Resonant Inelastic X-Ray Scattering*, Phys. Rev. Lett. **103**, 117003 (2009) [Chapter 4].

10. C. Ulrich, L. J. P. Ament, G. Ghiringhelli, L. Braicovich, M. Moretti Sala, N. Pezzotta, T. Schmitt, G. Khaliullin, J. van den Brink, H. Roth, T. Lorenz, and B. Keimer, *Momentum Dependence of Orbital Excitations in Mott-Insulating Titanates*, Phys. Rev. Lett. **103**, 107205 (2009) [Chapter 5].

11. V. Bisogni, L. J. P. Ament, C. Aruta, G. Balestrino, N. B. Brookes, F. Forte, G. Ghiringhelli, P. G. Medaglia, J. van den Brink, and L. Braicovich, *Effect of the chemical pressure on bimagnons in antiferromagnetic insulators:* $CaCuO_2$ *and* $BaCuO_2$ *studied with Cu-*L_3 *resonant inelastic X-ray scattering*, Eur. Phys. J. Special Topics **169**, 141 (2009) [Chapter 4].

12. L. Braicovich, L. J. P. Ament, V. Bisogni, F. Forte, C. Aruta, G. Balestrino, N. B. Brookes, G. M. De Luca, P. G. Medaglia, F. Miletto Granozio, M. Radovic, M. Salluzzo, J. van den Brink, and G. Ghiringhelli, *Dispersion of Magnetic Excitations in the Cuprate* La_2CuO_4 *and* $CaCuO_2$ *Compounds Measured Using Resonant X-Ray Scattering*, Phys. Rev. Lett. **102**, 167401 (2009) [Chapter 4].

13. F. Forte, L. J. P. Ament, and J. van den Brink, *Single and double orbital excitations probed by resonant inelastic x-ray scattering*, Phys. Rev. Lett. **101**, 106406 (2008) [Chapter 5].

14. D. Kleckner, I. Pikovski, E. Jeffrey, L. J. P. Ament, J. van den Brink, and D. Bouwmeester, *Creating and Verifying a Quantum Superposition in a Micro-optomechanical System*, New J. of Phys. **10**, 095020 (2008).

15. F. Forte, L. J. P. Ament, and J. van den Brink, *Magnetic excitations in* La_2CuO_4 *probed by indirect resonant inelastic x-ray scattering*, Phys. Rev. B **77**, 134428 (2008) [Chapter 4].

16. L. J. P. Ament, F. Forte, and J. van den Brink, *Ultrashort Lifetime Expansion for Indirect Resonant Inelastic X-ray Scattering*, Phys. Rev. B **75**, 115118 (2007) [Chapter 3].

17. L. J. P. Ament and C. W. J. Beenakker, *Deterministic quantum state transfer from an electronic charge qubit to a photonic polarization qubit*, Phys. Rev. B **73**, 121307(R) (2006).

Curriculum Vitae

Personalia

Full name: Lucas Johannes Peter Ament
Born: Winterswijk, 16 November 1982
Email: luukament@gmail.com
Website: http://www.lorentz.leidenuniv.nl/~ament/

Education

2006 – 2010 **Ph.D. in theoretical physics** at the Institute-Lorentz, Leiden University

- Thesis advisor: Prof. Dr. J. van den Brink
- Worked, a.o., in Stuttgart, KITP Santa Barbara, Argonne National Laboratory and Stanford
- Presented research abroad on 15 occasions
- Co-organized the Cambridge-Leiden workshop on quantum matter in May 2009
- Teaching assistant for the courses Quantum Theory and Quantum Field Theory

2001 – 2006 **Doctoraal in physics** (MSc), Leiden University

- Graduated cum laude
- Thesis advisor: Prof. Dr. C. W. J. Beenakker

1995 – 2001 **VWO** at Christelijk College Schaersvoorde, Aalten

Employment

2002 – 2006 **Teaching assistant** at Stichting Studiebegeleiding Leiden

- Subjects: mathematics, physics, economics

Prizes

2008 Third prize in the postercompetition at 'Physics@FOM 2008'

- 300 contestants

2003 Winner of PION '03 (national physics olympiad for students)

- In a team with 3 fellow students